Universität Zürich

Dissertation

Microwave-Assisted Synthesis of Nanostructured Gallium Oxide Materials

Zur Erlangung der naturwissenschaftlichen Doktorwürde (Dr. sc. nat)

Mathematisch-naturwissenschaftliche Fakultät

Franziska Conrad

Promotionskommitee

1. Prof. Dr. Greta R. Patzke

2. Prof. Dr. Roger Alberto

3. Prof. Dr. Roland Sigel

4. Prof. Dr. Heinz Berke

Zürich, 2012

Indes sie forschten, röntgten, filmten, funkten,

entstand von selbst die köstlichste Erfindung:

der Umweg als die kürzeste Verbindung zwischen zwei Punkten.

Erich Kästner

Table of contents

Abbreviations

BET	Brunauer-Emmett-Teller
CB	conduction band
DSC	differential scanning calorimetry
ED	electron diffraction
EDX	energy-dispersive X-ray
EPR	electron paramagnetic resonance
EXAFS	extended X-ray absorption fine structure
FIB	focused ion beam
FWHM	full width at half maximum
HRTEM	high resolution transmission electron microscopy
HT	hydrothermal
LED	light emitting diode
PEEK	polyetheretherketone
LA-ICP-MS	laser ablation inductively coupled plasma mass spectrometry
MSR	methanol steam reforming
MW	microwave
MW-HT	microwave-hydrothermal
OES	plasma emission spectroscopy
PXRD	powder X-ray diffraction
RhB	rhodamine B
SAED	selected area electron diffraction
SEM	scanning electron microscopy
SQUID	superconducting quantum interference device
STEM	scanning transmission electron microscopy
TEM	transmission electron microscopy
TG	thermogravimetry
TPR	temperature programmed reduction
UV/Vis	ultra violet/visible
VB	valence band
WOC	water oxidation catalyst
XANES	X-ray absorption near edge structure
XPS	X-ray photoelectron spectroscopy
XRF	X-ray fluorescence

Publications

The following parts of this PhD thesis have been published:

Chapter 1

Greta R. Patzke, Ying Zhou, Roman Kontic and Franziska Conrad, *"Oxide Nanomaterials: Synthetic Developments, Mechanistic Studies and Technological Innovations*", *Angew. Chem. Int. Ed*. **2011**, 50, 826-859.

Furthermore, Chapter 1 contains adopted passages of abstracts or introductions of the following manuscripts:

Chapter 2

Franziska Conrad, Ying Zhou, Maxim Yulikow, Kathrin Hametner, Stephen Weyeneth, Gunnar Jeschke, Detlef Günther and Greta R. Patzke, *"Microwave-hydrothermal synthesis of nanostructured Zn-Cu gallates"*, *Eur. J. Inorg. Chem.* **2010**, 13, 2036-2043.

Chapter 3

Franziska Conrad, Cyriac Massue, Stefanie Kühl, Edward Kunkes, Frank Girgsdies, Igor Kasatkin, Bingsen Zhang, Matthias Friedrich, Yuan Luo, Marc Armbrüster, Greta R. Patzke and Malte Behrens, *"Microwave-hydrothermal synthesis and characterization of nanostructured copper substituted ZnM_2O_4 (M = Al, Ga) spinels as precursors for thermally stable Cu catalyst"*, *Nanoscale* **2012**, 4, 2018-2028.

Experiments were partially designed and performed by F. Conrad as well as the reduction tests of the gallium catalyst. Structural and catalytical investigations were performed at FHI Berlin and MPI Dresden.

Chapter 4

Franziska Conrad, Matthias Bauer, Stephen Weyeneth, Ying Zhou, Kathrin Hametner, Detlef Günther, and Greta R. Patzke, *"Copper incorporation into gallium spinels through microwave-hydrothermal methods"*, **2011**, submitted.

Chapter 5.5

Franziska Conrad, Matthias Bauer, Denis Sheptyakov, Stephen Weyeneth, Dominik Jaeger, Kathrin Hametner, Pierre-Emmanuel Car, Jörg Patscheider, Detlef Günther and Greta R. Patzke, *"New Spinel Oxide Catalysts for Visible-Light-Driven Water Oxidation"*, RSC Advances **2012**, 7, 3076-3082.

1 Introduction

The development of functional oxide-based nanomaterials has continuously increased over the last years.[1-3] Nevertheless, it remains a challenging field in modern materials chemistry that brings forward new compounds with interesting properties and a high application potential.[4-11]

The application reservoir of oxidic nanomaterials is rich and ranges from catalysts[12] over semiconductors to sensors[13, 14] and many other devices. The special properties of nanostructured oxides in these fields may solve global environmental problems, e.g. the restricted access to clean water.[15] Applying oxide nanomaterials as state-of-the-art photocatalysts and advanced energy systems[16, 17] or in other current technologies such as solid oxide fuel cells[18] may help to overcome the environmental problems of the 21st century. Therefore, new strategies for the straightforward synthesis of nanomaterials – with special emphasis on morphology, phase and composition – encompassing a wide arsenal of chemical[19-22] techniques are required. Furthermore, the combination of nanotechnology with life sciences is expedited[23-25] and sheds new light on therapeutic developments such as the targeting of tumors through magnetic oxide nanoparticles[26] or artificial tissue engineering.[27] Additionally, their application in food technologies, e.g. as food packaging, new polymers and nanosensors[28] becomes more and more important.

Regarding the aforementioned wide application potential of nanomaterials which has been extensively discussed,[29-34] new and easily applicable synthetic methods for nanostructured functional oxides need to be developed.

Interestingly, materials in the nanometer range exhibit different materials properties than their larger dimensioned counterparts which influences their electronic[35, 36] and magnetic properties,[37, 38] as well as mechanical plasticity[37, 39, 40] or phase transition temperature,[41-44] only to mention a few of these size-dependent effects. Unfortunately, only few concepts are available to fully explain and explore the advantages of nanomaterials, e.g. correlation of particle sizes with the characteristic length scale of a specific property. Ferroelectric and ferromagnetic materials may serve as an example, because they exhibit domain sizes which are connected with particle dimensions.[45] On the other hand, nanomaterials often have surfaces with plenty of atoms, especially in particles below 10 nm[46] which influence the reactivity of

the material significantly, e.g. resulting in decreased glass transition temperature in thin films of polymer glasses.[42]

In the following, a survey of the challenging synthesis and the huge application potential of transition metal nano-oxides is given. Special emphasis is placed on state-of-the art synthetic techniques such as microwave-assisted approaches. The basics of microwave-matter-interactions are explained, followed by the general implementation of microwave radiation in daily laboratory work for synthetic approaches on a minute scale. Starting from structural insights into spinels as one of the most important functional oxide type, the effect of Jahn-Teller ions (preferably 3d transition metals) incorporated in the spinel matrix will be discussed. Additionally, the consequences of structural changes within the spinel lattice are pointed out from the materials properties point of view – the special magnetic behaviour of spinels together with further structural investigations upon Jahn Teller ion containing oxides are addressed. Finally, the discussion is rounded off with a demonstration of how tailoring oxide nanomaterials paves new ways to the most relevant catalytic applications, such as water splitting, methanol steam reforming or CO conversion.

Therefore the focus of the following section (1.1) is placed on the synthesis and characterization of nanostructured oxidic materials. On the other hand, the technical and theoretical perspectives of the materials under investigation are the scope of Chapter 1.2.

1.1 Nanoscale transition metal oxides and their synthetic challenges

The abovementioned indispensability of oxide materials as technological building blocks can be further amplified through the synthesis of oxide solid solutions and their transformation into nanoscale dimensions.[47, 48]

Over the past centuries, traditional solid state synthesis methods, e.g. ceramic high-temperature techniques, have been well established[49, 50] and they are still applied for many large-scale technological productions, but are not very well suited for nanomaterials synthesis. Therefore, new methods have been developed for nanoparticle synthesis within the past decades to face this problem. Hydrothermal (HT) approaches, for example, excel through simple set-ups, low synthesis temperatures, morphology control and preference for crystalline products.[3] On the other hand, this synthetic technique also has some disadvantages: the parameter

systems are often too complex for the limited number of theoretical hydrothermal concepts to be applied in a predictive manner. Moreover, solvents can participate in the reaction, *in situ* analysis of synthetic processes is difficult due to the closed reaction systems and, more importantly, due to the long initial heating period to the desired temperature which directly influences the homogenous heat profile within the autoclave.

In the following, new developments for the targeted syntheses of nano-oxides are presented that have a high potential for time and energy saving technical processes.

1.1.1 Microwave-assisted strategies

Microwave-solvothermal processes (MW-ST) overcome the heating problems of conventional HT methods by rapid and homogenous heating of the reaction mixture to the desired temperature (Figure 1.3). Therefore, they open up new options for energy- and cost-saving approaches towards nanoparticles production.[51, 52] In addition, this state-of-the-art technique is also time-saving through dramatically increased crystallization kinetics and it provides access to novel or metastable phases.[53]

The efficiency of microwaves to enhance organic reactions as well as the synthesis of solid materials has been widely demonstrated.[54, 55] This effect has been explained on the basis of several hypotheses: in addition to the increase of the net rate through rapid and more uniform heating, microwaves also change the association between reactive species and give rise to superheating phenomena. The creation of "hot spots" and the enhanced dissolution of reactants can furthermore promote the reactivity of microwave-assisted processes.[54] Further details towards *in situ* methods are described in Chapter 1.1.6.

Microwave-assisted synthesis of key building block nanomaterials

In the following, the rapid development of MW-HT techniques for the synthesis of zinc oxides as key building block for the $ZnGa_2O_4$ spinels investigated in this thesis is illustrated, followed by an outlook on new synthetic avenues to other interesting oxide-based materials. A survey of recent literature for further reading can be found in Table 1.1-3 on pages 9 and 10.

Among the multitude of publications on the synthesis of ZnO due to its unique optical and electronic properties, a recent study on the non-aqueous microwave synthesis of ZnO nanoparticles clearly demonstrates the advantages of the microwave-mediated route over conventional synthetic approaches on the basis of kinetic investigations.[56]

Given that MW-ST processes offer even more reaction parameters than conventional approaches, methodological investigations are indispensable to explore the full potential of this new synthetic method. The applied microwave power, for example, exerts a tremendous effect on the morphology of the hierarchical ZnO nanostructures emerging from the water/ethylene glycol (EG) system.[57] Such phenomena are discussed in Chapter 3. Another powerful strategy for MW-ST morphology control is the solvent composition as has been illustrated recently for the formation of ZnO particles in water/EG mixtures.[58] As an additional benefit, the obtained materials display enhanced photocatalytic activity.

Furthermore, the wide parameter window for controlling microwave-assisted processes is evident from a recently reported self-assembly route towards ZnO nanostructures using solvents with dual functions – namely as a capping agent and for adjusting the pH value which is a key parameter to adjust the product morphology within a remarkably short reaction time of 90 seconds.[59]

Microwave-assisted syntheses are currently being explored for the synthesis of a wide spectrum of target materials ranging from binary functional oxides to the more complex ternary ones. The formation of α-Fe_2O_3 nanorings, for example, sheds an interesting light on the superheating and nonthermal effects during microwave-assisted processes.[60]

1.1.2 Application potential of $ZnGa_2O_4$ spinels

Spinels are an important class of materials among the large family of functional oxides and zinc gallate, $ZnGa_2O_4$, is a particularly interesting representative that attracts considerable research attention. Firstly, this transparent and conductive material has a high application potential in field emission displays (FEDs), electroluminescent components (ELDs)[61, 62] or in plasma display panels for novel LED technologies that are superior to the conventional light sources.[63, 64] Moreover, $ZnGa_2O_4$ displays promising photocatalytic properties in the degradation of benzene[65] or methylene blue (MB)[66] as important representative compounds for environmental pollutants. Furthermore, the high potential of $ZnGa_2O_4$ materials for photocata-

lytic water splitting[67, 68] is just being explored. Generally, control over the particle size, surface area, crystallinity and dopant content is indispensable to develop $ZnGa_2O_4$-based photocatalysts for urgent environmental applications. The regular and oxidation-stable spinel lattice of $ZnGa_2O_4$ is not only an ideal catalytic matrix but also very interesting from the structural point of view for the study of solid solutions and their resulting electronic properties.[69]

The optical band gap of $ZnGa_2O_4$ ranges from 4.4 to 5.0 eV[70] and the resulting blue emission can be shifted to green and red by doping with Mn^{2+} and Cr^{3+} ions, respectively.[61, 71, 72] The remarkable effect of guest cations on the optical, structural and morphological properties of mixed zinc gallates has been demonstrated in numerous works.[63, 72-77] However, little is known about Cu-substituted zinc gallates and the investigation of the effect of copper substitution on the luminance and conductivity of mixed zinc gallates is one of the very few works in this direction.[77] Cu-containing zinc gallium spinels are interesting precursors for new materials, such as nanoscale Cu catalyst centers that are embedded into a stable and inert oxide matrix.[78] New results on nanostructured Cu^{2+}-substituted $ZnGa_2O_4$ spinels are reported in Chapter 2.

1.1.3 Application spectrum of ZnM_2O_4 (M = Al, Ga)

The informed design and understanding of oxide catalysts is a topic of urgent research interest for the synthesis of basic chemicals as well as for sustainable energy strategies, such as CO_2 conversion or clean hydrogen production.[79] Methanol, for example, covers present synthetic needs and will become even more essential as a fuel carrier for next-generation technologies.[80-83] Although the massive worldwide methanol demands are well covered with the industrial $Cu/ZnO/Al_2O_3$ catalysts for the conversion of syngas ($CO/CO_2/H_2$) into methanol, the underlying reaction mechanisms still remain to be explored.[84] This has aroused intense research interest in the structure and reactivity of this catalytic oxide system and related materials.[85] $Cu/ZnO/Al_2O_3$ catalysts are furthermore active in the mostly undesired and concurring reverse water gas shift reaction of CO_2 and H_2 to CO and H_2O as well as in the far more important recovery of H_2 from methanol/H_2O mixtures known as the methanol steam reforming reaction (MSR). Commercial catalysts have been thoroughly tailored for industrial methanol synthesis (elevated pressure, 200 – 300 °C), but further optimization of their activity, selectivity and stability is required for their allround use, especially in MSR reactions for future hydrogen-based technologies.

For this purpose, the influence of the preparative strategy on the final catalyst properties has to be known in detail. Industrial $Cu/ZnO/Al_2O_3$ catalyst synthesis is a complex multi-step process[86] that depends on the controlled segregation of CuO and ZnO from a homogeneous hydroxycarbonate precursor, followed by the efficient reduction of the resulting CuO nanoparticles to accessible Cu catalyst centers. The composition of the precursor phase is vital for controlling the catalyst microstructure which in turn determines particle size, crystallinity, Cu lattice strain and particle embedment.[85, 87] All these factors affect the exposed Cu surface of the final catalytically active Cu/ZnO composites via their metal-oxide interactions. This is a major driving force for the exploration of novel precursor compounds with structurally flexible arrangements of Cu^{2+}, Zn^{2+} and Al^{3+} in search of $Cu/ZnO/Al_2O_3$ catalysts with new microstructures and improved CO_2 hydrogenation or MSR performance.

In this context, the spinel-type oxide $A^{II}B^{III}_2O_4$ (A = Cu, Zn; B = Al or Ga) is an attractive oxide matrix due to its high thermal stability and mechanical resistance together with the advantage of hosting all three relevant metal species in a mixed cation lattice. The catalytic investigations are discussed in Chapter 3.

1.1.4 Challenging access to γ-Ga_3O_4:Cu^{2+} spinels

Gallium oxide and its mesostructured forms are promising catalytic materials, e.g. for epoxidation reactions[88, 89] and photocatalytic processes.[90] Therefore, it has been accessed with a wide range of preparative methods, such as precipitation,[91] adsorption[92] and microwave-assisted techniques.[93] Nevertheless, the catalytic potential of the defect spinel modification γ-Ga_2O_3 [94] has rarely been explicitly investigated – in sharp contrast to the multitude of studies on γ-Al_2O_3 and selected reports on mixed γ-Ga_2O_3-Al_2O_3 catalysts, e.g. for NO reduction.[95] Despite its favorable catalytic[96, 97] and optoelectronic[98] behavior, the specific host properties of the gallium oxide spinel matrix for metal catalyst incorporation are far less explored than their Al-containing counterparts. In addition, structural insight into this material is difficult to obtain: after the first analysis in 1968,[99] many decades passed until more profound preparative and analytical studies followed.[100, 101] As a consequence, the first syntheses of nanosized γ-Ga_2O_3, including template-assisted microwave methods,[93] have only recently been published[102, 103] and spinel-type gallium oxynitrides have been accessed with advanced high pressure approaches.[104]

However, copper incorporation into nanostructured γ-Ga_2O_3 host matrices has not been reported to date, although this is a topic of urgent interest, given that spinel phase formation is often involved in the synthesis of industrial Cu/ZnO/Al_2O_3 catalysts for methanol synthesis.[105] Amorphous as well as crystalline copper-containing catalysts in general display a wide application range in environmental and synthetic chemistry, e.g. for water-gas shift reactions or NO_x reduction.[106] Whereas $CuGa_2O_4$ has been applied in the catalytic steam reforming of dimethyl ether,[107] or for visible-light-driven H_2 production from H_2S after doping with Fe^{III},[108] the full application potential of nanoscale γ-Ga_2O_3:Cu^{2+} remains to be discovered. First reports on Cu-containing Ga_2O_3, albeit with no detailed investigations of phases and morphologies involved, showed promising results in NO_x reduction[109] and copper-doped mixed γ-Ga_2O_3-Al_2O_3 materials were applied for steam reforming of dimethyl ether.[110]

A new preparative route towards nanostructured copper substituted γ-Ga_2O_3 is presented in Chapter 4, together with comprehensive analytical investigations, such as EXAFS and XPS, and according preliminary reduction tests for catalytic applications.

1.1.5 Cobalt and manganese gallium oxide spinels

Consequently, binary Co- and Mn-oxides have been identified as WOCs, e.g. Co_3O_4 and manganese oxide clusters on silica scaffolds,[111] α- and β-MnO_2 nanowires[112] or nanostructured Mn-oxide films with Mn(III) species.[113] Only recently have the first ternary Co- or Mn-based oxide WOCs been discovered, such as $CaMn_2O_4 \cdot xH_2O$ as the first bio-inspired heterogeneous catalyst[114] or spinel-type $LiMn_2O_4$ as a source for λ-MnO_2 WOCs with Mn_4O_4-motifs.[115] Generally, the structural and compositional variability of spinels render them an inexhaustible source for new catalytic materials as demonstrated by newly synthesized nanostructured $Co_xMn_{3-x}O_4$ electrocatalysts for oxygen reduction/evolution.[116] Although Zn/Ga-oxide[117] and oxynitride[118] photocatalysts have attracted intense research interest as water splitting catalysts, they still require activation with noble metal containing cocatalysts. Likewise, spinel-type MGa_2O_4 (M = Zn, Ni) catalysts are only catalytically active under UV light when activated with RuO_2 or Rh_2O_3.[67, 119] Therefore, the highly tuneable and chemically stable compound family of gallium spinels remains to be explored for the development of convenient visible-light-driven WOCs.[120]

1.1.6 *In situ* investigation of microwave-assisted processes

Microwave-assisted techniques provide access to otherwise elusive nanomaterials on a rapid timescale. In order to control their large-scale technological application, their reaction pathways and mechanisms need to be developed.

Investigating the influence of reaction parameters, such as temperature and power of the microwave device is important to understand these "black box" systems. By varying the power of the microwave, completely different morphologies of ZnO hierarchical nanostructures were obtained.[57] The formation of nanostructured α-Fe_2O_3 toroids could be explained by superheating and nonthermal effects[60] which may result in the frequently discussed occurrence of "hot spots". Numerous of these "hot spots" may lead to nucleation, crystal growth and the formation of seeds caused by microwave irradiation.

All in all, it will be a challenging task for scientists worldwide to investigate and then to elucidate the mechanisms taking place during a microwave-assisted synthesis in their entirety. *In situ* investigations will be a crucial point for further development of this method, especially in terms of technical microwave applications. Recently, first concepts to understand the mechanism of MW-ST reactions were obtained by comparing the kinetics of organic side reactions with the growth rates of nanoscale ZnO products.[56] This elegant indirect method is a promising starting point and should be extended into more direct *in situ* methods as will be discussed in Chapter 6.

Table 1.1. Selected recent hydro- and solvothermal approaches to oxide nanomaterials (target oxides are listed in alphabetical order and proceeding from binary to higher systems).

Oxide	Solvent/Additives	Morphology	Lit.
Morphology control of binary oxides			
CeO_2, CuO, Co_3O_4, Fe_2O_3, MgO, NiO	Water, glucose	Nanoparticles, arranged in hollow microspheres	[121]
CuO	Water, sodium citrate	Nanosheets, -rods, -stars	[122]
Fe_2O_3, Fe_3O_4	Water, Na_2SO_4/Na_2HPO_4	Short nanotubes	[123]
Fe_3O_4	Water/ethanol, oleic acid	Nanocubes	[124]
ZnO:Co/Mn	Benzyl alcohol/anisole	Nanoparticles, -rods, -fibres (depending on solvent mixture)	[125]

Table 1.2. Synthesis of ZnO nanomaterials with microwave-assisted techniques (MW = microwave, ST = solvothermal, HT = hydrothermal, cf. discussion in section 1.1.2.).

Oxide	Technique	Morphology / Special Features	Lit.
ZnO	Nonaqueous sol-gel MW approach	Kinetic correlation between organic reaction process and ZnO particle growth	[56]
	MW-ST with ethylene glycol	Bundles, flower-like morphologies and microspheres depending on heating parameters	[57]
	Co-doped ZnO MW-ST with ethylene glycol	Nanopowders (particle size < 50 nm)	[126]
	MW-ST with ethylene glycol	Variety of ZnO nanoparticles (rods, spheres, peanut-shaped…) depending on ethylene glycol content	[58]
	MW-HT and MW-ST, different precursors and various solvents/capping agents	Wide nanoparticle spectrum (rods, needles, disks, star-shapes, spheres etc.)	[127]
	MW synthesis using triethanolamine as capping agent	Spherical, raspberry-like and hollow spherical nanostructures by self-assembly of Zn^{2+} ionic complexes	[59]
	MW-ST using hexamethylenetetramine (HMT)	ZnO rods with various morphologies like bi-, tri- and tetrapods, oriented growth	[128]
	MW-HT	Zincite structure	[129]

Table 1.3. Combined synthetic routes to nanostructured oxides (examples are sorted in alphabetical order).

Oxide	Technique	Morphology / Features	Lit.
CuO	MW-IL using [Bmim][BF_4]	Leaf-, chrysanthemum- and rod-like shapes with varying IL concentration	[130]
	MW-IL using [Omim][TA]	Flower- and leaf-like structures with varying IL concentration	[131]
	US-IL using [C_4mim][TF_2N]	Rod-like shapes (30-100 nm in length and 10 nm in diameter)	[132]
ZnO	MW-IL	Flower- (more water) and needle-like (more IL) shapes	[56]
	US-IL using [C_4mim][Tf_2N]	Rod-like shape (50-100 nm length range) and 20 nm diameter	[133]
Other oxides			
FeOOH, α-Fe_2O_3	MW-IL using [Bmim][BF_4]	Hollow spheres in μm range for FeOOH, spherical α-Fe_2O_3 particles (~ 20 nm) synthesized without IL	[134]
$La_{0.8}Sr_{0.2}Co_{0.5}Fe_{0.5}O_{3\pm\delta}$	MW + sol-gel using [Bmim][BF_4]	Perovskite structure with spherical morphology	[135]

1.2 Microwave-hydrothermal techniques[136, 137]

Microwaves have a wavelength between 0.01 and 1 m which corresponds to frequencies between 30 and 0.3 GHz covering the range from radio waves to infrared light in the electromagnetic spectrum. Ever since Maxwell predicted the existence of electromagnetic waves in 1873, the development of microwaves especially for application in daily life increased tremendously: their first practical use was in radar techniques during World War II and since 1960 a flurry of commercial manufacturing microwave devices and processes followed, especially for food preparation (tempering frozen food, pasta drying, baking, sterilization, vacuum drying etc.). Navigation and communication developments within the last decades, e.g. radar, mobile devices and Bluetooth®, only to mention a few branches, play an important role in the information technology of the 21st century.

1.2.1 Microwave-matter interactions

The interaction between microwaves and matter is similar to the interplay of light waves with materials: they change direction while moving from one dielectric material into another (i.e. they are refracted) and reflection occurs for metallic objects as well as absorption by some dielectric media.

In principle, waves are transitions between positive and negative values of a given entity that either reinforce or cancel each other. Hence, areas of high and low energy, so-called *modes*, are generated for stationary waves as well as points of zero energy (*nodes*). Any substance in a vessel – may it be a beaker or a cup of milk – placed at the border between modes and nodes, will be superheated due to different energy absorption modes. Therefore, conventional microwave ovens are equipped with turning tables to prevent boiling delay.

Each material has a specific ability to absorb microwave energy and to convert it into heat which causes microwave dielectric heating. Microwaves are high frequency oscillating electric and magnetic fields (cf. Figure 1.1) and anything exposed to their field will be affected – if electrically or magnetically polarized at the respective oscillation frequency. Interaction of the electric field component of the wave with charged particles in the material leads to heating effects.

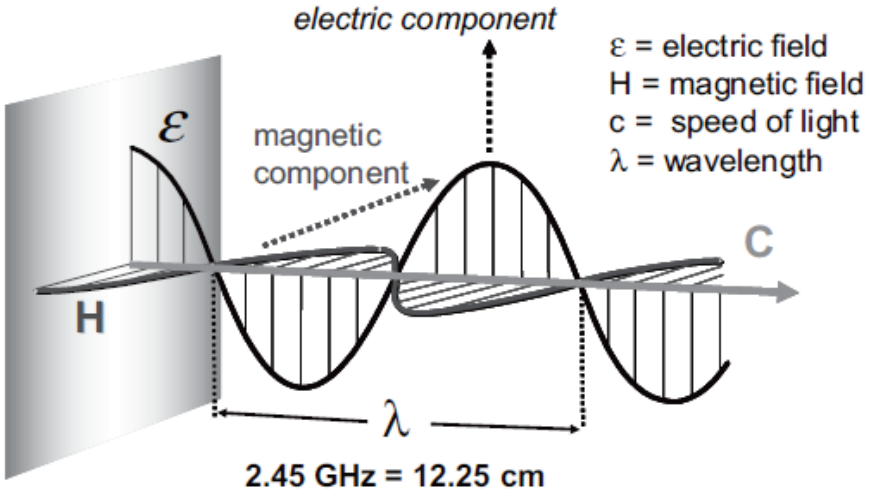

Figure 1.1. Schematic illustration of electric and magnetic field interactions. Picture taken from [136].

There are two pathways for microwave-induced heating effects, namely ionic conduction or dipolar polarization, as described below.

If the irradiated sample is an electrical conductor, the charge carriers (electrons, ions, etc.) are moved through the material under the influence of the electric field, ***E***, resulting in polarization, ***P*** (cf. Figure 1.2b). The charged particles move under the influence of the electric field and collide with their neighboring molecules or atoms to induce heating. This so-called conduction effect is most important for the heating properties of ionic liquids as key solvents for modern synthetic applications.

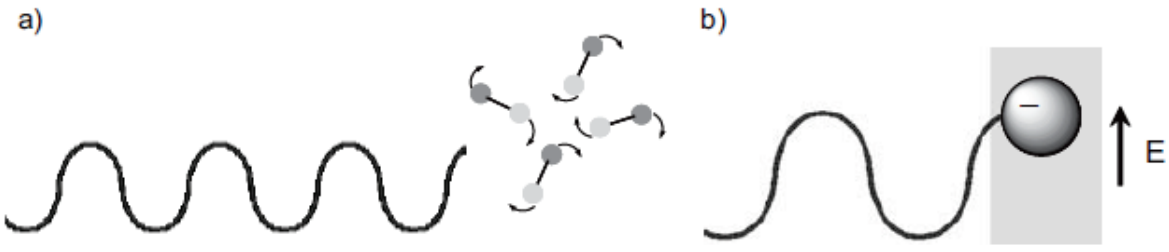

Figure 1.2. Two pathways of microwave heating: (a) dipolar polarization mechanism: dipole moments of the molecules try to align with the oscillating electric field and (b) charge carriers move in the electric field and ionic conduction results. Picture taken from [136].

The effect of ionic conduction is much stronger with respect to heat-generating capacity than the second option of microwave heating – the dipolar polarization. This heating method is mainly caused by the interaction of the electric field with the dipole moments of the molecules. The oscillating electric field causes molecule rotation which is equivalent with the alignment of polar entities with the changing field (cf. Figure 1.2 a). The moving molecules generate thermal energy which leads to the rapid temperature increase that renders microwave methods so powerful.

1.2.2 Microwave-assisted chemistry

As microwave irradiation ranges at such low frequency in the electromagnetic spectrum, it will only cause bonds to rotate, not to break - this renders it suitable for promoting chemical reactions.

Since the 1970s tremendous efforts have been made to establish microwave heating in chemical synthesis. The advantages of microwave-assisted techniques are:[138]

- Rapid heating to target temperature
- Increased reaction kinetics by one to two orders of magnitude
- Access to novel/metastable phases
- Selective crystallization/new particle morphologies

Over the past decades, the development of microwave-assisted syntheses has been driven forward, especially in organic reactions.[139, 140] The advantage of microwave-hydrothermal (MW-HT) over conventional hydrothermal (CV-HT) heating is demonstrated in Figure 1.3: the desired temperature is reached much faster with microwave-assisted techniques. In contrast, conventional heating methods suffer from slow and inefficient energy transport and furthermore depend on the thermal conductivity of the various materials.

On the other hand, the homogenous heat distribution throughout the reaction vessel as shown in Figure 1.4 (left) prevents superheating and causes instant temperature increase within seconds. The applied vessels are made of microwave transparent media (e.g. borosilicate glass, quartz or Teflon®) so that the waves can pass the vessel walls which cause an inverted temperature gradient if compared to the conventionally heated sample.

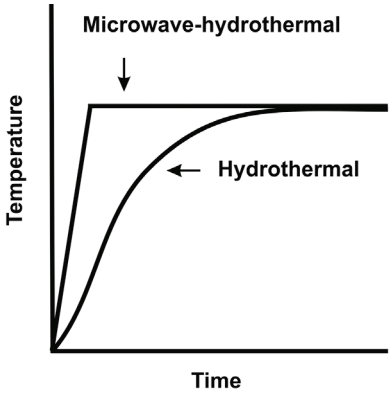

Figure 1.3. Comparison of microwave-assisted and conventional hydrothermal heating. Picture taken from [3].

The increasing temperature is homogenously distributed through the sample if the microwave cavity is thoroughly designed – as, for example, in the MARS5 microwave reactor (CEM Corporation) used within this study (Figure 1.4 right). The MARS5 system consists of a multi-mode cavity which produces a microwave field of multiple modes with additional variations of energy intensity.

a)

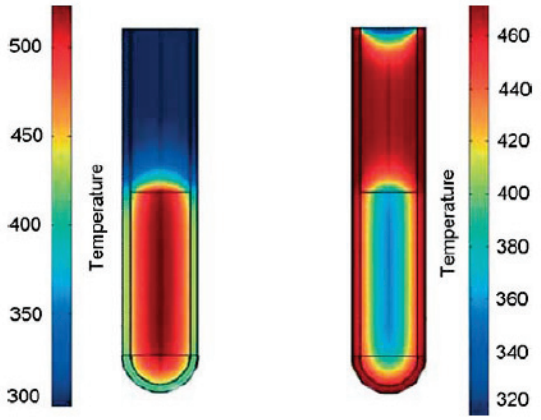

b)

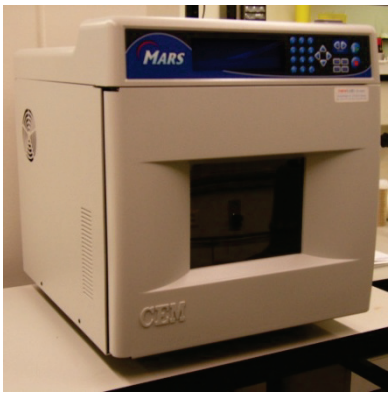

Figure 1.4. (a) Temperature profiles affected by microwave irradiation (left) and by oil bath heating (right); (b) MARS5 microwave reactor (CEM Corporation) used for the MW-HT synthesis in this study.

The above MARS5 microwave reactor model has a continuous power delivery of 1600 W and can be equipped with 5 - 12 Teflon® reaction vessels (95 ml) for one synthesis run. Temperature and pressure control are directly achieved with a single reference vessel which contains a microwave transparent fiber optic temperature and an appropriate pressure sensor. Additionally, the temperature of all vessels is monitored by IR sensors so that real-time internal temperatures can be obtained which notably enhances the safety of the

microwave reactor. The so-called DuoTemp system adjusts the method in response to the measured temperatures in all vessels and regulates the microwave power accordingly. The measured temperature and pressure values can be observed online throughout the whole synthesis.

1.3 Structure and coordination of spinels[141-143]

Generally, spinels are AB_2X_4 type compounds which can be formed from oxides, sulfides, selenides or halogenides. Ideal oxidic spinels consist of a cubic closed packing of oxygen atoms with 1/3 of the metal ions located in the tetrahedral voids (A sites) and 2/3 the octahedral voids (B sites), resulting in the general formula $A_T[B_2]_OO_4$. Figure 1.5 shows the corner sharing tetra- and octahedra (left) as well as the spinel unit cell (right). The tetrahedral voids are smaller than the octahedral ones and the metal ions on the A sites should thus be smaller compared to the ions on the B sites.

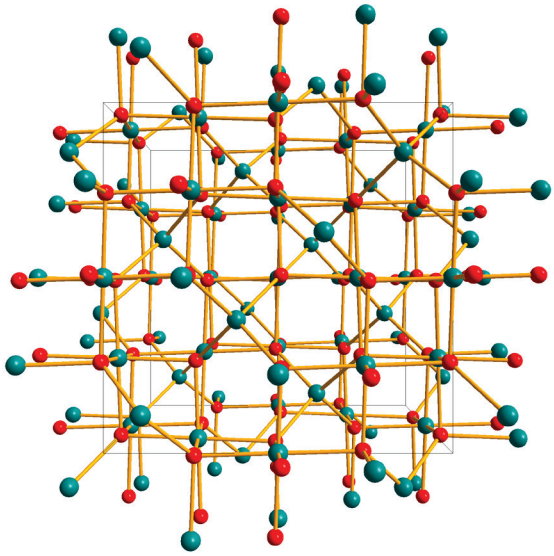

Figure 1.5. Six oxygen atoms coordinate a metal ion (B site) and form octahedra which are edge linked to tetrahedra build from four oxygen atoms surrounding an A ion. A representative unit cell of $CoGa_2O_4$ is shown.

Inverse spinels are important exceptions from the above rule: here, the B ions occupy tetrahedral and octahedral voids, whereas the A ions are relocated to octahedral sites. The degree of inversion is indicated with an index (y) in the formula: $(A_{1-y}B_y)_T[A_yB_{2-y}]_OX_4$. The according polyhedra of the inverse γ-Ga_2O_3 are presented in Figure 1.6 (right).

The estimation of the cationic distribution and degree of spinel inversion only on the basis of cationic radii is an incomplete approach. Most real spinel-type compounds are distorted due to enlarged tetrahedral voids so that their interpretation in terms of cationic radii and electrostatic interactions is insufficient. This applies especially for transition metal compounds with significant ligand field effects. The influence of high and low spin states caused by the strength of the ligands is crucial for the formation of inverse spinels.

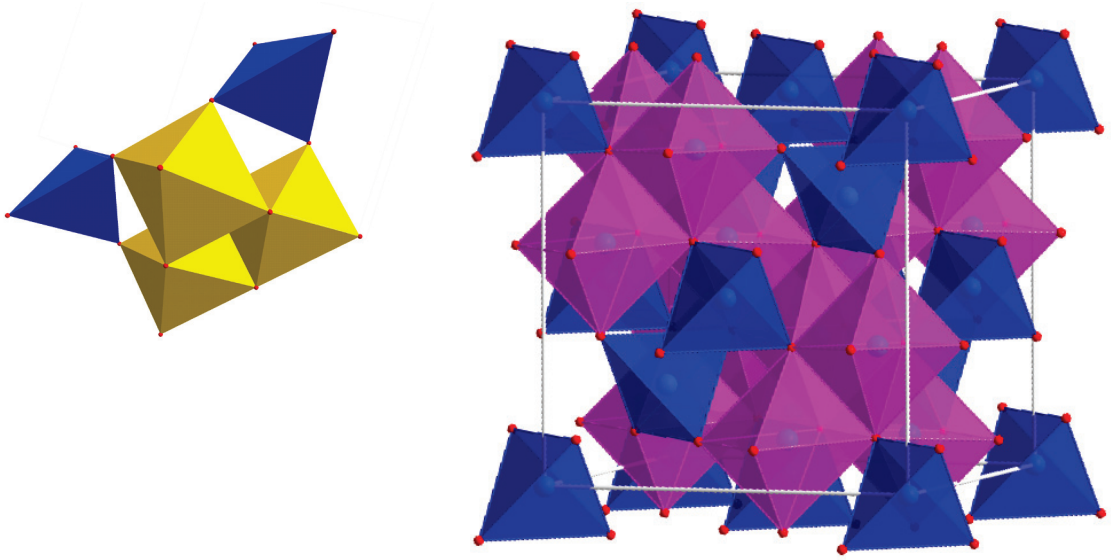

Figure 1.6. Polyhedra illustration of inverse spinels: corner sharing tetrahedra and the edge sharing octahedra in $CoGa_2O_4$ (left) and unit cell of Ga_2O_3 (right).

Additionally, the distribution of the cations is influenced by their radii which decrease within the 3d transition metal row ($Mn^{2+} > Fe^{2+} > Co^{2+} > Ni^{2+} > Cu^{2+} > Zn^{2+}$) with the tetrahedral coordination becoming more favorable towards the end of the series (cf. Figure 1.7). Two observed minima are observed for high-spin compounds due to the ligand field stabilization energy: d^3 and d^8 (Ni^{2+}) for octahedral and d^2 and d^7 (Co^{2+}) for tetrahedral coordination.

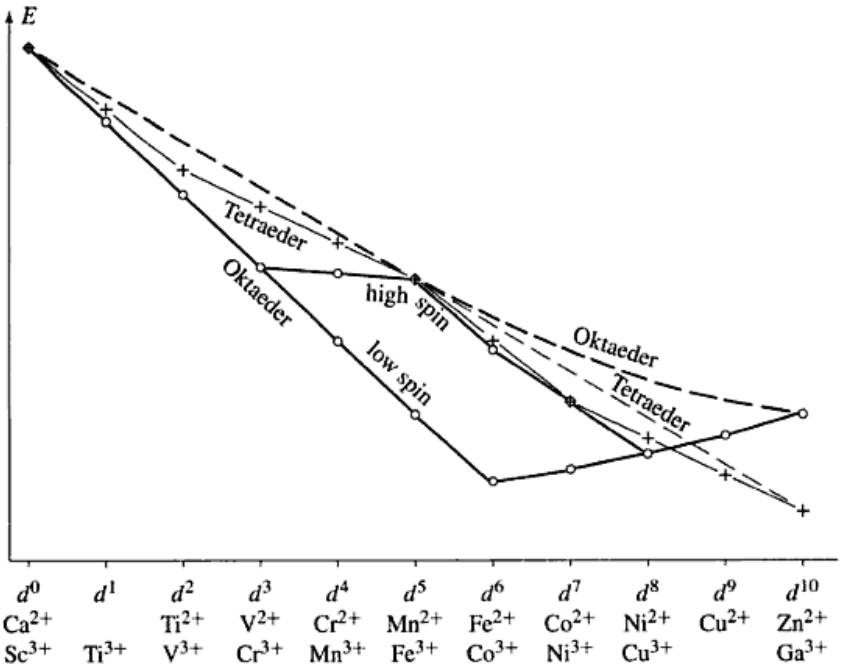

Figure 1.7. Relative ligand field stabilization energy for 3d-ions without Jahn Teller effect. Bold lines: octahedral field, fine lines: tetrahedral field, dashed lines: energy for (fictitious) spherical d-electron distribution. If the Jahn Teller theorem is considered, the value for octahedral Cu^{2+} coordination is downshifted towards an energetically favored constitution. Picture taken from [142].

1.3.1 Jahn Teller effect

For some paramagnetic substances the e_g degenerated orbitals are only partially occupied and therefore cause a strong repulsion towards the binding electrons of the ligands in z direction. These ligands are pushed away, resulting in an energetically preferred, elongated octahedron as can be seen in Figure 1.8. Examples for this Jahn Teller distortion in octahedral coordination can be found for electron configurations such as d^4 high spin [Cr(II), Mn(III)], d^7 [Ni(III)] or d^9 [Cu(II)]. Analogous distortions are also observed for tetrahedral coordination: flattened tetrahedra result for d^4 and d^9 systems, whereas for d^3 and d^8 configuration, elongation is expected.

If the Jahn Teller effect for cubic crystallized compounds is significant and leads to extreme elongation along the octahedral z axis, the overall symmetry is lowered to tetragonal.

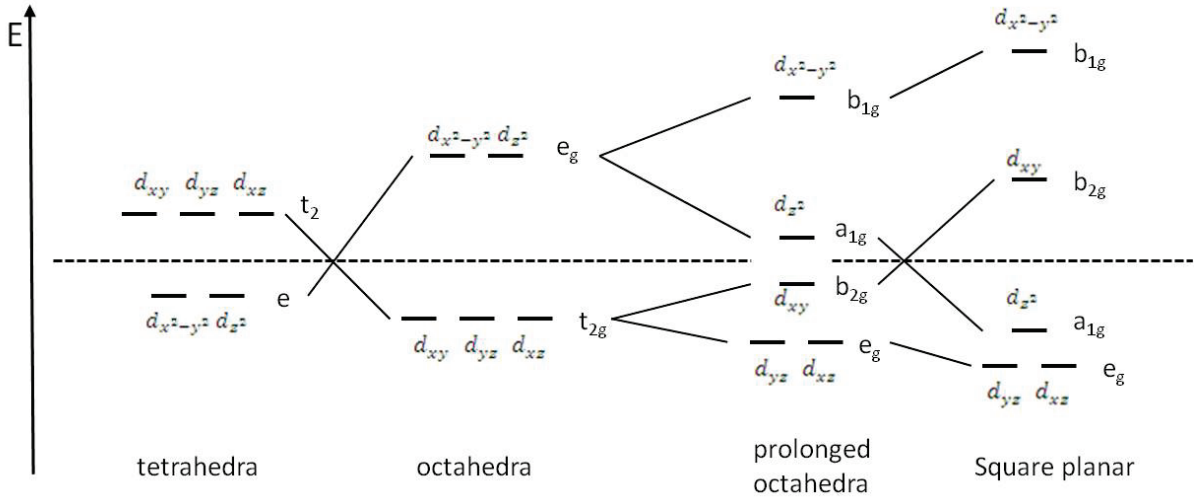

Figure 1.8. Relative energy diagram for electrons in d-orbitals within different geometric constitutions. Picture adopted from [142].

In summary, for the estimation of cationic distribution and inversion in spinels, manifold parameters (e.g. cationic radii, electrostatic interactions, high or low spin configurations and Jahn Teller distortions) need to be taken into consideration.

1.4 Magnetism of transition metal compounds[144, 145]

In magnetic and isotropic media the magnetic field strength ***H*** and the magnetic flux density ***B*** are oriented equally so that these two forces can only be oriented in a parallel or antiparallel manner. Generally, the magnetization ***M*** is proportional to the magnetic field strength and can be described as $\boldsymbol{M} = \chi \boldsymbol{H}$ (χ = dimensionless magnetic susceptibility). Nevertheless, the molar susceptibility χ_{mol} (in m^3/mol) is preferred for practical reasons.

Three types of magnetism in materials can be distinguished: diamagnetism, collective magnetism and paramagnetism. Compounds without unpaired electrons possess a resulting magnetic moment of zero and are therefore diamagnets. On the other hand, compounds with unpaired electrons exhibit paramagnetic behavior and show positive susceptibility which becomes more pronounced with decreasing temperature. Ideally, the magnetic susceptibility is inversely proportional to the temperature (Curie law, $\chi_{mol} = \frac{C}{T}$) but most often a discrepancy to this ideal behavior is observed (Figure 1.9), caused by spin ordering below a substance specific temperature.

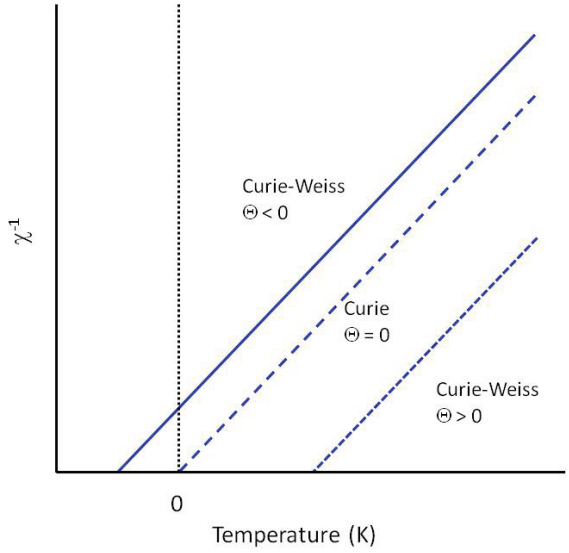

Figure 1.9. Characteristic susceptibility vs. temperature plots for Curie and Curie-Weiss behavior; adopted from [145].

The influence of the temperature requires a correction parameter θ to be included in the Curie-Weiss-Law as follows:

$$\chi_{mol} = \frac{C}{(T-\theta)}. \qquad \text{(Eq. 1.1)}$$

The Weiss constant θ specifies the magnetic behavior of paramagnetic substances below the Curie temperature T_C. A positive value for θ is observed for compounds showing ferromagnetism – parallel ordering of all spins – below a certain T_C. Interestingly, a slight deviation of the linearity is monitored at low temperatures due to short range order. For antiparallel ordering within a sample, which is typical for antiferro- or ferrimagnetism, the θ parameter is negative below a specific *Néel* (T_N) or Curie temperature T_C (cf. Figure 1.10). Another and herein applied description of the Curie-Weiss-Law is:

$$\chi_{mol} = \mu_0 \frac{N_A \mu_B^2 \mu_{eff}^2}{3 k_B T}. \qquad \text{(Eq. 1.2)}$$

Relevant for transition metal compounds concerning their magnetic behavior is the strength of the ligand (Figure 1.11). Depending on the ligand field, high or low spin compounds with different magnetic behavior are observed.[146] The Mn^{2+} ion is an illustrative example which shows μ_{eff} of 5.65 - 6.10 for high spin and μ_{eff} of 1.80 - 2.10 in case of low spin compounds.

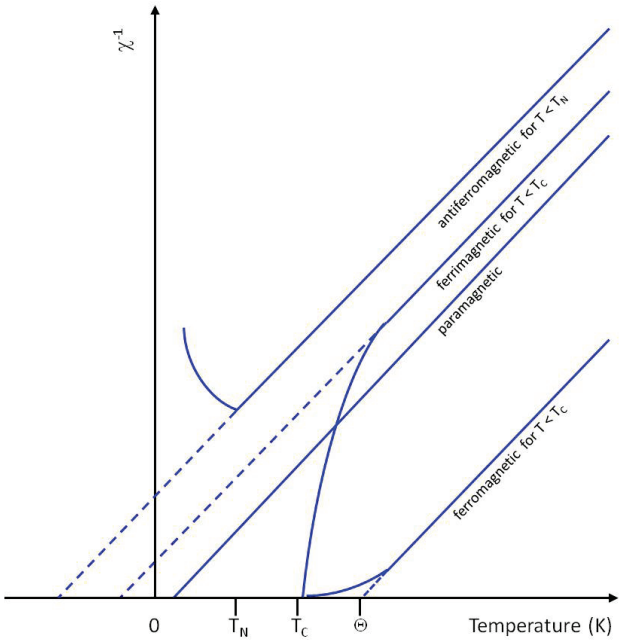

Figure 1.10. Schematic curves of temperature-dependent reciprocal molar susceptibility. Picture modified from [142].

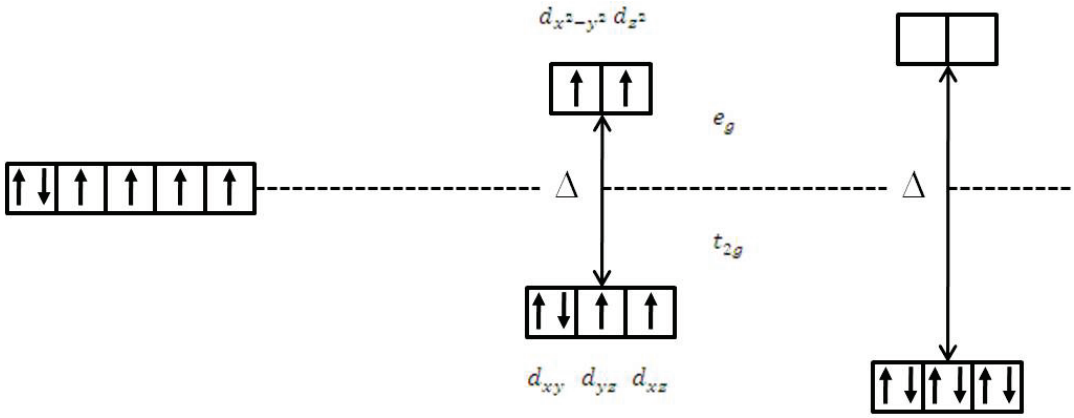

Figure 1.11. Magnetic behavior of octahedral $3d^6$ compounds such as Ni^{2+} (left: high spin; right: low spin).

1.4.1 Magnetic properties of spinels

Antiferromagnetism is frequently observed for cubic or tetragonal centered lattices. The dipole alignments at the corners of the crystal lattice (sublattice A) are antiparallel towards the centered dipols (sublattice B). Such systems can be described as two interlocked sublattices with A and B pointing into opposite directions (Figure 1.12). This results in ferromagnetism all over the crystal lattice or - in case of different values for the A and B dipoles - in ferrimagnetism.[146]

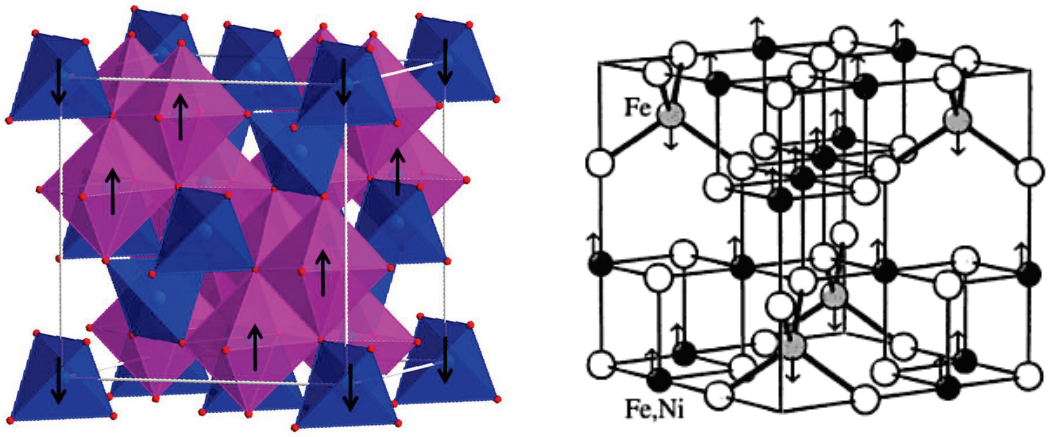

Figure 1.12. Different magnetic dipoles within a spinel lattice (left) and spin orientation within the ferrimagnetic inverse spinel $NiFe_2O_4$ (right; picture right taken from [142]).

1.5 Catalytic applications of oxide materials

1.5.1 Water oxidation

The quest for alternative energy sources and global climate control are major research challenges of the 21st century. This applies especially for renewable energy systems and the access to clean water resources. Artificial photosynthesis, i.e. chemical water splitting might be the basis for future hydrogen or methanol-supported fuel technology which would be an elegant way to solve both problems in one go.

Recently, great progress has been achieved to develop manganese containing compounds which catalyze water oxidation reactions in a bio-inspired manner starting from nature's photosystem II. These achievements have been realized with a robust cubane-related manganese oxocluster core in combination with calcium cations,[147, 148] and intense synthetic

efforts are still in progress on bio-inspired Mn complexes as homogeneous water oxidation catalysts (WOCs).[149-153] In parallel, cobalt compounds, such as amorphous cobalt phosphate WOCs,[154] have long attracted attention in water splitting research via homo- and heterogeneous catalysis.[155]

Furthermore, semiconductor-based photocatalysts are more and more in the focus of worldwide research – may it be as metal oxides[68, 156-161] or as composite semiconductors[162-164]. Additionally, metal oxynitrides and -sulfides[159] as well as molecular catalysts[165, 166] are promising new types of water oxidation photocatalysts.

1.5.1.1 Mechanisms of photocatalytic processes

The absorption of photons to form electron – hole pairs is the initial step of the photocatalytic reaction and the according scheme for semiconducting materials is shown in Figure 1.13. According to electronic band structure theory, the energetic difference between valence band (VB) and conduction band (CB) is referred to as band gap (usually given in eV). Holes as well as electrons are generated in both bands if the incident light energy is larger than the respective band gap which is available for redox reactions: reduction of water molecules takes place to form H_2 whereas O_2 is formed through hole-induced water oxidation. The band gap plays an important role in the water splitting mechanism since the redox potential of H^+/H_2 (0 V vs. NHE) needs to be overcome (more negative ground level of the CB). On the other hand, the top level of the VB requires more positive values than the redox potential of O_2/H_2O (1.23 V). Obviously, 1.23 eV, which corresponds to a wavelength of about 1100 nm, is the minimum required band gap for water splitting reactions.[167] It is essential to decrease the recombination possibility of photo-induced holes and electrons. Therefore, crystal structure as well as particle size play important roles within this process as can be seen in Figure 1.14.[161, 167]

One of the most widely applied and investigated photocatalysts is TiO_2 due to its high efficiency and non-toxicity. Nevertheless, the activation of TiO_2 with a wide band gap of 3.2 eV ($\lambda < 387$ nm) is limited to UV irradiation. Therefore, the development of new photocatalysts for visible light driven water splitting is required.

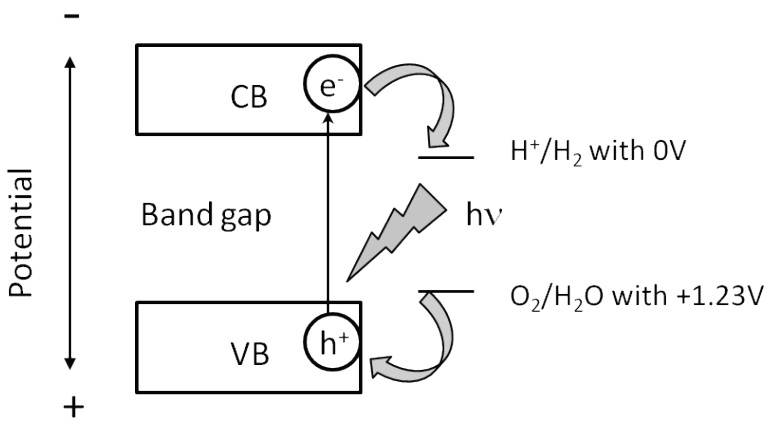

Figure 1.13. Priciple of water splitting with semiconducting photocatalysts. Picture taken from [167].

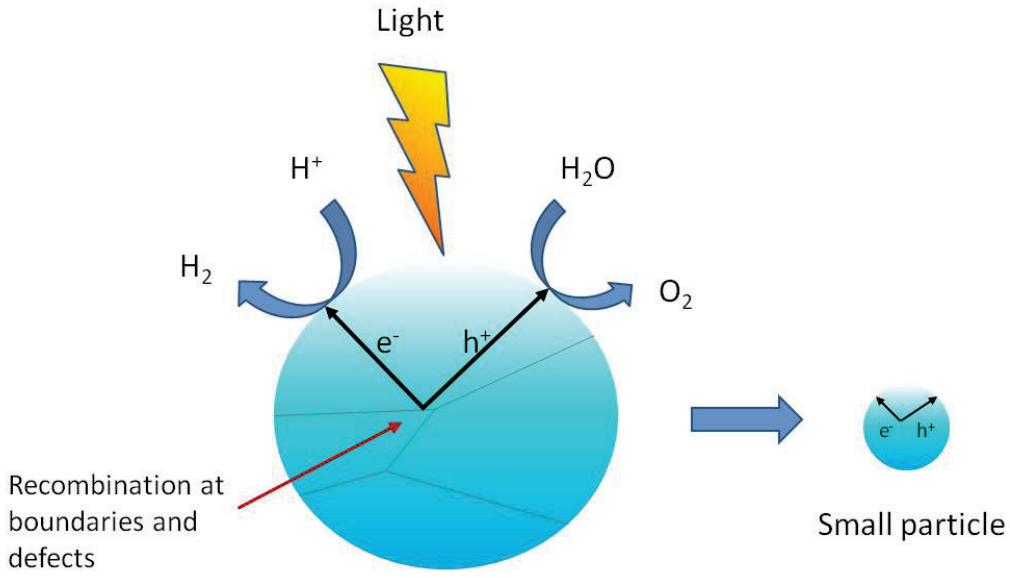

Figure 1.14. Effects of particle size and defects on photocatalytical activity. Picture taken from [167].

1.5.1.2 Water oxidation with the $Ru^{2+}(bpy)_3$–$S_2O_8^{2-}$ system

The photocatalytic oxidation of water reported herein was performed with the well-established $Ru^{2+}(bpy)_3$–$S_2O_8^{2-}$ method which is often implemented for cobalt and manganese containing polyoxometalates[112, 114, 150] to investigate the activities of multi-electron catalysts. Visible light is absorbed by the $Ru^{2+}(bpy)_3$ sensitizer on the surface of the multi-

electron catalyst which in the following step transfers electrons to the sacrificial electron acceptor, namely $S_2O_8^{2-}$, which is finally reduced to SO_4^{2-} (cf. Figure 1.15). In detail, oxidation of the excited sensitizer leads to the formation of $Ru^{3+}(bpy)_3$ by electron uptake from the multi-electron catalyst and finally water is oxidized to form oxygen on the catalyst surface. A slightly acidic and Na_2SiF_6 buffered reaction medium is required to prevent accelerated degeneration of the Ru-photosensitizer at higher pH values. Within the herein reported water oxidation setup, illumination with visible light (λ = 470 nm) takes place with a state-of-the-art LED lamp at very low power (4650 lux).

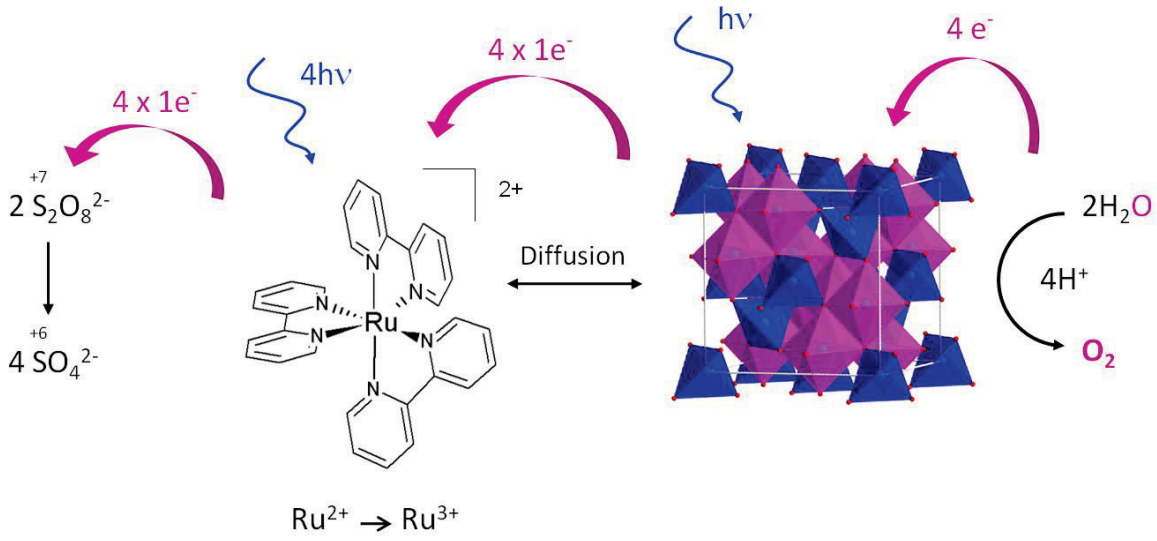

Figure 1.15. Schematic illustration of the mechanism for the water oxidation applying the $Ru^{2+}(bpy)_3$–$S_2O_8^{2-}$ system.

1.5.2 Methanol steam reforming and CO_2 hydrogenation

The synthesis of methanol from syngas is a top ten industrial process with an annual volume of 46 megatons in over 90 worldwide production plants.[168] The application of methanol as chemical feedstock or as a transportation fuel requires a daily production of more than 100.000 tons. Methanol is one of the most important basic chemicals for many industrial processes:[168]

- Production as surfactant in fuels
- Oxidation with Ag catalysts into formaldehyde
- Synthesis of acetic acid, chloromethane or methylethers

- Production of methylamines as intermediate for pigments, pharmaceuticals and crop protection products
- Application in plastic recycling (methanolyse of PET)
- Solvent and anti-freeze agent

The demand might increase, because methanol as hydrogen source may become the main energy carrier in fuel cells.

The first low pressure synthesis in 1966 with syngas was catalyzed by a mixture of $Cu/ZnO/Al_2O_3$ at 230 – 250 °C which is still the standard technical catalyst.[169, 170] Formally, syngas mixtures ($CO/CO_2/H_2$) are converted over $Cu/ZnO/Al_2O_3$ catalysts according to

$$CO_2 + 3\ H_2 \rightarrow CH_3OH + H_2O. \qquad \text{(Eq. 1.3)}$$

Recent investigations are inspired by the potential of the methanol synthesis reaction for the chemical fixation of the greenhouse gas CO_2[171] and the potential use of methanol as a synthetic fuel[172] or as hydrogen storage molecule.[81] Furthermore, spinel phases can be formed during the catalytic process[169, 173] as demonstrated in Figure 1.16 which was the inspiration for the catalytical investigations reported in Chapter 3.

Hydrogen can be liberated from methanol via the methanol steam reforming reaction (MSR)

$$CH_3OH + H_2O \rightarrow CO_2 + 3\ H_2. \qquad \text{(Eq. 1.4)}$$

For application in CO_2 hydrogenation, i.e. in feed gas mixtures without CO, the selectivity of the catalysts needs improvement, because this reaction (Equation 1.4) is coupled with the reverse water gas shift reaction (rWGS)

$$CO_2 + H_2 \rightarrow CO + H_2O, \qquad \text{(Eq. 1.5)}$$

which yields significant amounts of undesired CO. For the MSR reaction, higher stability and selectivity towards CO_2 are mandatory.[174] Therefore, the influence of the preparative strategy on the final catalyst properties has to be known in detail.

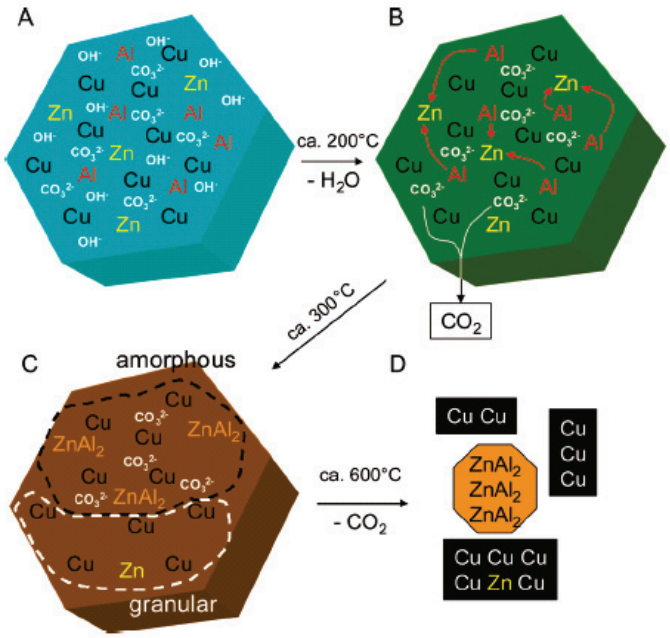

Figure 1.16. Schematic model of the Al segregation. A) initial state of precursor (element symbols represent the metal ions with their oxygen surrounding); B) loss of interlayer water and hydroxyl groups, start of Al segregation to fulfill the Zn:Al ratio of 1:2 for spinel formation; C) resulting microstructure with Al depleted (Cu-rich) and dense Al-rich areas; D) complete segregation into crystalline CuO and $ZnAl_2O_4$. Graph taken from [173].

References

[1] G. A. Ozin, L. Cademartiri, *Small* **2009**, *5*, 1240.

[2] G. A. Ozin, L. Cademartiri, *Concepts of Nanochemistry*, Wiley-VCH, Weinheim, **2009**.

[3] G. R. Patzke, Y. Zhou, R. Kontic, F. Conrad, *Angew. Chem. Int. Ed.* **2011**, *50*, 826.

[4] H. Goesmann, C. Feldmann, *Angew. Chem. Int. Ed.*, *49*, 1362.

[5] Y. E. Gogotsi, *Nanomaterials Handbook*, CRC Press, Boca Raton, **2006**.

[6] G. A. Ozin, A. C. Arsenault, *Nanochemistry: A Chemical Approach to Nanomaterials*, RSC Publishing, **2005**.

[7] G. R. Patzke, F. Krumeich, R. Nesper, *Angew. Chem. Int. Ed.* **2002**, *41*, 2446.

[8] C. N. R. Rao, A. Müller, A. K. Cheetham, *The Chemistry of Nanomaterials* Wiley-VCH, Weinheim, **2004**.

[9] J. A. Rodriguez, M. Fernandez-Garcia, *Synthesis, Properties and Applications of Oxide Nanomaterials*, Wiley InterScience, Weinheim, **2007**.

[10] D. Vollath, *Nanomaterials*, Wiley-VCH, Weinheim, **2008**.

[11] S. T. Bromley, I. d. P. R. Moreira, K. M. Neyman, F. Illas, *Chem. Soc. Rev.* **2009**, *38*, 2657.

[12] N. R. Shiju, V. V. Guliants, *Appl. Catal. A-General* **2009**, *356*, 1.

[13] R. Bogue, *Sensor Rev.* **2009**, *29*, 194.

[14] F. Hernandez-Ramirez, J. D. Prades, R. Jimenez-Diaz, T. Fischer, A. Romano-Rodriguez, S. Mathur, J. R. Morante, *Phys. Chem. Chem. Phys.* **2009**, *11*, 7105.

[15] T. Pradeep, Anshup, *Thin Solid Films* **2009**, *517*, 6441.

[16] A. Weidenkaff, R. Robert, M. H. Aguirre, L. Bocher, L. Schlapbach, *Phys.Status Solidi-R. R. L.* **2007**, *1*, 247.

[17] M. Zach, C. Hagglund, D. Chakarov, B. Kasemo, *Curr. Opin. Solid State Mater. Sci.* **2006**, *10*, 132.

[18] J. Garcia-Barriocanal, A. Rivera-Calzada, M. Varela, Z. Sefrioui, M. R. Diaz-Guillen, K. J. Moreno, J. A. Diaz-Guillen, E. Iborra, A. F. Fuentes, S. J. Pennycook, C. Leon, J. Santarnaria, *ChemPhysChem* **2009**, *10*, 1003.
[19] K. Byrappa, T. Adschiri, *Prog. Cryst. Growth Charact. Mater.* **2007**, *53*, 117.
[20] B. L. Cushing, V. L. Kolesnichenko, C. J. O'Connor, *Chem. Rev.* **2004**, *104*, 3893.
[21] X. Wang, Y. Li, *Inorg. Chem.* **2006**, *45*, 7522.
[22] W.-T. Yao, S.-H. Yu, *Int. J. Nanotechnol.* **2007**, *4*, 129.
[23] C. S. S. R. E. Kumar, *Nanomaterials for the Life Sciences*, Wiley-VCH, Weinheim, **2010**.
[24] W. H. Suh, Y.-H. Suh, G. D. Stucky, *Nano Today* **2009**, *4*, 27.
[25] J. S. Murday, R. W. Siegel, J. Stein, J. F. Wright, *Nanomed. Nanotechnol. Biol. Med.* **2009**, *5*, 251.
[26] J. Gao, H. Gu, B. Xu, *Acc. Chem. Res.* **2009**, *42*, 1097.
[27] Y. W. Chun, T. J. Webster, *Ann. Biomed. Eng.* **2009**, *37*, 2034.
[28] N. Sozer, J. L. Kokini, *Trends Biotechnol.* **2009**, *27*, 82.
[29] M. G. Blamire, J. L. MacManus-Driscoll, N. D. Mathur, Z. H. Barber, *Adv. Mater.* **2009**, *21*, 3827.
[30] A. Ghicov, P. Schmuki, *Chem. Comm.* **2009**, 2791.
[31] R. J. Gorte, J. M. Vohs, *Curr. Opin. Colloid Interface Sci.* **2009**, *14*, 236.
[32] P. Nalawade, B. Aware, V. J. Kadam, R. S. Hirlekar, *J. Sci. Ind. Res.* **2009**, *68*, 267.
[33] M. Osada, T. Sasaki, *J. Mater. Chem.* **2009**, *19*, 2503.
[34] Z. Yang, D. Choi, S. Kerisit, K. M. Rosso, D. Wang, J. Zhang, G. Graff, J. Liu, *J. Power Sources* **2009**, *192*, 588.
[35] T. M. Shaw, S. Trolier-McKinstry, P. C. McIntyre, *Ann. Rev. Mater. Sci.* **2000**, *30*, 263.
[36] W. Steinhogl, G. Schindler, G. Steinlesberger, M. Engelhardt, *Phys. Rev. B* **2002**, *66*.
[37] E. Arzt, *Acta Mater.* **1998**, *46*, 5611.
[38] Q. A. Pankhurst, J. Connolly, S. K. Jones, J. Dobson, *J. Phys. D - Appl. Phys.* **2003**, *36*, R167.
[39] G. Dehm, T. J. Balk, H. Edongue, E. Arzt, *Microelectron. Eng.* **2003**, *70*, 412.
[40] P. A. Gruber, E. Arzt, R. Spolenak, *J. Mater. Res.* **2009**, *24*, 1906.
[41] P. Buffat, J. P. Borel, *Phys. Rev. A* **1976**, *13*, 2287.
[42] J. A. Forrest, K. DalnokiVeress, J. R. Stevens, J. R. Dutcher, *Phys. Rev. Lett.* **1996**, *77*, 2002.
[43] G. F. Goya, T. S. Berquo, F. C. Fonseca, M. P. Morales, *J. Appl. Phys.* **2003**, *94*, 3520.
[44] R. D. Priestley, C. J. Ellison, L. J. Broadbelt, J. M. Torkelson, *Science* **2005**, *309*, 456.
[45] R. Cornell, U. Schwertmann, *The Iron Oxides*, 2nd ed., Wiley-VCH, Weinheim, **2003**.
[46] Y. Ju-Nam, J. R. Lead, *Sci. Total Environ.* **2008**, *400*, 396.
[47] M. Niederberger, G. Garnweitner, N. Pinna, N. G., *Prog. Solid State Chem.* **2005**, *33*, 59.
[48] C. N. R. Rao, F. L. Deepak, G. Gundiah, A. Govindaraj, *Prog. Solid State Chem.* **2005**, *31*, 5.
[49] P. Bowen, C. Carry, *Powder Technol.* **2002**, *128*, 248.
[50] M. Jansen, *Angew. Chem. Int. Ed.* **2002**, *41*, 3747.
[51] F. Gao, Q. Lu, X. Meng, S. Komarneni, *J. Mater. Sci.* **2008**, *43*, 2377.
[52] V. Polshettiwar, M. N. Nadagouda, R. S. Varma, *Aust. J. Chem.* **2009**, *62*, 16.
[53] S. Komarneni, H. Katsuki, *PureAppl. Chem.* **2002**, *74*, 1537.
[54] W. C. Conner, G. A. Tompsett, *J. Phys. Chem. B* **2008**, *112*, 2110.
[55] K. J. Rao, B. Vaidhyanathan, M. Ganguli, P. A. Ramakrishnan, *Chem. Mater.* **1999**, *11*, 882.
[56] I. Bilecka, P. Elser, M. Niederberger, *ACS Nano* **2009**, *3*, 467.
[57] P. L. Zhu, J. W. Zhang, Z. S. Wu, Z. J. Zhang, *Cryst. Growth Des.* **2008**, *8*, 3148.
[58] L. Zhang, Y. J. Zhu, *Appl. Phys. A -Mater. Sci. Process.* **2009**, *97*, 847.
[59] M. S. Mohajerani, M. Mazloumi, A. Lak, A. Kajbafvala, S. Zanganeh, S. K. Sadrnezhaad, *J. Cryst. Growth* **2008**, *310*, 3621.
[60] X. L. Hu, J. C. Yu, J. M. Gong, Q. Li, G. S. Li, *Adv. Mater.* **2007**, *19*, 2324.
[61] J. S. Kim, S. G. Lee, H. L. Park, J. Y. Park, S. D. Han, *Mater. Lett.* **2004**, *58*, 1354.
[62] T. Minami, T. Maeno, Y. Kuroi, S. Takata, *Jpn. J. Appl. Phys. Part 2 - Lett.* **1995**, *34*, L684.
[63] Y. S. Jeong, J. S. Kim, H. L. Park, *Solid State Commun.* **2006**, *139*, 157.
[64] J. A. Losilla, D. Coutinho, K. J. Balkus, *Microporous Mesoporous Mater.* **2008**, *113*, 325.
[65] X. Chen, H. Xue, Z. H. Li, L. Wu, X. X. Wang, X. Z. Fu, *J. Phys. Chem. C* **2008**, *112*, 20393.
[66] W. Zhang, J. Zhang, Z. Chen, T. Wang, *Catal. Comm.* **2009**, *10*, 1781.

[67] K. Ikarashi, J. Sato, H. Kobayashi, N. Saito, H. Nishiyama, Y. Inoue, *J. Phys. Chem. B* **2002**, *106*, 9048.
[68] F. E. Osterloh, *Chem. Mater.* **2008**, *20*, 35.
[69] L. Pisani, T. Maitra, R. Valenti, *Phys. Rev. B* **2006**, *73*.
[70] S. Y. Bae, J. Lee, H. Jung, J. Park, J. P. Ahn, *J. Am. Chem. Soc.* **2005**, *127*, 10802.
[71] P. Dhak, U. K. Gayen, S. Mishra, P. Pramanik, A. Roy, *J. Appl. Phys.* **2009**, *106*.
[72] J. S. Kim, J. S. Kim, T. W. Kim, H. L. Park, Y. G. Kim, S. K. Chang, S. Do Han, *Solid State Comm.* **2004**, *131*, 493.
[73] J. J. Krebs, G. H. Stauss, J. B. Milstein, *Phys. Rev. B* **1979**, *20*, 2586.
[74] T. Maitra, R. Valenti, *J. Phys. - Cond. Matt.* **2005**, *17*, 7417.
[75] Q. Shi, J. Y. Zhang, C. Cai, L. Cong, T. M. Wang, *Mater. Sci. Eng. B - Adv. Funct. Solid-State Mater.* **2008**, *149*, 82.
[76] Z. H. Xu, Y. X. Li, Z. F. Liu, Z. Xiong, *Mater. Sci. Eng. B - Solid State Mater. Adv. Technol.* **2004**, *110*, 302.
[77] S. H. Yang, M. Yokoyama, *Jpn. J. Appl. Phys. Part 1 - Regul. Pap. Short Notes Rev. Pap.* **1998**, *37*, 6429.
[78] Y. Tang, Y. Liu, P. Zhu, Q. Xue, L. Chen, Y. Lu, *Aiche J.* **2009**, *55*, 1217.
[79] A. Kudo, Y. Miseki, *Chem. Soc. Rev.* **2009**, *38*, 253.
[80] www.methanol.org, **2011**.
[81] G. A. Olah, A. Goeppert, G. K. S. Prakash, Wiley-VCH, Weinheim, **2009**.
[82] R.Schlögl, *ChemSusChem* **2010**, *3*, 209.
[83] M. Saito, *Catal. Surv. Japn.* **1998**, *2*, 175.
[84] J. B. Hansen, *H. N. P. Methanol Synthesis. In Handbook of Heterogenous Catalysis* 2nd ed., Wiley-VCH, Weinheim, **2008**.
[85] M. Behrens, I. Kasatkin, S. Kühl, G. Weinberg, *Chem. Mater.* **2010**, *22*, 386.
[86] C. Baltes, S. Vukojevic, F. Schüth, *J. Catal.* **2008**, *258*, 334.
[87] B. L. Kniep, F. Girgsdies, T. Ressler, *J. Catal.* **2005**, *236*, 34 (b).
[88] P. P. Pescarmona, P. A. Jacobs, *Catal. Today* **2008**, *137*, 52.
[89] P. P. Pescarmona, K. P. F. Janssen, P. A. Jacobs, *Chem. Eur. J.* **2007**, *13*, 6562.
[90] K. Shimura, T. Yoshida, H. Yoshida, *J. Phys. Chem. C* **2010**, *114*, 11466.
[91] M. Yada, H. Takenaka, M. Machida, T. Kijima, *J. Chem. Soc. - Dalton Trans.* **1998**, 1547.
[92] X. M. Sun, Y. D. Li, *Angew. Chem. Int. Ed.* **2004**, *43*, 3827.
[93] C. A. Deshmane, J. B. Jasinski, M. A. Carreon, *Microporous Mesoporous Mater.* **2010**, *130*, 97.
[94] J. Böhm, *Angew. Chem.* **1940**, *53*, 131.
[95] T. Nakatani, T. Watanabe, M. Takahashi, Y. Miyahara, H. Deguchi, S. Iwamoto, H. Kanai, M. Inoue, *J. Phys. Chem. A* **2009**, *113*, 7021.
[96] J. C. Lavalley, M. Daturi, V. Montouillout, G. Clet, C. O. Arean, M. R. Delgado, A. Sahibed-dine, *Phys. Chem. Chem. Phys.* **2003**, *5*, 1301.
[97] I. Nowak, J. Quartararo, E. G. Derouane, J. C. Vedrine, *App. Catal. A - General* **2003**, *251*, 107.
[98] T. Wang, S. S. Farvid, M. Abulikemu, P. V. Radovanovic, *J. Am. Chem. Soc.* **2010**, *132*, 9250.
[99] K. Pohl, *Z. Naturw.* **1968**, *55*, 82.
[100] C. O. Arean, A. L. Bellan, M. P. Mentruit, M. R. Delgado, G. T. Palomino, *Microporous Mesoporous Mater.* **2000**, *40*, 35.
[101] M. Zinkevich, F. M. Morales, H. Nitsche, M. Ahrens, M. Ruhle, F. Aldinger, *Z. Metallkunde* **2004**, *95*, 756.
[102] C.-C. Huang, C.-S. Yeh, *New J. Chem.* **2010**, *34*, 103.
[103] Y. Zhao, R. L. Frost, W. N. Martens, *J. Phys. Chem. C* **2007**, *111*, 16290.
[104] S. A. Hering, C. E. Zvoriste, R. Riedel, I. Kinski, H. Huppertz, *Z. Naturforschung B - J. Chem. Sci.* **2009**, *64*, 1115.
[105] M. Behrens, I. Kasatkin, S. Kuehl, G. Weinberg, *Chem. Mater.* **2010**, *22*, 386.
[106] S. Bennici, A. Auroux, C. Guimon, A. Gervasini, *Chem. Mater.* **2006**, *18*, 3641.
[107] K. Faungnawakij, N. Shimoda, T. Fukunaga, R. Kikuchi, K. Eguchi, *Appl. Catal. A - General* **2008**, *341*, 139.

[108] K. Gurunathan, J. O. Baeg, S. M. Lee, E. Subramanian, S. J. Moon, K. J. Kong, *Int. J. Hydro. Energy* **2008**, *33*, 2646.
[109] K. A. Bethke, M. C. Kung, B. Yang, M. Shah, D. Alt, C. Li, H. H. Kung, *Catal. Today* **1995**, *26*, 169.
[110] T. Mathew, Y. Yamada, A. Ueda, H. Shioyama, T. Kobayashi, *Appl. Catal. A - General* **2005**, *286*, 11.
[111] F. Jiao, H. Frei, *Energy Environ. Sci.* **2010**, *3*, 1018.
[112] V. B. R. Boppana, F. Jiao, *Chem. Comm.* **2011**, *47*, 8973.
[113] Y. Gorlin, T. F. Jaramillo, *J. Am. Chem. Soc.* **2010**, *132*, 13612.
[114] M. M. Najafpour, T. Ehrenberg, M. Wiechen, P. Kurz, *Angew. Chem. Int. Ed.* **2010**, *49*, 2233.
[115] D. M. Robinson, Y. B. Go, M. Greenblatt, G. C. Dismukes, *J. Am. Chem. Soc.* **2010**, *132*, 11467.
[116] F. Cheng, J. Shen, B. Peng, Y. Pan, Z. Tao, J. Chen, *Nature Chem.* **2011**, *3*, 79.
[117] T. Hisatomi, K. Miyazaki, K. Takanabe, K. Maeda, J. Kubota, Y. Sakata, K. Domen, *Chem. Phys. Lett.* **2010**, *486*, 144.
[118] K. Maeda, K. Teramura, D. L. Lu, T. Takata, N. Saito, Y. Inoue, K. Domen, *Nature* **2006**, *440*, 295.
[119] H. Xue, Z.-h. Li, L.-J. Zhu, *Chin. J. Struct. Chem.* **2010**, *29*, 1828.
[120] N. Kumagai, L. Ni, H. Irie, *Chem. Comm.* **2011**, *47*, 1884.
[121] M. M. Titirici, M. Antonietti, A. Thomas, *Chem. Mater.* **2006**, *18*, 3808.
[122] H.-M. Xiao, S.-Y. Fu, L.-P. Zhu, Y.-Q. Li, G. Yang, *Eur. J. Inorg. Chem.* **2007**, 1966.
[123] C.-J. Jia, L.-D. Sun, F. Luo, X.-D. Han, L. J. Heyderman, Z.-G. Yan, C.-H. Yan, K. Zheng, Z. Zhang, M. Takano, N. Hayashi, M. Eltschka, M. Klaeui, U. Ruediger, T. Kasama, L. Cervera-Gontard, R. E. Dunin-Borkowski, G. Tzvetkov, J. Raabe, *J. Am. Chem. Soc.* **2008**, *130*, 16968.
[124] S.-B. Wang, Y.-L. Min, S.-H. Yu, *J. Phys. Chem. C* **2007**, *111*, 3551.
[125] G. Clavel, M. G. Willinger, D. Zitoun, N. Pinna, *Adv. Funct. Mater.* **2007**, *17*, 3159.
[126] J. Fidelus, R. R. Piticescu, R. M. Piticescu, W. Lojkowski, L. Giurgiu, *Z. Naturforsch. (B)* **2008**, *63*, 725.
[127] S. Cho, S. H. Jung, K. H. Lee, *J. Phys. Chem. C* **2008**, *112*, 12769.
[128] X. L. Hu, Y. J. Zhu, S. W. Wang, *Mater. Chem. Phys.* **2004**, *88*, 421.
[129] A. S. Shaporev, V. K. Ivanov, A. E. Baranchikov, Y. D. Tret'yakov, *Inorg. Mater.* **2007**, *43*, 35.
[130] X. D. Xu, M. Zhang, J. Feng, M. L. Zhang, *Mater. Lett.* **2008**, *62*, 2787.
[131] J. X. Xia, H. M. Li, Z. J. Luo, H. Shi, K. Wang, H. M. Shu, Y. S. Yan, *J. Phys. Chem. Solids* **2009**, *70*, 1461.
[132] T. Alammar, A. Birkner, A. V. Mudring, *Eur. J. Inorg. Chem.* **2009**, 2765.
[133] T. Alammar, A. V. Mudring, *Mater. Lett.* **2009**, *63*, 732.
[134] S. W. Cao, Y. J. Zhu, *Acta Materialia* **2009**, *57*, 2154.
[135] S. M. Liu, X. L. Qian, J. Z. Xiao, *J. Sol-Gel Sci. Technol.* **2007**, *44*, 187.
[136] C. O. Kappe, A. Stadler, *Microwaves in Organic and Medicinal Chemistry*, Wiley-VCH, **2005**.
[137] A. Loupy, *Microwaves in Organic Synthesis*, 2 ed., Wiley-VCH, Weinheim, **2006**.
[138] S. Komarneni, H. Katsuki, *Pure Appl. Chem.* **2002**, *9*, 1537.
[139] I. Bilecka, M. Niederberger, *Nanoscale* **2010**, *2*, 1358.
[140] C. O. Kappe, *Angew. Chem. Int. Ed.* **2004**, *43*, 6250
[141] W. Borchardt-Ott, *Kristallographie*, Springer-Verlag, Berlin, Heidelberg, **2002**.
[142] U. Mueller, *Anorganische Strukturchemie*, 6th ed., Vieweg Teubner, Wiesbaden, **2008**.
[143] L. Smart, E. A. Moore, *Solid State Chemistry: An Introduction* Crc Pr Inc, **2005**.
[144] H. Lueken, *Magnetochemie*, B. G. Teubner, Stuttgart · Leipzig, **1999**.
[145] M. McElfresh, in *Quantum Design*, **1994**.
[146] W. P. Wolf, *Ferrimagnetism*, Oxford, **1961**.
[147] H. Dau, C. Limberg, T. Reier, M. Risch, S. Roggan, P. Strasser, *ChemCatChem* **2010**, *2*, 724.
[148] P. E. M. Siegbahn, *Acc. Chem. Res.* **2009**, *42*, 1871.
[149] K. Beckmann, H. Uchtenhagen, G. Berggren, M. F. Anderlund, A. Thapper, J. Messinger, S. Styring, P. Kurz, *Energy Environ. Sci.* **2008**, *1*, 668.
[150] R. Brimblecombe, A. Koo, G. C. Dismukes, G. F. Swiegers, L. Spiccia, *J. Am. Chem. Soc.* **2010**, *132*, 2892.

[151] R. Brimblecombe, A. Koo, G. C. Dismukes, G. F. Swiegers, L. Spiccia, *ChemSusChem* **2010**, *3*, 1146.
[152] V. Kotzabasaki, M. Siczek, T. Lis, C. J. Milios, *Inorg. Chem. Comm.* **2011**, *14*, 213.
[153] F. Zhang, C. W. Cady, G. W. Brudvig, H. J. M. Hou, *Inorg. Chim. Acta* **2011**, *366*, 128.
[154] M. W. Kanan, Y. Surendranath, D. G. Nocera, *Chem. Soc. Rev.* **2009**, *38*, 109.
[155] V. Artero, M. Chavarot-Kerlidou, M. Fontecave, *Angew. Chem. Int. Ed.* **2011**, *50*, 7238.
[156] M. Gratzel, *Chem. Lett.* **2005**, *34*, 8.
[157] F. Jiao, H. Frei, *Angew. Chem. Int. Ed.* **2009**, *48*, 1841.
[158] M. W. Kanan, D. G. Nocera, *Science* **2008**, *321*, 1072.
[159] K. Maeda, K. Domen, *J. Phys. Chem. C* **2007**, *111*, 7851.
[160] R. van de Krol, Y. Liang, J. Schoonman, *J. Mater. Chem.* **2008**, *18*, 2311.
[161] Y. Zhou, K. Vuille, A. Heel, B. Probst, R. Kontic, G. R. Patzke, *Appl. Catal. A - General* **2010**, *375*, 140.
[162] H. Hata, Y. Kobayashi, V. Bojan, W. J. Youngblood, T. E. Mallouk, *Nano Lett.* **2008**, *8*, 794.
[163] R. Ma, Y. Kobayashi, W. J. Youngblood, T. E. Mallouk, *J. Mater. Chem.* **2008**, *18*, 5982.
[164] K. Maeda, K. Teramura, D. Lu, N. Saito, Y. Inoue, K. Domen, *Angew. Chem. Int. Ed.* **2006**, *45*, 7806.
[165] C. W. Cady, R. H. Crabtree, G. W. Brudvig, *Coord. Chem. Rev.* **2008**, *252*, 444.
[166] M. Yagi, A. Syouji, S. Yamada, M. Komi, H. Yamazaki, S. Tajima, *Photochem. Photobiol. Sci.* **2009**, *8*, 139.
[167] A. Kudo, Y. Miseki, *Chem. Soc. Rev.* **2009**, *38*, 253.
[168] www.methanol.org.
[169] M. Behrens, *J. Catal.* **2009**, *267*, 24.
[170] M. Behrens, F. Girgsdies, A. Trunschke, R. Schloegl, *Eur. J. Inorg. Chem.* **2009**, 1347.
[171] M. Saito, *Catal. Surv. Japan* **1998**, *2*, 175.
[172] R. Schloegl, *ChemSusChem*, *3*, 209.
[173] M. Behrens, I. Kasatkin, S. Kuehl, G. Weinberg, *Chem. Mater.*, *22*, 386.
[174] M. Behrens, *Methanol Steam Reforming. In Catalysis for Alternative Energy Generation, Vol. (in press)*, Springer, **2011**.

2 Microwave-hydrothermal synthesis of nanostructured zinc-copper gallates

Zinc gallate is an important semiconductor for manifold applications, e.g. in field emission displays or as a photocatalyst for water splitting. In addition to these interesting properties, zinc gallate is also an excellent matrix material that can be furthermore tuned through the incorporation of guest cations to form functional solid solutions with new optical and catalytic properties. Within this Chapter a convenient microwave-hydrothermal synthesis of nanostructured Cu^{2+}-substituted $ZnGa_2O_4$ spinels and their characterization with respect to morphology, chemical composition, structural, magnetic and optical properties is presented. The microwave-based approach offers a convenient and one-step access to nanostructured zinc gallate-based materials and related compounds as a new preparative advantage. As the properties of mixed spinel-based solid solutions strongly depend on the distribution of the guest ions between the different lattice sites, a wide range of analytical techniques was employed to investigate the physico-chemical properties of the obtained copper-containing zinc gallate materials. The EXAFS analyses at the Cu K- and Zn K-edge, respectively, show a difference in the coordination environments. Zn mainly occupies the tetrahedral sites of the spinel lattice, whereas Cu is located on the octahedral sites of the nanostructured $ZnGa_2O_4$:Cu^{2+} materials.

2.1 Introduction

The properties of zinc gallates in general are a function of their "preparative history" and of the resulting morphology, such as nanowires,[1-3] polyhedron-related, rod-like or irregular shapes.[4] The prevailing synthetic approaches to pristine and substituted $ZnGa_2O_4$ materials are solid-state reactions,[5-11] sol-gel methods,[12-14] pulsed laser deposition techniques,[15] co-precipitation,[5] chemical transport,[16] thermal evaporation,[1-3, 17] the Pecchini approach[18] and hydrothermal methods[4, 6, 9, 19-23] (cf. survey in Table 2.1). Among these techniques, hydrothermal syntheses are of special interest, because they can provide homogeneous phases and particle size distributions as well as tuneable particle morphologies in a single reaction step.[24-28] The production of metal oxides with microwave-assisted hydrothermal syntheses is even superior to conventional hydrothermal routes due to enhanced crystallization kinetics, shorter reaction times and energy saving through rapid heating of the entire reaction mixture.[29, 30] Recently, the use of ionic liquids

has opened up new preparative avenues[31] and microwave-hydrothermal technologies are likely to replace the conventional routes in future technical implementations.

In this Chapter, a new microwave-hydrothermal synthesis of nanostructured Cu^{2+}-containing zinc gallium spinels is presented. These nanostructured $ZnGa_2O_4$:Cu^{2+} spinels are obtained under mild thermal conditions on a minute scale and the presented synthetic route furthermore offers different degrees of Cu-doping and morphology tuning options. The influence of the microwave treatment parameters on the chemical composition and the morphology of the mixed spinels was monitored with a wide repertoire of methods (electron microscopy including STEM/EDXS, LA-ICP-MS and magnetic measurements as well as UV/Vis spectroscopy). Note that it is very difficult to differentiate Zn, Cu and Ga with conventional X-ray diffraction methods so that element-specific methods were used to investigate the coordination environment of the Cu^{2+} ions within the $ZnGa_2O_4$ host matrix, namely X-ray absorption spectroscopy, i.e. XANES (X-ray absorption near edge structure) and EXAFS (extended X-ray absorption fine structure), as well as electron paramagnetic resonance spectroscopy (EPR).[32-34]

2.2 Results and discussion

In the following, the microwave-hydrothermal synthesis of $ZnGa_2O_4$:Cu^{2+} solid solutions is discussed in detail, because this innovative low-temperature method offers a convenient time- and energy-saving access to nanostructured spinels as advantages over other synthetic routes.[30, 35] Although both gallium- and zinc-containing oxidic materials in particular have been efficiently synthesized through microwave-hydrothermal treatments (e.g. gallium zinc phosphate NTHU-4 [36] and hierarchical ZnO nanostructures[37]), the synthesis of $ZnGa_2O_4$ as a technically relevant ternary oxide has never been pursued via this approach and little is known about its Cu^{2+}-doped nanoscale derivatives. Therefore, a process for tuning Cu^{2+}-containing $ZnGa_2O_4$ solid solutions starting from the readily available precursor materials $Ga_2(SO_4)_3 \cdot xH_2O$, $ZnSO_4 \cdot 7H_2O$ and $CuCl_2 \cdot 2H_2O$ was developed.

Table 2.1. Survey of preparative and physico-chemical studies on $ZnGa_2O_4$-based materials.

Method/Scope	Dopant	Features and properties under investigation	Lit.
Hydrothermal Synthesis		Variable morphology	[4]
		Parameter studies and post-treatment for variable morphologies	[19-21]
		Self-regulation synthesis of spherical particles	[22]
		Hydro-/solvothermal synthesis of oxide and chalcogenide nanoparticles	[23]
Solid State Reaction		Optical properties of different spinels	[10]
		Redox behaviour of the materials	[9]
	Li, Cu , Zn	Luminance and conductivity studies	[11]
	Ge^{4+}, Li^{+}, Mn^{2+}	Application for plasma display panels	[7]
	Cr^{3+}, Mn^{2+}	Energy transfer investigations	[8]
Sol-Gel		Combined with thermolysis	[14]
		Colloidal nanocrystals with photoluminescent properties	[12]
Citrate Sol–Gel	Eu^{3+}	Photoluminescent properties	[13]
Thermal Evaporation		Morphology: helical nanowires	[1]
		High temperature vapour synthesis of nanowires	[3]
		One-step synthesis of oxide mixtures	[2]
		Synthesis on Si substrates via catalyst-free chemical vapor deposition	[17]
		Chemical transport investigations using Cl_2 and HCl as transport agents	[16]
Other Methods		Co-precipitation method and photocatalytic benzene degradation studies	[5]
		Pulsed laser deposition technique with pre-sintered targets	[15]
		Single-crystalline spinel via a single-source inorganic precursor route	[38]
	Tb^{3+}	Nanocrystalline phosphors via the Pecchini method	[18]
		Twin boundaries in the ZnO/Ga_2O_3 system and TEM investigations	[39]
	Fe^{3+}, Mn^{2+}	EPR investigations	[40]
	Fe^{3+}	Ferromagnetic properties	[41]
	Mn^{2+}	EPR investigations	[42]

2.2.1 Morphology and composition

Microwave-assisted hydrothermal synthesis of Cu^{2+}-substituted $ZnGa_2O_4$ at 150 °C brings forward hierarchically structured spherical particles and agglomerates (cf. SEM images in Figure 2.1). Henceforth, it is refered to the products as the $ZnGa_2O_4$:Cu^{2+}_n se-

ries with n representing the initial Cu^{2+} fraction (at %) of the total metal content (for further details on the preparation and the sample nomenclature cf. Chapter 7). The size of the individual $ZnGa_2O_4$:Cu^{2+} nanoparticle building units is as low as 10 - 20 nm (cf. Figure 2.2). Only the sample with maximum initial copper content (denoted as $ZnGa_2O_4$:Cu^{2+}_25(12), with 12 indicating the number of vessels in the microwave during synthesis) consists of microspheres with an average diameter of approximately 1 μm (cf. Figure 2.3 a). Other than the remaining samples, this one was synthesized using all 12 vessels of the microwave system simultaneously in order to investigate the scale-up options for zinc gallates with maximum copper contents as especially promising precursors for the fabrication of Cu-based nanocatalysts.[43] This morphology variation indicates that the load of the equipment is a key factor that has to be taken into account when employing microwave-hydrothermal reactors for large scale productions.

Interestingly, the analogous conventional-hydrothermal approach towards nanostructured Cu^{2+}-containing $ZnGa_2O_4$ failed to generate phase pure products with homogeneously distributed morphologies (Figure 2.3 b). This indicates the advantages of microwave-hydrothermal syntheses over the classic techniques in terms of shorter reaction times and homogeneous products.

The compositional homogeneity of the $ZnGa_2O_4$:Cu^{2+} mixed spinel series is confirmed by energy-dispersive X-ray (EDX) analyses that indicate constant ratios of Zn, Cu and Ga within a given sample (for a representative example cf. Figure 2.4). The overall elemental compositions of the zinc copper gallates were determined with state-of-the-art laser ablation inductively coupled plasma mass spectrometry (LA-ICP-MS). This highly sensitive analytical method permits advanced multi-element identification of a wide range of solid samples (e.g. geological and ceramic materials) and it is also a powerful tool for the characterization of otherwise insoluble nanostructured oxide materials. The unique combination of laser ablation and inductively coupled plasma as ionization source minimizes the experimental error due to the loss of volatile elements such as zinc.[44]

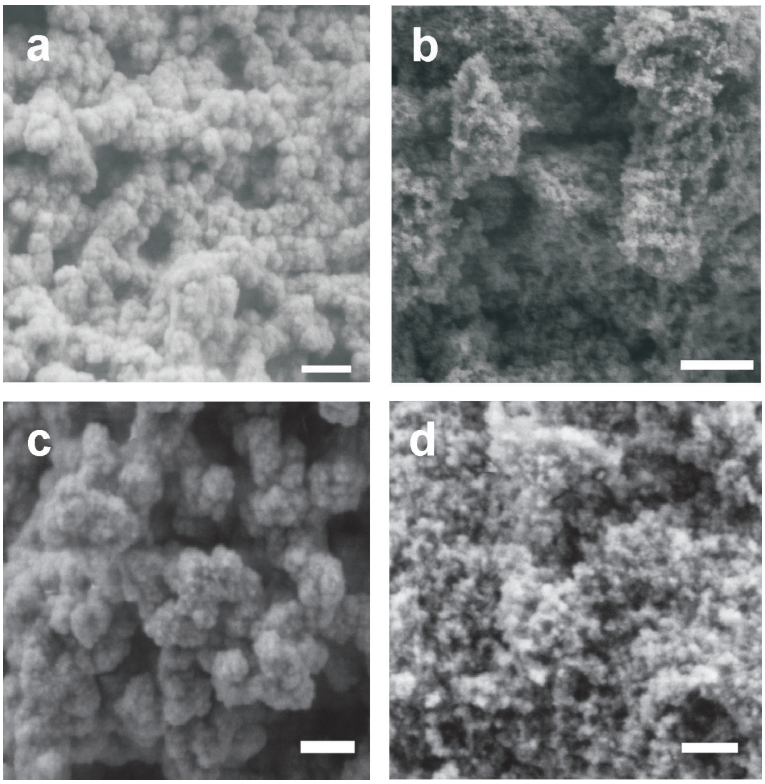

Figure 2.1. Representative SEM images of (a) $ZnGa_2O_4:Cu^{2+}$_25, (b) $ZnGa_2O_4:Cu^{2+}$_14, (c) $ZnGa_2O_4:Cu^{2+}$_4, (d) $ZnGa_2O_4:Cu^{2+}$_2 (scale bar = 200 nm).

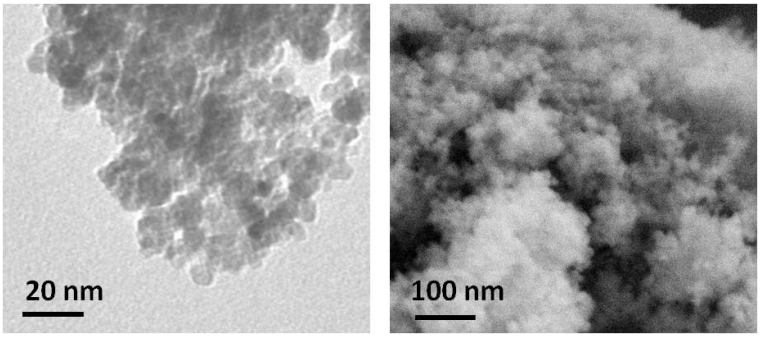

Figure 2.2. TEM (left) and SEM (right) image recorded at high magnification of the sample $ZnGa_2O_4:Cu^{2+}$_1.

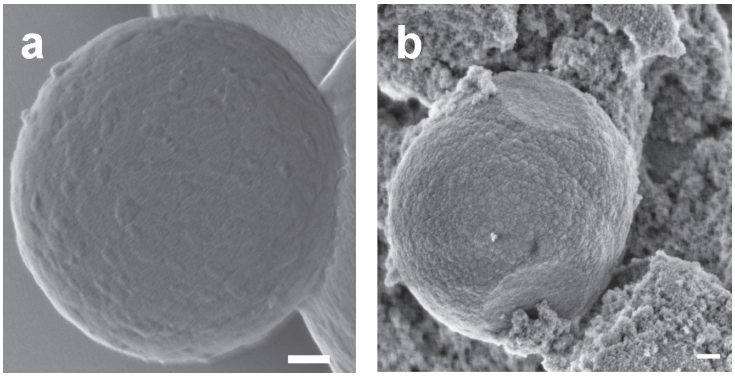

Figure 2.3. Representative SEM images of (a) $ZnGa_2O_4:Cu^{2+}$_25(12), (b) $ZnGa_2O_4:Cu^{2+}$_25_HY (scale bar = 200 nm; HY = conventional hydrothermal conditions).

The elemental compositions of microwave-hydrothermally synthesized Cu^{2+}-substituted $ZnGa_2O_4$ samples according to LA-ICP-MS analyses are summed up in Table 2.2 (for experimental parameters cf. Table 7.1). Under the given microwave-hydrothermal conditions, a maximum solubility of Cu^{2+} in the spinel lattice of ca. 5 at % (based on the metal content) is observed.

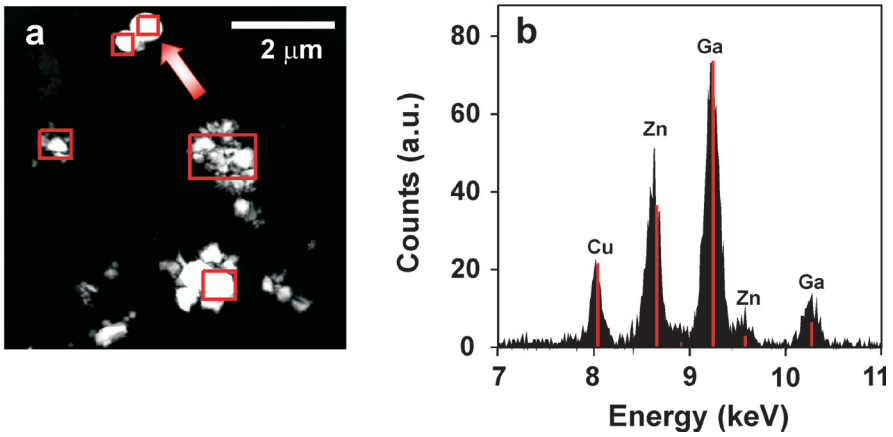

Figure 2.4. (a) STEM image (inset with spots indicating EDX analyses) and (b) representative EDX spot analysis of sample $ZnGa_2O_4$:Cu^{2+}_25(12).

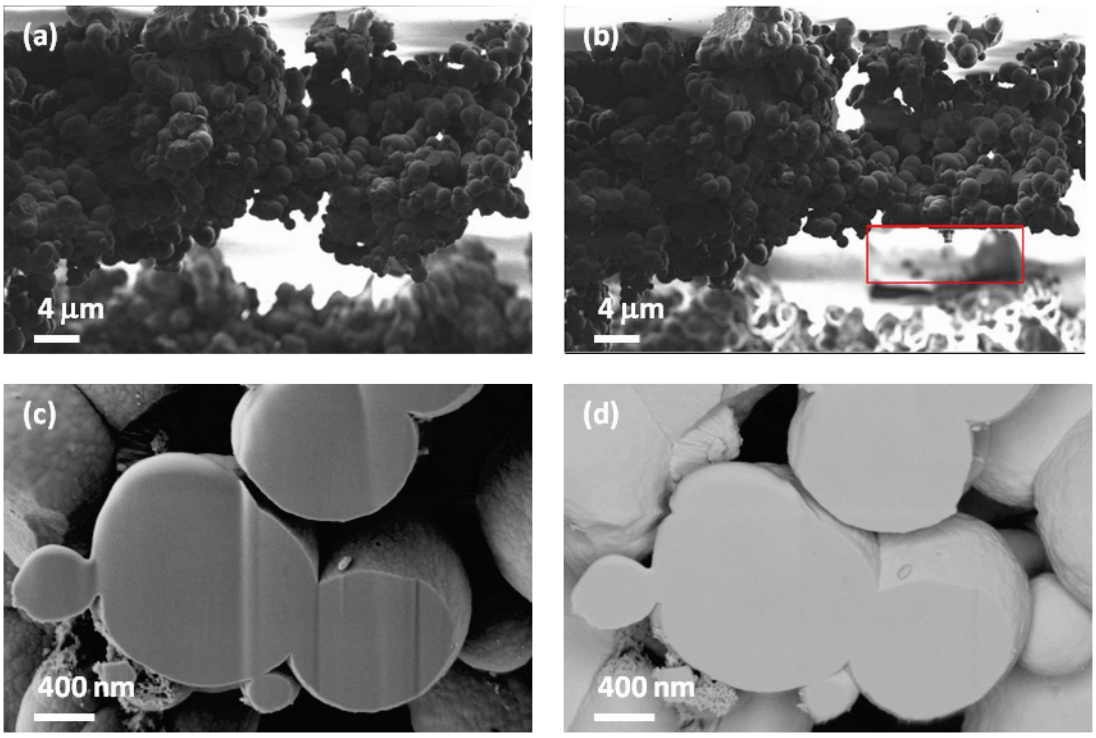

Figure 2.5. $ZnGa_2O_4$:Cu^{2+}_25(12) before (a, b) and after (red box) applied FIB, respectively. Both SE (c) and BSE signals (d) show no inhomogeneities.

Furthermore, the Cu^{2+}-substituted $ZnGa_2O_4$ samples were investigated with focused ion beam which is coupled with electron microscopy (FIB-SEM) analyses for further homogeneity tests. For this purpose, the sample $ZnGa_2O_4$:Cu^{2+}_25(12) was dispersed on Si-wafer placed on a SEM stub and FIB cross sections were taken in a shallow angle of 12°. Figure 2.5 clearly demonstrates that the particles do not exhibit any heterogeneous areas.

Table 2.2. Composition of the $ZnGa_2O_4$:Cu^{2+} solid solutions as determined from LA-ICP-MS analyses.

Sample	w % Cu	w % Zn	w % Ga
$ZnGa_2O_4$:Cu^{2+}_14	3.5	21.9	48.5
$ZnGa_2O_4$:Cu^{2+}_4	1.1	23.7	49.7
$ZnGa_2O_4$:Cu^{2+}_2	0.6	23.7	49.5
$ZnGa_2O_4$:Cu^{2+}_1	0.4	24.1	48.9

2.2.2 Structural investigations

X-ray diffraction patterns recorded for the series of microwave-hydrothermally synthesized nanostructured Cu^{2+}-substituted $ZnGa_2O_4$ spinels are shown in Figure 2.6. All diffraction peaks can be indexed to the regular spinel structure of $ZnGa_2O_4$ (S.G. *Fd-3m*, cf. JCPDF No. 38-1240) and the diffraction patterns of the mixed spinels display a significant peak broadening, thereby confirming the nanostructuring of all samples.

Generally, the assignment of structural sites to guest ions in nanostructured solid solutions is important for tuning and understanding their properties, but this can become a demanding task. In the present case, X-ray diffraction investigations with Rietveld methods[45] regarding the localization of Cu^{2+} ions are further impeded by the similar scattering factors of copper, zinc and gallium so that the Rietveld refinement attempts failed to provide detailed information about the coordination environment of the individual cations. Table 2.3 shows that the lattice constants of all samples do not vary significantly with the copper content.

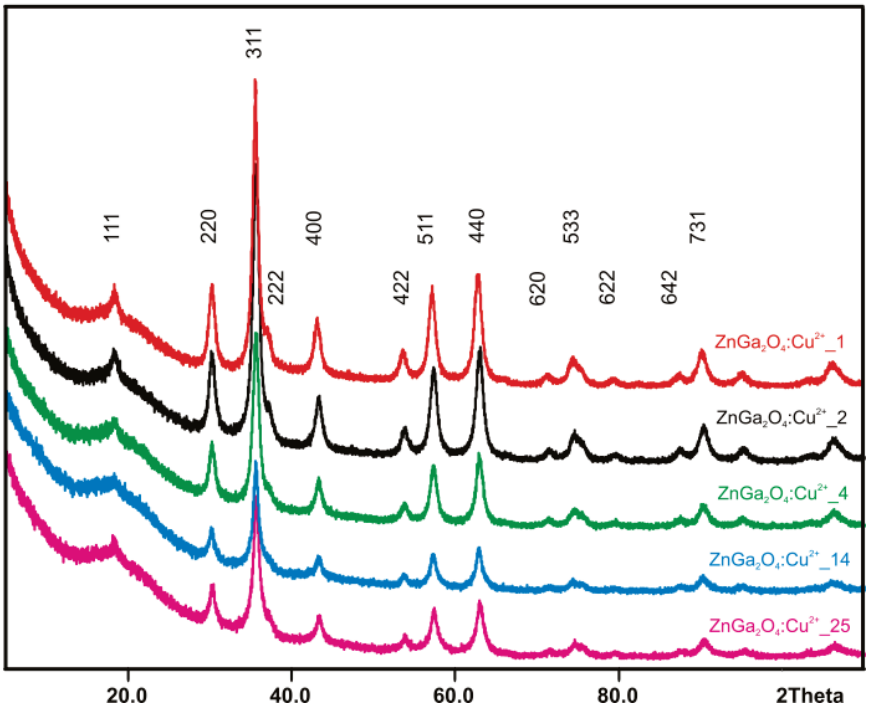

Figure 2.6. X-ray diffraction patterns of the Cu^{2+}-substituted $ZnGa_2O_4$ series synthesized with microwave-hydrothermal techniques.

XANES and EXAFS are complementary tools to XRD in order to characterize the local electronic and geometrical environment of a target element in a crystalline or amorphous matrix in an element-specific manner. Therefore, the coordination of copper within the zinc gallate matrix with the help of these methods was determined.

Table 2.3. Cell constants, cell volumes and FWHM values of the $ZnGa_2O_4:Cu^{2+}$ series.

Sample	a / Å	V / Å^3	FWHM
$ZnGa_2O_4:Cu^{2+}$_25	8.342(1)	580.4	0.79
$ZnGa_2O_4:Cu^{2+}$_14	8.342(5)	580.5	0.71
$ZnGa_2O_4:Cu^{2+}$_4	8.340(6)	580.0	0.78
$ZnGa_2O_4:Cu^{2+}$_2	8.340(6)	580.1	0.82
$ZnGa_2O_4:Cu^{2+}$_1	8.340(4)	580.1	0.83

Figure 2.7 (top) shows the background subtracted and normalized XANES spectra recorded at the Cu K-edge of the CuO reference and of the $ZnGa_2O_4:Cu^{2+}$_4 and $ZnGa_2O_4:Cu^{2+}$_25(12) samples. It has been reported that the A and C resonances increase as B decreases with the reduction of the formal copper valency.[46, 47] The XANES spectra

of the samples $ZnGa_2O_4$:Cu^{2+}_4 and $ZnGa_2O_4$:Cu^{2+}_25(12) are quite similar (Figure 2.7, see related features A - C) and there is no indication for CuO segregation. Copper seems to be in an octahedral environment with an oxidation state +2, especially since comparable results have been observed in $CuFe_2O_4$-NiO nanocomposites.[48]

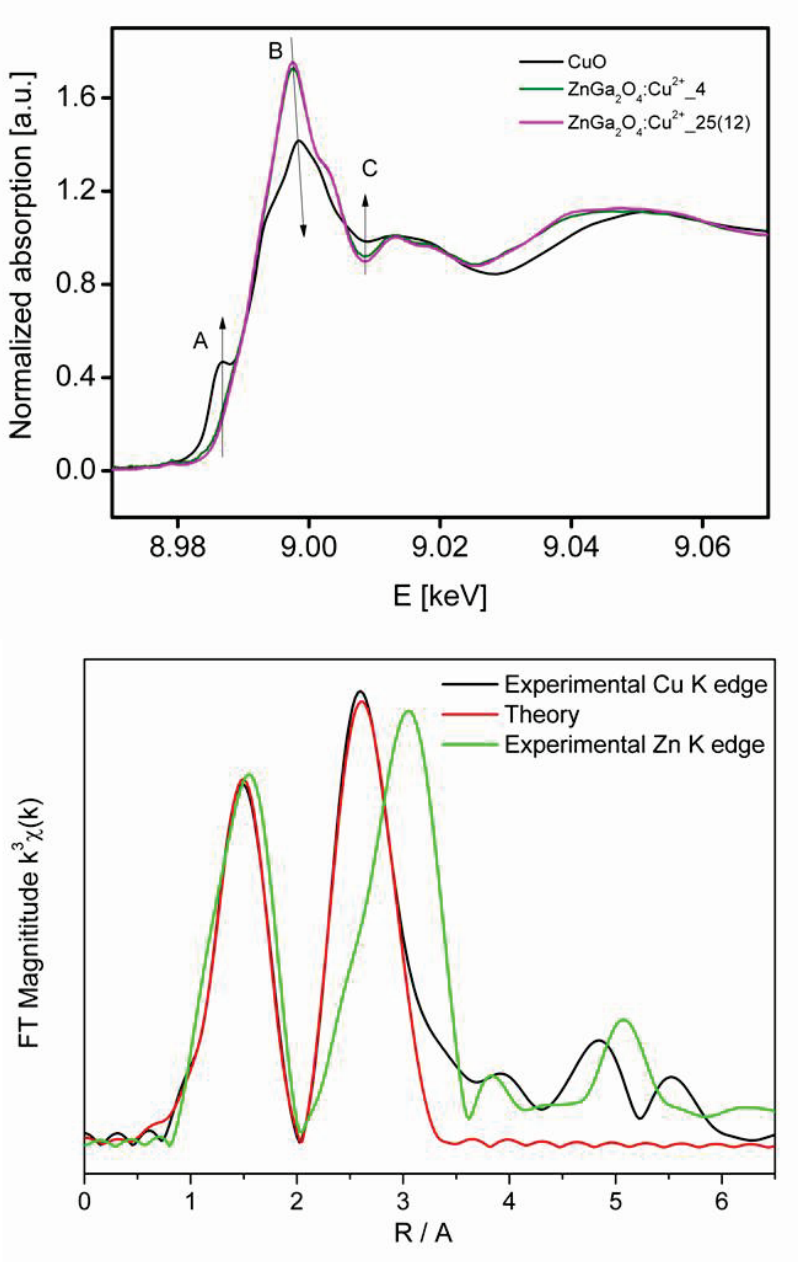

Figure 2.7. Top: Cu K XANES spectra of the CuO reference and of the samples $ZnGa_2O_4$:Cu^{2+}_4 and $ZnGa_2O_4$:Cu^{2+}_25(12). Bottom: Fitting results of the Cu K-edge k^3-weighted EXAFS data at the Cu K- and Zn K-edge of the $ZnGa_2O_4$:Cu^{2+}_25(12) sample.

In order to obtain more in-depth structural information, EXAFS studies were performed on the $ZnGa_2O_4:Cu^{2+}$_25(12) sample. The Fourier transformed of the $k^3\chi(k)$ EXAFS data at the Cu K- and Zn K-edge are shown in Figure 2.7 (bottom; without phase shift correction). The difference in the second shell shows clearly a difference in coordination geometry (cf. Figure 2.7 top). The structural parameters deduced from the EXAFS data analysis are given in Table 2.4. For this purpose Cu was either placed on a tetrahedral or an octahedral site. Only the octahedral site resulted in reasonable fits at the Cu K-edge whereas Zn exhibits mainly tetrahedral geometry. Copper on a tetrahedral site resulted in too short Cu-Ga distances and an unreasonable energy shift. The fits can be improved by placing copper into a distorted octahedral environment - but this also increases the number of free fitting parameters.

Table 2.4. Fit results at the Zn K-edge and Cu K-edge for the $ZnGa_2O_4:Cu^{2+}$_25(12) sample.

Edge	**Shell**	**Absorber**	**CN**	**R/Å**	**σ^2/Å^{-2}**	**E_0/eV**	**Res.**
Zn K-edge	1	Zn-O	4[a]	1.99	0.011	-3.4	9.7
Tetrahedral Zn	2	Zn-Ga	12[a]	3.41	0.015	-5.5	
Cu K-edge	1	Cu-O	4[a]	1.94	0.007	-8.6	12.0
Assuming tetrahedral Cu	2	Cu-Ga	12[a]	3.19	0.012	-29.6	
Cu K-edge	1	Cu-O	6[a]	1.95	0.011	-8.6	12.1
Assuming octahedral Cu	2	Cu-Ga	6[a]	2.98	0.010	2.4	
Cu K-edge	1	Cu-O	3.4 (1)	1.95	0.006	-4.1	6.9
Assuming octahedral Cu	2	Cu-Ga/Cu	6[a]	2.99	0.010	1.2	
Cu K-edge	1	Cu-O	4[a]	1.97	0.007	-1.7	4.6
Assuming octahedral Cu	2	Cu-O	2[a]	2.25	0.014	6.7	
	3	Cu-Ga/Cu	6[a]	2.98	0.009	0.4	

[a] CN: number of neighbours, δ_i: Debye–Waller factor, R_i: interatomic distance, ΔE_i: energy difference (eV), Res.: residual; values labelled with an asterisk (*) were kept constant during the fit assuming $ZnGa_2O_4$ structure and copper replacing either the place of Zn or Ga.

EPR spectroscopy was performed on selected Cu^{2+}-substituted $ZnGa_2O_4$ samples to back the conclusions drawn from the EXAFS investigations. The CW-EPR X- and W-band spectra for Cu centres are shown in Figure 2.8. The spectra indicate the presence of a single type of Cu-centres with $g_{\|} = 2.34$, $A_{\|} = 0.0118$ cm^{-1} and $g_{\perp} = 2.07$. At higher doping levels the magnetic coupling between Cu-centres is observed which leads to the "exchange narrowed" line in the centre of the original uncoupled spectrum. Such large values of the parallel components of the g-tensor and hyperfine tensor are rather unusual for a Cu(II) centre with tetrahedral coordination.[49]

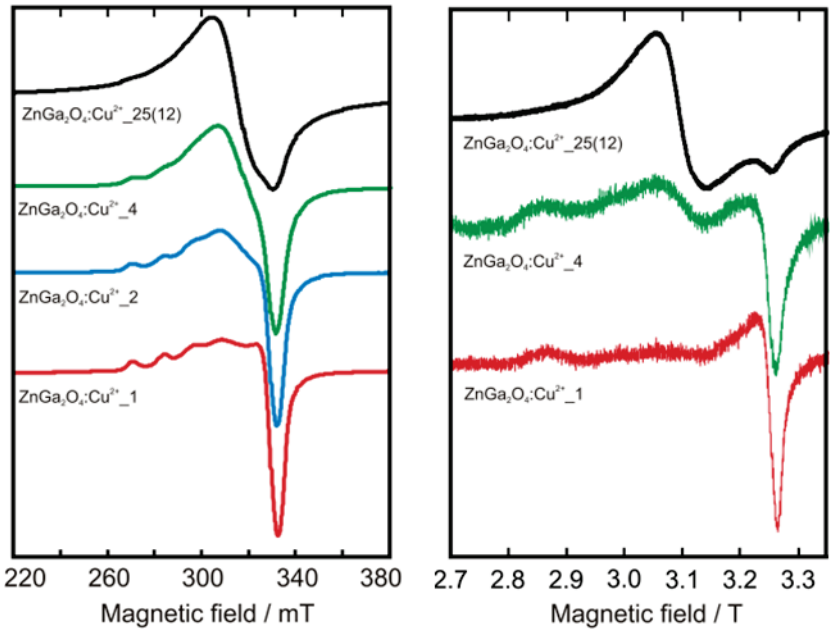

Figure 2.8. Room temperature CW EPR spectra for Cu-containing zinc gallate spinels with different copper concentrations: (left) X-band (9.87 GHz) and (right) W-band (94 GHz).

Nevertheless, reference EPR data on similar inorganic oxide systems permit the conclusion that the observed species are Cu^{2+} ions in octahedral coordination. For copper-containing spinel solid solutions of the $Cu_xMg_{1-x}Al_2O_4$-type, the presence of Cu centres in both octahedral and tetrahedral environments has been observed with XPS and XRD.[50, 51] The obtained EPR spectra displayed *g*-values which are very close to the ones reported here ($g_{\|} = 2.32$ - 2.35 and $g_{\perp} = 2.04$ - 2.06).[50] The EPR active species were attributed to the paramagnetic Cu-centres in a Jahn Teller distorted octahedral coordination. The EPR spectra of tetrahedrally coordinated Cu^{2+} in BeO and ZnO show *g*-values well below 2 in contrast to the results ($g_{\|} = 0.74$, $g_{\perp} = 1.531$ for Cu/ZnO;[52] $g_{\|} = 1.709$, $g_{\perp} = 2.379$ for Cu/BeO[53]). The experimental spectra of the Cu^{2+}-substituted $ZnGa_2O_4$ samples could only

be recorded at temperatures below 30 K, which is consistent with the measured *g*-values, as both phenomena can be interpreted in terms of strong admixing of the angular momentum to the spin state of copper. The observed hyperfine couplings were approximately two orders of magnitude smaller than the one reported here.

To summarize, the observed EPR spectra were considered to arise from Cu^{2+} ions in a tetragonally distorted octahedral coordination. In principle, the presence of small amounts of tetrahedrally coordinated Cu-centres cannot be fully excluded, but they are not detectable at the given experimental conditions. At the lowest available temperature (4 K) no additional EPR signal was observed in the field range corresponding to *g*-values from 0.75 to 3.0. For example, the relative fraction of the copper-centres in octahedral coordination was reported to decrease with the increase of the Cu content in the Mg/Al-spinel.[51] The EPR spectra are informative for the samples with substantially lower Cu content than those subjected to EXAFS investigations. For the samples with higher copper fractions, a single structureless EPR line was observed that is due to strong exchange coupling between different centres. This signal broadening could also conceal possible EPR signals from Cu^{2+} in tetrahedral coordination.

It should furthermore be noted that in the samples with high density of copper centres both the hyperfine coupling to copper nuclei and the anisotropy of the *g*-tensor are averaged out in the EPR spectra. This implies either a distribution of the directions of tetragonal distortion within every single crystallite or a strong coupling between copper centres in different crystallites.

Table 2.5. BET specific surface areas of $ZnGa_2O_4:Cu^{2+}$ spinels.

Sample	**BET [m^2/g]**
$ZnGa_2O_4:Cu^{2+}$_25(12)	29±2
$ZnGa_2O_4:Cu^{2+}$_25	65±3
$ZnGa_2O_4:Cu^{2+}$_14	79±4
$ZnGa_2O_4:Cu^{2+}$_4	72±4
$ZnGa_2O_4:Cu^{2+}$_2	94±5
$ZnGa_2O_4:Cu^{2+}$_1	100±5
$ZnGa_2O_4$	63±3

2.2.3 Materials properties

The BET surface areas of the microwave-hydrothermally synthesized $ZnGa_2O_4$:Cu^{2+} spinel series are summarized in Table 2.5. Obviously, increasing copper contents lead to a decreasing surface area of the solid solutions. In comparison with literature data for the surface areas (12 and 37 m^2/g)[1, 42], the pristine $ZnGa_2O_4$ obtained from microwave-assisted methods exhibits a significantly enhanced surface area of 63 m^2/g.

The solid solution series of Cu^{2+}-doped $ZnGa_2O_4$ spinels was furthermore characterized through UV/Vis spectroscopy. Obviously, the absorption edge displays a red shift with increasing copper contents in the spinel lattice (Table 2.6 and Figures 2.9). The according band gaps can be assigned through extrapolation of the absorbance edge to the wavelength axis. The value 4.3 eV of the pristine $ZnGa_2O_4$ is in line with the literature range of 4.4 to 5.0 eV.[1, 5, 10, 38] The absorption maxima of the $ZnGa_2O_4$:Cu^{2+} series show a very slight tendency towards a blue shift with decreasing copper content that is not contradictory to the trends in individual particle sizes (Figure 2.2) and BET surfaces (Table 2.5).

Table 2.6. Band gaps among the Cu^{2+}-doped $ZnGa_2O_4$ spinel series.

Sample	Peak position / nm	Band gap /
$ZnGa_2O_4$:Cu^{2+}_25	257	4.1
$ZnGa_2O_4$:Cu^{2+}_25(12)	253	4.3
$ZnGa_2O_4$:Cu^{2+}_14	254	4.3
$ZnGa_2O_4$:Cu^{2+}_4	245	4.5
$ZnGa_2O_4$:Cu^{2+}_2	245	4.4
$ZnGa_2O_4$:Cu^{2+}_1	245	4.4
$ZnGa_2O_4$	254	4.3

Macroscopic support for the presence of Cu^{2+} in the spinel lattice stems from the temperature dependence of the magnetization *M*. The measurements were performed on two 30 mg powdered samples of $ZnGa_2O_4$:Cu^{2+} spinels with different copper contents ($ZnGa_2O_4$:Cu^{2+}_14 and $ZnGa_2O_4$:Cu^{2+}_1) in a magnetic field $\mu_0 H$ of 0.1 T. The magnetic behavior is presented in Figure 2.10, exhibiting a pronounced Curie-dependence.

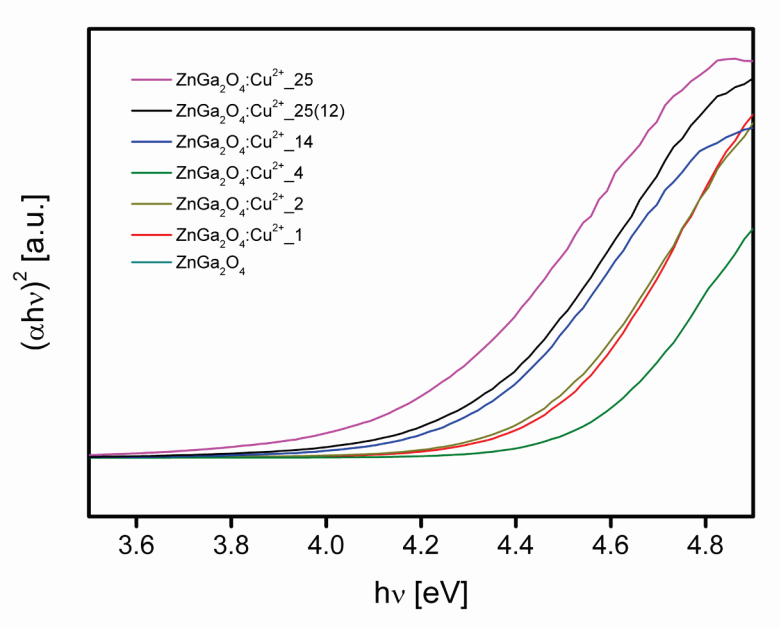

Figure 2.9. UV/Vis spectra of the nanostructured $ZnGa_2O_4:Cu^{2+}$_n mixed spinels (values of n are indicated at the respective curves).

Deviations at high temperatures are due to the difficulty in probing the reduced magnetic moment in the magnetometer – this effect was especially pronounced in the less magnetic spinel sample with low copper content ($ZnGa_2O_4:Cu^{2+}$_1). The molar susceptibility $\chi_m = M/(Hn_{Cu})$ is calculated taking the molar density n_{Cu} of Cupper ions (derived from Table 2.2) into account. For estimating the effective magneton number p_{Cu} of the Cu^{2+} state, the molar susceptibility is analysed according to the Curie law

$$\chi_m = (N_A \mu_0 \mu_B^2 / 3 k_B T)\, p_{Cu}, \qquad \text{(Eq. 2.1)}$$

as described in.[32] As a result, p_{Cu} values of $p_{ZnGa2O4:Cu2+\_14} = 2.2(2)$ and $p_{ZnGa2O4:Cu2+\_1} = 2.1(2)$ are found for $ZnGa_2O_4:Cu^{2+}$_14 and $ZnGa_2O_4:Cu^{2+}$_1, respectively. They are in good agreement with the expected values for a free Cu^{2+} ionic state.

2.3 Sensor and catalytic properties

In the following, unpublished results of sensor and catalytic investigations on $ZnGa_2O_4:Cu^{2+}$ are presented. The results were either not promising or obtained after publication of the original manuscript.

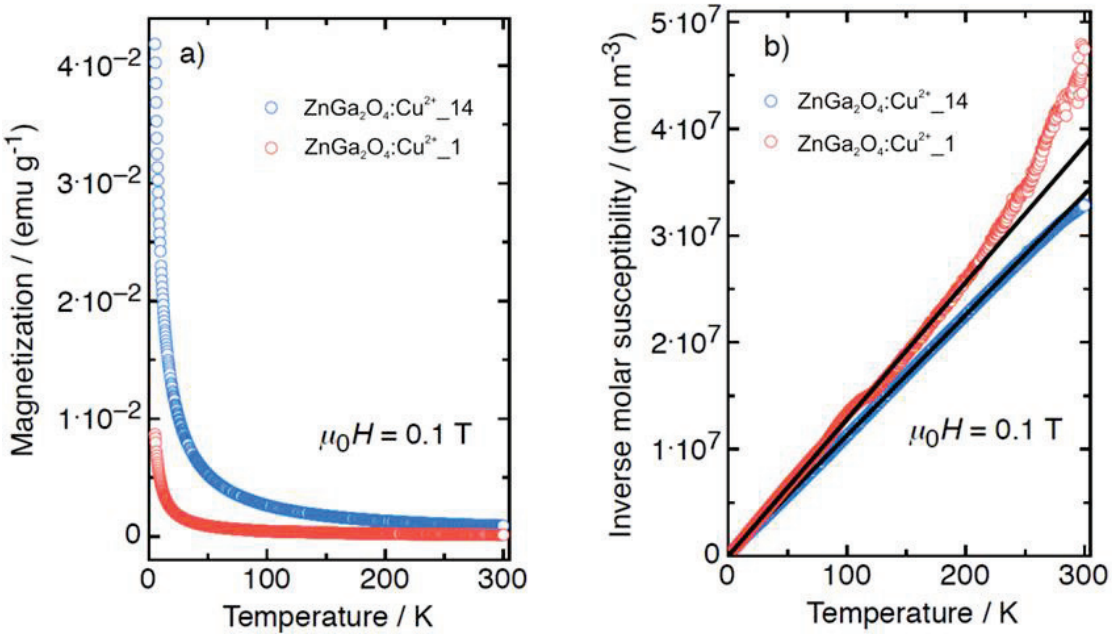

Figure 2.10. (a) Magnetization of two powder samples ($ZnGa_2O_4:Cu^{2+}$_14 and $ZnGa_2O_4:Cu^{2+}$_1) measured in a magnetic field of 0.1 T as a function of temperature; (b) derived inverse molar susceptibility from the magnetization data analyzed according to Eq. (2.1), wherefrom the effective magneton number was calculated.

2.3.1 Gas sensing properties

The gas sensing properties of $ZnGa_2O_4$ for liquid petroleum gas (LPG) had already been reported.[54] Therefore, copper substituted as well as pristine $ZnGa_2O_4$ were tested with several gases such as NH_3 or liquefied petrol gas. The copper-rich sample $ZnGa_2O_4:Cu^{2+}$_25 shows semiconducting behaviour (Figure 2.11) but unfortunately no sensitivity towards any test gas, including LPG. On the other hand, pristine $ZnGa_2O_4$ and the slightly Cu-doped sample $ZnGa_2O_4:Cu^{2+}$_0.16 are still insulating at 300 °C, which is the highest temperature available in the experimental setup. As a consequence, no sensing properties could be measured.

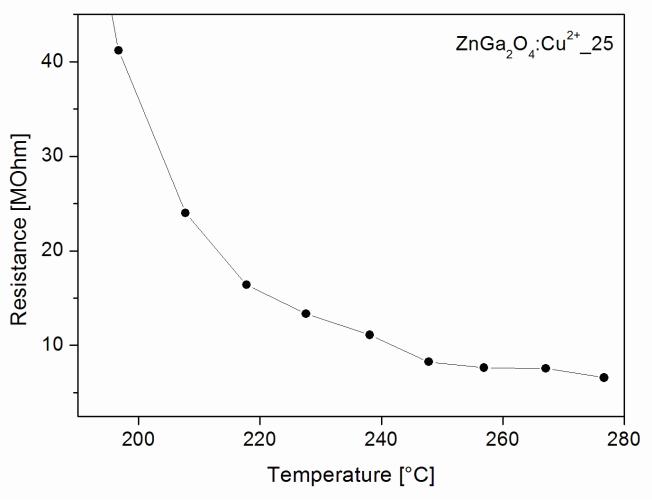

Figure 2.11. Semiconducting behaviour of the powder sample $ZnGa_2O_4$:Cu^{2+}_25.

2.3.2 Photocatalytic degradation of organic dyes

Pristine $ZnGa_2O_4$ and the sample $ZnGa_2O_4$:Cu^{2+}_4 show photocatalytic degradation of RhB up to 80 % within 360 min under daylight irradiation. A representative decomposition process is shown for pristine $ZnGa_2O_4$ in Figure 2.12. On the other hand, upon irradiation of $ZnGa_2O_4$:Cu^{2+}_4 with blue light only ~25 % of RhB is decomposed. Surprisingly, applied DUV (deep ultra violet) light induces complete RhB decomposition within less than 60 min. Reference tests in the absence of catalysts resulted in complete degradation within 120 min. Irradiation with TUV already decomposes organic dyes without any catalyst which is known from water cleaning of ponds.[55-58] In summary, the best photocatalytic degradation of RhB was achieved with pristine $ZnGa_2O_4$ or the sample $ZnGa_2O_4$:Cu^{2+}_4 under daylight irradiation.

2.4 Conclusion

The present study demonstrates that microwave-assisted hydrothermal methods are an efficient access to nanostructured Cu^{2+}-containing $ZnGa_2O_4$ solid solutions. The homogeneous products are obtained within less than two hours of microwave synthesis with no further post-treatment requirements. Although the process is in principle scalable, the vessel load of the microwave reactor has to be carefully calibrated. Under the given microwave-hydrothermal conditions, the solubility of the copper ions in the spinel matrix reaches maximum values around 5 at %.

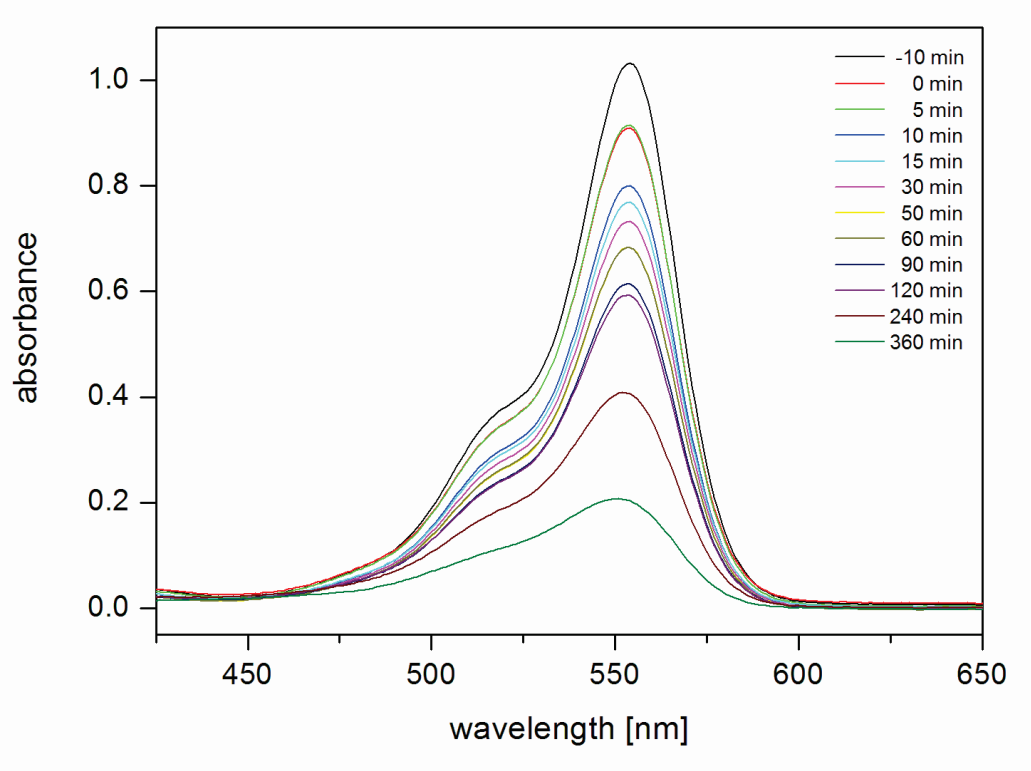

Figure 2.12. Photocatalytic degradation of rhodamine B with nanostructured pristine $ZnGa_2O_4$.

The coordination environment of the Cu^{2+} ions has been investigated with a wide range of complementary analytical methods and their coordination can best be described as a tetragonally distorted octahedral environment. Microwave-hydrothermal methods are especially well suited for the nanoscale synthesis of ternary and higher oxide phase diagrams with volatile and redox active components that are difficult to access with classic sintering methods. Therefore, a novel microwave-assisted synthesis of nanoscale Ga_3O_4:Cu^{2+} has also been developed and will be reported in Chapter 4. The main advantage of the newly presented synthetic approach is that these well-characterized nanostructured spinel materials are now available in larger quantities from a versatile protocol so that their sensor and photocatalytic properties could also be investigated in more detail. Most importantly, the selective reduction of Cu^{2+} centres within the "redox-inert" $ZnGa_2O_4$ spinel matrix is being explored to generate novel catalysts with metal nanoparticles embedded into a structurally stable and well-defined environment (cf. Chapter 3).

References

[1] S. Y. Bae, J. Lee, H. Jung, J. Park, J. P. Ahn, *J. Am. Chem. Soc.* **2005**, *127*, 10802.

[2] L. Xu, Y. Su, Q. T. Zhou, S. Li, Y. Q. Chen, Y. Feng, *Cryst. Growth Des.* **2007**, *7*, 810.

[3] Z. Yu, H. Chen, Z. W. Li, Z. M. Yang, H. B. Song, Y. L. Gao, Y. S. Zhang, Y. Jin, Z. F. Jiao, M. Gong, J. G. Zhu, X. S. Sun, *Mater. Lett.* **2009**, *63*, 37.

[4] L. M. Chen, Y. N. Liu, Z. G. Lu, K. L. Huang, *Mater. Chem. Phys.* **2006,** *97*, 247.

[5] X. Chen, H. Xue, Z. H. Li, L. Wu, X. X. Wang, X. Z. Fu, *J. Phys. Chem. C* **2008**, *112*, 20393.

[6] U. K. Gautam, Y. Bando, J. H. Zhan, P. Costa, X. S. Fang, D. Golberg, *Adv. Mater.* **2008**, *20*, 810.

[7] Y. S. Jeong, J. S. Kim, H. L. Park, *Solid State Commun.* **2006**, *139*, 157.

[8] J. S. Kim, J. S. Kim, T. W. Kim, H. L. Park, Y. G. Kim, S. K. Chang, S. Do Han, *Solid State Comm.* **2004**, *131*, 493.

[9] J. S. Kim, H. L. Park, C. M. Chon, H. S. Moon, T. W. Kim, *Solid State Comm.* **2004**, *129*, 163.

[10] S. K. Sampath, J. F. Cordaro, *J. Am. Ceram. Soc.* **1998**, *81*, 649.

[11] S. H. Yang, M. Yokoyama, *Jpn. J. Appl. Phys. Part 1 - Regul. Pap. Short Notes Rev. Pap.* **1998**, *37*, 6429.

[12] M. Cao, I. Djerdj, M. Antonietti, M. Niederberger, *Chem. Mater.* **2007**, *19*, 5830.

[13] Q. Shi, J. Y. Zhang, C. Cai, L. Cong, T. M. Wang, *Mater. Sci. Eng. B - Adv. Funct. Solid-State Mater.* **2008**, *149*, 82.

[14] K. Sung, T. M. Chung, C. G. Kim, *Mater. Lett.* **2007**, *61*, 1011.

[15] R. Reshmi, K. M. Krishna, R. Manoj, M. K. Jayaraj, *Surf. Coat. Technol.* **2005**, *198*, 345.

[16] G. R. Patzke, S. Locmelis, R. Wartchow, M. Binnewies, *J. Cryst. Growth* **1999**, *203*, 141.

[17] X. T. Zhang, Y. Y. Rao, Y. Liang, R. Deng, Z. Liu, S. Hark, Y. Yuen, S. P. Wong, *J. Phys. D: Appl. Phys.* **2008**, *41*, 095104.

[18] Z. H. Xu, Y. X. Li, Z. F. Liu, Z. Xiong, *Mater. Sci. Eng. B - Solid State Mater. Adv. Technol.* **2004**, *110*, 302.

[19] M. Hirano, *J. Mater. Chem.* **2000**, *10*, 469.

[20] M. Hirano, M. Imai, M. Inagaki, *J. Am. Ceram. Soc.* **2000**, *83*, 977.

[21] M. Hirano, N. Sakaida, *J. Am. Ceram. Soc.* **2002**, *85*, 1145.

[22] Y. D. Li, X. F. Duan, H. W. Liao, Y. T. Qian, *Chem. Mater.* **1998**, *10,* 17.

[23] M. Rajamathi, R. Seshadri, Curr. Opin. *Solid State Mater. Sci.* **2002**, *6*, 337.

[24] K. Byrappa, M. Yoshimura, Handbook of Hydrothermal Technology, Noyes, Park Ridge, N. J., **2001**.

[25] R. Kiebach, N. Pienack, W. Bensch, J. D. Grunwaldt, A. Michailovski, A. Baiker, T. Fox, Y. Zhou, G. R. Patzke, *Chem. Mater.* **2008**, *20*, 3022.

[26] A. Michailovski, M. Worle, D. Sheptyakov, G. R. Patzke, *J. Mater. Res.* **2007**, *22*, 5.

[27] G. R. Patzke, F. Krumeich, R. Nesper, *Angew. Chem. Int. Ed.* **2002**, *41*, 2446.

[28] M. Schaefer, D. Kurowski, A. Pfitzner, C. Nather, Z. Rejai, K. Moller, N. Ziegler, W. Bensch, *Inorg. Chem.* **2006**, *45*, 3726.

[29] S. Baldassari, S. Komarneni, E. Mariani, C. Villa, *J. Am. Ceram. Soc.* **2005**, *88*, 3238.

[30] S. Komarneni, H. Katsuki, *Pure Appl. Chem.* **2002**, 1537.

[31] G. Buhler, A. Zharkouskaya, C. Feldmann, *Solid State Sci.* **2008**, *10*, 461.

[32] A. Le Nestour, M. Gaudon, G. Villeneuve, R. Andriessen, A. Demourgues, *Inorg. Chem.* **2007**, *46*, 2645.

[33] A. Le Nestour, M. Gaudon, G. Villeneuve, M. Daturi, R. Andriessen, A. Demourgues, *Inorg. Chem.* **2007**, *46*, 4067.

[34] M. Robbins, L. Darcy, *J. Phys. Chem. Solids* **1966**, *27*, 741.

[35] A. Sonnauer, N. Stock, *J. Solid State Chem.* **2008**, *181*, 3065.

[36] J. A. Losilla, D. Coutinho, K. J. Balkus, *Microporous Mesoporous Mater.* **2008**, *113*, 325.

[37] P. L. Zhu, J. W. Zhang, Z. S. Wu, Z. J. Zhang, *Cryst. Growth Des.* **2008**, *8*, 3148.

[38] L. Zou, X. Xiang, M. Wei, F. Li, D. G. Evans, *Inorg. Chem.* **2008**, *47*, 1361.

[39] J. Barf, T. Walther, W. Mader, in EuroConference on Structure and Composition of Interfaces in Solids, Kluwer Academic Publ, Kloster Irsee, GERMANY, **2002**, pp. 213.

[40] J. J. Krebs, G. H. Stauss, J. B. Milstein, *Phys. Rev. B* **1979**, *20*, 2586.
[41] T. Maitra, R. Valenti, *J. Phys. - Cond. Matt.* **2005**, *17*, 7417.
[42] V. R. Kumar, K. V. Narasimhulu, N. O. Gopal, H. K. Jung, R. P. S. Chakradhar, J. L. Rao, *J. Phys. Chem. Solids* **2004**, *65*, 1367.
[43] M. Behrens, J. Catal. **2009**, *267*, 24.
[44] D. Gunther, B. Hattendorf, *TrAC-Trends Anal. Chem.* **2005**, *24*, 255.
[45] H. M. Rietveld, *J. Appl. Crystallogr.* **1969**, *2*, 65.
[46] D. Grandjean, H. L. Castricum, J. C. van den Heuvel, B. M. Weckhuysen, *J. Phys. Chem. B* **2006**, *110*, 16892.
[47] T. Vitova, J. Hormes, K. Peithmann, T. Woike, *Phys. Rev. B* **2008**, *77*, 10.
[48] R. K. Selvan, V. Krishnan, C. O. Augustin, H. Bertagnolli, C. S. Kim, A. Gedanken, *Chem. Mater.* **2008**, *20*, 429.
[49] J. R. Pilbrow, Transition Ion Electron Paramagnetic Resonance, Clarendon Press, Oxford, **1990**.
[50] P. K. Sharpe, J. C. Vickerman, *J. Chem. Soc. Faraday Trans.* **1977**, *73*, 505.
[51] J. S. D. Vinuela, C. O. Arean, *Phys. Status Solidi A - Appl. Res.* **1987**, *101*, 57.
[52] R. E. Dietz, H. Kamimura, A. Yariv, M. D. Sturge, *Phys. Rev.* **1963**, *132*, 1559.
[53] M. Dewit, A. R. Reinberg, *Phys. Rev* **1967**, *163*, 261.
[54] L. Satyanarayana, C. V. G. Reddy, S. V. Manorama, V. J. Rao, *Sensors Actuators B - Chem.* **1998**, *49*, 283.
[55] http://www.ponduvfilter.org/.
[56] R. Gori, C. Caretti, *Water Sci. Technol.* **2008**, *58*, 217.
[57] P. Savoye, M. L. Janex, V. Lazarova, *Water Sci. Technol.* **2001**, *43*, 163.
[58] H. S. Son, S. B. Choi, K. D. Zoh, E. Khan, *Water Sci. Technol.* **2007**, *55*, 209.

3 Nanostructured copper substituted ZnM_2O_4 (M = Al, Ga) spinels as precursors for thermally stable Cu catalysts

3.1 Introduction

Methanol steam reforming (MSR) or CO_2 hydrogenation are important industrial processes which are generally catalyzed by $Cu/ZnO/Al_2O_3$ as described in Chapter 1.5.2. The synthesis of such catalysts is a complex multi-step process[1,2] that depends on the controlled segregation of CuO and ZnO from a homogeneous hydroxycarbonate precursor, followed by reductive treatment to generate accessible Cu nanocatalyst centers.[3] Different mixed Cu/Zn-precursor phases lead to various catalyst microstructres[4,5] of the resulting Cu/ZnO composites which differ in particle sizes, crystallinity, Cu lattice strain and particle embedment. These properties have been shown to affect the intrinsic activity of the exposed Cu surface probably by metal-oxide interactions.[6-8] This is a major driving force for exploring novel precursor compounds with a mixed cationic lattice of Cu^{2+}, Zn^{2+} and Al^{3+} to find $Cu/ZnO/Al_2O_3$ related catalysts with new microstructures and superior catalytic properties in CO_2 hydrogenation or MSR.

In this context, the spinel-type oxide $A^{II}B^{III}{}_2O_4$ (A = Cu, Zn; B = Al) is an attractive oxide matrix due to its high thermal stability and mechanical resistance together with the advantage of hosting all three relevant metal species in a mixed cation lattice. This is a good prerequisite for the required homogeneous distribution of Cu^{2+} ions in the precursor. $ZnAl_2O_4$ has already attracted interest as a support for Cu-based methanol synthesis catalysts[9] and $ZnAl_2O_4$:Cu^{2+} materials are furthermore useful for the selective reduction of NO_x as well as for methane combustion.[10,11]

While conventional $Cu/ZnO/Al_2O_3$ catalyst precursor materials, such as hydroxy-carbonates, generate porosity through thermally degradable anions, spinel precursors need to be directly prepared via flexible synthetic methods in a nanosized form with high specific surface area.

For this purpose, microwave-assisted techniques are an up-to-date approach that offers parameter control to generate materials with low particle sizes and high surface areas.[12,13] Microwave-solvothermal (MW-ST) synthesis of $ZnAl_2O_4$ and its Pt- and Pd-loaded forms as well as the MW-HT synthesis of pristine $ZnAl_2O_4$ have been described,[14] and $ZnAl_2O_4$/CuO composites as catalysts for o-alkylation of phenol have been obtained with

conventional-hydrothermal strategies.[15,16] Only recently $ZnAl_2O_4$/CuO catalysts have been accessed for soot oxidation with a microwave-glycothermal route.[17] Furthermore, microwave treatment of $CuO/ZnO/Al_2O_3$ obtained from conventional co-precipitation has been shown to have a beneficial effect on the MSR activity of the resulting $Cu/ZnO/Al_2O_3$ catalysts after reduction.[18] This effect has been attributed to increased strain in the Cu particles.

However, the effect of MW-HT treatment on the materials properties and catalytic performance of $Cu/ZnO/Al_2O_3$ catalysts has never been investigated. In Chapter 2, a newly developed MW-HT approach for the production of otherwise elusive nanostructured $ZnGa_2O_4$:Cu^{2+} materials is described. It permits adjustment of their copper content in a single reaction step from metal sulfates and chlorides.

In this Chapter, the application of this approach for the preparation of $Cu/ZnO/Al_2O_3$ related catalysts from $Cu_xZn_{(1-x)}Al_2O_4$ spinel precursors is reported. The resulting materials were tested in CO_2 hydrogenation and MSR in comparision with conventionally prepared $Cu/ZnO/Al_2O_3$ reference catalysts. Furthermore, the Al-containing materials are compared to their Ga-containing spinel analogues[19] in order to explore the potential of gallium oxides as an emerging and flexible catalyst source.

Note, that the priliminary experiments of the $Cu_xZn_{(1-x)}Al_2O_4$ spinel precursors were designed by the author of this thesis who also performed the TPR measurements of the gallium catalyst. The catalytic and detailed structural experiments were executed by collaborators from Fritz Haber Institute of Max Planck Society Berlin and from Max-Planck-Institut für Chemische Physik fester Stoffe Dresden (cf. thesis survey page VI), followed by joint evaluation.

Table 3.1. Overview of the $Cu_xZn_{1-x}M_2O_4$ (M = Al, Ga) catalyst precursors prepared with a nominal Cu:Zn ratio of ¼ : ¾ at 150 °C.

Sample	FHI-DB#[a]	Precipitating agent	pH[b]	MW-time (h)
Al_7.5_NH3_1	9735	NH_3	7	1
Al_9_NH3_1	9671	NH_3	9	1
Al_9.5_NH3_1	9674	NH_3	9.5	1
Al_9_NaOH_1	9742	NaOH	9	1
Al_10_NaOH_1	9770	NaOH	10	1
Al_10_NaOH_2	9828	NaOH	10	2
Al_10.5_NaOH_1	9771	NaOH	10.5	1
Al_11_NaOH_2	9830	NaOH	11	2
Al_11.5_NaOH_2	9831	NaOH	11.5	2
Ga_10.5_NH3_1	10016	NH_3	10.5	1

[a] sample number in FHI-AC database (http://reload.rz-berlin.mpg.de/sndb/adm.epl?mode=login), [b] initial pH of suspension before MW treatment.

3.2 Results and discussion

First, the focus is placed on the influence of the MW-HT parameters on composition, morphology and surface area of the spinel materials. Next, the thermal redox behavior of the different spinel types is compared, followed by a discussion of their catalytic performance in methanol synthesis by CO_2 hydrogenation and methanol steam reforming.

3.2.1 MW-HT synthesis and characterization of $Cu_{1-x}Zn_xAl_2O_4$

The materials obtained in the Cu-Zn-Al system generally exhibit only weak and broad reflections in their XRD patterns indicative of poor crystallinity and/or small crystallite sizes (Figure 3.1). Background modulations are detected near positions where strong lines of the $ZnAl_2O_4$ spinel are expected. The sample obtained with NaOH as precipitating agent shows a slightly better crystallinity. The absence of well-defined peaks prevents the analysis of the cationic composition of the material by XRD, which is generally difficult due to the closely related scattering factors of Cu and Zn, the similar ionic radii of Cu^{2+} and Zn^{2+}, and the effect of the cation distribution on the lattice parameter of the spinel.[20] The question whether copper was effectively incorporated into the spinel phase was adressed using a combination of integral and local chemical analysis (see below).

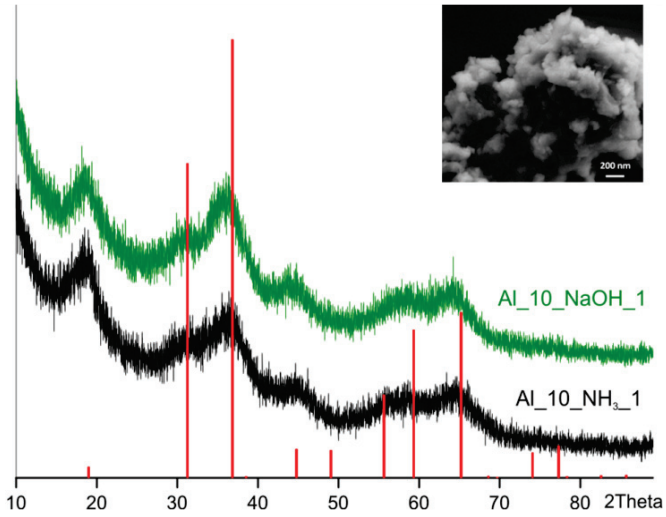

Figure 3.1. Representative XRD patterns of the $Cu_xZn_{1-x}Al_2O_4$ spinel phase obtained by MW-HT treatment of Cu-, Zn- and Al-nitrates precipitated with NH_3 at pH 9 (Al_9_NH3_1) and NaOH at pH 10 (Al_10_NaOH_1).

Variation of synthesis parameters, which is described in detail in Chapter 7, has shown that the pH value of the initial suspension is a key parameter for spinel formation. The pH window is rather narrow and depends on the precipitating agent (NH_3 or NaOH). The optimal values are pH 9 with NH_3 and pH 10 with NaOH. With NH_3 as a precipitating agent, initial pH values which are above 9 favor the formation of aluminium oxide hydroxide (boehmite, ICSD PDF 11-1283). Therefore, the presence of side products can not be completely excluded (cf. UV/Vis spectra in Figure 3.7). Poorly crystalline CuO (ICSD PDF 48-1548) is formed if NaOH is used at pH > 10. Prolonging the reaction time to 2 h was found to reduce the formation of unwanted CuO particles (Figure 3.3 and section 3.3). On the other hand, hydrotalcite-type compounds with nitrate anions are formed if the pH is further lowered.

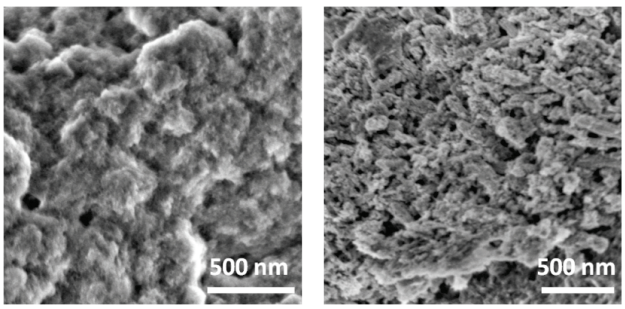

Figure 3.2. Scanning electron microscopy images of $Cu_xZn_{1-x}Al_2O_4$ prepared via MW-treatment from suspensions with initial pH values of 7 (left) and 9.5 (right) with NH_3.

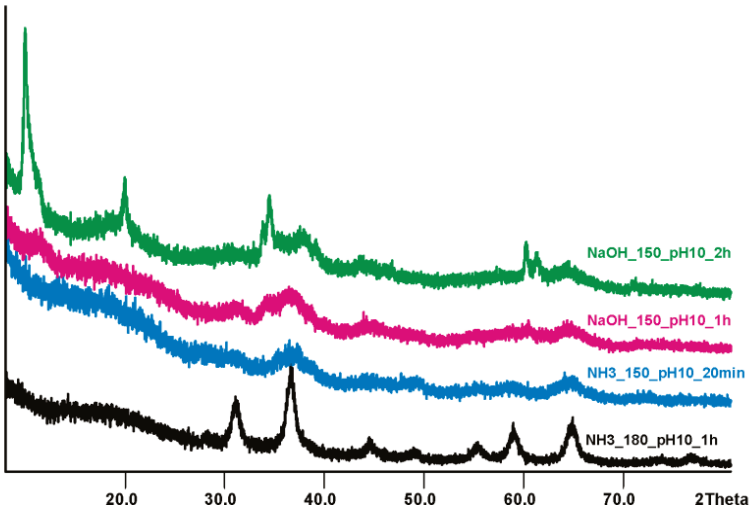

Figure 3.3. Parameter variation study of pristine $ZnAl_2O_4$: PXRD pattern of samples prepared all at pH 10 with NaOH (green – with only 1400 W containing hydrotalcite and 2 h, pink – with 1600 W for 1 h) and synthesized with NH_3 (blue – only for 20 min, black – 1 h at 180 °C).

Although mixed Cu,Zn,Al hydrotalcites have been shown to be suitable precursor materials for Cu-based catalysts in a number of reports,[5,21-23] they are not further considered in the present study that aims at the potential of mixed spinels as precursor compounds. Furthermore, SEM-EDX investigations have shown that the hydrotalcite-containing samples obtained here did not show the desired homogeneous distribution of the metal species (Figure 3.2).

Electron microscopy reveals the presence of hierachically arranged particles with sizes below 10 nm as can be seen in Figure 3.4 a. HRTEM shows that the very broad width of the XRD peaks can be attributed to small crystalline domain sizes. Figures 3.4 b and c show representative images of the samples Al_10_NaOH_1 and Al_9_NH3_1 with crystallite sizes around 5 nm. The lattice fringes could be assigned to the spinel structure (Figure 3.4 b and c insets). Judging from the HRTEM micrographs, the material was not completely crystallized after the MW treatment, and the amount of amorphous material was estimated to be higher for the sample obtained with NH_3 as precipitating agent in agreement with the XRD analysis.

Thermogravimetric measurements of Al_10_NaOH_1 display a considerable mass loss of 28 % up to 500 °C (Figure 3.5 and 3.6) which is attributed to desorption of water

molecules (94 °C, ca. 11 %) and decomposition of OH-groups tentatively located in the amorphous domains of the as-prepared material (247 °C, ca. 17 %). Assuming that the amorphous domains consist of hydroxides, the fraction of uncrystallized material can be estimated on the basis of TGA results to approximately 50 % in the as-prepared sample. Accordingly, calcination at 800 °C leads to a significant intensity increase of the characteristic spinel reflections in the XRD pattern (Figure 3.5). The residue obtained after heating to 1400 °C under N_2 atmopshere displays a distinct spinel pattern with pronounced and sharp high intensity reflections.

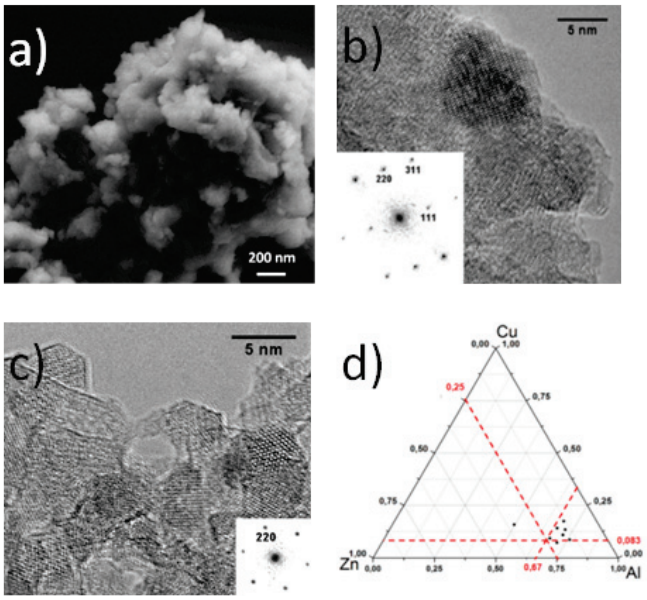

Figure 3.4. Representative electron microscopy images of $Cu_xZn_{1-x}Al_2O_4$ prepared under MW-HT conditions: a) SEM image of Al_10_NaOH_1, b) HRTEM micrographs of the spinel particles in Al_9_NH3_1 (zone axis [211]), c) in Al_10_NaOH_1 (zone axis [111]), and d) local elemental composition of Al_10_NaOH_1 determined at different locations by TEM-EDX. The red lines indicate the nominal composition.

Local EDX analyses of the as-prepared materials (not shown) revealed that all elements are relatively homogeneously distributed in the material and, thus, serve as an additional indicator that Cu is incorporated into the $ZnAl_2O_4$ spinel. The local Cu:Zn ratios determined from LA-ICP-MS measurements are presented in Table 3.2.

In case of the sample prepared with NH_3, the Cu:Zn ratio after the synthesis was significantly below the nominal value of 25:75 (Table 3.2), thereby indicating a loss of copper during MW-HT treatment.

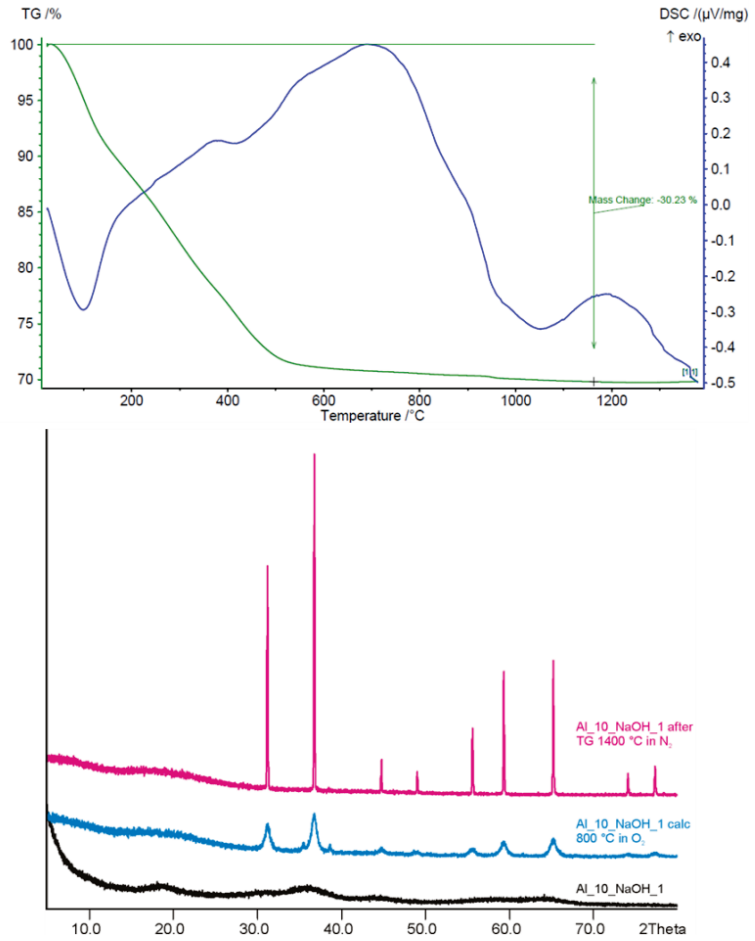

Figure 3.5. TG/DSC (top) and PXRD (bottom) of Al_10_NaOH_1 as prepared spinel, after calcinations at 800 °C in O_2 and after TG/DSC at 1400 °C in N_2.

This can be explained with the formation of soluble blue copper ammine complexes, which prevent a significant fraction of the Cu from precipitation and colorize the supernatant solution. In comparison to MW-HT reactions in NH_3 media, the use of NaOH improves the degree of copper incorporation and affords a Cu:Zn ratio of the products, which is closer to the composition of the starting solution (Table 3.2).

From the observation of spinel formation with XRD and HRTEM in combination with the absence of any segregated Cu phase and the agreement of the local, integral and nominal composition in samples prepared under optimal conditions, the successful incorporation of Cu^{2+} in the $ZnAl_2O_4$ spinel lattice and formation of a mixed spinel $Cu_{1-x}Zn_xAl_2O_4$ can be concluded.

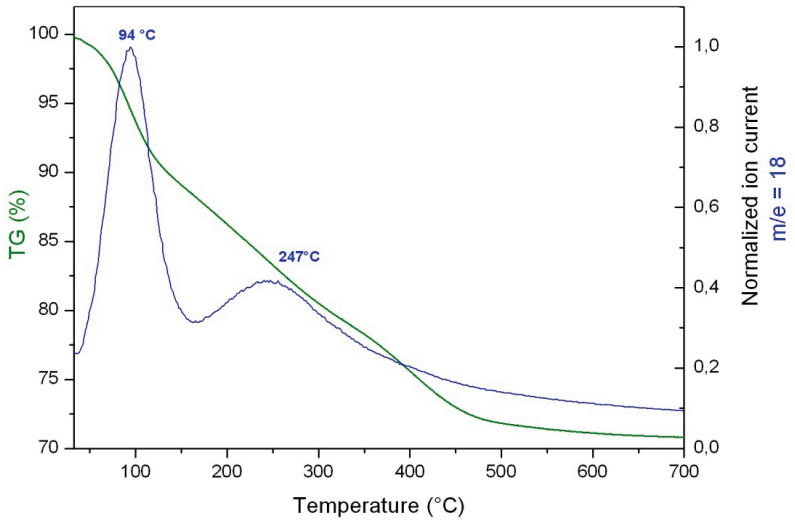

Figure 3.6. TG-MS of Al_10,5_NaOH_2 in synthetic air (21 % O_2 in N_2) showing at least two mass loss steps due to evolving H_2O.

Specific surface areas around 300 m^2/g were determined by N_2 physisorption (Table 3.2). This value is very high[24,25] and in agreement with the nanostructured nature of the crystallites observed by XRD and TEM. The high surface area may be in part attributed to the amorphous domains of the material observed in TEM. After thermal reduction in hydrogen at 310 °C (see below), the sample Al_NaOH_10_2 still exhibits a specific surface area of 101 m^2/g.

Table 3.2. Chemical compositions obtained from LA-ICP-MS analytics (with an average of 5 - 10 local measurements) and BET-surface areas of selected spinel samples.

Sample	Composition	BET (m^2/g)
Al_9_NH_3_1	$Cu_{0.12}Zn_{0.88}Al_2O_4$	299
Al_10_NaOH_2	$Cu_{0.35}Zn_{0.65}Al_2O_4$	268
Al_10.5_NaOH_1	$Cu_{0.36}Zn_{0.64}Al_2O_4$	334
Ga_10.5_NH_3_1	$Cu_{0.05}Zn_{0.95}Ga_2O_4$	72

The analytical data in their entirety show that MW-HT methods provide a nanostructured spinel material $Cu_{1-x}Zn_xAl_2O_4$ ($x \approx 0.7$) with a homogeneous incorporation of Cu^{2+} in the host lattice together with a high surface area. NaOH solutions for pH adjustment are the medium of choice, because they promote copper incorporation and particle crystallinity in comparison with aqueous NH_3.

3.2.2 MW-HT parameter influence on $ZnGa_2O_4:Cu^{2+}$

The synthesis of copper substituted $ZnGa_2O_4$ nanostructured spinels via MW-HT techniques has been described in Chapter 2.

The influence of microwave power and device type on the quality of the products is a well known phenomenon in microwave-assisted materials synthesis.[13] Reference experiments on the MW-HT formation of pristine $ZnAl_2O_4$ in a different device with 1600 W microwave power (MARS 5, cf. Chapter 7) led to spinel-type products with better crystallinity (Figure 3.2).

Generally, the extent of copper incorporation into nanostructured $ZnGa_2O_4$ is lower than the copper uptake of the $ZnAl_2O_4$ matrix under MW-HT conditions: whereas in the latter a Cu:Zn ratio around 10:90 is possible, their gallium-containing analogues can host a Cu:Zn ratio of max. 5:95 under optimized MW-HT preparation conditions.

When comparing the preparative parameters for the Ga- and Al-containing systems, it is noteworthy that the practical handling of the Al-based spinels is less facile than the workup of zinc gallates: whereas the latter can be easily filtered off and washed to generate dry powders, the colloidal and viscous nature of the $ZnAl_2O_4$ samples renders them difficult to isolate and to purify. This technical inconvenience is a side effect of their superior BET surface areas (cf. Table 3.2). In terms of MW-HT synthesis, both systems are accessible from comparably straightforward one-step protocols. The copper host matrices have individual assets and drawbacks: whereas the crystallinity of nanoscale $ZnGa_2O_4:Cu^{2+}$ is considerably higher, $ZnAl_2O_4:Cu^{2+}$ synthesis offers the opportunity of incorporating higher copper amounts into high surface area materials.

UV/Vis spectra of selected spinel samples were recorded to determine the optical band gaps of the compounds (Figure 3.7). As outlined above, the copper substituted $ZnAl_2O_4$ prepared with ammonia shows impurities which could be confirmed with UV/Vis measurements, because two absorption bands were detected. The broadend peak around 700 nm can be attributed to Cu^{2+} in the spinel matrix and corresponds to the light blueish green color of the materials. $Cu_{1-x}Zn_xAl_2O_4$ samples synthesized in the presence of NaOH (reaction times of 1 or 2 h), however, display identical UV/Vis spectra and their band gaps were determined around 3.2 eV (~390 nm), whereas the gallium containing catalyst exhibits a much wider band gap at 4.5 eV (245 nm).

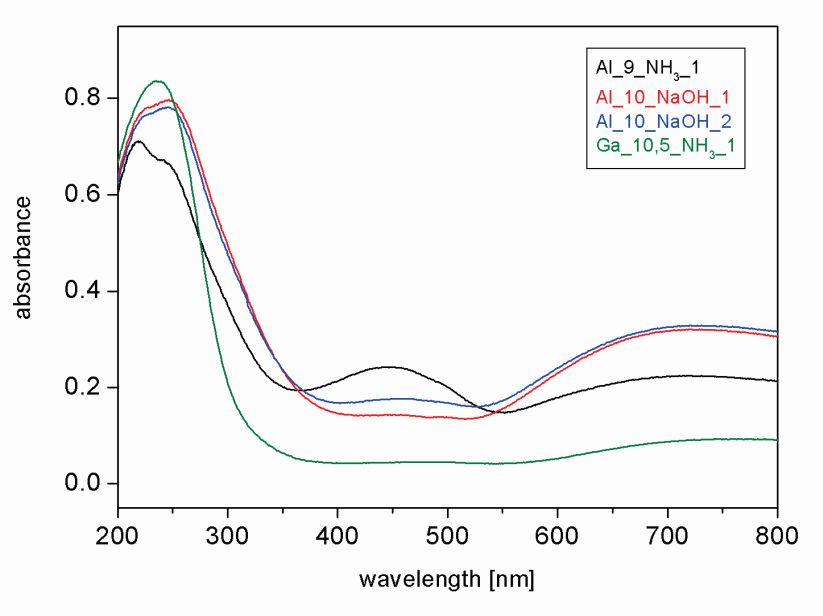

Figure 3.7. UV/Vis spectra of $Cu_{1-x}Zn_xAl_2O_4$ synthesized at different reaction conditions in comparison with $ZnGa_2O_4$:Cu^{2+}.

3.2.3 Redox behavior of the copper centers in $Cu_xZn_{1-x}M_2O_4$ (M = Al, Ga)

$Cu_xZn_{1-x}Al_2O_4$ samples were subjected to temperature programmed reduction (TPR) up to 500 °C and the results are shown in Figure 3.8.

The TPR profile of Al_10_NaOH_1 (Figure 3.8 a) shows one asymmetric peak at 318 °C indicating the presence of a single Cu species. Shoulders at the low temperature side of the TPR profiles are usually observed for the reduction of nanostructured Cu(II) catalyst precursors and are attributed to the intermediate formation of Cu(I) species.[26] The relatively high reduction temperature indicates strong interaction between Cu and the oxide as expected for Cu^{2+} incorporation into the spinel lattice. The absence of other peaks indicated the homogeneous distribution of Cu^{2+}.

The sample prepared at a higher pH of 11 contains segregated CuO (see section 3.1), which is seen in the TPR profile as an additional peak at lower temperature (Figure 3.8 b). Given that no such peaks at lower temperature occur in the TPR profile of Al_10_NaOH_1 (Figure 3.8 a), the presence of even low amounts of CuO in this sample can be excluded, confirming that pH 10 is the optimal value for the synthesis of $Cu_{1-x}Zn_xAl_2O_4$. From the integral of the TPR curve and calibration with a pure CuO standard sample, the degree of Cu(II) → Cu(0) reduction in Al_10_NaOH_1 was determined as 99 %.

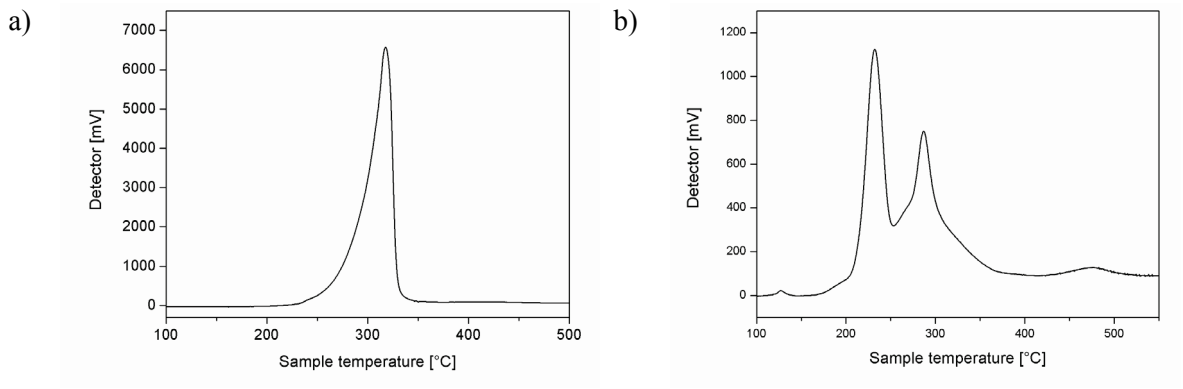

Figure 3.8. TPR profiles showing the hydrogen consumption during reduction of $Cu_xZn_{1-x}Al_2O_4$ samples: a) phase pure spinel isolated at pH 10 (Al_10_NaOH_1) and b) CuO-containing sample synthesized at pH 11, (Al_11_NaOH_2).

Based on the TPR results, 310 °C was chosen as a suitable reduction temperature to mildly release the Cu component from the mixed spinel by reduction in hydrogen for 30 min. TEM investigations on accordingly synthesized samples reveal the formation of metallic Cu nanoparticles that are aggregated with spinel particles (Figure 3.9 a and b). A mean Cu particle diameter of 3.3 nm ± 0.9 was obtained from particle statistics based on hundred particles and fitted with a log-normal distribution (Figure 3.9 c).

The metallic copper surface after reduction was determined by N_2O reactive frontal chromatography (RFC) to 8.2 m^2/g. This value is significantly lower than the accessible Cu surface area in industrial methanol synthesis catalysts, which typically ranges from 20 to 30 m^2/g for Cu particles around 10 nm. Nevertheless, these results show that a $Cu/ZnO/Al_2O_3$ based catalyst has been prepared from the spinel precursor with very small and relatively uniform Cu particles and a clearly measureable Cu surface area. Assuming a spherical shape of the particles and bulk density of Cu, a theoretical Cu surface area of the hypothetically unsupported Cu nanoparticles can be calculated from the TEM results. Comparison with the measured Cu surface area reveals that only a fraction of approximately 32 % of the Cu particles' surface is accessible to the gas phase, while 68 % are covered with the oxide matrix. Thus, the particles are in average more strongly embedded into the oxide matrix than has been observed for conventionally prepared $Cu/ZnO/Al_2O_3$ catalysts.[27] Together with the small size of the Cu nanoparticles, the embedment can be seen as a special characteristic of the microstructre of the ex-spinel $Cu/ZnO/Al_2O_3$ catalyst. Both properties can be attributed to the homogeneous distribution and strong interaction of Cu^{2+} in the spinel lattice of the precursor.

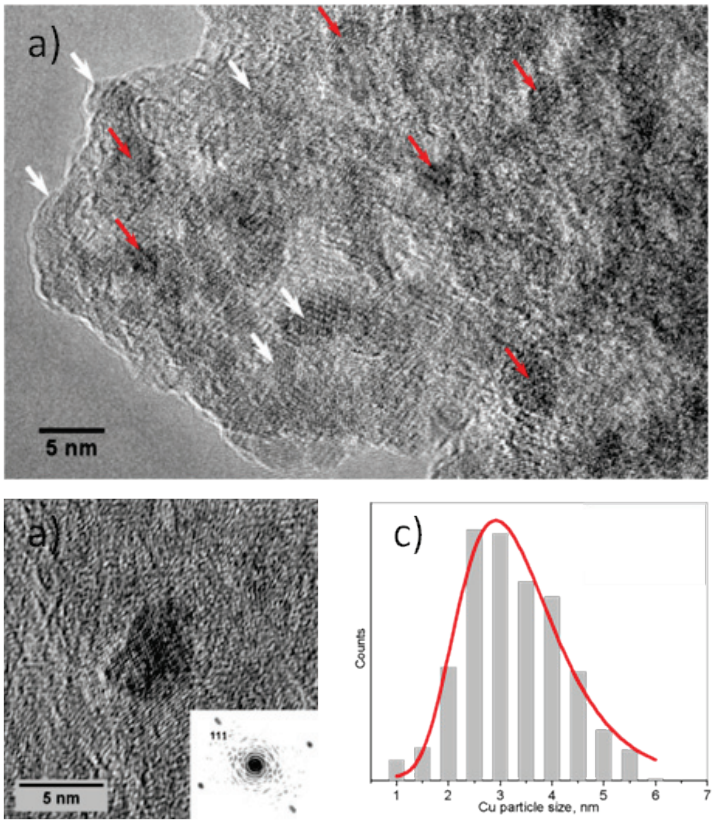

Figure 3.9. a) HRTEM image of Al_10_NaOH_1 after reductive thermal treatment in hydrogen at 310 °C (cf. Figure 2 b, c for pristine sample, red arrows – Cu metal, white arrows – spinel). b) HRTEM image of an individual Cu(0)-particle with power spectrum (zone axis [110]). c) particle size distribution of the copper nanoparticles.

In order to further characterize the redox chemistry of the spinel material, the above sample was thermally reduced at 500 °C and re-examined after 11 days of storage in the reaction container under ambient conditions and after re-oxidation in 5 % O_2 at 500 °C by XRD analysis (Figure 3.10).

Broad reflections of the spinel phase can be seen in all XRD patterns. The improved crystallinity compared to the as-prepared state (Figure 3.1) can be attributed to the crystallization of the amorphous domains observed in HRTEM (Figure 3.4). HRTEM (Figure 3.9) of the sample reduced at 310 °C and XRD after treatment at 500 °C indicate only minor increase of the spinel crystallites due to sintering of the oxide. Even the Cu phase does not show any sharp and well-developed XRD peaks after reduction at a temperature as high as 500 °C (Figure 3.10 a), thus indicating that Cu remains nano-structured. This is remarkable, given that conventional $Cu/ZnO/Al_2O_3$ catalysts are typically very prone to sintering and as a rule of thumb should not be treated at temperatures exceeding 300 °C.[28]

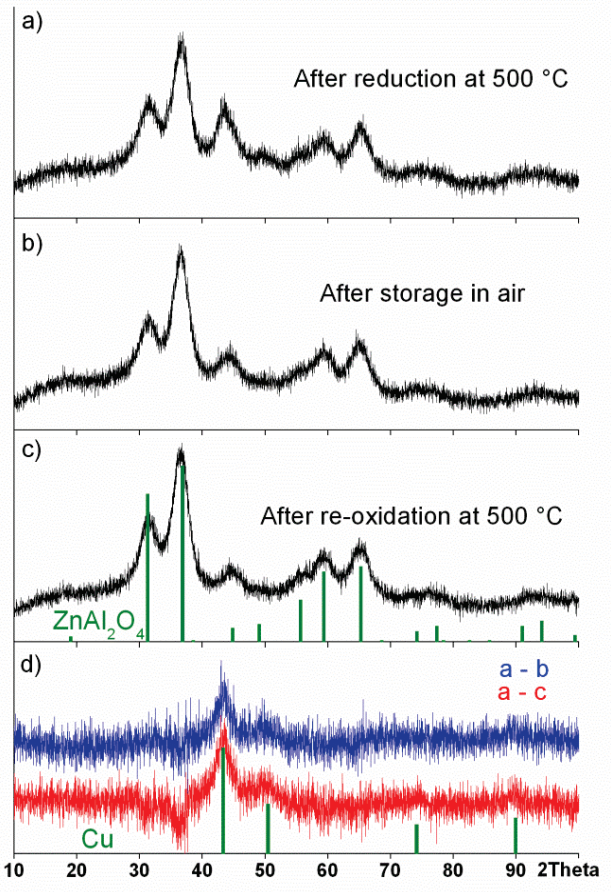

Figure 3.10. XRD patterns of the $Cu_{1-x}Zn_xAl_2O_4$ sample Al_10_NaOH_1 after different pre-treatments: a) after reduction in hydrogen at 500 °C, b) after storage in air for 11 days, c) after re-oxidation in oxygen at 500 °C. Difference patterns are shown in d). The bar graph in c) refers to $ZnAl_2O_4$ (PDF 5-669), that in d) to Cu (PDF 4-836).

Cu nanoparticles are known to oxidize in contact with oxygen and partial and full re-oxidation is expected in air at ambient temperature and by heating in oxygen, respectively. The subtle changes in the diffractograms (Figure 3.10 b and c) are best evaluated by substracting the normalized patterns from that of the reduced sample and analyzing the difference pattern (Figure 3.10 d).

The signature of metallic Cu is clearly seen confirming that Cu^{2+} from the spinel lattice was reduced. In case of the sample stored in air the contribution of metallic Cu to the pattern is lowered indicating a partial re-oxidation of the Cu centers by air contact. Treatment in oxygen minimizes the content of metallic Cu. Attempts to refine the XRD patterns are reported as supporting information (Figure 3.11), but their significance should be dealt with caution due to the low pattern quality of the poorly crystalline and nanostructured samples.

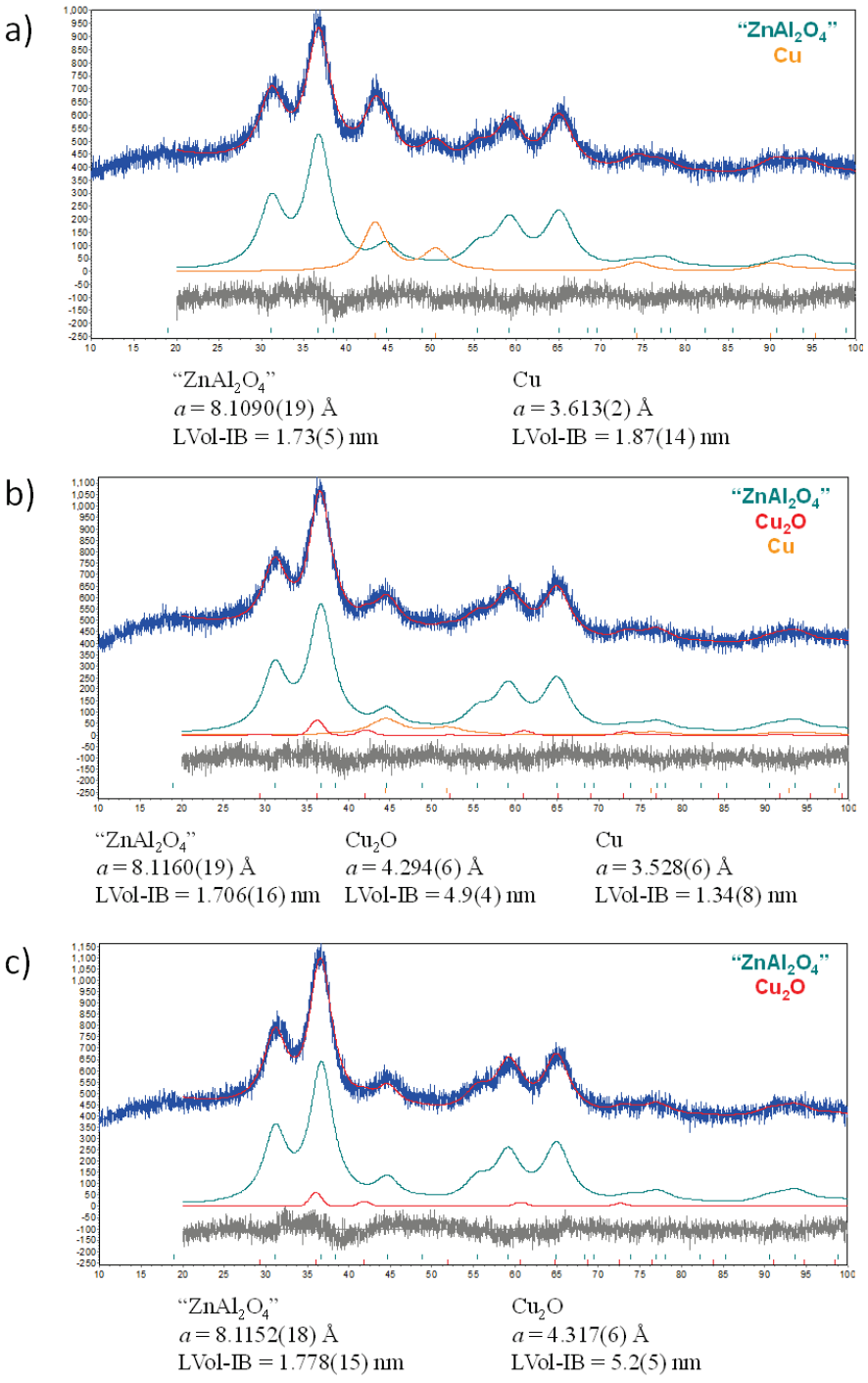

Figure 3.11. Rietveld refinements of the sample Al_10_NaOH_1 after reduction at 500 °C in hydrogen (a), storage in air for 11 days (b) and re-oxidation in oxygen at 500 °C (c) using the TOPAS software package [A.A. Coelho, TOPAS Version 3.0 Bruker AXS GmbH, Germany].

In case of the re-oxidized sample, the fit improves if small amounts of Cu_2O are included in the refinement. This result is confirmed by HRTEM investigations, which show the presence of only few Cu_2O particles and an otherwise homogeneous Cu distribution in this sample (Figure 3.12).

No crystalline CuO could be detected. On the basis of these results it is estimated that approximately 80 % of the metallic Cu had been regenerated as Cu^{2+} and restored in the $Cu_xZn_{1-x}Al_2O_4$ spinel, whereas the remaining fraction of Cu had been partially oxidized to Cu_2O. This observation is in line with literature reports.[29] Thus, an at least partial oxidative regeneration of the Cu dispersion after catalyst deactivation is feasible in this system.

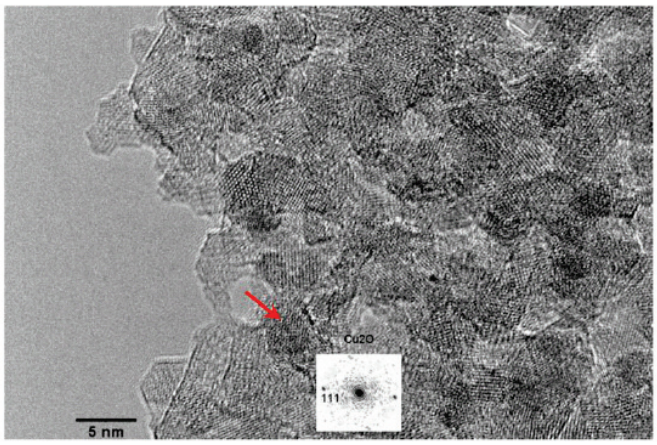

Figure 3.12. HRTEM-image of Al_10_NaOH_1 after reduction at 500 °C in hydrogen and subsequent re-oxidation in oxygen at 500 °C showing remaining oxidized copper particles indentified as Cu_2O (according to Fourier transform of the diffraction pattern).

As outlined in Chapter 7, Ga_10.5_NH_3_1 was heated to 600 °C in helium atmosphere in order to distinguish possible sintering phenomena from reduction-induced effects during the *in situ* XRD experiment. This permits a clear-cut investigation of the reduction options for the incorporated copper ions with respect to catalytic applications. Neither sintering nor significant changes in the cell parameters were observed up to 400 °C and reductive thermal treatment did not change the crystallite sizes or the appearance of new diffraction peaks either. Spinel sintering sets in around 500 °C and leads to slight alterations of the unit cell dimensions that could only be detected with long-time measurements at room temperature. Although these experiments clearly show the presence of phase pure spinel, the embedding of the Cu^{2+} species into this matrix apparently minimizes their reducibility. Related phenomena have been observed for $ZnAl_2O_4$ matrices with low degrees of copper incorporation.[17] Given that the initial copper metal content in the sample is below 5 % (Table 3.2), the reduction process may well fall below the limits of XRD sensitivity. Nevertheless, TPR measurements (Figure 3.13) display a reduction process that is obviously not reflected in a significant change of the lattice constants. Whether its initial

stages involve hydrogen incorporation,[30] partial reduction of Cu^{2+} to Cu^{+} or reduction of XRD-invariant surface/amorphous regions can only be speculated at this point.

TPR measurement of Ga_10.5_NH_3_1 was performed in the range from RT to 700 °C to investigate the optimal range for reduction experiments (Figure 3.13). Two peaks were recorded: whereas the first peak at 280 °C arises from Cu^{2+} species incorporated inside the spinel structure, the second broad peak around 500 °C might be assigned to the partial reduction of Ga^{3+} in the spinel and formation of defects, e.g. oxygen vacancies. It has been shown that such defects are formed in β-Ga_2O_3, by O-abstraction in reducing atmosphere at temperatures above 300 °C.[31,32] *Ex situ* XRD measurements after the reduction confirmed that the TPR treatment did not significantly change the spinel structure (Figure 3.14).

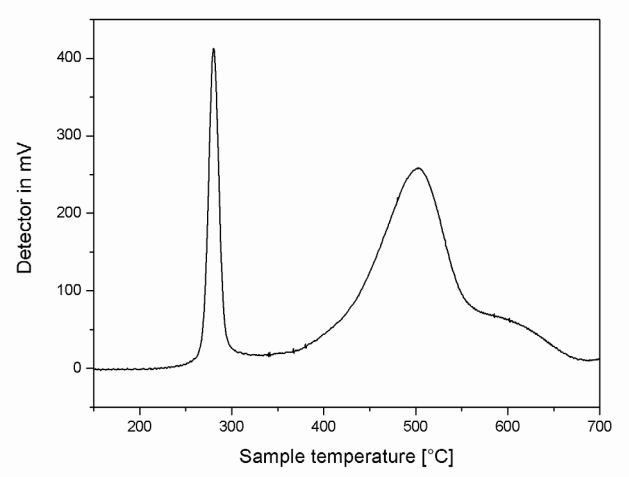

Figure 3.13. TPR of nanostructured $ZnGa_2O_4$:Cu^{2+} (sample Ga_10.5_NH_3_1).

Furthermore, a N_2O RFC after reduction at 300 °C was performed and the specific copper surface area was determined as 3.2 m^2/g. This value is 2.5 times lower compared to the Cu(0) surface area of 8.2 m^2/g observed for Al_10_NaOH_1. However, this was to be expected, given that the gallium containing material incorporates 2.75 times less copper in the spinel matrix than Al_10_NaOH_1. TEM investigation of the reduced sample show that the nano-structured nature of the sample has been maintained (Figure 3.15 a). Two different types of material can be detected. Larger particles on the right hand side of the aggregate shown in Figure 3.15 a and smaller grains on the opposite side. A HRTEM image of an area with smaller grains is shown in Figure 3.15 b confirming the presence of crystalline spinel. No metallic Cu particles could be observed, probably due to their small size and their strong embedment into the spinel matrix.

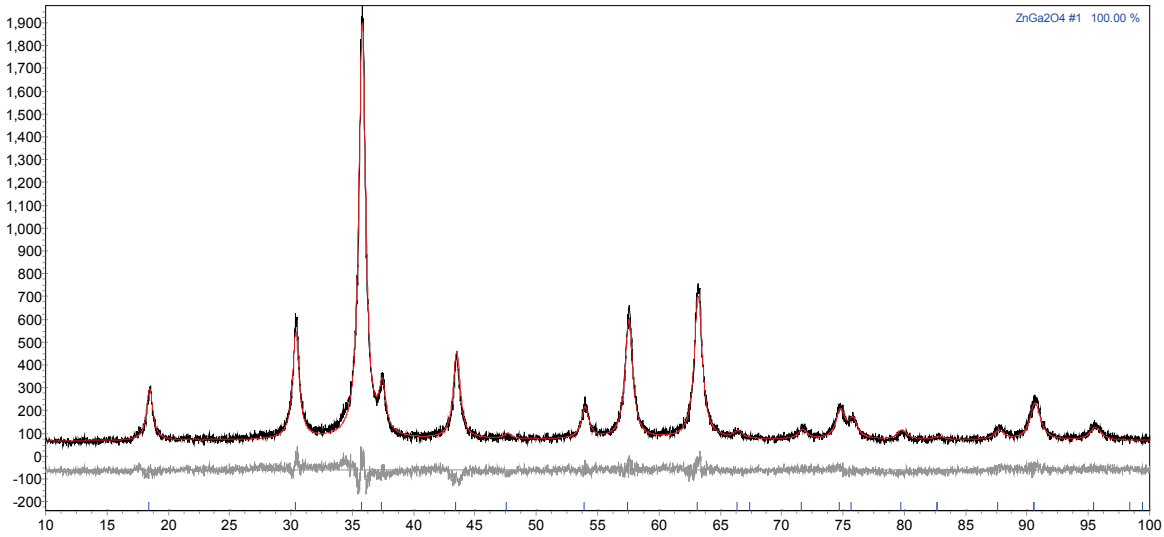

Figure 3.14. PXRD of Ga_10.5_NH_3_1after TPR at 500 °C. Formation of Cu metal is suggested by TPR (see main text), but the total amount of Cu in this sample is below the detection limit of XRD.

3.2.4 Catalytic performance of $Cu_{1-x}Zn_xM_2O_4$ catalysts (M = Al, Ga)

The previously described catalyst materials were tested in CO_2 hydrogenation and methanol steam reforming (MSR). Conventionally prepared Cu/ZnO/Al_2O_3 catalysts were used as references for both reactions.

Methanol synthesis tests were performed at 250 °C. An overall CO_2 conversion of 4 % was observed and the selectivity for CO (85 %) was considerably higher than for methanol (15 %). In comparison, the conventional catalyst exhibits 9 % CO_2 conversion and a methanol selectivity of 62 % already at a temperature of 220 °C (Table 3.3), at which the spinel-based catalysts did not show any activity.

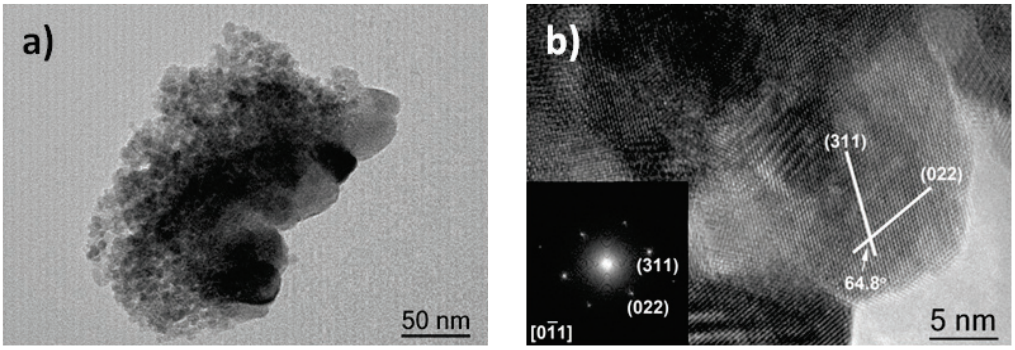

Figure 3.15. Representative TEM (a) and HRTEM (b) images of the reduced $ZnGa_2O_4$:Cu^{2+} sample Ga_10.5_NH_3_1.

The Cu surface area of the conventional catalysts was higher by a factor of ca. 3.7, but this alone cannot compensate for the differences in conversion considering the higher catalyst mass and reaction temperature of the spinel-based sample. Thus, the intrinsic activity of the exposed Cu surface of this sample is lower. Interestingly, also the selectivities of both samples differ considerably. While a large fraction of CO_2 is hydrogenated to methanol over the conventional catalyst, it is mostly converted into CO by the rWGS reaction over the spinel-based sample.

Table 3.3. Catalytic performance of ex-spinel and conventional $Cu/ZnO/Al_2O_3$ catalysts in methanol synthesis from CO_2/H_2 (with [a] in mg/h).

Parameter	conventional	spinel-based
Reaction temperature	220 °C	250 °C
Catalyst mass	0.2 g	1.0 g
CO_2 conversion	9 %	4 %
CO selectivity	38 %	85 %
CH_3OH selectivity	62 %	15 %
Yield CO[a]	3.6	12
Yield CH_3OH[a]	6.7	2.4

The MSR data after 2 and 20 h on stream are summarized in Table 3.4. Regarding the conversions, the methanol steam reforming experiments reveal a similar picture. After a period of 20 h on stream, the relative hydrogen yield (experimental relative to stoichiometric hydrogen yield) detected over 30 mg of the conventional reference sample decreases from 84 % to 65 %. On the other hand 125 mg of the reduced $Cu_{1-x}Zn_xAl_2O_4$ catalyst show a relative hydrogen yield of 45 - 54 %. Also in this reaction, the different Cu surface areas loaded into the reactor alone cannot explain the difference in performance. Contrary to CO_2 hydrogenation, in the MSR reaction the selectivities of the two Cu-Zn-Al catalysts are almost equal and higher than 98 %. 500 mg of the reduced $Cu_{1-x}Zn_xGa_2O_4$ catalyst only achieve ~20 % hydrogen yield. Furthermore, the selectivity to CO_2 exhibits only 65-70 %.

The lower total yield may be partly explained with the lower Cu surface area of the Ga-containing sample. The low CO_2 selectivity is either to be due to a higher activity of this sample for methanol decomposition in hydrogen and CO or for rWGS converting the MSR products H_2 and CO_2 into CO and H_2O. Since the main difference in the two spinel-based catalysts is the presence of Ga and Ga_2O_3 has been reported to be active in rWGS,[31] the latter explanation seems more likely.

Table 3.4. Catalytic performance of spinel and conventional $Cu/ZnO/Al_2O_3$ catalysts in methanol steam reforming (with [a] in mmol H_2 /g h, [b] in %).

Parameter	**conventional**		**spinel**			
			$Cu_{0.36}Zn_{0.64}Al_2O_4$		$Cu_{0.05}Zn_{0.95}Ga_2O_4$	
catalyst mass [mg]	30		125		500	
TOS	**2h**	**20h**	**2h**	**20h**	**2h**	**20h**
H_2 yield[a]	867	665	126	112	14	11
rel. H_2 yield[b]	84	65	54	45	22	17
S_{CO2}[b]	98.1	99.2	98.4	98.3	70.6	66.7

In summary, catalytic activity of the spinel $Cu_{1-x}Zn_xM_2O_4$ (M = Al, Ga) catalysts in CO_2 hydrogenation and MSR could be observed. However, despite the successful nanostructuring of the spinel precursor and the significant Cu surface area that is exposed to the feed gases, the spinel-based catalysts were found to be clearly inferior compared to state-of-the-art $Cu/ZnO/Al_2O_3$ catalysts. This result is an example that beyond the mere presence of the elements Cu-Zn-Al, their solid-state-chemical state and microstructural arrangement critically determines the performance of a $Cu/ZnO/Al_2O_3$ catalyst. The often observed synergetic effect of the ZnO-species,[33] on the intrinsic activity of Cu is not prevailing if Zn^{2+} is incorporated into a crystalline spinel matrix. This is probably due to the limited reactivity of the ionic Zn in the spinel lattice. Incorporation into the stable spinel decreases the reducibility of Zn^{2+} and hinders strong metal support interaction with Cu, which have been observed in various Cu/ZnO materials[34-36] and proposed to play a role for the catalytic performance. The results show that the lack of interaction with ZnO affects the activity as well as the selectivity of the exposed Cu surface and suggests participation of a distinct ZnO-species at the active site of methanol synthesis.

3.3 Conclusion

A microwave-hydrothermal synthesis method, previously developed for the preparation of Cu-doped $ZnGa_2O_4$,[19] has been successfully applied and optimized the preparation of a $Cu_{1-x}Zn_xAl_2O_4$ precusor material for a $Cu/ZnO/Al_2O_3$ catalyst of a unique microstructure. At optimal synthesis conditions, the precursor material was obtained in a nano-sized form with a homogeneous distribution of the Cu and Zn cations in the spinel lattice and with a high specific surface area around 300 m^2/g. Reduction in hydrogen yields very small Cu

particles (< 4 nm), which are partially embedded in the oxide matrix and exhibit an exposed Cu surface area of 8 m^2/g. Despite these promising properties, the catalytic performance of the material in CO_2 hydrogenation and methanol steam reforming was found to be inferior to conventionally prepared $Cu/ZnO/Al_2O_3$ catalysts. These results highlight the crucial role of the microstructural arrangement of the components in a $Cu/ZnO/Al_2O_3$ composite catalyst on the nanoscale and clearly show that the synergetic role of ZnO for Cu-based catalyst is not effective, if Zn is incorporated into a crystalline spinel matrix. The high thermal stability of the Cu nanoparticles and their embedment into the oxide matrix, however, render these catalysts promising candidates for applications at higher temperatures, where conventionly Cu-based catalysts strongly deactivate due to sintering and loss of active surface area.

In addition, a MW-HT prepared $ZnGa_2O_3:Cu^{2+}$ catalyst precursor was subjected to analogous reductive treatment and catalytic tests. Given that the gallium spinel matrix limits the copper uptake, the activity in MSR of the $ZnGa_2O_3:Cu^{2+}$-based catalyst is comparable to the copper-loaded zinc aluminium spinel, while the selectivity is influenced probably by participatation of Ga-centers at the catalytic reaction.

These results show how spinels – one of the most flexible and most stable classes of solid state materials – can be prepared in a nanostructured form allowing access to well-defined precursor materials for model composite catalysts, which have great potential to contribute to the understanding of the functionality of complex catalytic materials.

References

[1] D. Waller, D. Stirling, F. S. Stone, M. S. Spencer, *Farad. Discuss. Chem. Soc.* **1989**, *87*, 107.
[2] C. Baltes, S. Vukojević, F. Schüth, *J.Catal.* **2008**, *258*, 334.
[3] M. Behrens, *J. Catal.* **2009**, *267*, 24.
[4] B. L. Kniep, F. Girgsdies, T. Ressler, *J. Catal.* **2005**, *236*, 34.
[5] M. Behrens, I. Kasatkin, S. Kühl, G. Weinberg, *Chem. Mater.* **2009**, *22*, 386.
[6] M. Behrens, A. Furche, I. Kasatkin, A. Trunschke, W. Busser, M. Muhler, B. Kniep, R. Fischer, R. Schlögl, *ChemCatChem* **2010**, *2*, 816.
[7] M. M. Günter, T. Ressler, B. Bems, C. Büscher, T. Genger, O. Hinrichsen, M. Muhler, R. Schlögl, *Catal. Lett.* **2001**, *71*, 37.
[8] S. Kaluza, M. Behrens, N. Schiefenhövel, B. Kniep, R. Fischer, R. Schlögl, M. Muhler, *ChemCatChem* **2011**, *3*, 189.
[9] T. P. Maniecki, P. Mierczyński, W. Maniukiewicz, D. Gebauer, W. K. Jozwiak, *Kinet. Catal.* **2009**, *50*, 228.

[10] C. Kienle, C. Schinzer, J. Lentmaier, O. Schaal, S. Kemmler-Sack, *Mater. Chem. Phys.* **1997**, *49*, 211.
[11] C. Chauvin, J. Saussey, J.-C. Lavalley, H. Idriss, J.-P. Hindermann, A. Kiennemann, P. Chaumette, P. Courty, *J. Catal.* **1990**, *121*, 56.
[12] I. Bilecka, M. Niederberger, *Nanoscale* **2010**, *2*, 1358.
[13] F. Gao, Q. Lu, X. Meng, S. Komarneni, *J. Mater. Sci.* **2007**, *43*, 2377.
[14] W. Walerczyk, M. Zawadzki, J. Okal, *Appl. Surf. Sci.* **2011**, *257*, 2394.
[15] W. Mista, M. Zawadzki, H. Grabowska, *Res. Chem. Intermed.* **2003**, *29*, 137.
[16] M. Zawadzki, *Solid State Sci.* **2006**, *8*, 14.
[17] M. Zawadzki, W. Staszak, F. E. López-Suárez, M. J. Illán-Gómez, A. Bueno-López, *Appl. Catal A* **2009**, *371*, 92.
[18] X.-R. Zhang, L.-C. Wang, Y. Cao, W.-L. Dai, H.-Y. He, K.-N. Fan, *Chem. Comm.* **2005**, 4104.
[19] F. Conrad, Y. Zhou, M. Yulikov, K. Hametner, S. Weyeneth, G. Jeschke, D. Günther, J. Grunwaldt, G. R. Patzke, *Eur. J. Inorg. Chem.* **2010**, *13*, 2036.
[20] C. O. Arean, J. S. D. Vinuela, J. M. R. Gonzalez, A. M. Arjona, *Mater. Chem.* **1981**, *6*, 165.
[21] G. Busca, U. Costantino, F. Marmottini, T. Montanari, P. Patrono, F. Pinzari, G. Ramis, *Appl. Catal. A* **2006**, *310*, 70.
[22] Y. Tang, Y. Liu, P. Zhu, Q. Xue, L. Chen, Y. Lu, *AIChE J.* **2009**, *55*, 1217.
[23] S. Velu K. Suzuki, *Top. Catal.* **2003**, *22*, 235.
[24] N. Kumagai, L. Ni, H. Irie, *Chem. Commun.* **2010**, *47*, 1884.
[25] X. Zhang, J. Huang, K. Ding, Y. Hou, X. Wang, X. Fu, *Environ. Sci. Technol.* **2009**, *43*, 5947.
[26] M. M. Günter, T. Ressler, R. E. Jentoft, B. Bems, *J. Catal.* **2001**, *203*, 133.
[27] M. Behrens, A. Furche, I. Kasatkin, A. Trunschke, W. Busser, M. Muhler, B. Kniep, R. Fischer, R. Schlögl, *ChemCatChem* **2010**, *2*, 816.
[28] M. Twigg, M. S. Spencer, *Top. Catal.* **2003**, *22*, 191.
[29] K. Faungnawakij, T. Fukunaga, R. Kikuchi, K. Eguchi, *J. Catal.* **2008**, *256*, 37.
[30] L. M. Plyasova, L. P. Solovyeva, T. A. Krieger, O. V. Makarova, T. M. Yurieva, *J. Mol. Catal. A* **1996**, *105*, 61.
[31] W. Jochum, S. Penner, R. Kramer, K. Föttinger, G. Rupprechter, B. Klötzer, *J. Catal.* **2008**, *256*, 278.
[32] W. Jochum, S. Penner, K. Föttinger, R. Kramer, G. Rupprechter, B. Klötzer, *J. Catal.* **2008**, *256*, 268.
[33] M. S. Spencer, *Top. Catal.* **1999**, *8*, 259.
[34] N. Topsøe, H. Topsøe, *Top. Catal.* **1999**, *8*, 267.
[35] R. N. d' Alnoncourt, X. Xia, J. Strunk, E. Löffler, O. Hinrichsen, M. Muhler, *Phys. Chem. Chem. Phys.* **2006**, *8*, 1525.
[36] J.-D. Grunwaldt, A. Molenbroek, N.-Y. Topsøe, H. Topsøe, B. Clausen, *J. Catal.* **2000**, *194*, 452.

4 Copper incorporation into gallium spinels through microwave-hydrothermal methods

The promising properties of the defect spinel-type oxide γ-Ga_2O_3 as a catalytic material have been far less explored than its counterpart γ-alumina. This applies especially for the transition metal doping of γ-Ga_2O_3 hosts on the way to new heterogeneous catalysts. Therefore the first microwave-hydrothermal approach towards the rather challenging Cu(II)-incorporation into nanostructured γ-Ga_2O_3 has been established. Homogeneous γ-Ga_2O_3:Cu^{2+} materials with high surface areas are formed within less than 30 minutes and the copper content can be adjusted through the synthetic parameters. The copper distribution within the spinel matrix was analyzed with a wide range of compositional, structural, spectroscopic and magnetic characterizations.

4.1 Introduction

Although this approach is likely to bring forward attractive materials, little is still known about the effects of copper incorporation into pristine gallium oxide defect spinels. Moreover, γ-Ga_2O_3:Cu^{2+} is an interesting target from the structural and physico-chemical point of view, because the implementation of the Jahn Teller cation Cu^{2+} into an inert gallium oxide matrix has, for example, led to the discovery of spin glass states in spinels.[1]

Previous studies (reported in Chapter 2) on zinc gallates showed that copper-loading of nanoscale gallium-containing spinels is a preparative challenge:[2] therefore, microwave-hydrothermal (MW-HT) techniques are the method of choice for these demanding target compounds. Generally, they excel through their time- and energy-saving features in combination with access to metastable phases and special morphologies.[3-6] MW-HT approaches furthermore provide facile pathways to elusive products that are difficult to obtain with conventional methods or high throughput/combinatorial techniques.[7, 8]

This renders them ideal for the selective synthesis of γ-Ga_2O_3:Cu^{2+} in favor of the thermodynamically more stable competing phases, $CuGaO_2$ and $CuGa_2O_4$. In the following, a novel template-free MW-HT strategy to copper-doped gallium oxide defect spinels together with a comprehensive analysis of their properties with respect to their promising potential as heterogeneous catalysts is presented.

4.2 Results and discussion

4.2.1 Microwave-hydrothermal parameters

A thorough parameter screening was performed to obtain the desired nanoscale copper-containing γ-Ga_2O_3 defect spinels. Preliminary studies have demonstrated that even the solution-based and conventional solvothermal syntheses of phase pure $CuGa_2O_4$ spinels are frequently difficult due to the concurring formation of $CuGaO_2$ (Chapter 2 and 3). Prior to the microwave-hydrothermal study, conventional-hydrothermal experiments in ethylene glycol that had proven an appropriate solvent for the Cu/Ga/O-system were performed.[9] Parameter adjustments based on the preceding work[2] showed that the hydrothermal formation of phase pure copper gallium spinels was indeed far from straightforward. After manifold optimization runs, a spinel-type copper gallium oxide was finally obtained at pH 10.5 and 180 °C after 20 h of conventional-hydrothermal treatment, albeit not in phase pure form. Given that microwave-hydrothermal (MW-HT) strategies offer distinct operational advantages in comparison with standard hydrothermal approaches as detailed above, a short-time and low-temperature MW-HT approach towards the desired γ-Ga_2O_3:Cu^{2+} materials was developed.

According to the experimental details reported in Chapter 7, the γ-Ga_2O_3:Cu^{2+} materials were obtained with different microwave ramps which can be explained as follows: ramp to temperature is abbreviated as r, the reaction time as h and the cool down phase as c.

Figure 4.1 shows the temperature-dependent evolution of the spinel phase after an overall MW-HT treatment time of 25 min. Phase purity can be clearly assigned for synthesis temperatures of 130 °C and above, whilst spinel formation already sets in around 90 °C. This onset temperature is considerably below the temperature ranges reported for previous copper gallium spinel syntheses.

The pH value turned out to be the most influential parameter for the MW-HT synthesis of copper gallium spinels, because they were exclusively formed in basic media. Ammonia had proven effective in the MW-HT protocol for $ZnGa_2O_4$:Cu^{2+} spinels[2] and it offers the advantage of pH adjustment without the introduction of further cations into the reaction system that might give rise to side products. Starting from NaOH or KOH solutions, spinels were formed in the presence of CuO and/or Cu_2O as side products.

Figure 4.2 illustrates the rather narrow pH window for the formation of the spinel phase with an optimum pH value of 10.5 as can be seen from the disappearing impurity peak around 39° that conceals the (222) reflection (cf. Figure 4.1) in the diffraction patterns of samples obtained at lower pH values.

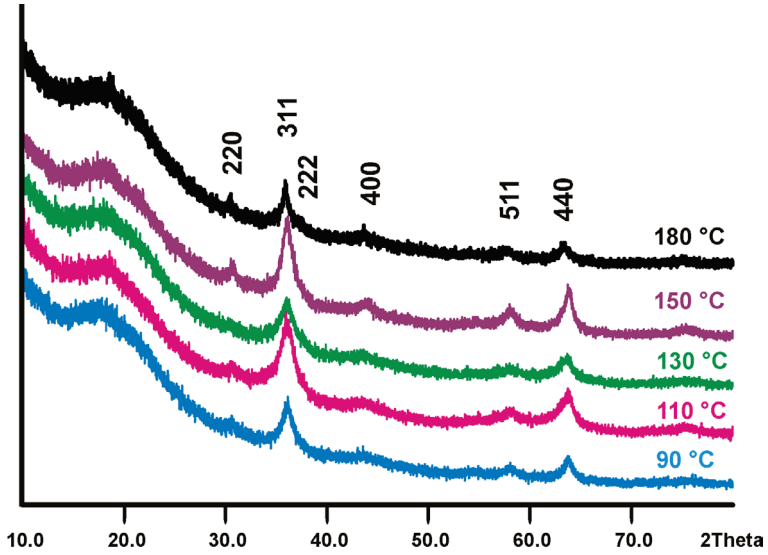

Figure 4.1. Representative XRD patterns of γ-Ga_2O_3:Cu^{2+} prepared at different reaction temperatures (r 10 min, h 15 min; reflections of the spinel phase are indexed).

The precursor materials appear to exert a less significant influence on the course of the reaction, i.e. metal chlorides can be replaced by nitrates or sulfates, respectively.

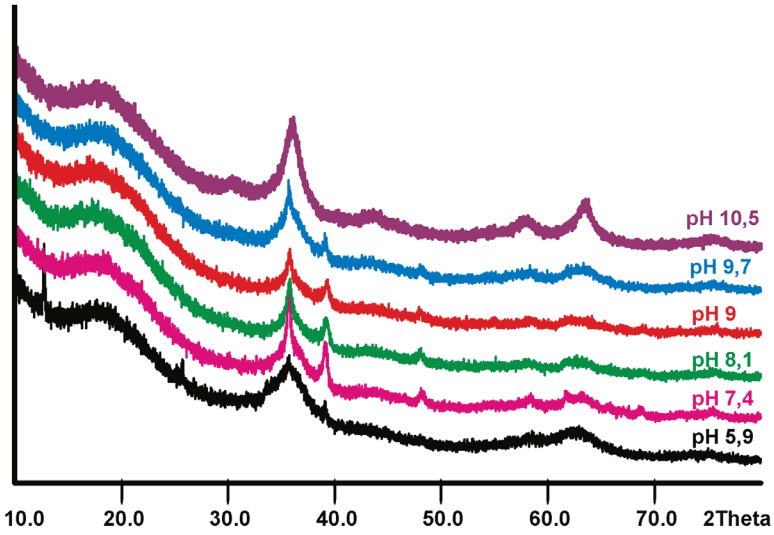

Figure 4.2. XRD patterns monitoring the formation of γ-Ga_2O_3:Cu^{2+} at different pH values in the presence of NH_3 (150 °C, r 30 min, h 60 min).

4.2.2 Morphology and composition of the products

SEM investigations showed that MW-HT treatment generally afforded nanostructured spinel microspheres with a hierarchical morphology. Figure 4.4 illustrates the characteristic growth pattern of the spinels: individual nanoparticles organize themselves into nanospheres that frequently consist of nanosheet aggregates. This phenomenon is observed over a remarkably wide range of synthesis temperatures and reaction times in principle, whereas the particular sizes and shapes of the spherical aggregates may vary. The size range of the individual platelets is below 100 nm and they form sheet-like arrangements with diameters of 100 – 600 nm (cf. Figures 4.4 b, c and e) or smaller building blocks in the 40 – 80 nm size range (cf. Figure 4.4 f). As a consequence, the BET surfaces reach values up to 120 m^2/g. This leads to broadened reflections in the XRD patterns (cf. Figure 4.1 and 4.2) that render detailed structural investigations difficult. Although higher BET areas had been reported for the template-assisted microwave synthesis of pristine mesoporous gallium oxide,[10] the obtained values for γ-Ga_2O_3:Cu^{2+} are still rather high for a template-free approach towards the demanding goal of homogeneous metal incorporation. All particle types were found to display homogeneous copper contents in the course of manifold energy-dispersive X-ray fluorescence (EDX) spot analyses (a representative result has been selected for Figure 4.3). This points to the formation of an overall phase pure product which is in line with the structural investigations below.

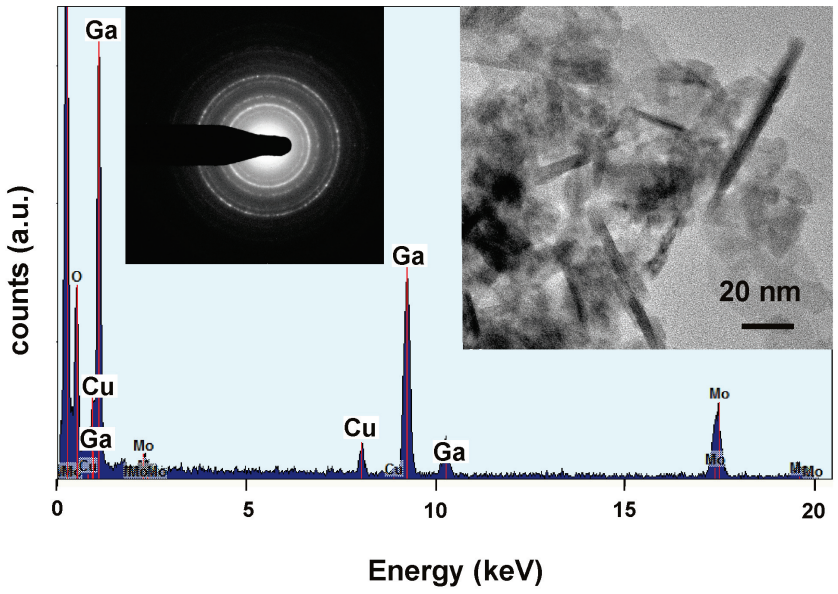

Figure 4.3. Representative STEM image and EDX spot analyses of a γ-Ga_2O_3:Cu^{2+} spinel sample obtained at 150 °C.

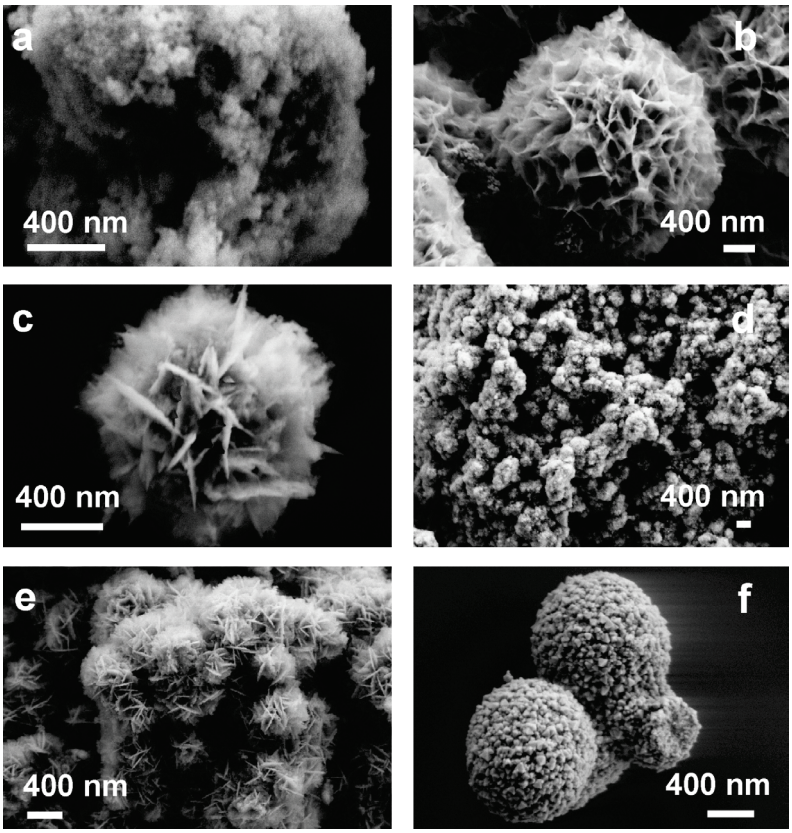

Figure 4.4. Representative SEM images of γ-Ga_2O_3:Cu^{2+} materials obtained from different MW-HT reaction conditions (r, h in min): (a) 90 °C, r 10 min, h 15 min; (b) 130 °C, r 30 min, h 60 min; (c) 150 °C, r 15 min, h 30 min; (d) 150 °C, r 30 min, h 60 min; (e) 150 °C, r 30 min, h 135 min, (f) 180 °C, r 10 min, h 15 min.

Elemental bulk analyses of the copper content were performed with state-of-the-art laser ablation inductively coupled mass spectrometry (LA-ICP-MS). Two key trends are evident from the results (Table 4.1).

Firstly, the Cu:Ga ratio is far below the 1:2 ratio of $CuGa_2O_4$, thus indicating the presence of a copper-substituted defect spinel. Secondly, the degree of copper incorporation into the gallium oxide matrix increases with the reaction temperature during MW-HT synthesis. The corresponding band gaps were determined from solid state UV/Vis spectra (cf. Figure 4.5). They confirm the above trend by decreasing from 3.8 to 1.8 eV with increasing copper content.

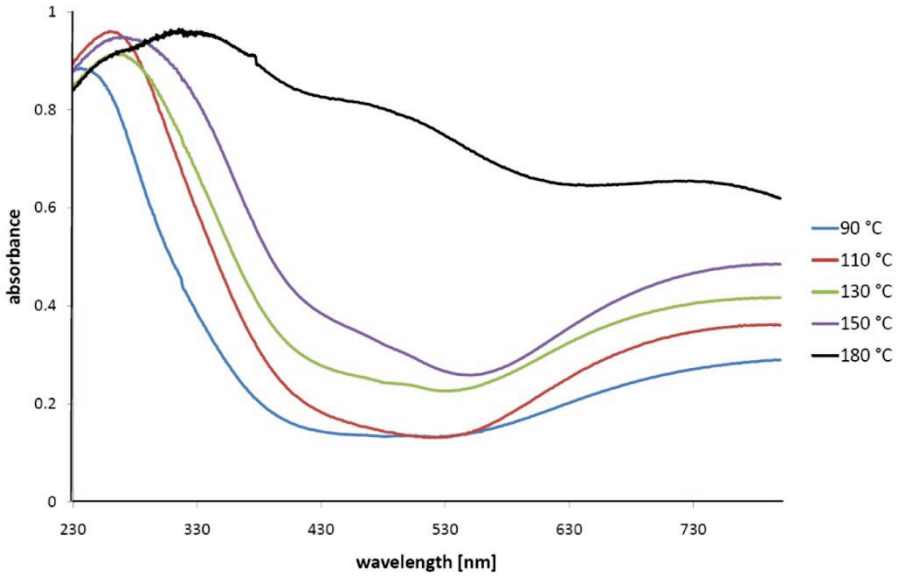

Figure 4.5. UV/Vis spectra of γ-Ga_2O_3:Cu^{2+} spinels synthesized at different reaction temperatures.

As a consequence, the first MW-HT route to nanostructured γ-Ga_2O_3:Cu^{2+} spinel materials is tunable with respect to the product composition. Most interestingly, reference MW-HT experiments at the pH optimum of 10.5 did not afford the expected pristine γ-Ga_2O_3 but resulted in the formation of GaOOH as a main product (Figure 4.6). Partial transformation of cubic gallium oxide into GaOOH has also been observed under hydrothermal conditions in ethylene diamine at 150 °C and recently a new MW-HT approach towards this promising photocatalytic material has been established.[11] This points to a structure-directing and stabilizing role of the Cu^{2+} ions towards the hitherto elusive metastable defect spinel phase of Ga_2O_3.

Table 4.1. Copper content of γ-Ga_2O_3:Cu^{2+} spinel samples obtained at different reaction temperatures (determined by LA-ICP-MS; * = calcinated at 600 °C for 2 h).

T / °C	w % Cu	w % Ga	Cu:Ga ratio	band gap/eV
90	4.9	51.0	0.095:1	3.8
110	4.0	50.8	0.08:1	3.5
130	4.0	50.9	0.08:1	3.3
150	5.5	52.0	0.11:1	3.0
180	7.6	51.3	0.15:1	1.8
130*	3.7	51.0	0.07:1	--
180*	8.0	51.6	0.16:1	--

In summary, a dual strategy for the selective production of γ-Ga_2O_3:Cu^{2+} was applied: firstly, the introduction of Cu^{2+} into the hydrothermal system promotes spinel formation in favor of GaOOH that emerges as the main phase in the absence of copper (Figure 4.6). Secondly, the use of NH_3 as a complexing agent for Cu^{2+} keeps a certain extent in solution, thereby preventing the formation of the copper-rich spinel phase $CuGa_2O_4$.

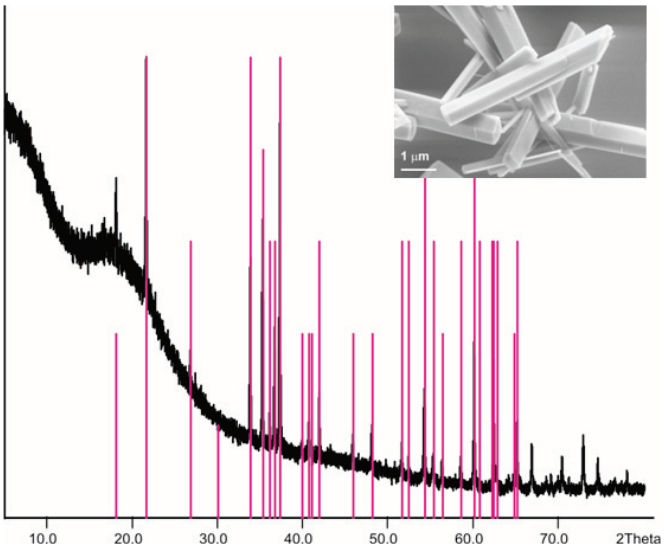

Figure 4.6. XRD pattern displaying GaOOH formation in copper-free media (green = experimental data, red = JCPDS data for GaOOH) and representative SEM image of GaOOH.

4.2.3 Structural characterization

A representative powder X-ray diffraction pattern of the γ-Ga_2O_3:Cu^{2+} materials is shown in Figure 4.7 a. Despite considerable efforts to optimize the measurement conditions, the data quality did not become suitable for a precise structure refinement due to the common problem of broadened reflections observed for nanostructured γ-Ga_2O_3 samples (the broadened peak around 20° arises from sample preparation).[12] Nevertheless, preliminary data fits clearly show that the structure of the obtained material is close to γ-Ga_2O_3 with vacancies in the gallium sublattice (which is thus also referred to as $Ga_{2.667}O_4$)[13] instead of the stoichiometric copper gallium spinel $CuGa_2O_4$.[14] Further neutron diffraction investigations were performed to obtain more detailed structural insight as had been suggested in earlier studies on γ-Ga_2O_3 (Figure 4.7 b).[13] However, the data resolution was not sufficient for a precise assignment of the copper distribution to the tetrahedral and octahedral sites of the defect spinel matrix. In Chapter 2, a related limitation of data accuracy is reported in the preceding studies on $ZnGa_2O_4$:Cu^{2+}.[2]

The possible presence of amorphous copper gallium oxide in the samples as suggested from the background of the XRD patterns does not generally stand in the way of their follow-up catalytic applications.[15] In addition, the copper representing the active species is homogeneously distributed throughout the sample (cf. Figure 4.4).

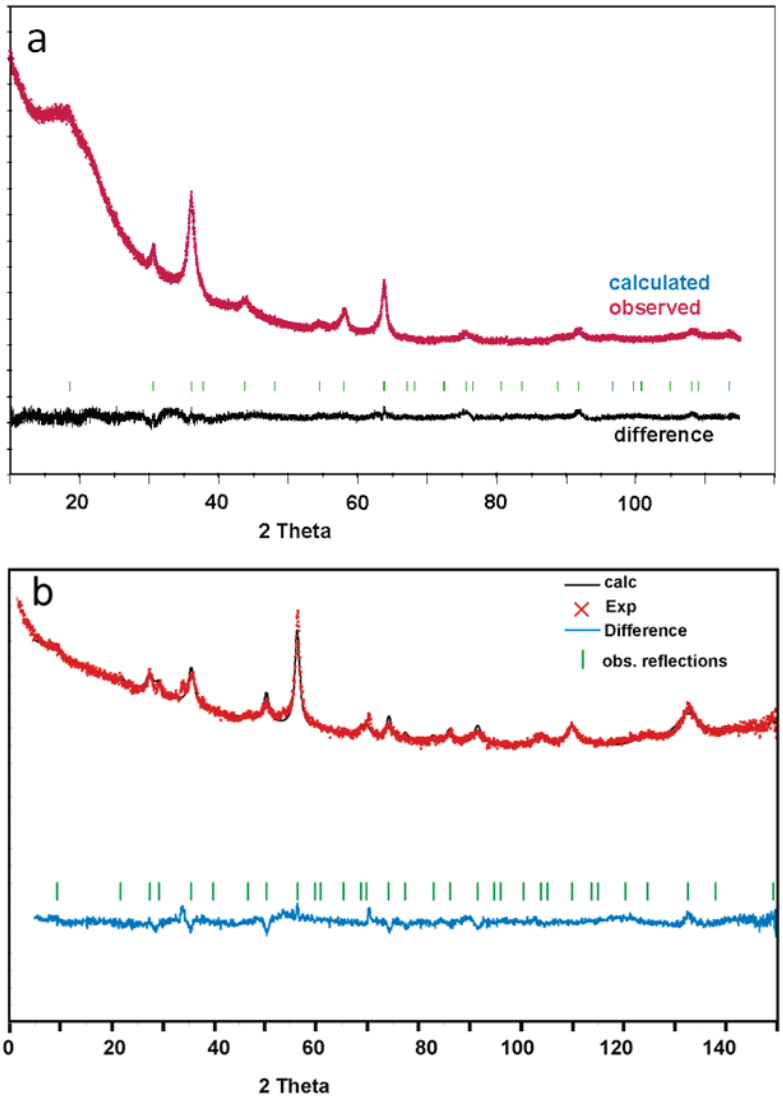

Figure 4.7. (a) Pattern fitting (prolonged measurement time) and (b) neutron diffraction data of nanostructured γ-Ga_2O_3:Cu^{2+}.

The nanostructured γ-Ga_2O_3:Cu^{2+} spinels display a high degree of thermal stability concerning their hierarchical morphology (Figure 4.8). They withstand calcination up to 600 °C and only after 20 h of thermal treatment in air the appearance of additional peaks in the XRD pattern (Figure 4.9) indicates the beginning of a decomposition into β-Ga_2O_3 and CuO.

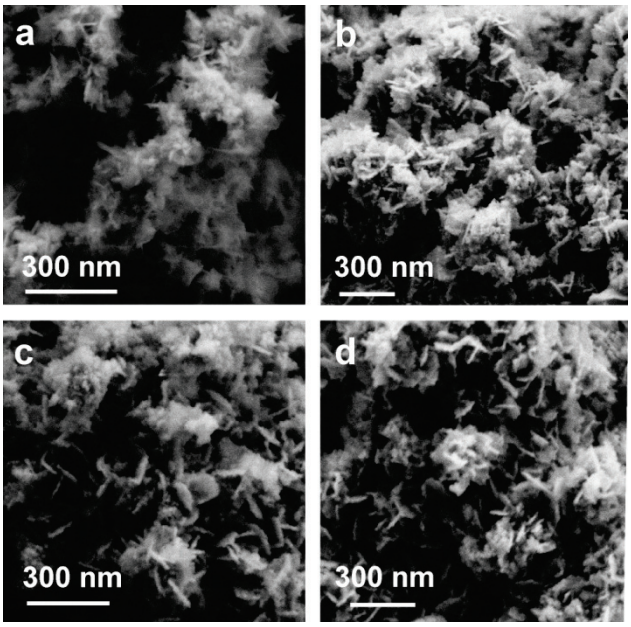

Figure 4.8. Representative SEM images of nanostructured γ-Ga_2O_3:Cu^{2+} samples before (a) and after thermal treatment at (b) 600 °C, (c) 700 °C, (d) 700 °C (20 h).

The persistence of nanostructuring is evident after prolonged heating at 700 °C (Figure 4.8 d). This is in line with previous observations on pristine γ-Ga_2O_3 samples that maintained a low crystallite size until transformation into β-Ga_2O_3 occurred after 20 h of treatment at 650 °C.[13] Thermoanalytic investigations on the Cu-containing gallium oxide spinels precisely confirmed that the introduction of Cu^{2+} ions into the crystal lattice does not significantly influence the transition temperature (Figure 4.10). Investigating the influence of Cu^{2+} on the proposed γ → γ' transition,[13] however, would be a structural and thermodynamic study in its own right.

Given that the X-ray diffraction pattern only permits the assignment of the spinel phase, spectroscopic backup methods are required to locate the position of the Cu^{2+} guest cations. EXAFS spectroscopy was performed to obtain more in-depth structural insight into the copper coordination in the γ-Ga_2O_3 matrix.[16, 17] Measurements were carried out both at the Cu and Ga K-edge for samples synthesized at 150 °C and 180 °C (cf. Table 4.1).

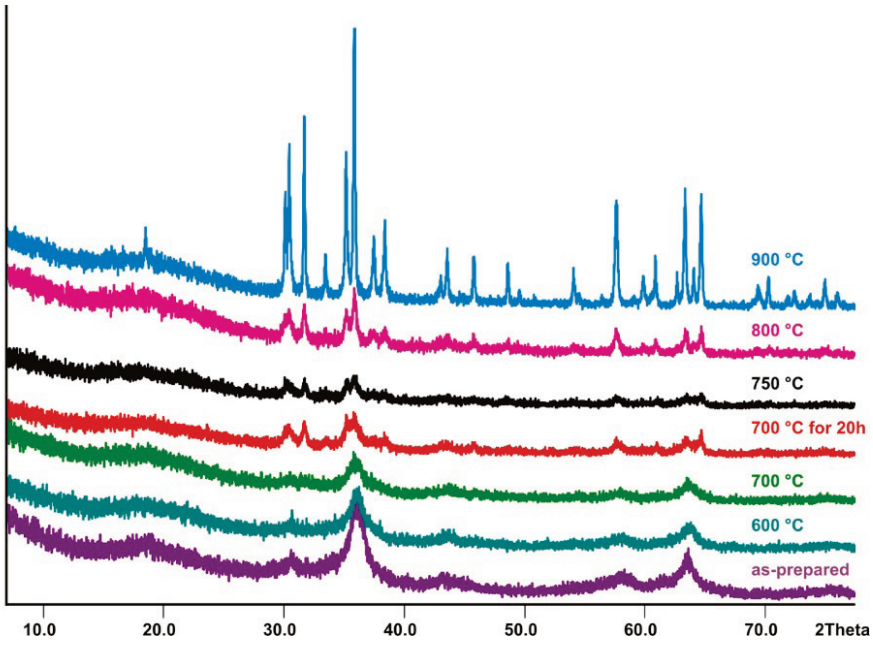

Figure 4.9. XRD patterns of γ-Ga_2O_3:Cu^{2+} after thermal treatment for 2 h (700 °C also for 20 h).

The EXAFS results afford characteristic coordination numbers for tetrahedral (2.2 and 2.4) and octahedral (3.3 and 3.5) sites (Figure 4.11 for Fourier-transformed fits and Table 4.2). Taking into account the error bars of the Ga-O coordination numbers, an approximate ratio of $^{[4]}$Ga: $^{[6]}$Ga = 1.5 is obtained if the upper limit of the $^{[4]}$Ga and the lower limit of the $^{[6]}$Ga coordination number is used.

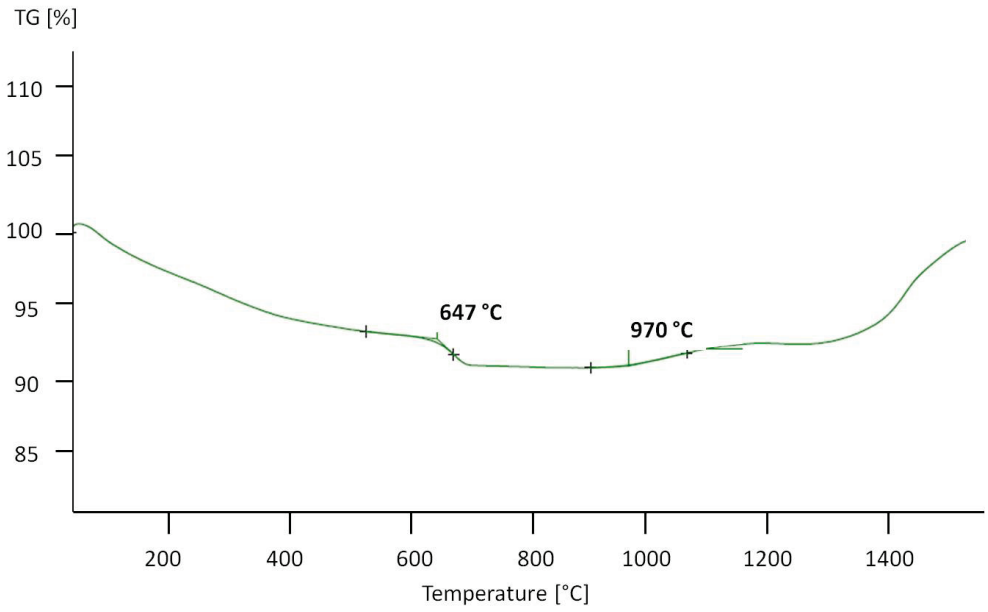

Figure 4.10. Representative thermogravimetric analysis of γ-Ga_2O_3:Cu^{2+} monitoring the onset of decomposition into β-Ga_2O_3 and CuO around 650 °C.

Based on the proposed space group *Fd-3m* for pristine γ-Ga_2O_3,[13] this would point to the location of tetrahedrally coordinated Ga^{3+} on the 8a site and octahedrally coordinated Ga^{3+} on the 16d site with defects in the oxygen sublattice. Additionally, the obtained Ga-Ga distances correspond well to the abovementioned defect spinel model, although the overall coordination numbers are too low which can be explained with disorder effects. The EXAFS results obtained at the copper K-edge indicate a tetragonally distorted octahedral coordination, as deduced from the 4+2 coordination numbers. Although the Cu-Ga coordination numbers are slightly reduced in comparison to the Ga-Ga coordination numbers obtained at the Ga K-edge, the incorporation of the Cu ions into the gallium oxide is confirmed, which is also in accordance with the Cu-Ga bond distances.

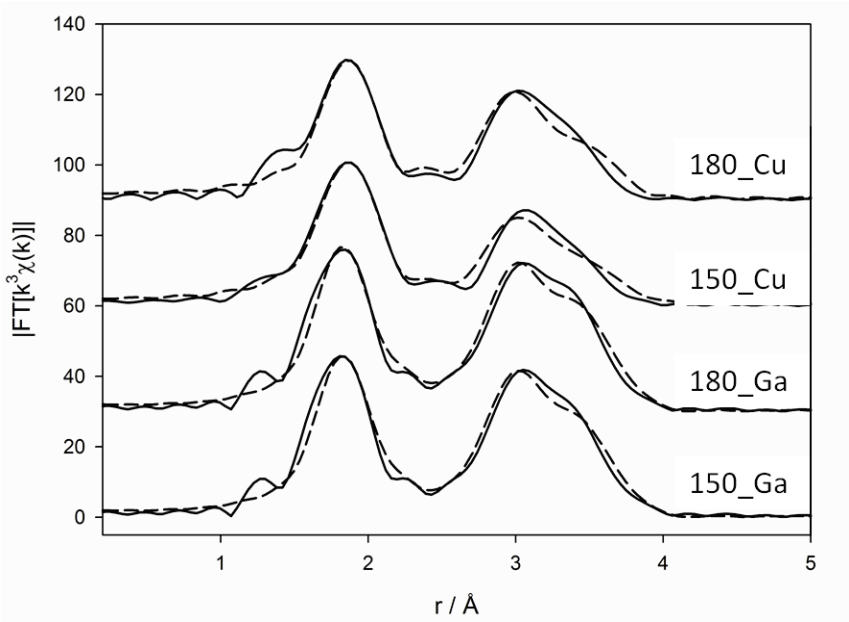

Figure 4.11. Fourier transformed EXAFS-fits.

The surface chemical states of γ-Ga_2O_3:Cu^{2+} (synthesized at 150 °C with r 30 min, h 60 min) before and after annealing at 600 °C were further analyzed by X-ray photoelectron spectroscopy (XPS). Core levels of Ga 2p, Cu 2p, and O 1s can be identified and no other impurities are observed. Figure 4.12 shows the Ga 2p and Cu 2p XPS spectrum of the sample before and after calcination at 600 °C. The gap between the Ga $2p_{3/2}$ position (1119.6 eV) and the Ga $2p_{1/2}$ peak (1146.5 eV) is 26.9 eV which is a typical value for Ga_2O_3.[18] Suboxides such as GaO and Ga_2O were not detected in both samples.

Table 4.2. Fit results at the Zn K-edge and Cu K-edge for γ-Ga_2O_3:Cu^{2+} spinel samples synthesized at 150 °C and 180 °C.

Sample	Abs-Bs[a]	N(Bs)[b]	R(Bs)[c] / Å	σ[d] / Å^2	R-factor / %
150 °C Ga K-edge	Ga-O	2.2 ±0.2	1.89 ±0.02	0.010 ±0.001	21.04
	Ga-O	3.3 ±0.3	2.01 ±0.02	0.024 ±0.002	
	Ga-Ga	5.5 ±1.1	2.99 ±0.03	0.025 ±0.005	
	Ga-Ga	1.9 ±0.4	3.43 ±0.03	0.016 ±0.003	
180 °C Ga K-edge	Ga-O	2.4 ±0.3	1.90 ±0.02	0.011 ±0.001	20.54
	Ga-O	3.5 ±0.4	2.03 ±0.02	0.024 ±0.002	
	Ga-Ga	5.6 ±1.2	2.98 ±0.03	0.025 ±0.005	
	Ga-Ga	2.1 ±0.1	3.43 ±0.03	0.016 ±0.002	
150 °C Cu K-edge	Cu-O	4.1 ±0.4	1.95 ±0.02	0.013 ±0.001	19.83
	Cu-O	2.0 ±0.2	2.13 ±0.02	0.025 ±0.003	
	Cu-Ga	3.7 ±0.8	2.95 ±0.03	0.025 ±0.005	
	Cu-Ga	1.8 ±0.1	3.40 ±0.03	0.020 ±0.004	
180 °C Cu K-edge	Cu-O	3.9 ±0.4	1.97 ±0.02	0.011 ±0.001	21.73
	Cu-O	2.2 ±0.3	2.16 ±0.02	0.018 ±0.002	
	Cu-Ga	4.8 ±1.0	2.95 ±0.03	0.025 ±0.005	
	Cu-Ga	1.3 ±0.2	3.42 ±0.03	0.014 ±0.003	

[a] Abs = X-ray absorbing atom, Bs = backscattering atom. [b] Number of backscattering atoms. [c] Distance Abs-Bs. [d] Debye-Waller like factor. [f] Quality of fit.

For the Cu 2p XPS spectrum, satellite peaks (binding energy between 940 - 945 eV) were observed which reveals the presence of Cu^{2+} species in the spinel host.[19] Moreover, the Cu $2p_{3/2}$ peaks of the samples before and after annealing are located at 933.5 eV. This points to Cu^{2+} ions at octahedral sites in the spinel,[20] because Cu^{2+} ions on tetrahedral spinel sites are reported to show a characteristic peak at 936.2 eV.[21] Therefore, the XPS results agree well with the observation from EXAFS that the incorporated Cu^{2+} ions are located on the octahedral sites. In addition, the nanostructured γ-Ga_2O_3:Cu^{2+} spinels exhibited high thermal stability. The oxidation states of Ga and Cu are not changed after heating to 600 °C.

4.2.4 Magnetic properties

Further evidence for the formation of nanostructured copper-doped γ-Ga_2O_3 was obtained by magnetic investigations. Measurements of the magnetic moment *m* were performed in various magnetic fields on a sample with the analytically determined Cu:Ga ratio of 0.05:1 and a mass of 35.87 mg, yielding the amount of copper $n_{Cu} = 1.84 \cdot 10^{-5}$ mol in the studied sample. The homogeneous distribution of copper centers in the same sample had been verified by EDX spot analyses (Figure 4.3). Whereas the magnetization measured in high fields saturates at low temperatures due to a polarization of the individual copper spins, its

susceptibiliy in the low field regime is representative for the magnetic response of the thermally excitated copper moments. In Figure 4.13 the inverse of the derived molar susceptibility $\chi_{mol} = m/(Hn_{Cu})$ for H=2000 Oe is presented as a function of temperature. The data exhibit a clear Curie-Dependence,[22] namely $\chi_{mol} = C_m/T$, wherefrom the effective magneton number is derived. Fitting this expression to the data results in C_m = 0.49 emu K/Oe and μ_{eff} = 2.0(1), consistent with the expectation for a Cu^{2+} ionic state. Notice that the here resulting value for μ_{eff} is in excellent agreement to those found earlier for the copper state in $ZnGa_2O_4:Cu^{2+}$ reported in Chapter 2.

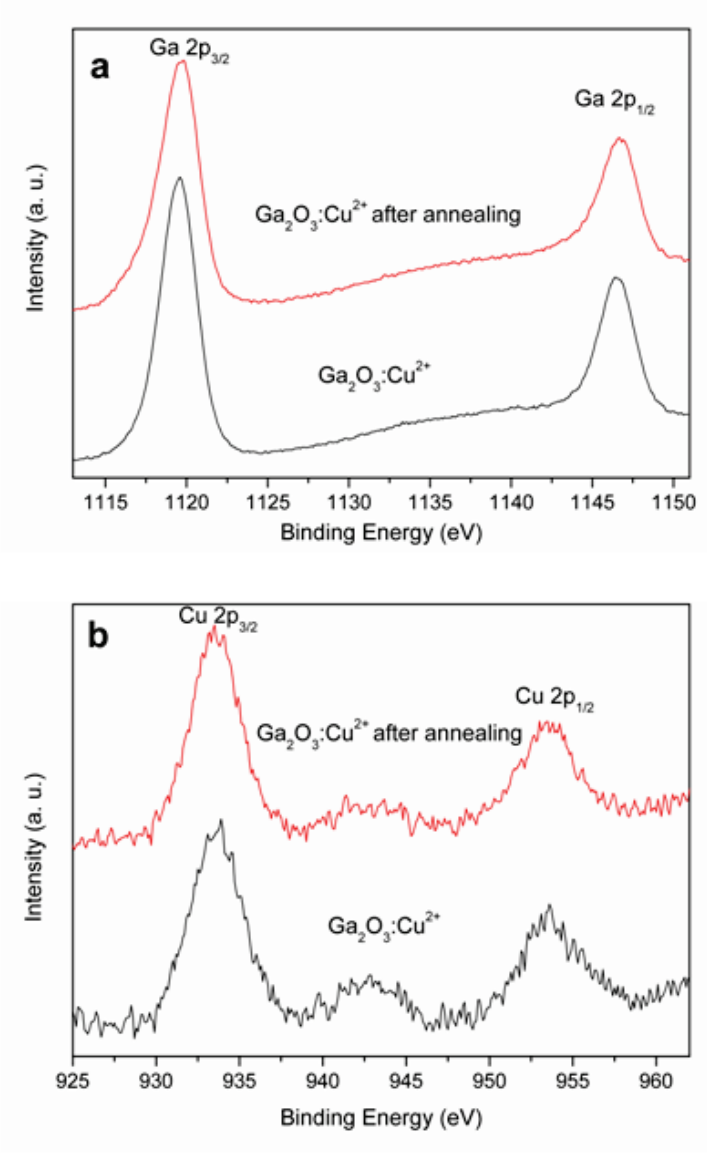

Figure 4.12. XPS spectra of γ-$Ga_2O_3:Cu^{2+}$ before and after annealing at 600 ° C: (a) Ga 2p and (b) Cu 2p.

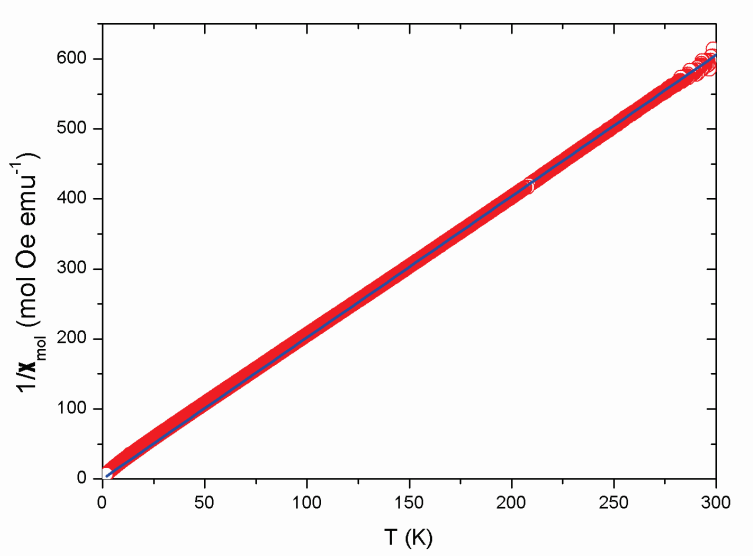

Figure 4.13. Inverse magnetic susceptibility, measured in 2000 Oe of γ-Ga_2O_3:Cu^{2+} (synthesized at 150 °C, r 30 min, h 60 min) as a function of temperature. The line is a fit of a Curie-Dependence to the data, as explained in the text.

4.3 Redox behaviour of the copper centres in γ-Ga_2O_3:Cu^{2+}

4.3.1 *In situ* XRD investigations

In order to further characterize the redox chemistry of the spinel material, the structure of the γ-Ga_2O_3:Cu^{2+} sample was investigated with *in situ* XRD techniques up to 400 °C and the results are presented in Figure 4.14. Unfortunately, the data quality does not reveal any satisfactory pattern fitting even though slight changes of the sample are visible. Sample changes under reductive conditions can be assigned to Cu formation in H_2 and the disappearance of Cu in oxygen atmosphere, respectively.

For the *in situ* investigations, the γ-Ga_2O_3:Cu^{2+} sample was first heated up to 400 °C in He atmosphere, followed by a heating period to the same temperature in 5 % H_2 and finalized by a last heating ramp to 400 °C in oxygen (see Chapter 7 for details). During the first step, the sample is reduced in helium atmosphere as indicated by the appearance of Cu peaks. The follow-up treatment in H_2 does not significantly affect the sample. Interestingly, the Cu peaks disappear during O_2 treatment and neither CuO nor Cu_2O are detectable.

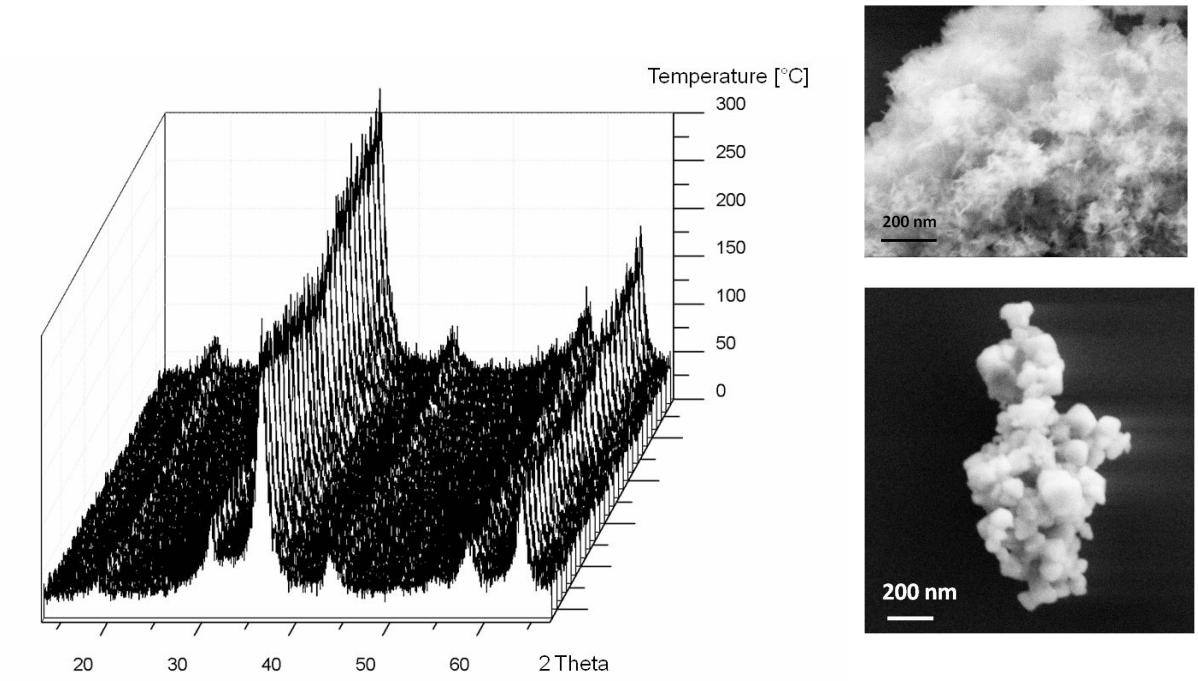

Figure 4.14. Temperature dependent *in situ* EDXRD scans up to 400 °C of γ-Ga_2O_3:Cu^{2+} (left) and representative SEM images after *in situ* treatment (right).

Another plot of the same *in situ* XRD scan is presented in Figure 4.15. The [111] reflection at 18° becomes less intense in helium atmosphere (cf. blue arrow) and remains constant afterwards. Cu reflections (red arrows) appear in He atmosphere and vanish again in the presence of O_2. A closer inspection of the more intense reflections reveals the following trend: minor intensity loss in He, then recovery (intensity back to original value) in O_2. Unfortunately, the reduction in He as well as the oxidation on O_2 result in an increased background, especially for the stronger spinel reflections at 28° and 40° (green arrows). This observation may be explained with the formation of nano-crystalline or amorphous materials but hinders a thorough interpretation of the data.

In summary, the sample changes during redox investigations, i.e. the reversible formation of Cu, is promising for catalytic tests. The fact that the position of the spinel reflections remains unchanged as well as the possible formation of nano-crystalline or amorphous material accompanying each sample change are still in the way of a quantitative data evaluation. Therefore, the initial and final location of copper in the host matrix during the redox process remains unknown.

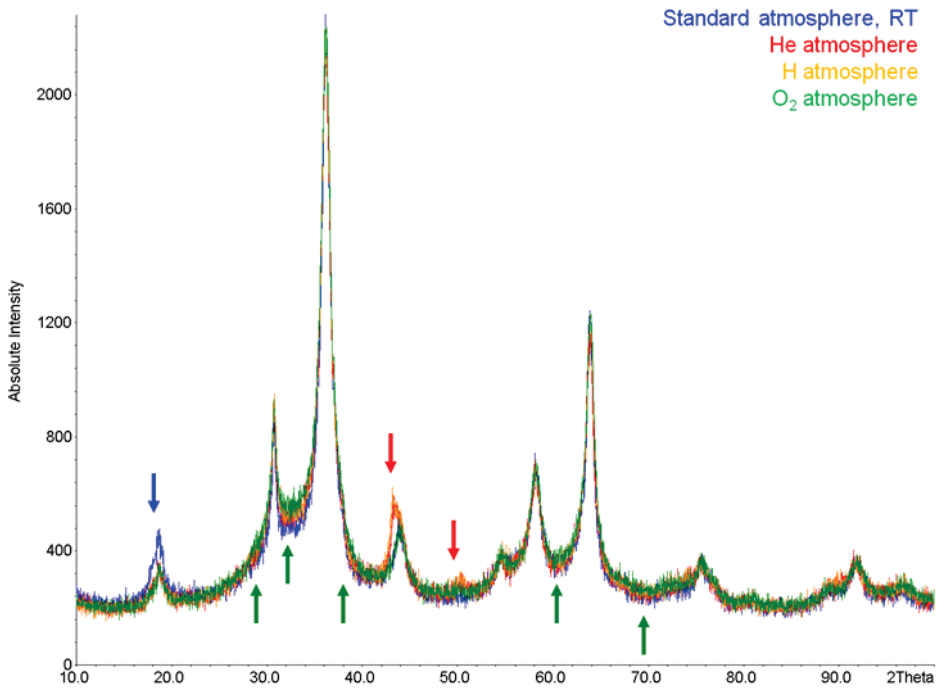

Figure 4.15. *In situ* XRD plot of four scans under different atmospheric conditions: standard air (blue), He (red), H_2 (orange) and O_2 (green) atmosphere.

4.3.2 Temperature programmed reduction profile of γ-Ga_3O_4:Cu^{2+}

Temperature programmed reduction (TPR) was performed as pre-test for a possible application of γ-Ga_3O_4:Cu^{2+} as a catalyst for methanol synthesis by CO_2 hydrogenation and methanol steam reforming. Therefore, the γ-Ga_3O_4:Cu^{2+} sample underwent a TPR screen up to 800 °C and the result is presented in Figure 4.16. The temperature programmed reduction (TPR) profile is characterized by two peaks (215 and 245 °C) resulting from two different Cu species. The most probable explanation is the presence of Cu particles that display different degrees of interaction with gallium oxide. Whereas the first peak at 215 °C might be assigned to CuO, the second peak around 245 °C cannot be unambiguously assigned. Additional N_2O reactive frontal chromatography (RFC) tests revealed a specific copper surface area of ~3 m^2/g.

Further TEM investigations of the reduced catalyst (after treatment at 260 °C in 5 % H_2) clearly show the high homogeneity of the sample and the existence of metallic copper particles (PDF card 04-0836) as well as of Ga_2O_3 (PDF card 76-0573, cf. Figure 4.17).

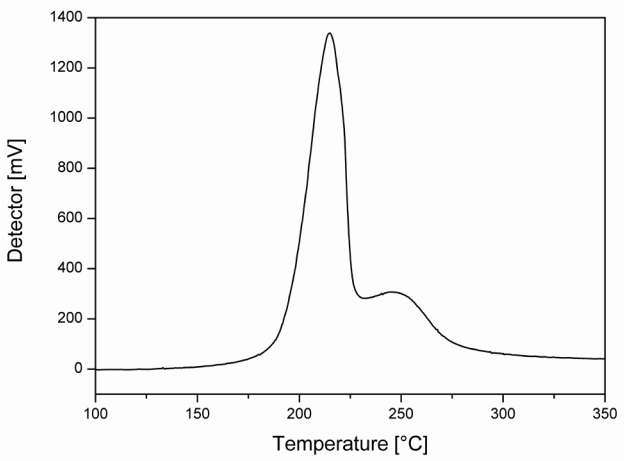

Figure 4.16. Temperature programmed reduction (TPR) profile of γ-Ga_2O_3:Cu^{2+}.

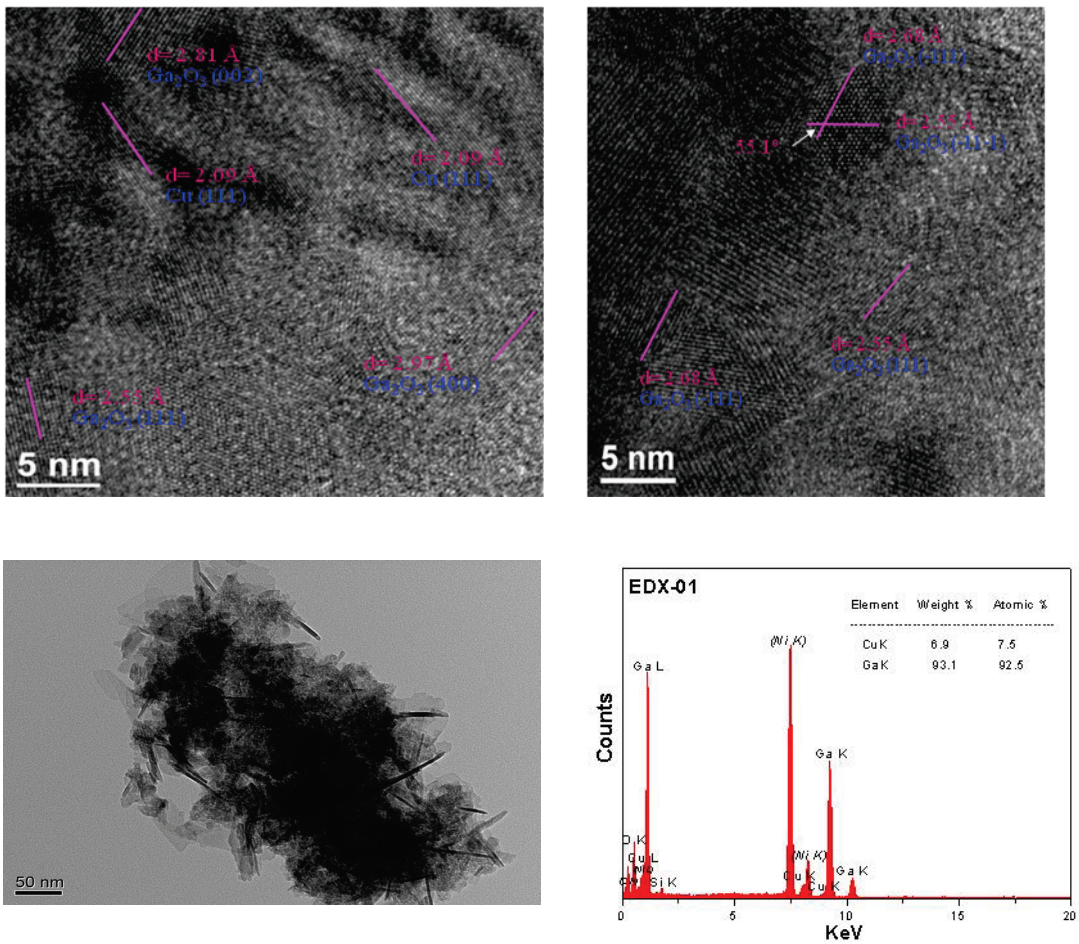

Figure 4.17. HRTEM images including EDX analyses of a representative γ-Ga_2O_3:Cu^{2+} sample after TPR (260 °C) reveal the formation of Cu (PDF card 04-0836) as well as of Ga_2O_3 (PDF card 76-0573) particles together with a high homogeneity throughout the sample.

4.4 Sensor and catalytic properties

4.4.1 Gas sensing properties

Given that $CuGa_2O_4$ exhibits sensing potential towards H_2, LPG and NH_3,[23] the gas sensing properties of the γ-Ga_2O_3:Cu^{2+} sample were investigated. The observed sensing behaviour of γ-Ga_2O_3:Cu^{2+} differs from pristine and copper substituted $ZnGa_2O_4$ samples (cf. Chapter 2.3.1). It is slightly conducting at 20 °C (~10 MΩ) and becomes completely insulating upon heating (cf. Figure 4.18).

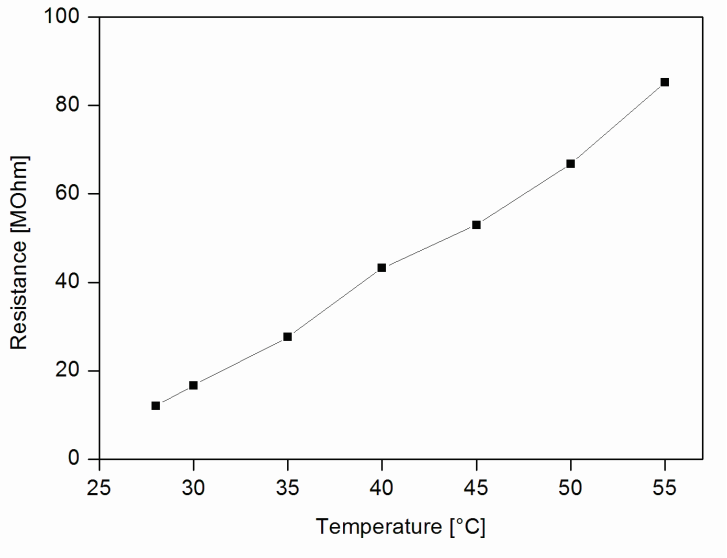

Figure 4.18. Temperature-dependent resistance of a representative γ-Ga_2O_3:Cu^{2+} sample.

4.4.2 Photocatalytic degradation of organic dyes

γ-Ga_2O_3:Cu^{2+} shows activity in the photocatalytic degradation of rhodamine B (RhB) within 90 min if irradiated with daylight. However, the extent of RhB decomposition is only ~25 % (cf. Figure 4.19) which is far below the catalytic activity observed for the copper substituted or pristine $ZnGa_2O_4$ (cf. Chapter 2.3.3). This decreased photocatalytic activity might be explained with a smaller band gap of the γ-Ga_2O_3:Cu^{2+} compared to the $ZnGa_2O_4$ materials which exhibit a band gap of 4.1 to 4.3 or by surface effects.

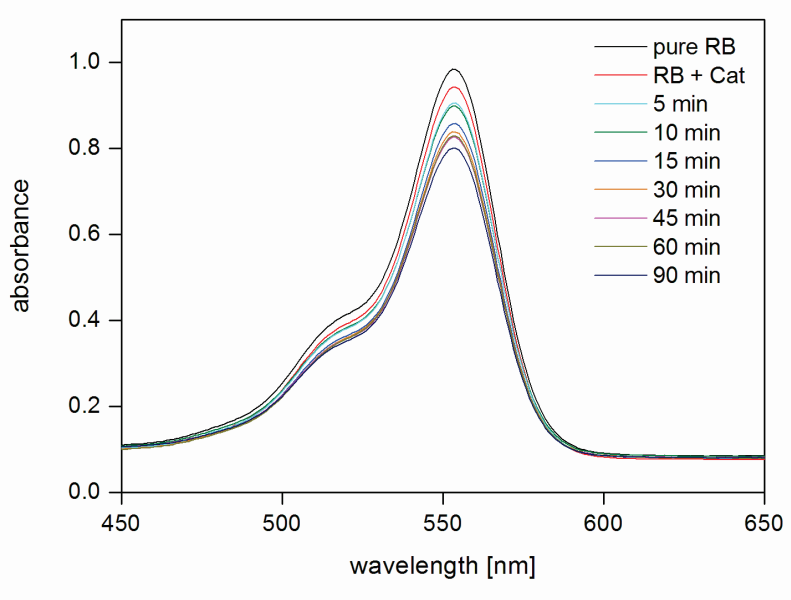

Figure 4.19. Photocatalytic degradation of RhB with γ-Ga_2O_3:Cu^{2+} as catalyst.

4.4 Conclusion

The present study provides new insights into the production of copper-doped functional gallium oxides. The first microwave-hydrothermal approach to copper-containing gallium spinels of the γ-Ga_2O_3:Cu^{2+} type has been established. This convenient and template-free microwave-assisted procedure affords the products on a minute scale at temperatures as low as 90 °C – far below the conventional solid state routes. Once the pH of the reaction system has been adjusted to a working point of 10.5, the overall MW-HT reaction time can be varied between 25 min and 1-2 h to generate the target spinel material. Likewise, different metal salt precursors can be used and the temperature window of the reaction ranges from ca. 90 °C to 180 °C. The hierarchically nanostructured samples display microspherical morphologies consisting of individual nanoparticles of < 100 nm in size. This leads to BET surfaces around 120 m^2/g which renders the materials attractive for further catalytic implementation. Additionally, the results of EXAFS and XPS analyses both demonstrate that Cu^{2+} ions are located on the octahedral sites of the γ-Ga_2O_3 host lattice.

Moreover, the copper content of the samples can be adjusted via the synthesis temperature. In this way, the band gap of γ-Ga_2O_3:Cu^{2+} could be narrowed from 3.8 to 1.8 eV by increasing the copper content. Magnetic measurements display perfect Curie behavior of the mixed spinels, thus indicating a homogeneous distribution of Cu^{2+} in the

host oxide that is in line with EDX spot analyses. Thermal treatment up to 600 °C does not affect the nanostructuring of the γ-Ga_2O_3:Cu^{2+} samples, thereby proving their stability for high-temperature applications.

The results in their entirety indicate that the newly developed MW-HT access is a major step towards the selective tuning and exploration of nanoscale transition-metal containing γ-Ga_2O_3 phases that have been widely unexplored to date. Catalytic tests have been performed with special emphasis on photocatalytic processes, because the γ-Ga_2O_3:Cu^{2+} samples with higher copper contents display band gaps in the interesting region for visible-light-driven reactions, but the obtained degradation of rhodamine B of 25 % did not meet the expectations. First investigations on the reductive behaviour of the γ-Ga_2O_3:Cu^{2+} revealed a specific copper surface area of 3 m^2/g. TPR and *in situ* XRD studies combined with follow-up TEM investigations confirmed that copper incorporated into a γ-Ga_2O_3 matrix is accessible while reduction. Therefore, the nanostructured γ-Ga_2O_3:Cu^{2+} materials are possible catalysts for methanol steam reforming or CO_2 conversion.

References

[1] G. A. Petrakovskii, K. S. Aleksandrov, L. N. Bezmaternikh, S. S. Aplesnin, B. Roessli, F. Semadeni, A. Amato, C. Baines, J. Bartolome, M. Evangelisti, *Phys. Rev. B* **2001**, 63.
[2] F. Conrad, Y. Zhou, M. Yulikov, K. Hametner, S. Weyeneth, G. Jeschke, D. Guenther, J.-D. Grunwaldt, G. R. Patzke, *Eur. J. Inorg. Chem.* **2010**, 2036.
[3] I. Bilecka, M. Niederberger, *Nanoscale* **2010**, *2*, 1358.
[4] F. Gao, Q. Lu, X. Meng, S. Komarneni, *J. Mater. Sci.* **2008**, *43*, 2377.
[5] G. R. Patzke, Y. Zhou, R. Kontic, F. Conrad, *Angew. Chem. Int. Ed.* **2011**, *50*, 826.
[6] V. Polshettiwar, M. N. Nadagouda, R. S. Varma, *Austr. J. Chem.* **2009**, *62*, 16.
[7] J. Hulliger, M. A. Awan, *J. Comb. Chem.* **2005**, *7*, 73.
[8] A. Sonnauer, N. Stock, *Eur. J. Inorg. Chem.* **2008**, 5038.
[9] R. Srinivasan, B. Chavillon, C. Doussier-Brochard, L. Cario, M. Paris, E. Gautron, P. Deniard, F. Odobel, S. Jobic, *J. Mater. Chem.* **2008**, *18*, 5647.
[10] C. A. Deshmane, J. B. Jasinski, M. A. Carreon, *Microporous Mesoporous Mater.* **2010**, *130*, 97.
[11] M. Sun, D. Li, W. Zhang, X. Fu, Y. Shao, W. Li, G. Xiao, Y. He, *Nanotechnol.* **2010**, *21*.
[12] C. O. Arean, A. L. Bellan, M. P. Mentruit, M. R. Delgado, G. T. Palomino, *Microporous Mesoporous Mater.* **2000**, *40*, 35.
[13] M. Zinkevich, F. M. Morales, H. Nitsche, M. Ahrens, M. Ruhle, F. Aldinger, *Z. Metallkunde* **2004**, *95*, 756.
[14] J. M. R. Gonzalez, C. O. Arean, *J. Chem. Soc.-Dalton Trans.* **1985**, 2155.
[15] S. Bennici, A. Auroux, C. Guimon, A. Gervasini, *Chem. Mater.* **2006**, *18*, 3641.
[16] Y. G. Choi, J. Heo, V. A. Chernov, *J. Non-Cryst. Solids* **1997**, *221*, 199.
[17] K. Shimura, T. Yoshida, H. Yoshida, *J. Phys. Chem. C* **2010**, *114*, 11466.
[18] S. Y. Bae, H. W. Seo, C. W. Na, J. Park, *Chem. Comm.* **2004**, 1834.
[19] K. Faungnawakij, K. Eguchi, *Catal. Surv. Asia* **2011**, *15*, 12.
[20] A. Caballero, M. Cruz, L. Hernan, M. Melero, J. Morales, E. R. Castellon, *J. Electrochem. Soc.* **2005**, *152*, A552.
[21] A. C. Tavares, M. A. M. Cartaxo, M. I. D. Pereira, F. M. Costa, *J. Solid State Electrochem.* **2001**, *5*, 57.
[22] N. W. Ashcroft, N. D. Mermin, *Solid State Physics*, Saunders College Publishing, **1976**.
[23] S. K. Biswas, A. Sarkar, A. Pathak, P. Pramanik, *Talanta* **2010**, *81*, 1607.

5 3d transition metals in gallium oxide matrices

5.1 $NiGa_2O_4$

Nickel containing gallium oxides have been reported in several studies with the focus on photocatalytic applications,[1-16] but their facile synthesis still remains to be explored. Conventional solid state synthesis is most often the method of choice, but this technique provides some drawbacks for state-of-the art catalysts: e.g. small surface areas due to particle sizes in the micrometer range. Therefore the reported catalytic activity of Ni–Ga mixed oxide with 10 wt % Mn_2O_3 for the NO reduction is noticeable due to facile co-precipitation methods for the synthesis of the catalyst.[1] More often nickel doped Ga_2O_3 are investigated,[4] including overall photocatalytic splitting of water.[14] Co-catalysts further improve water splitting activities of nickel containing spinel oxides.[11, 16] Within this section, the straightforward synthesis of nickel containing gallium oxides is presented – including solid state, conventional hydrothermal and microwave-assisted techniques.

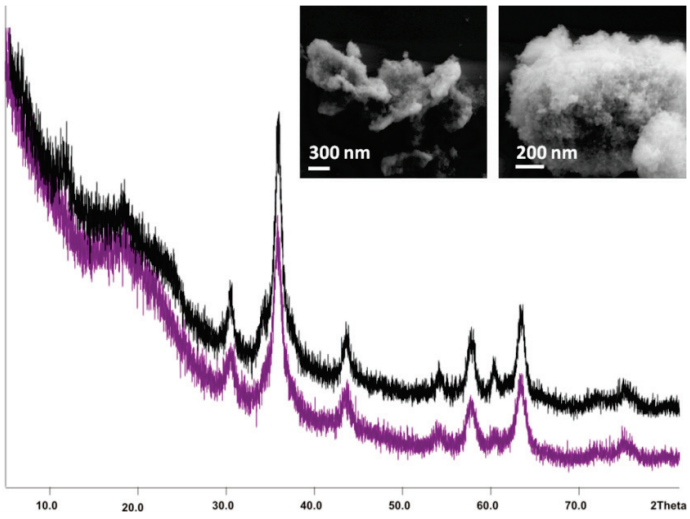

Figure 5.1. Representative XRD and SEM images of $NiGa_2O_4$ produced at 150 °C with NH_3 (purple and left inset) and NaOH (black and right inset).

5.1.1 Microwave-hydrothermal synthesis

Nickel containing gallium spinels could be obtained via MW-HT reaction within minutes as can be seen in Figure 5.1. The XRD pattern clearly indicates the formation of a spinel phase and the broad reflection can be attributed to nanostructuring of the products (cf. SEM images in Figure 5.1).

The pH value again plays an important role – a second phase of NiO arises after calcination up to 1400 °C as can be seen in the TG curve in Figure 5.2 and the corresponding XRD afterwards (Figure 5.3) if the pH value is too high (10.6). The TG investigations indicate a mass loss of ~8 % and two endothermic changes at ~280 and ~380 °C. The sample remains stable from 600 °C onwards. The SEM inset in Figure 5.3 shows two morphologies whereas the small spheres are attributed to NiO (ICSD PDF card 44-1159). So far, a pH of 9 - 10 combined with a reaction temperature of 150 °C led to the best results.

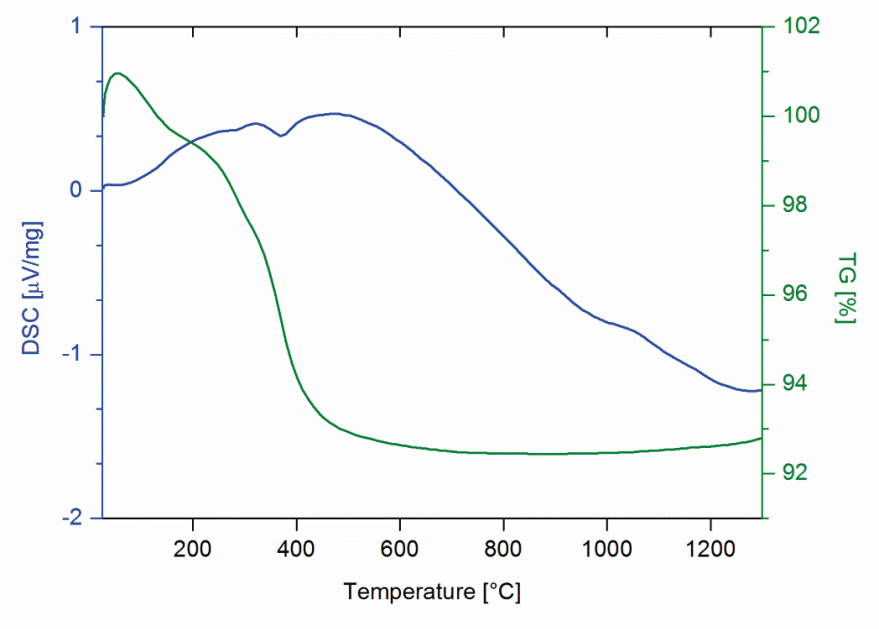

Figure 5.2. TG/DSC of $NiGa_2O_4$ (NaOH) produced with MW-HT synthesis at pH 10.6 and 180 °C.

XAS measurements were performed with the calcinated sample and afforded the formation of a completely inverse spinel as can be seen in Table 5.1. The nickel atom has six surrounding atoms and therefore occupies exclusively octahedral sites within the spinel lattice.[17] As a result, the gallium atoms are forced to occupy both spinel sublattices (tetra- and octahedral sites) and have a 4+2 symmetry pointing to elongated octahedra.

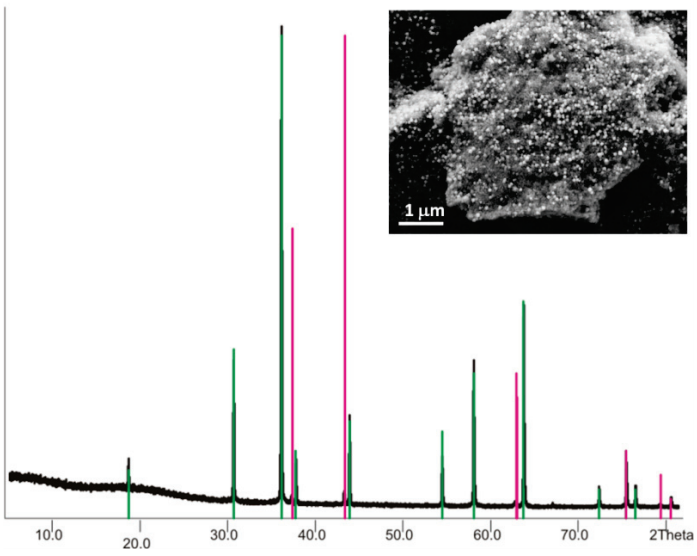

Figure 5.3. XRD pattern of $NiGa_2O_4$ after TG at 1400 °C in N_2 (ICSD PDF card 10-0114 in green and NiO ICSD PDF card 44-1159 in pink) and SEM picture clearly indicating two phases.

Table 5.1. Fitting results for experimental X-ray absorption spectra of the Ni-Ga spinel.

Sample	Edge	Abs-Bs	N(Bs)	R(Abs-Bs)
$NiGa_2O_4$_Ga	Ga K	Ga-O1	2.7 ± 0.3	1.88 ± 0.02
		Ga-O2	3.8 ± 0.4	2.00 ± 0.02
		Ga-Ga1	6.4 ± 1.2	2.92 ± 0.03
		Ga-Ga2	7.0 ± 1.4	3.42 ± 0.03
$NiGa_2O_4$_Ni	Ni K	Ni-O1	5.8 ± 0.6	2.05 ± 0.02
		Ni -Ga1	7.8 ± 1.6	2.92 ± 0.03
		Ni -Ga2	1.6 ± 0.3	3.44 ± 0.03

[a] Abs = X-ray absorbing atom, Bs = backscattering atom (neighbour), [b] number of backscattering neighbour atoms, [c] distance between absorbing and backscattering atom.

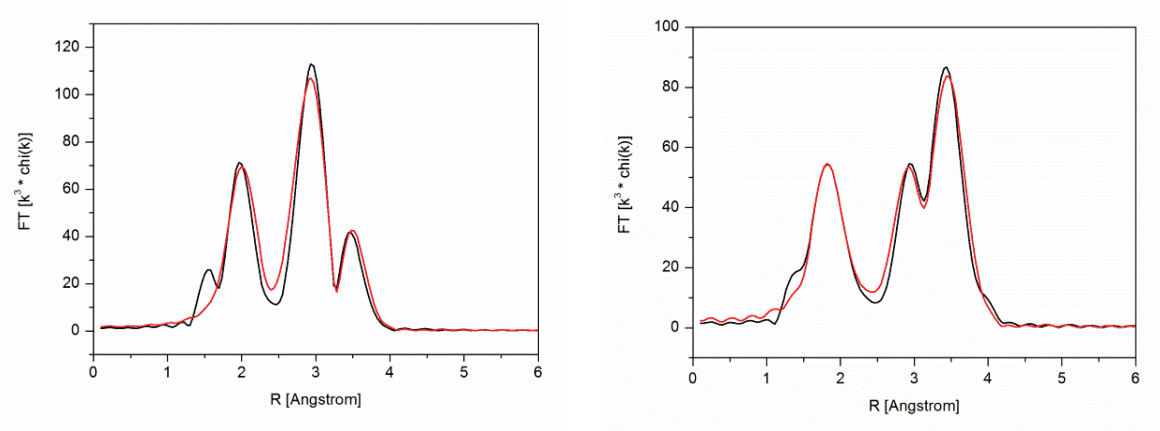

Figure 5.4. Fitting results of the *k*3-weighted EXAFS data of the $NiGa_2O_4$ at the Ni (left) and Ga edge (right).

XPS measurements were performed to investigate the oxidation states at the surface of the calcinated spinel. Figure 5.5 shows the absorption spectra of the Ni 2p and Ga 2p edges. Comparison of the obtained data with values reported in literature confirms the existence of nickel in the oxidation states +2. Lenglet[5, 6] and Töpfer et al.[18] reported values of the Ni 2p edge of 855.7 eV which is comparable with the obtained value of 854.6 eV. Furthermore, the difference of 6.2 eV between the two corresponding peaks (854.6 and 860.8 eV) confirms the oxidation state of +2.

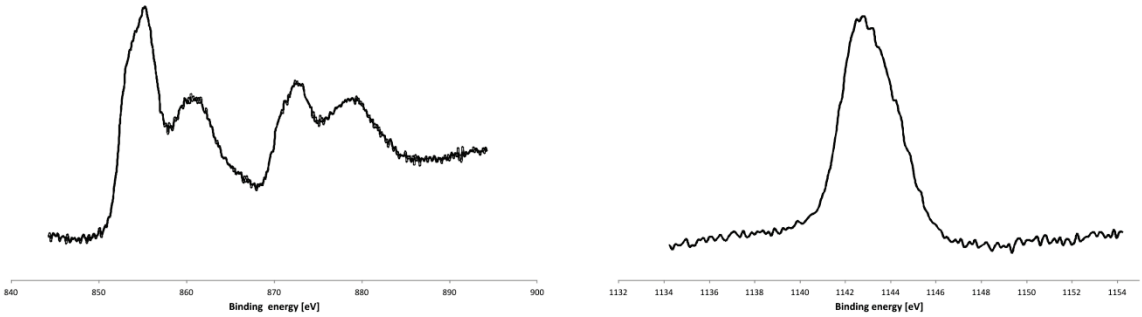

Figure 5.5. XPS spectra of the Ni 2p edge (left) and the Ga 2p edge (right).

5.1.2 Hydrothermal and solid state synthesis

Solid state reactions were carried out in alumina crucibles at 900 °C for 2 and 20 h reaction time and afforded spinel particles. Unfortunately, the products were not phase pure as can be seen in Figure 5.6.

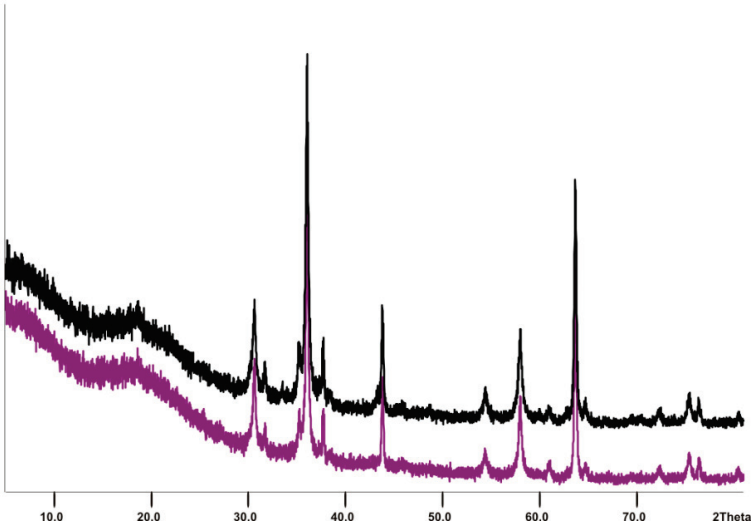

Figure 5.6. XRD pattern of $NiGa_2O_4$ obtained via the solid state route at 900 °C after 2 h (purple) and 20 h (black).

Conventional-hydrothermal heating yields almost phase pure and nanostructured products within two days of reaction time. The XRD pattern does not indicate impurities but SEM investigations confirmed the existence of two different morphologies (see Figure 5.7) if NaOH is used for pH adjustment. Diffraction peaks occurring from little amounts of impurities might be concealed by the background of the XRD pattern.

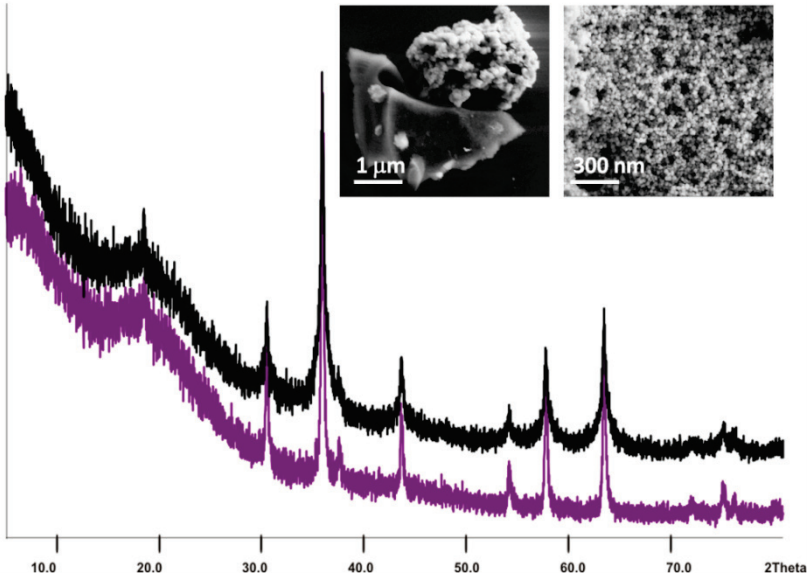

Figure 5.7. Representative XRD and SEM images of $NiGa_2O_4$ produced hydrothermally at 180 °C with NH_3 (purple and right inset) and NaOH (black and left inset).

5.1.3 Conclusion

The microwave-assisted route afforded nanostructured $NiGa_2O_4$ spinel particles within minutes and is superior to conventional reaction pathways reported here. The parameter screening shows strong pH dependency for the phase pure production of the spinels. The nickel gallium oxides are calcination stable up to 1400 °C and contain nickel in the oxidation state +2 developed by XPS measurements. Detailed structural analysis by EXAFS afforded 2+4 coordination of the gallium and exclusively octahedral nickel sites which points to a complete inverse spinel type. This is not surprising because nickel +2 tend to occupy octahedral sites within spinel structures.[17]

Nevertheless, further parameters optimizations are required to synthesize phase pure $NiGa_2O_4$ which will be subject of future investigations.

5.2 Iron gallium oxides

Iron oxide materials are fascinating due to their wide arsenal of oxidation states and outstanding magnetic properties. Therefore, it is surprising to find only few reports upon iron gallium oxides.[19-26] The question arises whether the synthesis of such compounds is difficult due to the active redox chemistry of iron. Most often solid state routes[20] or chemical vapor transport techniques have been chosen for the production of iron gallium spinel oxides which is a 53 % partially inverse compound.[24] Recently, the first solution based reactions were successful to generate hollow Fe-Ga oxide nanospheres using air bubbles as templates.[25,26]
Superparamagnetic behavior has been found for $FeGa_2O_4$ above 10 K[21, 22] which makes this compound even more interesting.

Therefore, one goal of this thesis was to generate spinel particles of the composition $FeGa_2O_4$ or iron substituted Ga_2O_3 by applying microwave-assisted techniques in aqueous media. The results of this study are presented in the following.

5.2.1 Microwave-hydrothermal synthesis

The facile microwave-assisted synthesis of iron containing gallium oxide shows promising results without calcination steps by using NaOH as pH adjusting agent (Figure 5.8). Nevertheless, more detailed X-ray diffraction investigations rather afford an iron gallate with the composition $Fe_{1.4}Ga_{1.6}O_4$ instead of the targeted spinel $FeGa_2O_4$ (Figure 5.9). Adjusting the pH value with aqueous ammonia does not produce phase pure iron gallium oxides. Instead, the incorporation of iron seems to be inhibited and only gallium compounds were produced, such as Ga_2O_3 (ICSD PDF card 43-1012) and GaO_2H (ICSD PDF card 06-0180). Therefore, the influence of the pH adjustment for the synthesis of transition metal gallates plays again an important role and NaOH is superior to NH_3 for this synthesis. Furthermore, the phase pure production of iron gallium oxides requires reaction temperatures of 180 °C – lower temperatures only generate product mixtures.

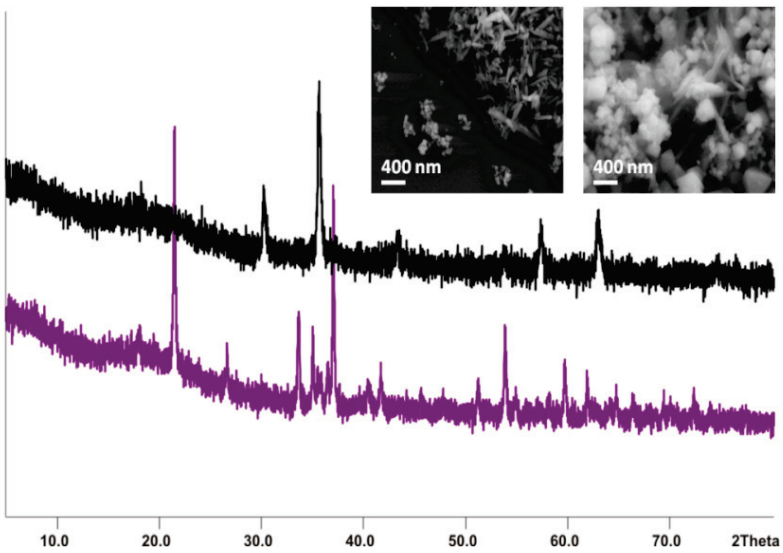

Figure 5.8. Representative XRD and SEM images of iron gallium oxide produced with MW-HT synthesis at 150 °C with NH_3 (purple and left inset) and at 180 °C using NaOH (black and right inset).

All other transition metal gallium oxides are stable while calcination as demonstrated in several Chapters (5.1 and 5.3-5) whereas the iron containing sample shows a mass change of 3.9 % as demonstrated by TG/DSC investigations. Detailed analyses affords an onset temperature of 338 °C as well as a phase transition between 746 and 992 °C (Figure 5.10) which can be attributed to the complete formation of a $FeGaO_3$ phase according PXRD after the TG/DSC investigations (Figure 5.11).

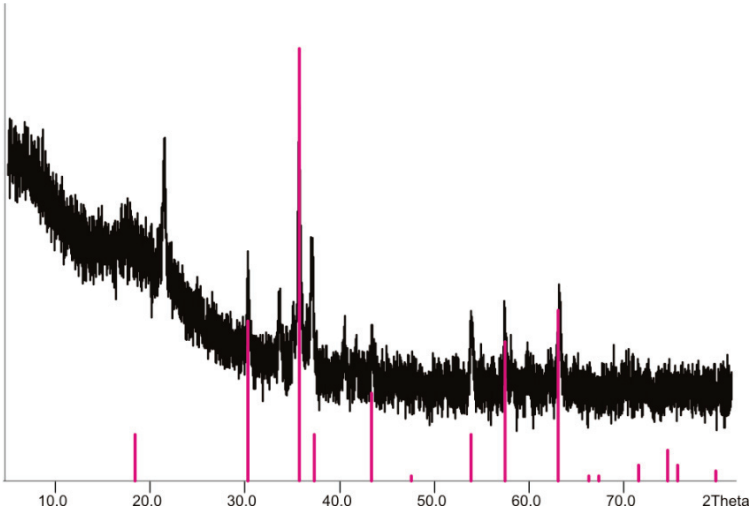

Figure 5.9. XRD pattern of $Fe_{1.4}Ga_{1.6}O_4$ (ICSD PDF card 74-2228) synthesized at pH 12 (NaOH) and 180 °C.

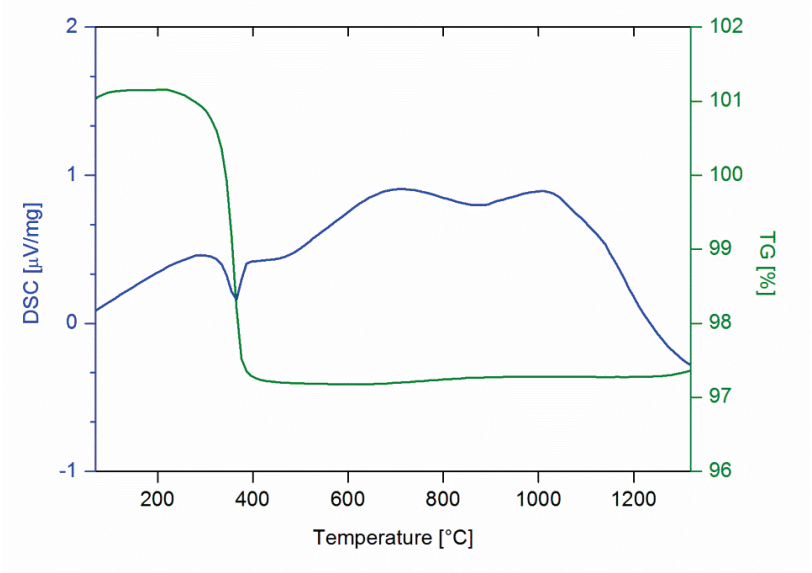

Figure 5.10. TG/DSC of "$FeGa_2O_4$" synthesized with NaOH at pH 12 and 180 °C.

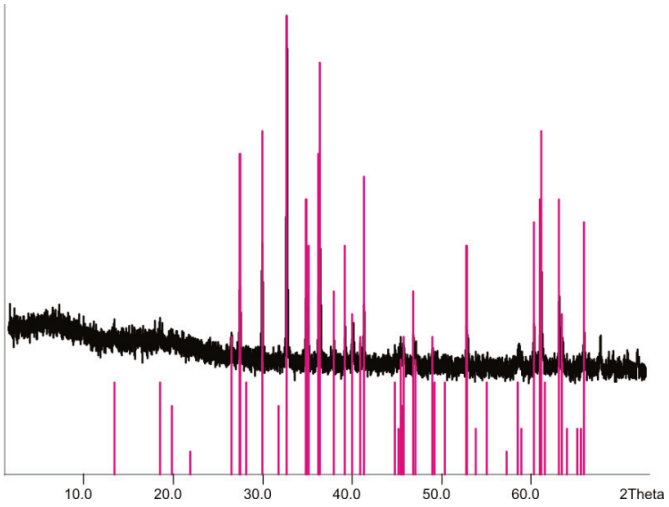

Figure 5.11. XRD of monoclinic $GaFeO_3$ (ICSD PDF card 28-0673) synthesized during TG at 1400 °C in N_2.

5.2.2 Hydrothermal and solid state synthesis

Similar to the nickel gallium oxide, the solid state synthesis of $FeGa_2O_4$ at 900 °C for 2 and 20 h resulted in Ga_2O_3 rather than the desired iron gallium spinel. Comparison with literature data (ICSD PDF card 43-1013) confirmed the formation of Ga_2O_3. The inset in Figure 5.12 clearly shows differences in the reaction time: the longer the synthesis takes, the more phases are formed .

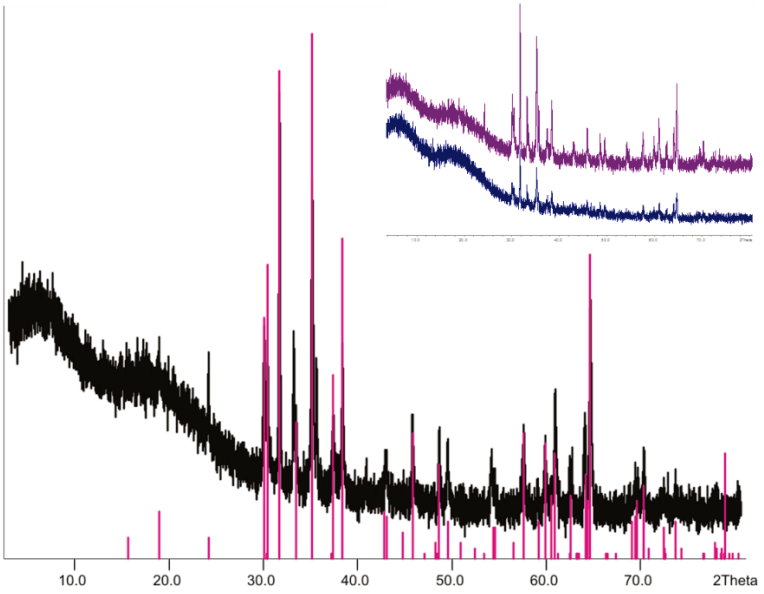

Figure 5.12. XRD pattern of the product obtained via solid state synthesis for 20 h compared to literature data Ga_2O_3 (ICSD PDF card 43-1012). The inset shows the XRD pattern directly after the MW-HT synthesis within 2 h (blue) and 20 h (violet).

Hydrothermal techniques for 48 h at 180 °C also afforded a product mixture of GaOOH (ICSD PDF card 26-0674) and Ga_2O_3 (ICSD pDF card 43-1013), but with additional production of the desired $FeGa_2O_4$ (ICSD pDF card 74-2229). This confirms the advantages of HT synthesis over conventional solid state reactions. Figure 5.13 demonstrates the XRD patter of hydrothermally synthesized product mixtures obtained using ammonia as well as NaOH. Both conventional synthetic ways did not result in phase pure products and only the HT technique produced small amounts of $FeGa_2O_4$.

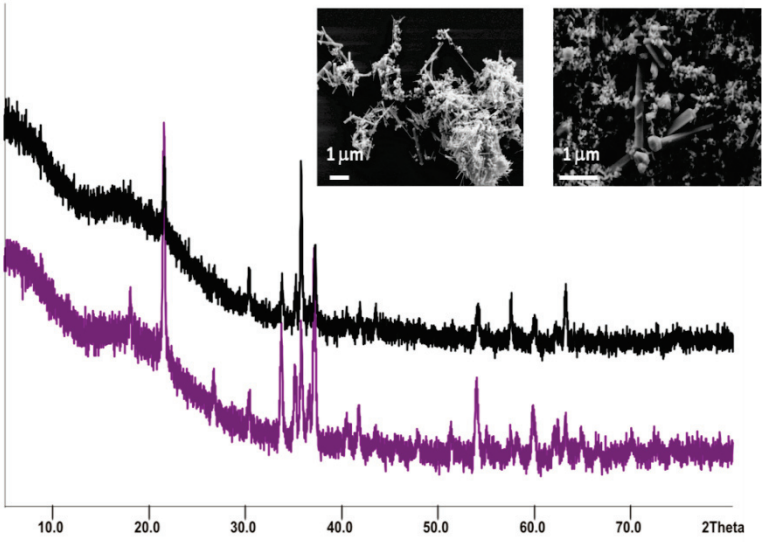

Figure 5.13. Representative XRD and SEM images of iron gallium oxide produced with hydrothermal synthesis at 180 °C with NH_3 (purple and right inset) and with NaOH (black and left inset).

5.2.3 Conclusion

In summary, the facile aqueous synthesis of $FeGa_2O_4$ still requires further exploration. These first results are promising for the MW-HT and conventional HT synthesis, but intense parameter optimizations are needed. None of the applied techniques afforded phase pure products whereas the MW-HT route is the most promising due to the fast formation of $Fe_{1.4}Ga_{1.6}O_4$. Most probably, the redox properties of iron render this synthesis to be more complicate than expected. The decomposition to other iron gallium oxides during calcination may support this hypothesis.

5.3 $MnGa_2O_4$ as a challenging synthetic target

Manganese oxides[27-34] as well as their combination with gallium[31, 32, 35-43] have attracted worldwide research interest due to their optical, magnetic and recently discovered catalytic properties. The inverse $MnGa_2O_4$, for example, shows antiferromagnetic behaviour on A sites of the spinel structure at low temperatures but paramagnetic on B sites[36] which is comparable with other magnetic studies of Mn-doped Ga_2O_3 thin film grown on sapphire substrate using pulsed-laser deposition techniques[39, 41] or radio frequency magnetron sputtering.[44] Normally, such manganese gallium oxides are fabricated with solid state techniques[37, 42, 43] or via coprecipitation methods.[38] Additionally, binary Mn-oxides have been identified as water oxidation catalyst (WOCs), e.g. manganese oxide clusters on silica scaffolds,[45] α- and β-MnO_2 nanowires[28] or nanostructured Mn-oxide films with Mn(III) species.[32] Only recently have the first ternary Mn-based oxide WOCs been discovered, such as $CaMn_2O_4 \cdot xH_2O$ as the first bio-inspired heterogeneous catalyst[46] or spinel-type $LiMn_2O_4$ as a source for λ-MnO_2 WOCs with Mn_4O_4-motifs.[33]

In the following, the facile synthesis of manganese gallium oxides via hydrothermal and microwave-assisted routes is presented. A detailed structural study shows the difficulties occurring during synthesis. Furthermore, the Chapter is rounded off with catalytic tests for water oxidation.

5.3.1 Microwave-hydrothermal synthesis

Detailed screening of the reaction parameters of the MW-HT synthesis of manganese containing gallium oxide afforded optimal conditions at 180 °C and a pH value of 12 if a NaOH solution (4 M) is used for pH adjustment. The broad reflections in the XRD pattern (Figure 5.14) point to nanostructuring of the obtained products which could be confirmed with electron microscopy (inset Figure 5.14). The particle sizes can be indicated with approximately 10 to 20 nm and the BET surface area could be determined as 39 m^2/g.

A detailed pH screening obtained the optimal pH value of 12 as can be seen in Figure 5.15. At low pH values GaOOH-related compounds (ICSD PDF 26-0674) are formed (black pattern). Only a slightly increasing pH already forms spinel-like particles (blue and red curves) which get more and more crystalline towards higher pH values.

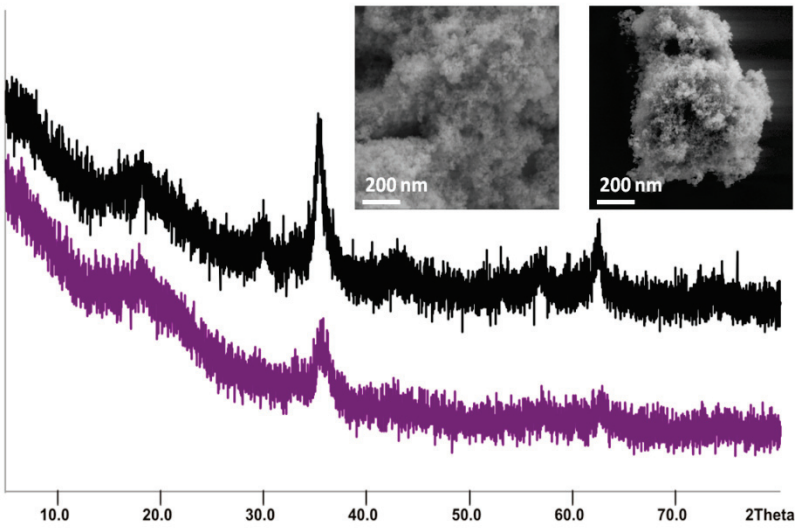

Figure 5.14. Representative XRD and SEM images of manganese gallium oxide synthesized with MW-HT techniques at 150 °C with NH_3 (purple and left inset) and with NaOH (black and right inset).

TG/DSC investigations were performed to verify the optimal calcination temperature because for detailed structural analysis more crystalline samples are required. The thermal treatment up to 1400 °C in N_2 affords an almost stable compound with a mass change of only 0.5 % as can be seen in Figure 5.16. The inset in this graphic demonstrates the DSC data over the temperature – the obtained slope does not point to significant structural changes.[47]

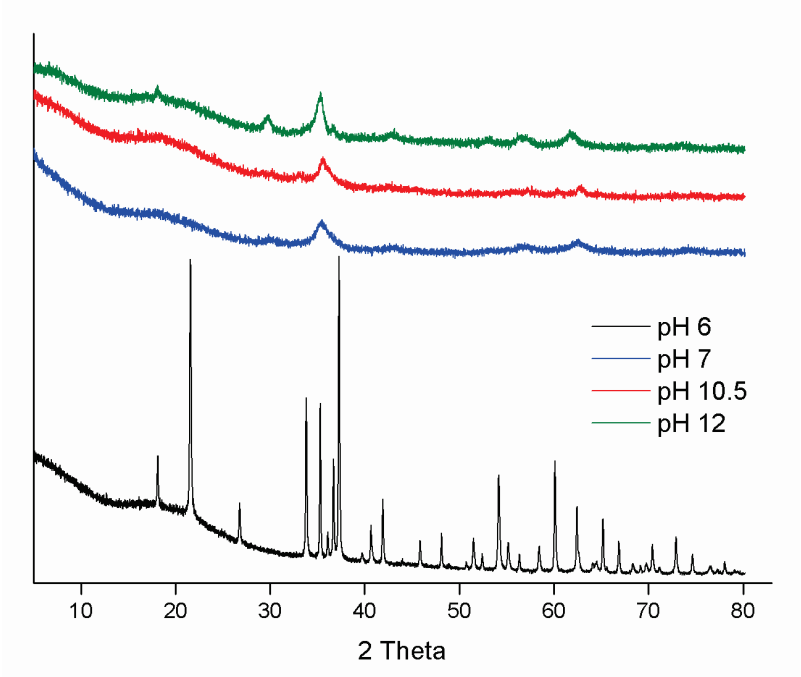

Figure 5.15. PXRD patterns monitoring the pH dependent MW-HT formation of Mn-Ga spinel. A GaOOH-related compound (cf. ICSD PDF 26-0674) is formed at low pH values (black) and the crystallinity of Mn-Ga spinel (upper colored patterns) increases with the pH of the reaction system.

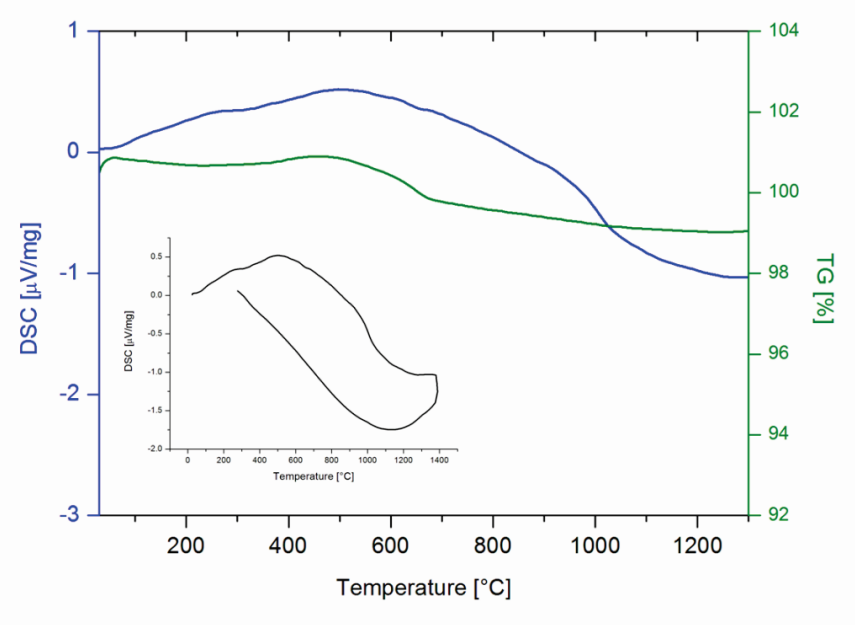

Figure 5.16. TG/DSC investigations of the Mn-Ga oxide synthesized with MW-HT using NaOH for pH adjustment (12) at 180 °C.

The optimal calcination temperature of 1000 °C improves the crystallinity of the manganese gallium oxide as can be seen in Figure 5.17. Additionally, there seems to be no structural changes visible in the XRD pattern. If the calcination step is operated in oxygen atmosphere at 1050 °C, a formation of Mn_2O_3 (ICSD PDF card 24-0508) is observed.

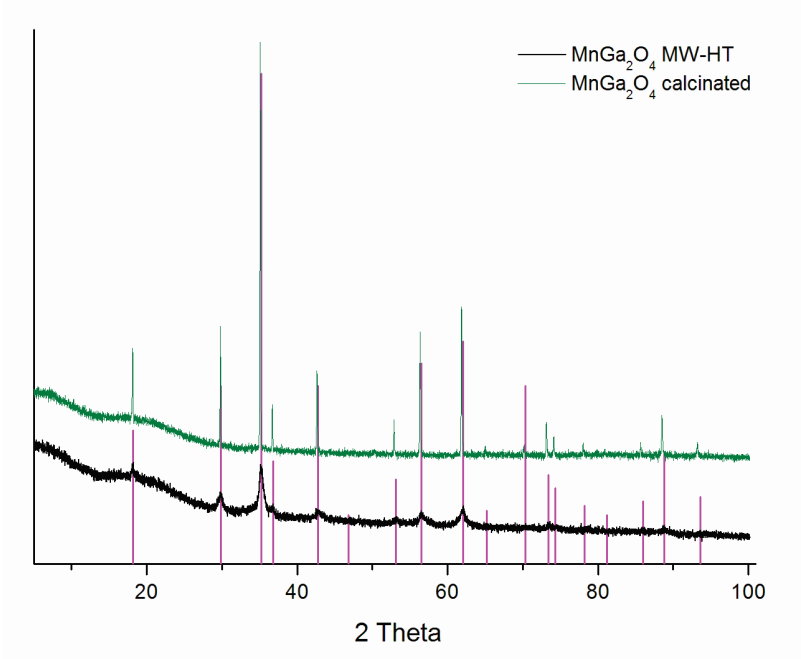

Figure 5.17. PXRD pattern of Mn-Ga spinel synthesized via microwave-hydrothermal route (bottom: black pattern) and calcinated at 1000 °C (top: green pattern) vs. reference data for $MnGa_2O_4$ (ICSD PDF card 36-0181, pink).

Microwave-assisted techniques successfully afforded manganese containing gallium oxides at a pH of 12 and an optimal reaction temperature of 180 °C. Additional calcination increased the crystallinity significantly.

5.3.2 Hydrothermal and solid state synthesis

XRD analysis of the Mn-Ga oxides obtained via solid state methods are presented in Figure 5.18 which clearly indicate the formation of two phases – namely $MnGa_2O_4$ (ICSD PDF card 36-0181) and Ga_2O_3 (ICSD PDF card 43-1012). The extention of the reaction time from 2 to 20 h increases the crystallinity.

Conventional hydrothermal techniques performed at 180 °C for 20 h using NaOH for adjusting the pH obtained GaOOH (ICSD PDF card 26-0674) as well as Ga_2O_3 (ICSD PDF card 43-1012) but the intended spinel $MnGa_2O_4$ could not be synthesized. The representative XRD pattern and SEM images (inset) of the HT synthesis are shown in Figure 5.19.

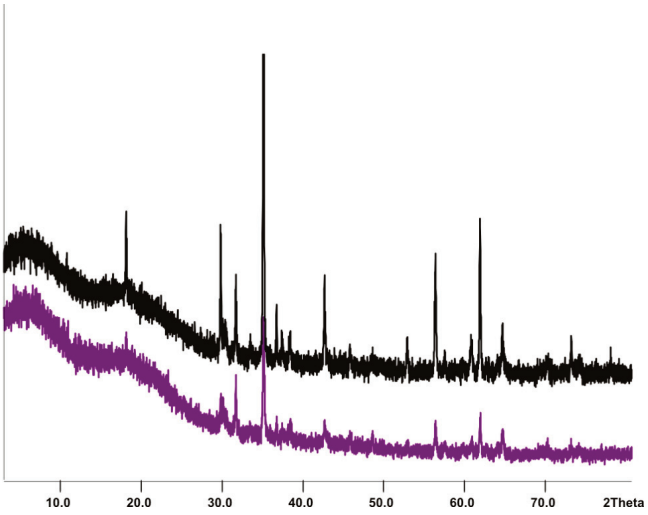

Figure 5.18. XRD pattern of the product obtained via solid state synthesis for 2 (purple) and 20 h (black).

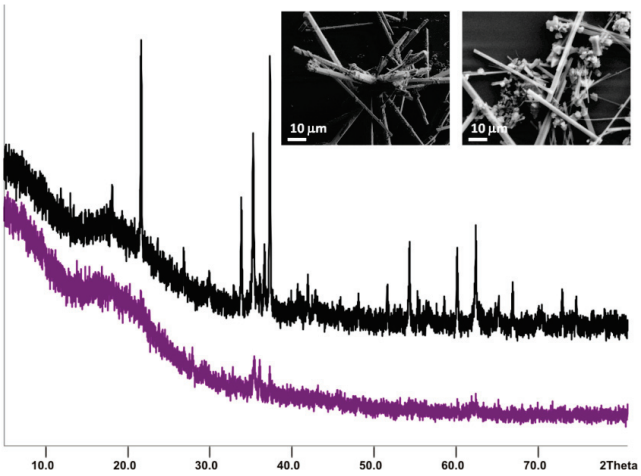

Figure 5.19. Representative XRD and SEM images of manganese gallium oxide synthesized with hydrothermal techniques at 180 °C with NH_3 (purple and right inset) and with NaOH (black and left inset).

5.3.3 XAS, surface investigations and magnetic properties

XAS measurements were performed to investigate structural details like the degree of inversion of the spinel as well as to determine the oxidation states of the manganese via XANES.

Fitting results of the EXAFS measurements are presented in Table 5.2. The inversion factor of approximately 65 % of the Mn-Ga spinel was obtained after fitting the Ga and the Mn K-edges. Furthermore, the numbers of backscattering neighbours indicate a tetrahedrally distorted octahedral environment of gallium as well as of manganese which occurs from the Jahn Teller distortion of Mn ions (cf. Chapter 1).

Table 5.2. Fitting results for experimental X-ray absorption spectra of the Mn-Ga spinel.

Sample	Edge	Abs-Bs[a]	N(Bs)[b]	R(Abs-Bs)[c]	Inversion factor
$MnGa_2O_4$_Ga	Ga K	Ga-O1	1.2 ± 0.1	1.95 ± 0.02	x_{O1}=0.60±0.06
		Ga-O2	4.1 ± 0.4	2.02 ± 0.02	
		Ga-Ga1	10.0 ± 2.0	2.99 ± 0.03	x_{O2}=0.78±0.08
		Ga-Ga2	3.6 ± 0.8	3.50 ± 0.04	
$MnGa_2O_4$_Mn	Mn K	Mn-O1	1.3 ± 0.2	1.93 ± 0.02	x_{O1}=0.68±0.07x
		Mn -O2	3.7 ± 0.4	2.08 ± 0.02	
		Mn -Ga1	4.8 ± 1.0	2.98 ± 0.03	$_{O2}$=0.62±0.06
		Mn -Ga2	5.5 ± 1.1	3.48 ± 0.03	

[a] Abs = X-ray absorbing atom, Bs = backscattering atom (neighbour), [b] number of backscattering neighbour atoms, [c] distance between absorbing and backscattering atom.

The oxidation states of the Mn-Ga spinel could be determined as follows from XANES investigations: 51.8 % Mn(II) and 48.7 % Mn(III). Note that the Mn(II) ions are underestimated with XANES measurements.

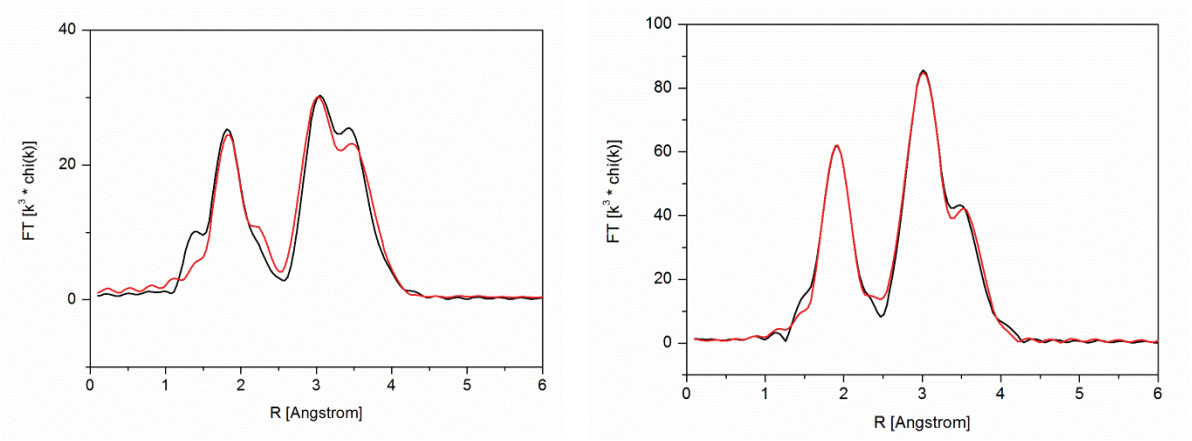

Figure 5.20. Fitting results of the *k*3-weighted EXAFS data of the Mn-Ga spinel at the Mn (left) and Ga edge (right).

XPS measurements show no differences at the Mn 2p edge (Figure 5.21 a) between the Mn-Ga spinel synthesized with MW-HT techniques and the calcinated sample. Interestingly, the Mn 3s spectra show shifts towards smaller binding energies of the Mn-Ga-O_calc sample which could not be attributed so far.

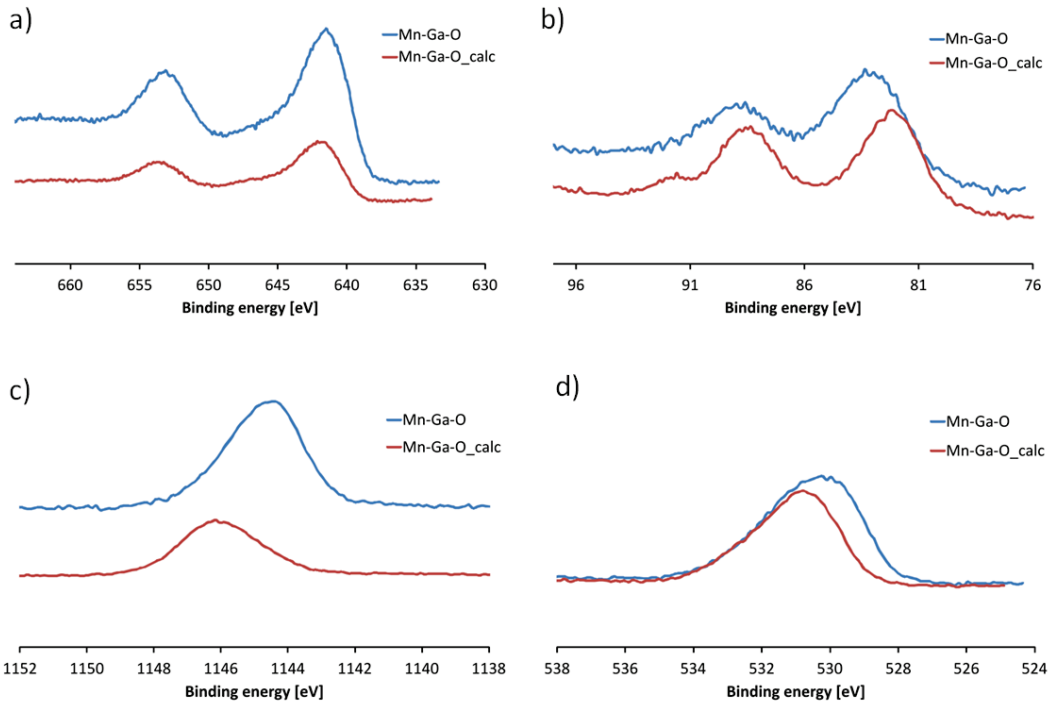

Figure 5.21. XPS spectra of the manganese gallium oxides as prepared via MW-HT and followed calcinations: a) Mn 2p, b) Mn 3s, c) Ga 2p and d) O 1s.

The magnetic susceptibility χ_m was studied for the Mn-Ga spinel sample using a *Quantum Design* SQUID magnetometer MPMS-XL. The temperature dependence of χ_m is shown for various magnetic fields in Figure 5.22. The measurements were performed for both, zero-field cooled and field-cooled histories. In low temperatures both branches show a clear hysteresis for the sample. The Mn-Ga spinel enters magnetically a ferrimagnetic state below 33 K. From the slope of $\chi_m^{-1}(T)$ above 100 K the effective magneton number μ_{eff} was deduced by applying the Curie-Weiss law $\chi_m^{-1}(T) = (T - \theta)/C$. All estimated values are found to scale according to the expected Hunds rule:

	$MnGa_2O_4$
C (Oe mol/emu K)	3.87
μ_B per f.u. (this work)	5.56
μ_B per f.u. (literature) [48]	~5.9
Néel temperature (K)	33
θ (K)	-117

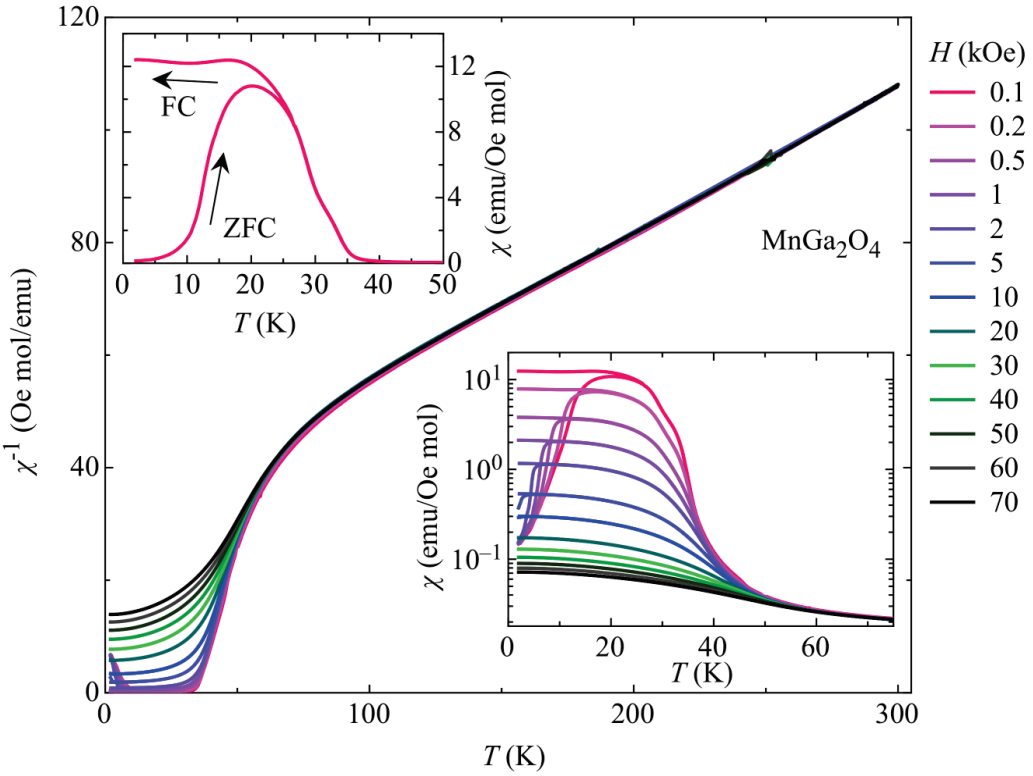

Figure 5.22. Temperature-dependent magnetic susceptibility χ_m measured in various magnetic fields for Mn-Ga oxide spinel (calculated regarding the composition $MnGa_2O_4$). Main graph: inverse magnetic susceptibility; lower right: low temperature regime; upper left: different cooling procedures used.

5.3.4 $MnGa_2O_4$ or Mn_2GaO_4

Performed LA-ICP-MS measurements first pointed towards the presence of another composition than the expected one, namely Mn_2GaO_4 instead of $MnGa_2O_4$. The measured w % of several different samples are shown below:

	sample preparation	Mn 55 [ppm]	theor. ppm	w %	theor. w %
Sample 1	diluted with Teflon	837880	212700	83.8	21.3
Sample 2	diluted with Teflon	846920		84.7	
Sample 2	pressed pure sample	580800		58.1	

These values clearly show that the obtained product is either a single phase with a composition being far away from the intended $MnGa_2O_4$ or a phase mixture was obtained with unknown compositions and ratios.

Therefore, intense XRD fitting was included to the wide analytical methods and the results are presented in the following:

The question arises whether Mn_2GaO_4 and $MnGa_2O_4$ can be distinguished with X-ray diffraction? In principle it is possible, but the precision is not very high, because Mn and Ga are close in the periodic table and therefore scatter X-rays very similarly. The better option to distinguish between the two elements in this case is neutron diffraction. Manganese and gallium show very high contrast for neutrons: Mn has a negative scattering length of -3.73 fm and Ga a positive one (+7.288 fm). In either of the cases (X-ray or neutron diffraction) the occupation factor of the oxygen sublattice has to be known. Making this assumption for the Mn-Ga XRD pattern (no vacancies, 100 % occupation), the following formula of the composition can be obtained: $(Mn_{0.74}Ga_{0.26})_T\ [Ga_{1.55}Mn_{0.45}]_O\ O_4$, which is close to $MnGa_2O_4$ (cf. refinement in Figure 5.23). This manganese gallium spinel composition under the assumption of a fully filled oxygen sublattice is in the range of the XANES-determined Mn(II) / Mn(III) ratio of 0.52 to 0.48.

If another assumption is made with just 5 % deficiency in oxygen, than the result transforms to: $(Mn_{0.97}Ga_{0.03})_T\ [Ga_{1.13}Mn_{0.87}]_O\ O_{3.8}$, which is rather close to $Mn_2GaO_{3.8}$.

The problem occurs that Mn and Ga are too close to each other in the periodic table and therefore are similar in X-ray scattering power. Slight variations in the assumed occupation of the weakly scattering oxygen would lead to huge differences in the refined mutual occupations of the cations. Neutron diffraction could bring more clarity to this question, since Mn and Ga are really strongly different for neutrons. This will be subject of follow-up investigations.

5.3.5 Oxygen production

The manganese gallium oxide spinels were investigated with respect to their performance as water oxidation catalysts (WOCs) under visible light irradiation. Catalytic tests were performed with $[Ru(bpy)_3]Cl_2$ as photosensitizer and $S_2O_8^{2-}$ as sacrificial electron acceptor. Oxygen evolution was observed for Mn-Ga spinels upon visible light illumination (λ = 470 nm) of the suspension with a LED lamp at very low power (4650 Lux). The optimal catalyst concentration for water oxidation was determined as 4.8 mmol/l for the Mn-Ga spinel (Figure 5.24). The obtained catalytic activity has to be taken as first promising result and requires further optimization if compared to other manganese WOCs.

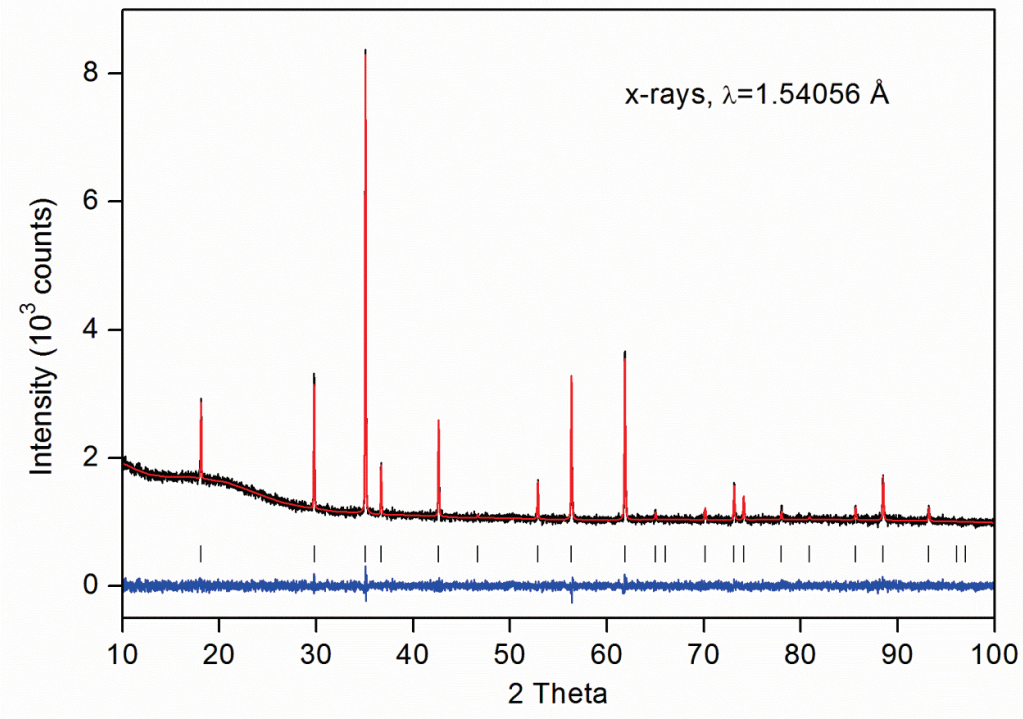

Figure 5.23. Rietveld refinement of the crystal structure parameters of Mn-Ga spinel from the data of X-ray powder diffraction experiments. Experimental (black) and calculated (red) profiles, difference (blue) curves and peak position markers (green) are shown.

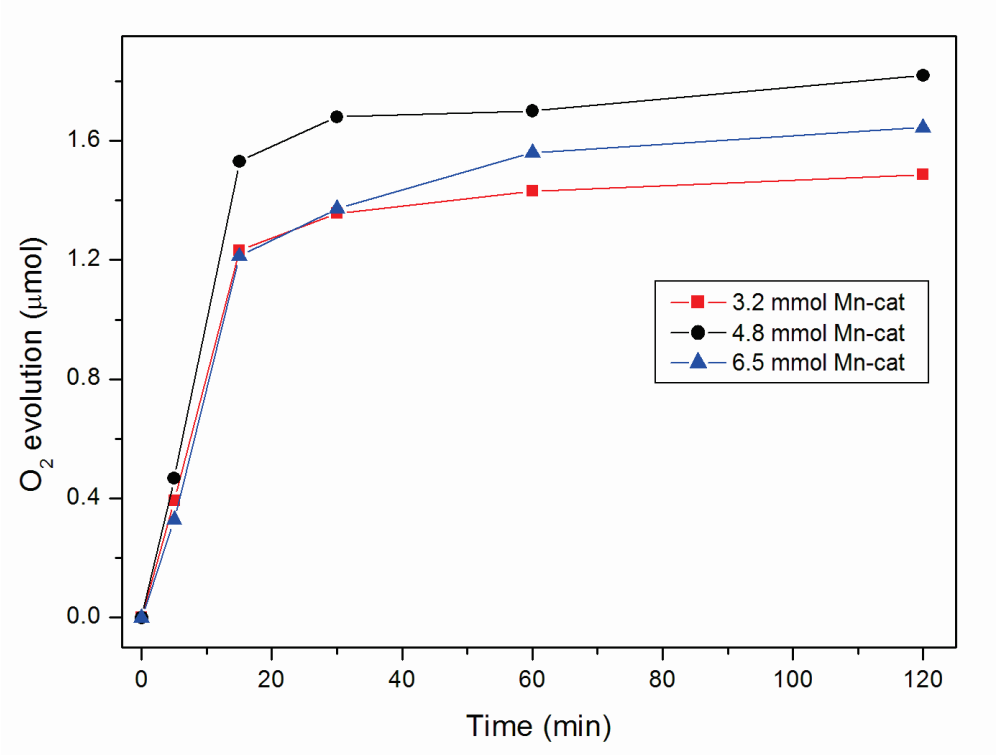

Figure 5.24. Concentration-dependent WOC activity of the Mn-Ga spinel.

5.3.6 Conclusion

In summary, the results obtained with the applied reaction techniques are promising especially with the microwave-assisted route. Nevertheless, the synthesis of manganese gallium oxide spinels needs further optimization. EXAFS measurements demonstrate a tetrahedrally distorted octahedral environment of gallium as well as of manganese and a Mn(II):Mn(III) ratio of roughly 1:1. The precise structural features of the produced Mn-Ga oxides remain unsolved and require neutron diffraction experiments. First experiments for visible-light-driven water oxidation catalyst were promising.

5.4 $CoGa_2O_4$ – A promising catalyst for water oxidation

Several reviews and articles have recently been published with the objective of the water splitting properties of cobalt compounds.[45, 49-51] Therefore, nanostructured cobalt gallium spinels[3, 52-64] are in the scope of this Chapter including synthetic details, magnetic properties and structural investigations. Furthermore, promising results on visible-light-driven water oxidation are presented. In general, $CoGa_2O_4$ oxides are accessed via chemical vapor transport technique[57] or solid state routes to investigate properties such as magnetic behavior.[55, 62, 64] Structural details are often obtained from single crystal experiments which indicated a 58 % inversion of the spinel.[57, 61] To amplify the properties of $CoGa_2O_4$ spinel, solid solution with its aluminum analog were recently investigated, especially their thermodynamic behavior.[58]

5.4.1 Microwave-hydrothermal synthesis

The formation of the $CoGa_2O_4$ spinel (ICSD PDF 11-0698) started with pH values above 7 (Figure 5.25) which demonstrates the importance of this parameter for microwave-hydrothermal syntheses. Below this pH value amorphous products or GaOOH-related compounds (ICSD PDF 26-0674) are obtained. The spinel particles get more and more crystalline with increasing pH. Testing the agents for adjusting the pH afforded NaOH to be superior to liquid ammonia. The best reaction conditions for the phase pure synthesis of nanostructured $CoGa_2O_4$ is a pH of 10 using NaOH and a temperature of 180 °C (Figure 5.26).

Additionally, elemental analysis (LA-ICP-MS and microprobe experiments) confirmed the compositional ratio of Co:Ga:O as 1:2:4. The particle sizes of the obtained nanostructures, which were analyzed with SEM and XRD techniques, ranges between 10 to 40 nm. These small particle sizes are in line with the high BET surface area of 63 m^2/g.

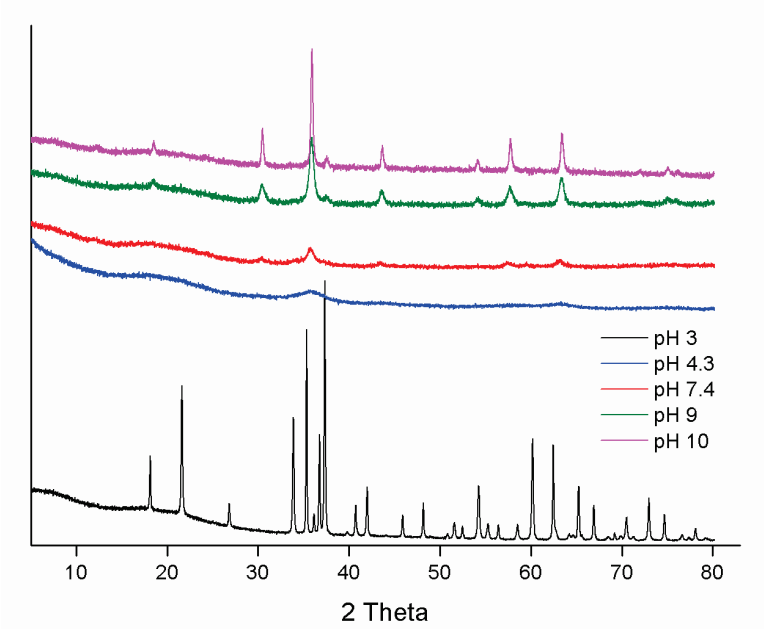

Figure 5.25. PXRD patterns monitoring the pH dependent Mw-HT formation of $CoGa_2O_4$ spinel. A GaOOH-related compound (ICSD PDF 26-0674) is formed at low initial pH values (black).

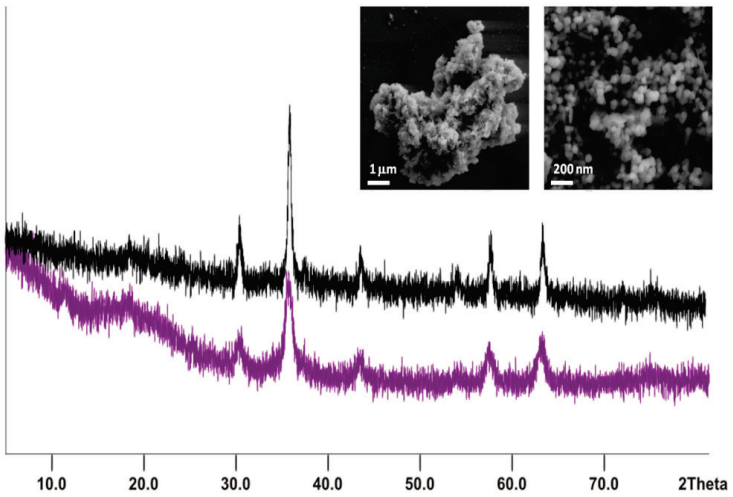

Figure 5.26. Representative XRD and SEM images of cobalt gallium oxide synthesized with MW-HT techniques at 150 °C with NH_3 (purple and left inset) and with NaOH (black and right inset).

The thermal stability of the cobalt gallium oxides was investigated with TG/DSC measurements (Figure 5.27) up to 1400 °C in nitrogen atmosphere. The obtained mass loss of around 1 % and can be attributed to fluctuations of the machine. The inset in Figure 5.27 shows the DSC signal versus the temperature whereas the curve affords no significant peaks. This indicates that the structure of the $CoGa_2O_4$ remains stable during calcination (Figure 5.28 and cf. Chapter 5.3.1).

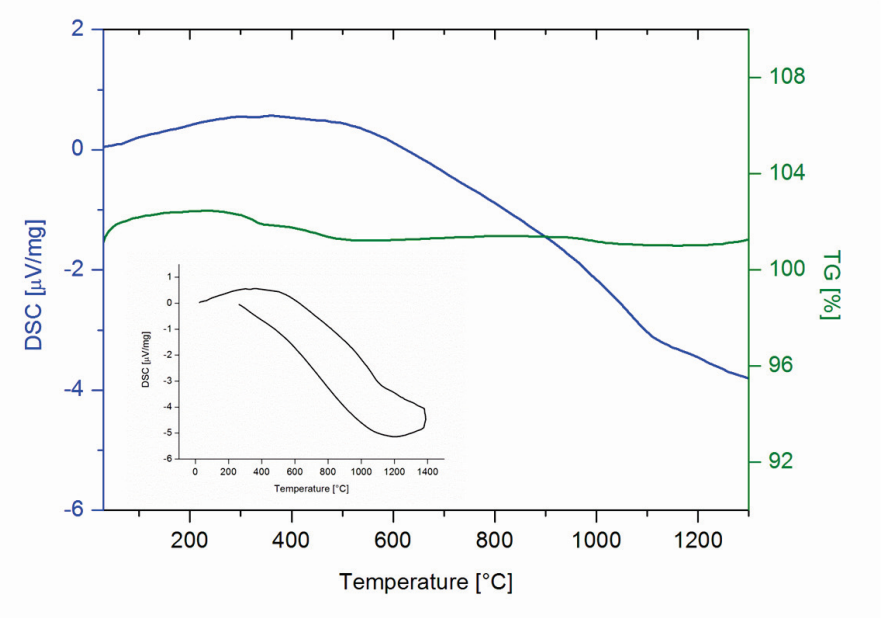

Figure 5.27. TG/DSC investigation of $CoGa_2O_4$ oxide synthesized with MW-HT using NaOH for pH adjustment (10) at 180 °C.

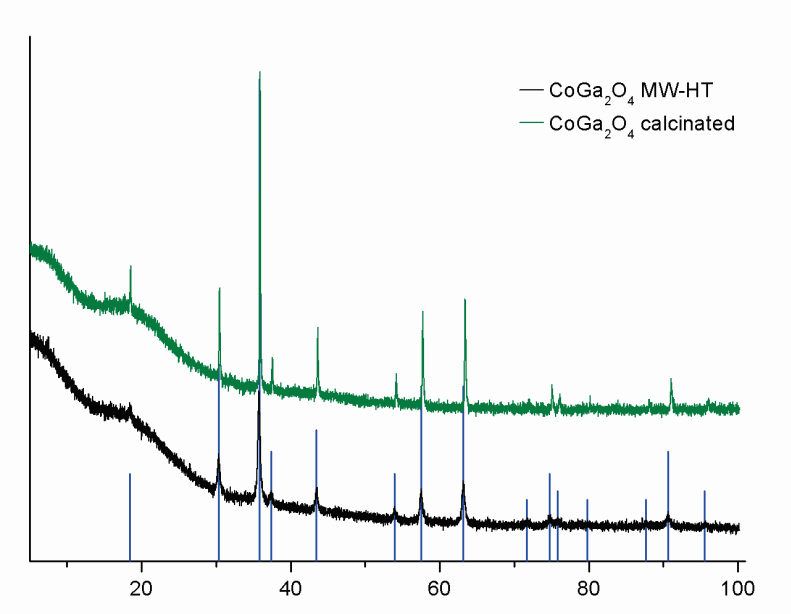

Figure 5.28. PXRD pattern of $CoGa_2O_4$ spinel synthesized via microwave-hydrothermal route (bottom: black pattern) and calcinated at 900 °C (top: green pattern) vs. reference data (ICSD PDF 11-0698, blue).

5.4.2 Hydrothermal and solid state synthesis

Both synthetic pathways – solid state and hydrothermal - produced the spinel product $CoGa_2O_4$ as can be seen in Figure 5.29 and 5.30. Note, that the fast XRD scan of the hydrothermally produced $CoGa_2O_4$ might not detect small impurities. Interestingly, the hydrothermal synthesis using NaOH as pH adjusting agent did not afford any product at all.

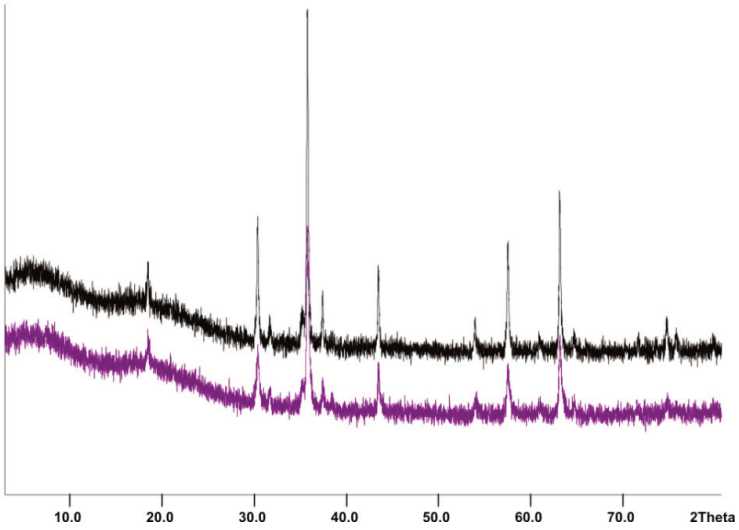

Figure 5.29. XRD pattern of the products obtained via solid state synthesis for 2 (purple) and 20 h (black).

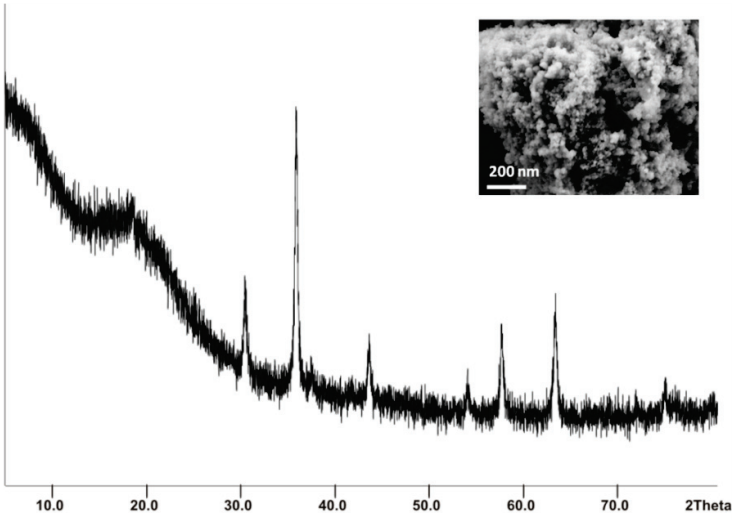

Figure 5.30. XRD of the hydrothermal product at 180 °C for 20 h with NH_3.

5.4.3 XAS, surface investigations and magnetic properties

XAS measurements afforded a coordination of 2+4 (Table 5.3) for the $CoGa_2O_4$ spinel which is due to Jahn Teller distortion of the cobalt ions. Therefore, cobalt as well as gallium ions have an elongated surrounding geometry and occupy both sites within the spinel lattice, namely tetrahedral A and octahedral B sites. The corresponding Fourier transformed EXAFS spectra are shown in Figure 5.31. Furthermore, the inversion factor of the $CoGa_2O_4$ spinel obtained after fitting the Ga and the Co K-edges was 60 % which is comparable with literature data.[61] The oxidation states of the $CoGa_2O_4$ spinel obtained from XANES measurements could be determined as follows: 74.1 % for Co(II) and 25.9 % for Co(III).

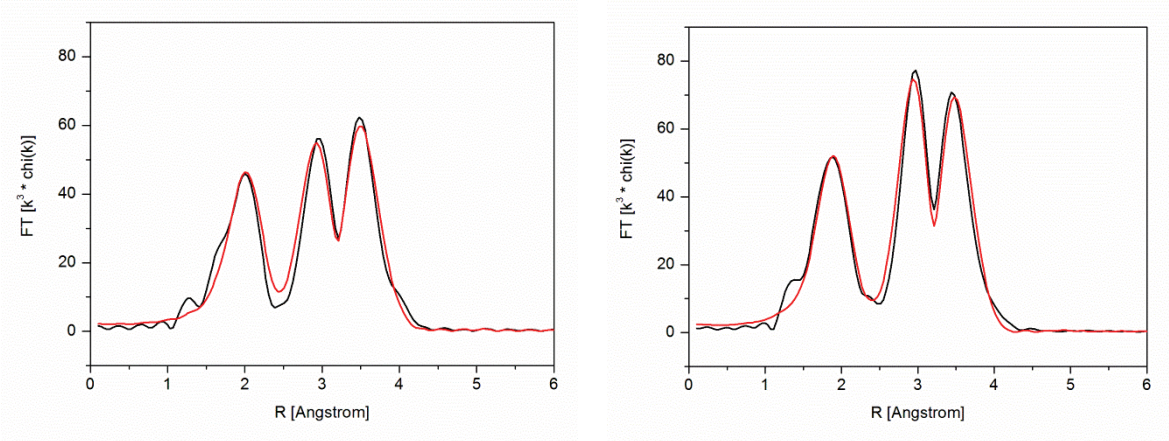

Figure 5.31. Fitting results of the *k*3-weighted EXAFS data of $CoGa_2O_4$ at the Co (left) and Ga edge (right).

Table 5.3. Fitting results for experimental X-ray absorption spectra of the $CoGa_2O_4$ spinel.

Sample	Edge	Abs-Bs[a]	N(Bs)[b]	R(Abs-Bs)[c]	Inversion factor
$CoGa_2O_4$_Ga	Ga K	Ga-O1	1.2 ± 0.1	1.94 ± 0.02	x_{O1}=0.60±0.06
		Ga-O2	4.3 ± 0.4	2.05 ± 0.02	
		Ga-Ga1	4.3 ± 0.8	2.92 ± 0.03	x_{O2}=0.60±0.06
		Ga-Ga2	7.7 ± 1.5	3.45 ± 0.03	
$CoGa_2O_4$_Co	Co K	Co-O1	0.8 ± 0.1	1.93 ± 0.02	x_{O1}=0.55±0.06
		Co-O2	5.2 ± 0.5	2.06 ± 0.02	
		Co -Ga1	6.8 ± 1.4	2.92 ± 0.03	x_{O2}=0.65±0.07
		Co -Ga2	10.0 ±2.0	3.45 ± 0.04	

[a] Abs = X-ray absorbing atom, Bs = backscattering atom (neighbour), [b] number of backscattering neighbour atoms, [c] distance between absorbing and backscattering atom.

The magnetic properties of the $CoGa_2O_4$ spinel were investigated and the temperature dependence of χ_m is shown for various magnetic fields in Figure 5.32. To compare the obtained data with the Mn-Ga (Chapter 5.3) and the mixed Co-Mn-Ga spinel (Chapter 5.5) the SQUID measurements were performed with zero-field cooled and field-cooled histories. All the spinel samples under investigation show a clear hysteresis in low temperatures. Interestingly, the $CoGa_2O_4$ spinel orders magnetically below 10 K into a Spin-Glass state. The measured magnetic behavior can be explained with the Curie-Weiss law.

	$CoGa_2O_4$
C (Oe mol/emu K)	2.94
μ_B per f.u. (this work)	4.85
μ_B per f.u. (literature)[48]	~4.8
Néel temperature (K)	10
θ (K)	-45

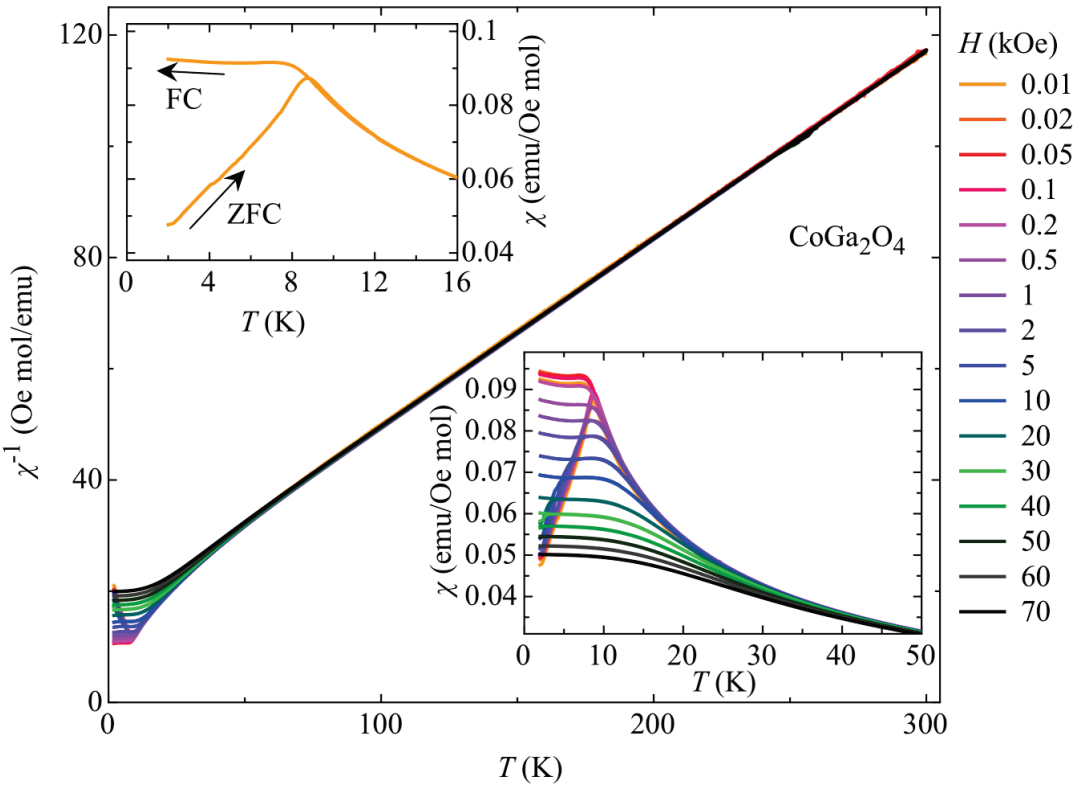

Figure 5.32. Temperature-dependent magnetic susceptibility χ_m measured in various magnetic fields for $CoGa_2O_4$. Main graph: inverse magnetic susceptibility; lower right: low temperature regime; upper left: different cooling procedures used.

5.4.4 Oxygen production

Cobalt gallium oxide spinels were investigated for their catalytic activity of water oxidation under visible light irradiation. The experiments were performed under the same conditions as for the Mn-Ga spinels described in Chapter 5.3.4. Oxygen evolution was observed for the cobalt gallium spinels with an optimal catalyst concentration of 9.5 mmol/l (Figure 5.33) which is twice the amount of catalyst compared to the manganese spinel analog. Note that the nanostructured $CoGa_2O_4$ catalyst also produced twice as much oxygen as the Mn-Ga oxide.

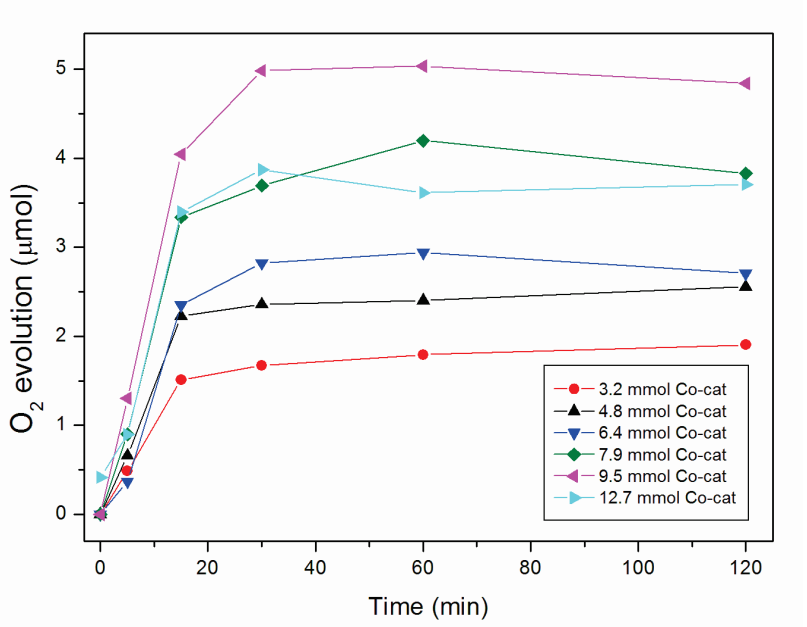

Figure 5.33. Concentration-dependent WOC activity of the $CoGa_2O_4$ spinel.

5.4.5 Conclusion

For the synthesis of nanostructured $CoGa_2O_4$ with high surface areas, microwave-assisted as well as conventional hydrothermal routes were successfully applied. Structural investigations with EXAFS methods afforded elongated surrounding of both metal ions and an inversion factor of 60 %. The ratio of the +2 and +3 Co oxidations states was determined around 4:1 from detailed XANES experiments. Most interestingly, the nanostructured $CoGa_2O_4$ spinels can be used as water oxidation catalysts.

5.5 Co/Mn-spinel catalysts for visible-light-driven water oxidation

5.5.1 Introduction

Nanoscale Co-Mn-Ga spinel nanoparticles benefit from a "synergistic" interaction of Co and Mn, thus paving the way to new concepts for tailored and flexible catalyst design for visible-light-driven water oxidation.

The quest for alternative energy sources and global climate control are major research challenges of the 21st century. Chemical water splitting with visible-light-driven and robust heterogeneous catalysts as one of the most direct solution attracts intense worldwide interest.[65, 66] Mn-containing water oxidation catalysts (WOCs) are closest to nature's photosystem II,[29, 34, 67] and several binary[32, 33, 45] as well as ternary[46] heterogeneous Mn-WOCs have recently been discovered. A wide spectrum of cobalt compounds ranging from amorphous solids to molecular catalysts is active in water splitting.[49, 50] However, the innovative potential of combining Co and Mn into mixed metal catalysts[68] still remains to be fully explored and the complex influence of structure, composition and preparative history renders systematic WOC synthesis a challenge. Co/Mn-spinels keep attracting widespread research interest,[69] but Co-Mn-Ga spinels have never been investigated in their own right.[70] Neither have gallium oxide spinels been used as visible-light-driven WOCs to date[71, 72], despite recent progress on other Ga-oxide[73] and oxynitride[74] photocatalysts.

Therefore a new concept to link the rich catalytic chemistry of Co- and Mn-oxides is presented: both cations are embedded into a redox-inert and highly stable gallium oxide spinel matrix where they interact in a "synergistic" fashion. Although spinel oxides of the MM'_2O_4 type are most versatile targets for catalyst design due to their tunability together with high stability, their potential as visible-light-driven water splitting catalysts remains to be explored. Here, a newly access to nanoscale Co-Mn-Ga spinel WOCs with a rapid and facile microwave-hydrothermal synthesis is reported.[75, 76]

5.5.2 Synthesis and characterization

Gallium nitrate, cobalt nitrate and/or manganese sulfate were dissolved in deionized water to afford nanoscale Co-Ga-, Mn-Ga- and Co-Mn-Ga-spinel materials, respectively, after 60 min of MW-HT treatment at 180 °C. pH control with NH_3 or NaOH is the decisive parameter to generate phase pure spinels: whereas Co-Ga (Figure 5.25 in Chapter 5.4) and Co-Mn-Ga (Figure 5.34) spinels require pH 10, Mn-Ga spinel emerges at a higher pH of

12 (Figure 5.15 in Chapter 5.3). PXRD patterns of the three pristine materials clearly indicate spinel formation and both particle size calculations and electron microscopy investigations are in the range between 15 and 40 nm (Figure 5.35 and Figures 5.14 in Chapter 5.3 and Figure 5.26 in Chapter 5.4). This correlates with BET surface area values of 63 m^2/g (Co-Ga spinel), 39 m^2/g (Mn-Ga spinel) and 70 m^2/g (Co-Mn-Ga spinel).

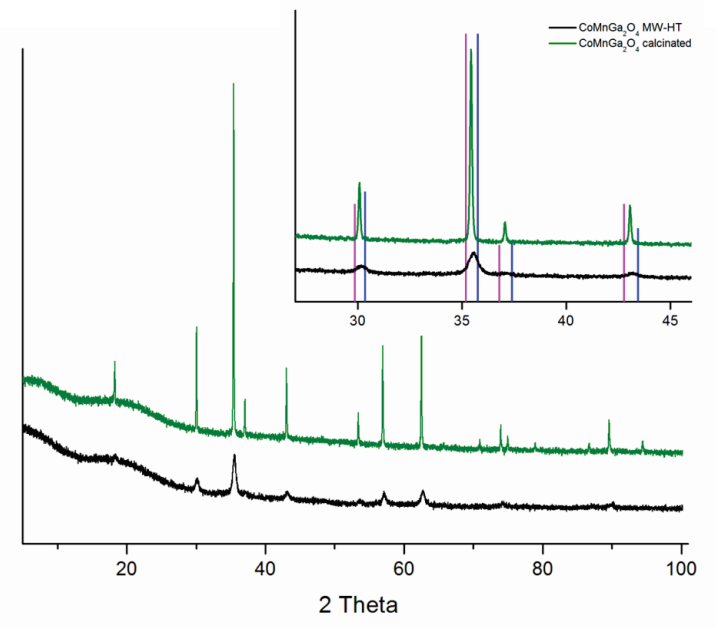

Figure 5.34. PXRD pattern of MW-HT synthesized Co-Mn-Ga spinel catalyst before (black) and after (green) calcination at 1050 °C; inset: comparison with literature data for $CoGa_2O_4$ (PDF 11-0698, blue) and $MnGa_2O_4$ (PDF 36-0181, pink).

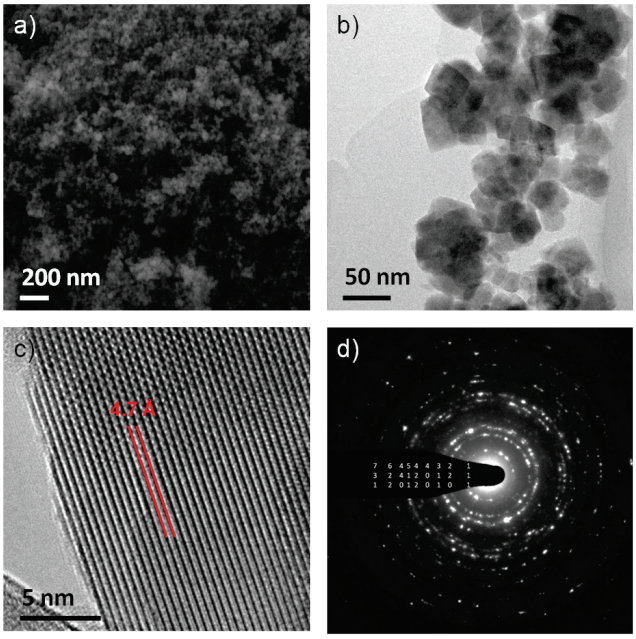

Figure 5.35. Representative SEM image of Co-Mn-Ga spinel (a), TEM image (b), HRTEM (c) and indexed ED (d).

5.5.3 Water oxidation under visible light irradiation

All three nanostructured spinels were compared with respect to their performance as WOCs under visible light irradiation. Catalytic tests were performed with $[Ru(bpy)_3]Cl_2$ as photosensitizer and $S_2O_8^{2-}$ as sacrificial electron acceptor (Figure 5.36).[46] Oxygen evolution was observed for Co-Ga, Mn-Ga and Co-Mn-Ga spinels upon visible light illumination (λ = 470 nm) of the suspension with a LED lamp at very low power (4650 Lux).

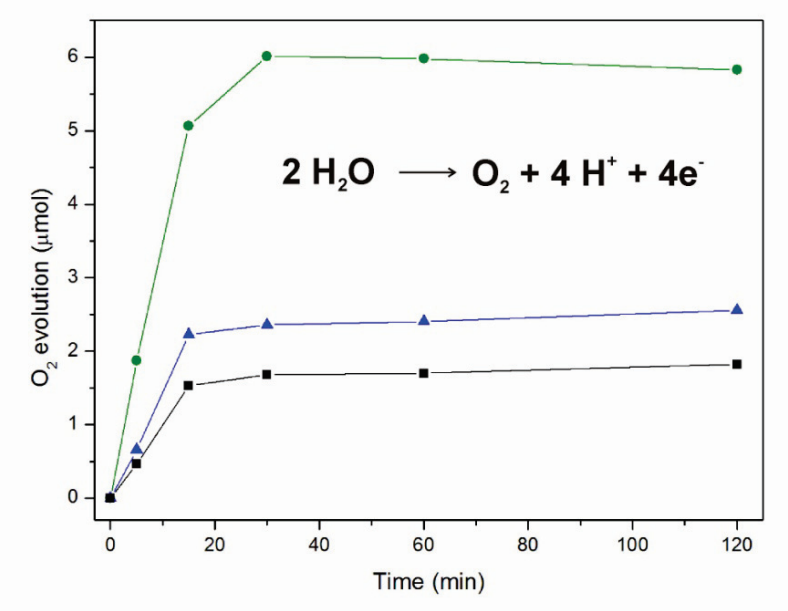

Figure 5.36. Visible-light-driven oxygen evolution for all three spinel-type catalysts (concentration 4.8 mmol/l; ■ Mn-Ga, ▲ Co-Ga, ● Co-Mn-Ga).

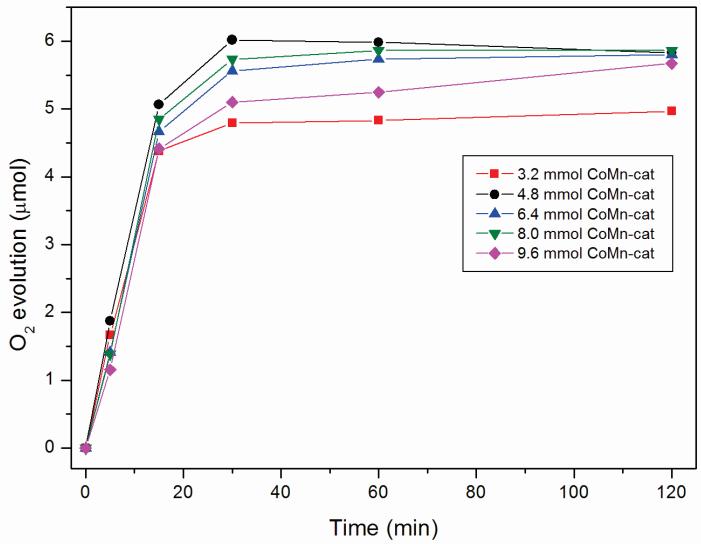

Figure 5.37. Concentration-dependent WOC activity of the mixed Co-Mn-Ga spinel.

A slightly acidic Na_2SiF_6 buffered reaction medium (pH 5.8) prevented the accelerated degeneration of the Ru-photosensitizer at higher pH values. Maximum oxygen production rates are reached after 30 min and remain at this level afterwards. The optimal catalyst concentration for water oxidation was determined as 4.8 mmol/l for both Mn-Ga and Co-Mn-Ga spinel (cf. Figure 5.24 and 5.33 in Chapter 5.3 and 5.4). A considerably higher concentration of Co-Ga spinel (9.5 mmol/l) is required to achieve comparable oxygen production rates despite its larger BET surface area (63 m^2/g) in comparison with Mn-Ga (39 m^2/g), and a further increase is counterproductive (cf. Figure 5.37 and Figure 5.24 and 5.33 in Chapter 5.3 and 5.4). Control experiments in the absence of catalysts did not lead to any oxygen evolution. Variations of the reaction medium, e.g. acetate buffered solutions, did not afford satisfying results and no photocatalytic activity was monitored in the presence of Fe^{3+} as sacrificial electron acceptor.[77] All catalysts are stable under the reaction conditions and could be recycled which demonstrates the stability of the spinel-WOCs in comparison with other Mn-catalysts.[46] Most importantly, the mixed Co-Mn-Ga spinel displays a significantly improved WOC performance in comparison with Co-Ga, Mn-Ga or MGa_2O_4 (M = Ni, Zn) spinels.[71, 72] The facile visible-light-driven operation with low power LEDs is another key advantage of the Co-Mn-Ga WOC over high energy light sources required for other heterogeneous Mn- and Co-catalysts, e.g. Ar ion lasers[51] or Xe lamps.[46, 71, 72]

5.5.4 Detailed analytical characterizations

To investigate the "synergistic" interaction of Co and Mn within the gallium oxide spinel matrix, a wide variety of analytical investigations was performed on the novel Co-Mn-Ga oxides.

The compositions of all spinel-type nanomaterials were analyzed with complementary LA-ICP-MS, ICP-MS and electron microprobe techniques. Whilst the composition of Co-Ga spinel is close to the expected formula $CoGa_2O_4$ (cf. Chapter 5.4), Mn-Ga spinel exhibits a significantly higher Mn:Ga-ratio than $MnGa_2O_4$ which is the only compositon charcterized hitherto (cf. Chapter 5.3.4). Further investigations on the formation of a new Mn-rich spinel phase are now in progress. The composition of nanoscale Co-Mn-Ga spinel was determined as $Co_{0.58}Mn_{0.95}Ga_{1.47}O_4$.

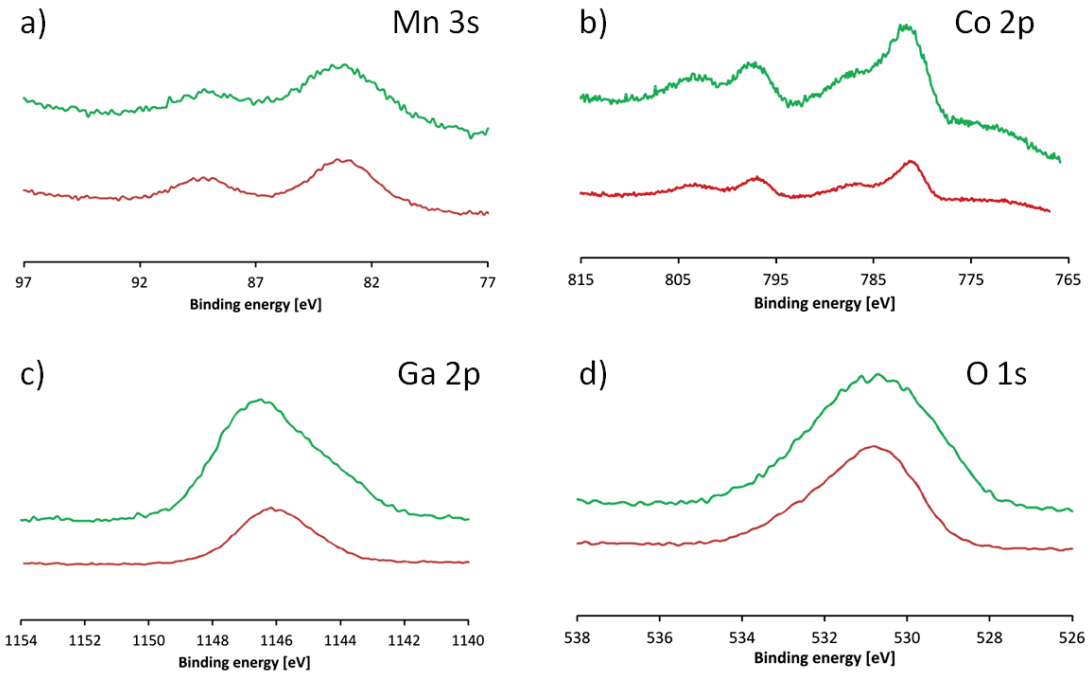

Figure 5.38. XPS spectra of the as-synthesized (green) and calcinated (red) Co-Mn-Ga mixed spinel oxide: a) Mn 3s, b) Co 2p, c) Ga 2p and d) O 1s.

XPS (X-ray photoelectron spectroscopy) measurements on as-synthesized Co-Mn-Ga spinel showed the presence of both Mn(II) and Mn(III) valence states on the surface (Figure 5.38 and Table 5.4). This is evident from comparison of the Mn $2p_{1/2}$ and $2p_{3/2}$ peak positions with manganese oxide references. Furthermore, the energy difference between the Mn $3s_{1/2}$ and $3s_{3/2}$ peaks falls within the characteristic range between Mn(II) and Mn(III).[18, 78] Likewise, the presence of both Co(II) and Co(III) states on the surface was assigned from deconvolution analyses of the Co 2p peaks (Figure 5.39).[79]

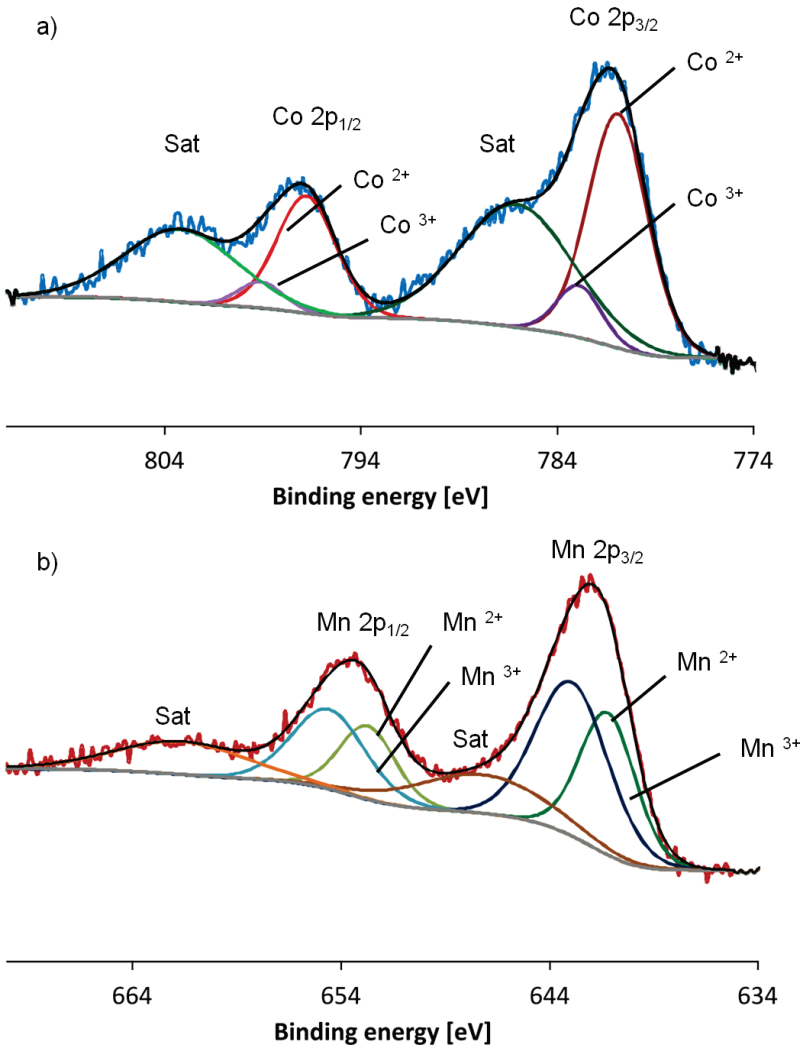

Figure 5.39 Analysis of XPS patterns of the Co-Mn-Ga spinel: (a) Co 2p region, (b) Mn 2p region.

Table 5.4. XPS peak positions (eV) of as-synthesized and calcinated Co-Mn-Ga spinel in comparison with reference data.

Peak	**Co-Mn-Ga (as-synth.)**	**ΔMn [eV]**	**Co-Mn-Ga (calcinated)**		**Reference**				**Lit.**
					MnO	**Mn_2O_3**	**Mn_3O_4**	**MnO**	
Mn $3s_{1/2}$	83.2		83.1						
Mn $3s_{3/2}$	89.0	5.8	89.1	6.0	6.1	5.3	5.4	4.5	[78]
Mn $2p_{3/2}$	641.8		641.8		641.0	641.5	641.9	642.6	[78]
Mn $2p_{1/2}$	653.7		653.5		653.0	653.8			[18]

DTA/TG measurements show high thermal stability of Co-Mn-Ga spinel up to 1400 °C with negligible mass loss (Figure 5.40). All spinel samples were calcinated (N_2; Mn-Ga: 1000 °C, Co-Ga and Co-Mn-Ga: 900 °C) to enable more detailed structural and magnetic investigations. The XPS spectra of Co-Mn-Ga spinel do not display significant changes after calcination (Figure 5.38). The increased crystallinities of all three post-treated spinels go hand in hand with microscale particle growth whilst phase changes were not observed (PXRD patterns in Figure 34, 5.17 in Chapter 5.3 and Figure 5.28 in Chapter 5.4). Note that the catalytic activity of the thermally post-treated samples is lowered to ca. 1/4 compared to the pristine samples despite closely related XPS spectra (Figure 5.38).

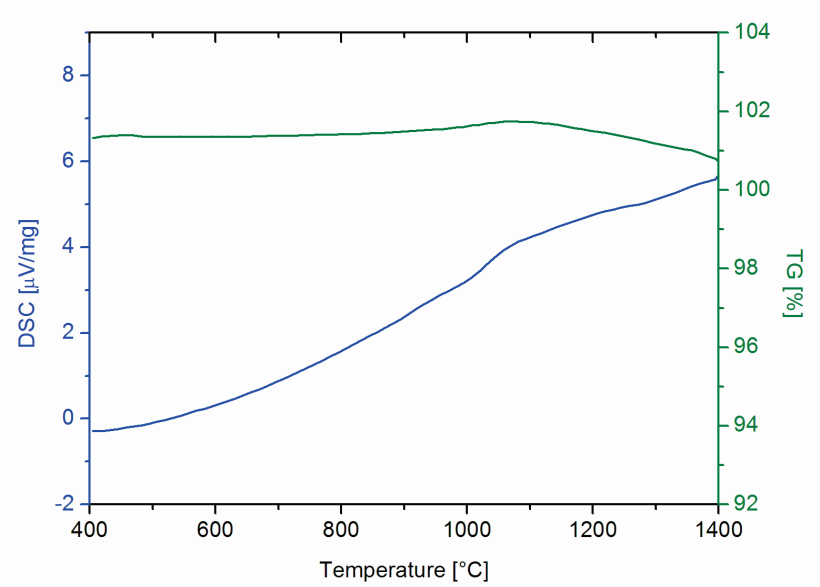

Figure 5.40. TG/DSC curve of Co-Mn-Ga spinel demonstrating thermal stability of the material up to 1400 °C (the appearing mass loss of ~0.5 % can be attributed to baseline fluctuations of the machine).

5.5.5 XAS spectroscopy

Local cationic coordination environments in all three post-treated bulk materials were investigated with X-ray absorption spectroscopy (XAS) measurements at the metal K-edges (Table 5.5, Figure 5.41). Oxygen coordination numbers obtained from EXAFS (extended X-ray absorption fine structure) allow the determination of tetrahedral and octahedral site occupancies based on their distinct M-O distances (M = Co, Mn, Ga; cf. Table 5.5).[37, 61] Fractional differences from 100 % arise from a fit procedure with minimal restrictions that is appropriate regardless of experimental errors (Table 5.5).

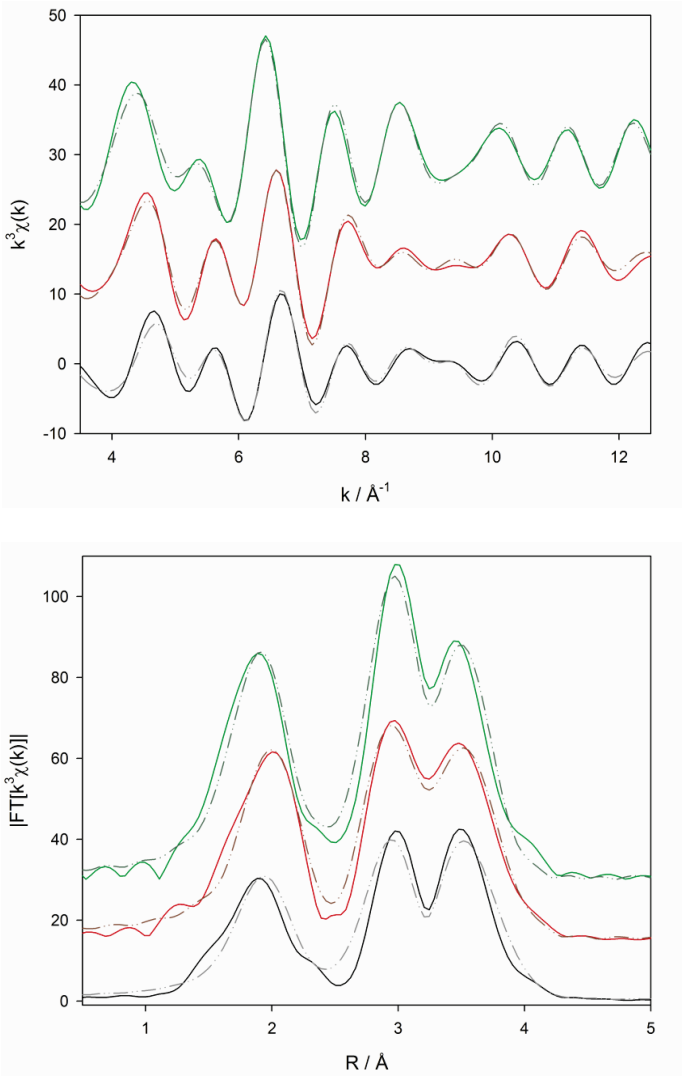

Figure 41. EXAFS spectra (top) of Co-Mn-Ga spinel, recorded at the Mn (black line), Co (red line) and Ga (green line) K-edge. The corresponding Fourier transformed functions are shown (bottom) as well as the theoretical spectra calculated according to the structural parameters given in Table 5.5 of the main text.

Higher shells were fitted as well, but the obtained coordination numbers have to be treated with caution, because the similar backscattering properties of all three metals render them indistinguishable. Therefore, all spectra were only fitted with Ga-Ga contributions, leading to less reliable coordination numbers. XANES (X-ray absorption near edge structure) spectra furthermore provide insight into the oxidation states of the metal cations with defined references for a linear-combination XANES-fit (LCF).[80] Given that HT treatments promote oxidation of Co^{2+}/Mn^{2+} containing precursors to M^{3+},[81, 82] Co- and Mn-oxides with various valence states were chosen as references. Only $M^{(II)}O$ and $M^{(II,\ III)}{}_3O_4$ (M = Co, Mn) references could be fitted to all three spinel materials and attempts to adjust M_2O_3 and MO_2 were not successful. Table 5.5 summarizes the results

and slight divergences at the Mn K-edge can be explained in terms of local structural differences between the reference oxides and the spinels under investigation. It is well known that the XANES peak shape is very sensitive to changes in the coordination, which might cause the deviations of the LC-XANES fits.

Table 5.5. Fitting results for experimental X-ray absorption spectra of Co-Mn-Ga spinel.

Edge	Abs-Bs[a]	N(Bs)[b]	$R_{(Abs-Bs)}$/Å[c]	Site occ. (x)	Oxid. state
Ga K	Ga-O1	1.2 ± 0.1	1.90 ± 0.02	^{IV}Ga: 0.30 ±0.05	
	Ga-O2	5.2 ± 0.5	2.00 ± 0.02	^{VI}Ga: 0.86 ± 0.11	
	Ga-Ga1	7.2 ± 1.5	2.96 ± 0.03		
	Ga-Ga2	5.2 ± 1.0	3.46 ± 0.04		
Co K	Co-O1	1.0 ± 0.1	1.98 ± 0.02	^{IV}Co: 0.25 ± 0.05	Co^{II}: 78%
	Co-O2	3.4 ± 0.3	2.07 ± 0.02	^{VI}Co: 0.56 ± 0.07	Co^{III}: 22%
	Co-Ga1	4.8 ± 0.5	2.93 ± 0.03		
	Co-Ga2	7.6 ± 0.8	3.46 ± 0.04		
Mn K	Mn-O1	2.0 ± 0.4	1.95 ± 0.02	^{IV}Mn: 0.50 ± 0.06	Mn^{II}: 42%
	Mn-O2	3.3 ± 0.9	2.07 ± 0.02	^{VI}Mn: 0.55 ± 0.07	Mn^{III}: 58%
	Mn-Ga1	5.3 ± 0.5	2.94 ± 0.03		
	Mn-Ga2	8.7 ± 0.8	3.47 ± 0.04		

[a] Abs = X-ray absorbing atom, Bs = backscattering atom (neighbour), [b] number of backscattering neighbour atoms, [c] distance between absorbing and backscattering atom.

5.5.6 Structural model: PXRD/neutron diffraction and magnetic measurements

Both X-ray and neutron diffraction measurements done on the same Co-Mn-Ga spinel sample were analyzed by Rietveld refinement (Figure 5.42). All three sorts of cations were assumed to occupy both the 8*a* (1/8,1/8,1/8) and 16*d* (1/2,1/2,1/2) positions with soft constraints based on the initial chemical composition (S.G. *Fd3m*, *a* ~8.398 Å, microprobe cation ratios). This allowed to conclude on the distribution of elements on the structure sites (cf. Table 5.6) and on oxygen anions to be fully occupying the 32*e* (x,x,x) site with a refined value of x=0.2598(1), resulting in the composition $(Co^{2+}_{0.46}Mn^{2+}_{0.54})[Co^{3+}_{0.12}Mn^{3+}_{0.41}(^{IV}Ga_{0.34}{}^{VI}Ga_{1.13})]O_4$ according to elemental analyses. This supports the significant fraction of tetrahedrally coordinated Ga^{3+} observed from XAS investigations (Table 5.5) and also points to the distribution of M^{II} and M^{III} (M = Mn, Co) over both sites.

Table 5.6. Results of the joint Rietveld refinement based on neutron (HRPT, λ = 1.1545 Å) and PXRD ($Cu_{K\alpha 1}$) data (space group *Fd3m*) for Co-Mn-Ga spinel. Soft constraints used: overall cation ratio in the sample: n(Mn)/n(Co)/n(Ga)=0.95/0.58/1.47 (derived from microprobe analyses).

***a*, Å**		**8.3946(3)**
site *8a* (1/8,1/8,1/8),	n(Mn)/n(Co)/n(Ga) (fractional)	0.347 (16) / 0.339 (39) / 0.314
	B_{iso} (Å^2)	0.02 (11)
site *16d* (1/2,1/2,1/2),	n(Mn)/n(Co)/n(Ga) (fractional)	0.302 (8) / 0.12 (2) / 0.578 (11)
	B_{iso} (Å^2)	0.31 (5)
site *32e* (*x*,*x*,*x*)	O	0.2598 (1)
	B_{iso} (Å^2)	1.11 (3)

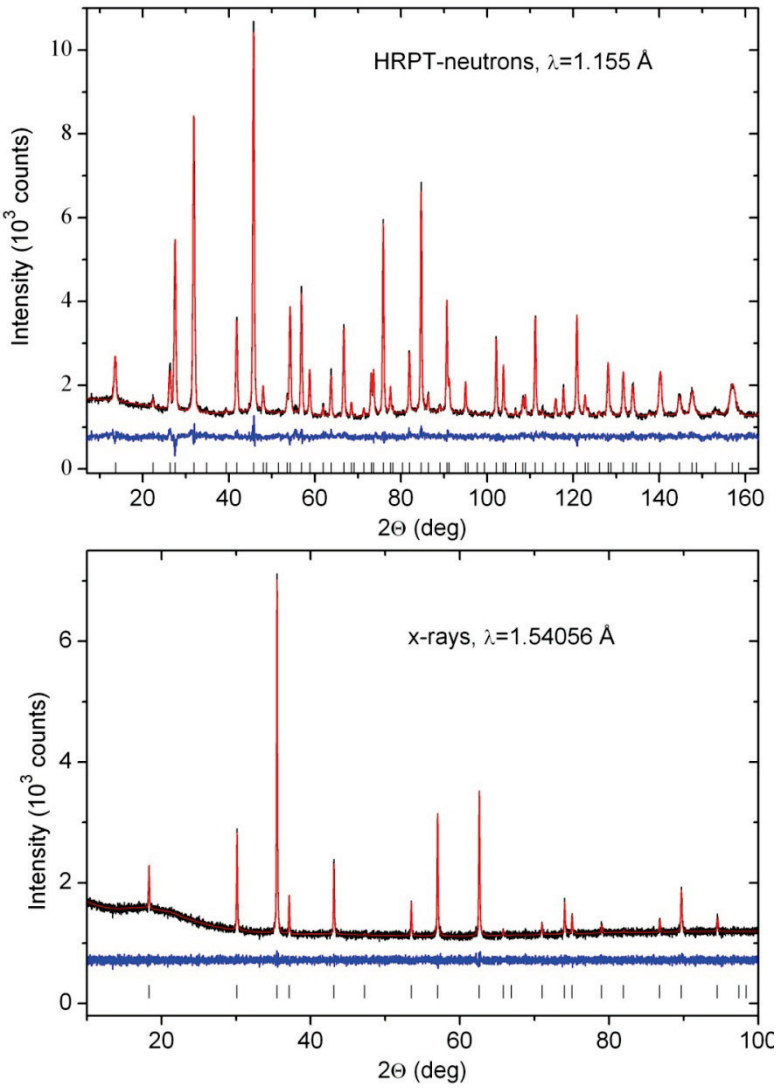

Figure 42. Joint Rietveld refinement of the crystal structure parameters of Co-Mn-Ga spinel from the data of neutron (top) and X-ray (bottom) powder diffraction experiments. Experimental (black) and calculated (red) profiles, difference (blue) curves and peak position markers (green) are shown.

Finally, investigations of the magnetic susceptibility χ_m of $Co_{0.58}Mn_{0.95}Ga_{1.47}O_4$ for both zero-field cooled and field-cooled histories and the temperature dependence of χ_m provided interesting results (Figure 5.43). The magnetic ordering below 25 K resembles ferrimagnetic order. From the slope of $\chi_m^{-1}(T)$ above 100 K, well beyond the ferrimagnetic state, an effective magneton number of $\mu_{eff} = 4.25\ \mu_B$ was obtained by invoking the Curie-Weiss law.[48] Due to four different magnetic ions, i.e. $Mn^{2+/3+}$ and $Co^{2+/3+}$, in Co-Mn-Ga spinel the overall magnetic character is a sophisticated interplay of $3d^4$, $3d^5$, $3d^6$, and $3d^7$ electrons. Importantly, the experimental result of 4.25 μ_B lies well within the ballpark of magnetic moments for these electron configurations. However, a theoretical calculation of the expected magneton number must involve both spin and angular momentum of each electronic level which is subject of a follow-up study.

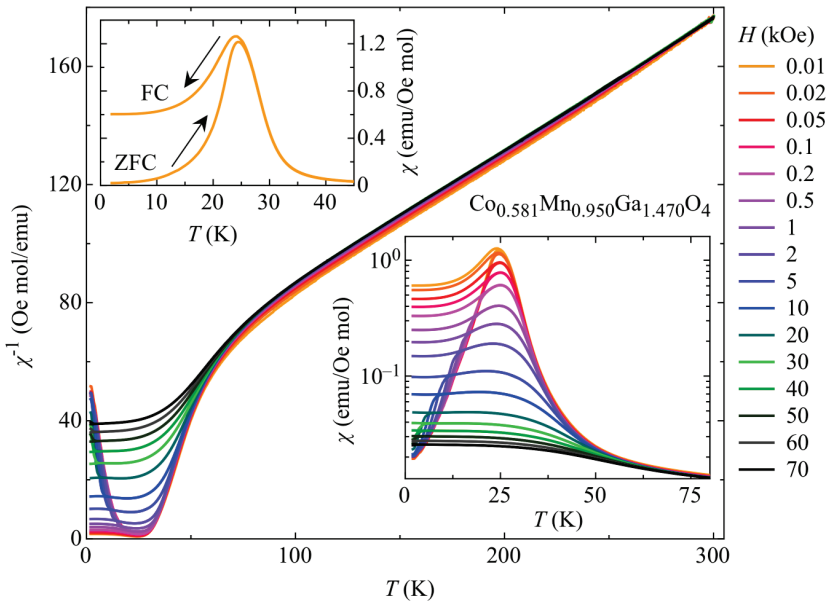

Figure 5.43. Temperature-dependent magnetic susceptibility χ_m measured in various magnetic fields for $Co_{0.58}Mn_{0.95}Ga_{1.47}O_4$. Main graph: inverse magnetic susceptibility; lower right: low temperature regime; upper left: different cooling procedures used.

All in all, nanoscale Co-Mn-Ga WOC is available from air-stable precursors with a quick MW-HT approach, and the new photocatalyst type excels through robust operation under visible light irradiation. The as-synthesized catalyst can be used right away with no need for thermal post-treatment. The combination of mixed M(II)/M(III) (M = Co, Mn) valence states on the surface of as-synthesized Co-Mn-Ga spinel probably enhances the catalytic activity with respect to the binary Co-Ga and Mn-Ga catalysts by favoring synergistic interactions between the two types of catalytic centers.

Synthetic flexibility and tunability of the spinel host lattice now leave room for optimization of this principle, thus rendering the Co-Mn-Ga WOCs promising prototypes for large scale water splitting applications. Further mechanistic investigations on the Co-Mn interaction are in progress.

References

[1] L. Y. Chen, T. Horiuchi, T. Mori, *Appl. Catal. A* **2001**, *209*, 97.
[2] X. T. Ge, D. R. Fang, X. Q. Liu, *Acta Phys.-Chim. Sinica* **2005**, *21*, 10.
[3] I. Katayama, N. Kemori, Z. Kozuka, *J. Chem. Thermodyn.* **1979**, *11*, 757.
[4] W. Laqua, S. Dudda, B. Reuter, *Mater. Res. Bull.* **1984**, *19*, 339.
[5] M. Lenglet, A. Dhuysser, C. K. Jorgensen, *Eur. J. Solid State Inorg. Chem.* **1994**, *31*, 277.
[6] M. Lenglet, F. Hochu, J. Durr, M. H. Tuilier, *Solid State Comm.* **1997**, *104*, 793.
[7] S. Mathur, S. Barth, H. Shen, *Chem. Vap. Dep.* **2005**, *11*, 11.
[8] A. Pajaczkowska, O. Demelo, F. Leccabue, C. Pelosi, D. Fiorani, A. M. Testa, E. Paparazzo, *J. Cryst. Growth* **1990**, *104*, 498.
[9] F. N. Sayed, O. D. Jayakumar, C. Sudakar, R. Naik, A. K. Tyagi, *J. Nanosci. Nanotechnol.*, *11*, 3363.
[10] J. M. Shi, W. T. Yu, I. Bergmann, H. Bremers, V. Sepelak, W. Mader, K. D. Becker, *J. Alloys Comp.* , *504*, S432.
[11] H. Xue, Z. H. Li, Z. X. Ding, L. Wu, X. X. Wang, X. Z. Fu, *Cryst. Growth. Des.* **2008**, *8*, 4511.
[12] H. Xue, Z. H. Li, L. J. Zhu, *Chinese Journal of Structural Chemistry*, *29*, 1828.
[13] M. Zinkevich, S. Geupel, F. Aldinger, *J. Alloys Comp.* **2005**, *393*, 154.
[14] Y. Sakata, Y. Matsuda, T. Yanagida, K. Hirata, H. Imamura, K. Teramura, *Catal. Lett.* **2008**, *125*, 22.
[15] W. Xiao, L. Wang, L. Xu, Q. Wana, B. S. Zou, *Scripta Mater.* **2009**, *61*, 477.
[16] H. Xue, Z. Li, L. ZHU, *Chinese J. Struct. Chem.* **2010**, *29*, 1828.
[17] S. Greenwald, S. J. Pickart, F. H. Grannis, *J. Chem. Phys.* **1954**, *22*, 1597.
[18] J. Topfer, A. Feltz, D. Graf, B. Hackl, L. Raupach, P. Weissbrodt, *Phys. Stat. Solidi A* **1992**, *134*, 405.
[19] L. M. B. Alldredge, R. V. Chopdekar, B. B. Nelson-Cheeseman, Y. Suzuki, *Appl. Phys. Lett.* **2006**, *89*.
[20] J. M. G. Amores, V. S. Escribano, G. Busca, E. F. Lopez, M. Saidi, *J. Mater. Chem.* **2001**, *11*, 3234.
[21] J. Ghose, *J. Solid State Chem.* **1989**, *79*, 189.
[22] J. Ghose, G. C. Hallam, D. A. Read, *J. Phys. C - Solid State Phys.* **1977**, *10*, 1051.
[23] C. C. Huang, C. H. Su, M. Y. Liao, C. S. Yeh, *Phys. Chem. Chem. Phys.* **2009**, *11*, 6331.
[24] F. Leccabue, R. Panizzieri, B. E. Watts, D. Fiorani, E. Agostinelli, A. Testa, E. Paparazzo, *J. Cryst. Growth* **1991**, *112*, 644.
[25] C. H. Weng, C. C. Huang, C. S. Yeh, G. B. Lee, *2009 4th Ieee International Conference on Nano/Micro Engineered and Molecular Systems, Vols 1 and 2* **2009**, 219.
[26] C. H. Weng, C. C. Huang, C. S. Yeh, H. Y. Lei, G. B. Lee, *Microfluidics and Nanofluidics* **2009**, *7*, 841.
[27] K. Beckmann, H. Uchtenhagen, G. Berggren, M. F. Anderlund, A. Thapper, J. Messinger, S. Styring, P. Kurz, *Energy Environ. Sci.* **2008**, *1*, 668.
[28] V. B. R. Boppana, F. Jiao, *Chem. Comm.* **2011**, *47*, 8973.
[29] R. Brimblecombe, A. Koo, G. C. Dismukes, G. F. Swiegers, L. Spiccia, *J. Am. Chem. Soc.* **2010**, *132*, 2892.
[30] R. Brimblecombe, A. Koo, G. C. Dismukes, G. F. Swiegers, L. Spiccia, *ChemSusChem* **2010**, *3*, 1146.
[31] J. M. Cerrato, M. F. Hochella, W. R. Knocke, A. M. Dietrich, T. F. Cromer, *Environ. Sci. Technol.* **2010**, *44*, 5881.
[32] Y. Gorlin, T. F. Jaramillo, *J. Am. Chem. Soc.* **2010**, *132*, 13612.
[33] D. M. Robinson, Y. B. Go, M. Greenblatt, G. C. Dismukes, *J. Am. Chem. Soc.* **2010**, *132*, 11467.
[34] F. Zhang, C. W. Cady, G. W. Brudvig, H. J. M. Hou, *Inorg. Chim. Acta* **2011**, *366*, 128.
[35] B. Bocher, A. G. Herpin, A. Oles, *J. Appl. Phys.* **1966**, *37*, 960.
[36] B. Boucher, A. Oles, *J. Physique* **1966**, *27*, 51.

[37] P. G. Casado, I. Rasines, *Z. Kristall.* **1982**, *160*, 33.
[38] V. S. Escribano, E. F. Lopez, P. S. Huidobro, M. Panizza, C. Resini, J. M. Gallardo-Amores, G. Busca, *Solid State Sci.* **2003**, *5*, 1481.
[39] H. Hayashi, R. Huang, H. Ikeno, F. Oba, S. Yoshioka, I. Tanaka, S. Sonoda, *Appl. Phys. Lett.* **2006**, *89*.
[40] H. Hayashi, R. Huang, F. Oba, T. Hirayama, I. Tanaka, *J. Mater. Sci.*, *46*, 4169.
[41] R. Huang, H. Hayashi, F. Oba, I. Tanaka, *J. Appl. Phys.* **2007**, *101*.
[42] J. Y. Lee, D. S. Kim, C. W. Na, J. Park, *J. Phys. Chem. C* **2007**, *111*, 12207.
[43] Y. P. Song, P. W. Wang, X. Y. Xu, Z. Wang, G. H. Li, D. P. Yu, *Phys. E - Low-Dimens. Sys. Nanostruct.* **2006**, *31*, 67.
[44] J. H. Kim, K. H. Yoon, *J. Korean Phys. Soc.* **2008**, *53*, 818.
[45] F. Jiao, H. Frei, *Energy Environ. Sci.* **2010**, *3*, 1018.
[46] M. M. Najafpour, T. Ehrenberg, M. Wiechen, P. Kurz, *Angew. Chem. Int. Ed.* **2010**, *49*, 2233.
[47] C. Luo, Rheinisch-Westfälische Technische Hochschule (Aachen), **2005**.
[48] N. W. Ashcroft, N. D. Mermin, *Festkörperphysik*, Oldenbourg, **2001**.
[49] V. Artero, M. Chavarot-Kerlidou, M. Fontecave, *Angew. Chem. Int. Ed.* **2011**, *50*, 7238.
[50] M. W. Kanan, Y. Surendranath, D. G. Nocera, *Chem. Soc. Rev.* **2009**, *38*, 109.
[51] F. Jiao, H. Frei, *Angew. Chem. Int. Ed.* **2009**, *48*, 1841.
[52] A. Anichini, P. Porta, *Acta Cryst. A* **1975**, *31*, S84.
[53] C. O. Arean, E. G. Diaz, *Mater. Chem.* **1982**, *7*, 675.
[54] U. Bhattacharya, V. S. Darshane, *J. Mater. Chem.* **1993**, *3*, 299.
[55] D. Fiorani, S. Viticoli, *Solid State Comm.* **1978**, *25*, 155.
[56] W. E. Kramer, A. M. Stewart, R. H. Hopkins, *J. Cryst. Growth* **1985**, *73*, 329.
[57] F. Leccabue, C. Pelosi, E. Agostinelli, V. Fares, D. Fiorani, E. Paparazzo, *J. Cryst. Growth* **1986**, *79*, 410.
[58] K. I. Lilova, A. Navrotsky, B. C. Melot, R. Seshadri, *J. Solid State Chem.* **2010**, *183*, 1266.
[59] S. Mathur, C. Cavelius, H. Shen, *Ze. Anorg. Allg. Chem.* **2009**, *635*, 2106.
[60] B. C. Melot, K. Page, R. Seshadri, E. M. Stoudenmire, L. Balents, D. L. Bergman, T. Proffen, *Phys. Rev. B* **2009**, *80*.
[61] A. Nakatsuka, Y. Ikeda, N. Nakayama, T. Mizota, *Acta Cryst. Sec. E - Struct. Rep. Onl.* **2006**, *62*, I109.
[62] M. Ogata, H. Kozaka, N. Uryu, *Phys. Stat. Solidi B - Bas. Res.* **1985**, *127*, K33.
[63] G. R. Patzke, J. Koepke, M. Binnewies, *Z. Anorg. Allg. Chem.* **2000**, *626*, 1482.
[64] J. L. Soubeyroux, D. Fiorani, E. Agostinelli, *J. Magnet. Magn. Mater.* **1986**, *54-7*, 83.
[65] R. Eisenberg, H. B. Gray, *Inorg. Chem.* **2008**, *47*, 1967.
[66] A. Kudo, Y. Miseki, *Chem. Soc. Rev.* **2009**, *38*, 253.
[67] H. Dau, C. Limberg, T. Reier, M. Risch, S. Roggan, P. Strasser, *ChemCatChem* **2010**, *2*, 724.
[68] F. Cheng, J. Shen, B. Peng, Y. Pan, Z. Tao, J. Chen, *Nature Chem.* **2011**, *3*, 79.
[69] H. Bordeneuve, S. Guillemet-Fritsch, A. Rousset, S. Schuurman, V. Poulain, *J. Solid State Chem.* **2009**, *182*, 396.
[70] D. Reinen, O. Schmitzdumont, *Z. Anorg. Allg. Chem.* **1961**, *312*, 121.
[71] K. Ikarashi, J. Sato, H. Kobayashi, N. Saito, H. Nishiyama, Y. Inoue, *J. Phys. Chem. B* **2002**, *106*, 9048.
[72] H. Xue, Z.-h. Li, L.-J. Zhu, *Chin. J. Struct. Chem.* **2010**, *29*, 1828.
[73] T. Hisatomi, K. Miyazaki, K. Takanabe, K. Maeda, J. Kubota, Y. Sakata, K. Domen, *Chem. Phys. Lett.* **2010**, *486*, 144.
[74] K. Maeda, K. Teramura, D. L. Lu, T. Takata, N. Saito, Y. Inoue, K. Domen, *Nature* **2006**, *440*, 295.
[75] I. Bilecka, M. Niederberger, *Nanoscale* **2010**, *2*, 1358.
[76] F. Conrad, Y. Zhou, M. Yulikov, K. Hametner, S. Weyeneth, G. Jeschke, D. Guenther, J.-D. Grunwaldt, G. R. Patzke, *Eur. J. Inorg. Chem.* **2010**, 2036.
[77] Y. Zhou, K. Vuille, A. Heel, B. Probst, R. Kontic, G. R. Patzke, *Appl. Catal. A - General* **2010**, *375*, 140.
[78] V. d. Castro, G. Polzonetti, *J. Electron Spectrosc. Rel. Phenom.* **1989**, *48*, 117.
[79] H. Zhang, Z. Zhan, X. Liu, *J. Power Sources* **2011**, *196*, 8041.
[80] T. Ressler, *J. Phys. IV* **1997**, *C2–7*, 269.
[81] S. K. Tripathy, M. Christy, N.-H. Park, E.-K. Suh, S. Anand, Y.-T. Yu, *Mater. Lett.* **2008**, *62*, 1006.
[82] B. Zapata, M. A. Valenzuela, P. Bosch, G. Fetter, I. Córdova, S. O. Flores, A. Vázquez, *J. Metastab. Nanocryst. Mater.* **2004**, *20-21*, 163.

6 *In situ* investigations of microwave-hydrothermal processes

6.1 Introduction and scope of the project

The results of the previous Chapter reveal that microwave-assisted techniques provide access to otherwise elusive nanomaterials on a rapid timescale. In order to control their large-scale technological application, we need to understand their reaction pathways and mechanisms. Reaction parameters, e.g. temperature, time as well as set-up and power of the microwave oven are important factors for successful syntheses and therefore need to be investigated to understand reaction mechanisms taking place in the "black box" microwave. Only few investigations with hypotheses for the reaction pathways especially for inorganic materials were reported applying microwave-assisted techniques.[1-6] Anyhow, often indirect observation such as changes in side products or solvents, which can be monitored with standard analytical methods (IR spectroscopy), are the basis of mechanistic proposals.[7] The MW-assisted oxidation of primary and secondary alcohols was observed with an IR thermovision camera.[8, 9] The disadvantage of such temperature observations with the assistance of external IR sensors or with a fiber-optic from the inside of the reaction vessel – as also applied for the reactions reported in this thesis – is the measurement of the average bulk temperature. The surface temperature of the solids might be completely different.

In Chapter 1.1.6 the superheating and non-thermal effects which influence the formation of nanostructured α-Fe_2O_3 rings were briefly introduced[3] and they were explained with the possible occurrence of "hot spots". This raises the question: "What are hot spots or non-thermal effects and what is their influence?"

A special microwave effect caused by dielectric heating is the so-called superheating which is equal to a rapid temperature increase that is not achievable with conventional heating methods.[10] Some solvents will reach boiling temperatures under microwave irradiation up to 40 °C above their classical boiling point at standard conditions.[11] The superheating phenomena can be reduced if the reaction mixture is stirred during the reaction. Additionally, *molecular radiators* influence the heating and therefore the products. Such microscopic hot spots are produced if a component within the reaction mixture is selective-

ly heated because it couples with the microwaves and all other components are not affected. The heat transfer to all components is realized by the *molecular radiator*.[10]

In heterogeneous reaction mixtures, in particular if solids are involved, a selective heating in macroscopic areas may occur which results in hot spots with temperatures of 100 - 150 °C above that of the bulk[12] and can easily reach temperatures up to 1000 °C.[10, 13] Investigations in MW-assisted organic syntheses are easier to realize as for inorganic reaction which is reflected in numerous publications.[10, 12, 14]

All in all, the above mentioned investigations are indirect and thus provide only limited information of the reaction mechanism. *In situ* measurements – with real time observations – are necessary to understand reactions which are carried out in the "black box" microwave. Recently, the first *in situ* experiments (e.g. XRD, EXAFS) were reported for MW-assisted synthesis of inorganic compounds. [1, 4-6, 15]

The syntheses for the nanostructured gallium oxides reported in Chapters 2-5 were performed hydrothermally in a sealed vessel. This combination of hydrothermal and microwave-assisted syntheses makes *in situ* experiments even more difficult because laboratory microwave ovens are difficult to place inside a X-ray or synchrotron beam which is necessary for *in situ* XRD or EXAFS measurements, respectively. The conventional vessels used for microwave-hydrothermal reactions are not suitable for *in situ* measurements because the walls are too thick and in combination with the Teflon® material the beam would not pass through. Therefore, a new vessel was developed as can be seen in Figure 6.1. The vessel is adopted from PARR steel autoclaves: the material was changed to PEEK (polyetheretherketone), the wall thickness at the lower part of the vial was reduced to 2 mm and the diameter of the vessel was decreased to 1 cm. With this design the synchrotron beam during the *in situ* EXAFS experiments should be able to penetrate the reaction vessel.

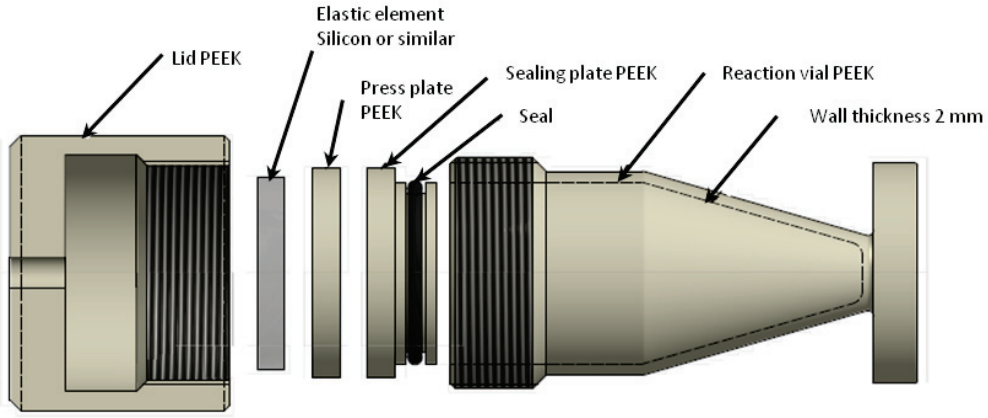

Figure 6.1. Newly designed PEEK vessel for *in situ* EXAFS measurements.

The space within a synchrotron beamline is limited and the microwave oven used for the herein reported spinels would not fit in between the experimental EXAFS set up. Therefore, a smaller microwave oven (WaveBox®, cf Figure 6.2) was applied: commonly used camping microwaves have small dimensions (38x27x26 cm outer and 25x17x25 cm inner) with power of 660 W and have three different possible power supplies (standard, 12 V and car battery). As an adaptation to the EXAFS beamline two holes need to be drilled in the front and back side so that the synchroton beam can pass through. Scanning the reaction mixture in different areas of the autoclave (heights) would give information of solid and liquid phases and therefore a more detailed picture of the reaction mechanism.

Figure 6.2. Small microwave oven for *in situ* EXAFS measurements.

6.2 Nanoscale $ZnGa_2O_4$

For first experiments a standard protocol for the formation of $ZnGa_2O_4$ was adopted and carried out for 6 min (for details see Experimental in Chapter 7). The *in situ* vessel was placed in the middle of the WaveBox®. Within these 6 min of reaction time a phase pure and crystalline $ZnGa_2O_4$ product could be obtained which was confirmed with X-ray diffraction (cf. Figure 6.3 left, ICSD card 38-1240). The particles show spherical morphology with particle sizes between 10 - 20 nm which agglomerate to spheres with diameters around 600 nm as can be seen in Figure 6.3 (right).

Even though this set-up produced phase pure material within short reaction times, the shape of the newly designed vessel requires further development to minimize superheating at the border from the cylindrical to the straight part. Additionally, the combination of vessel and microwave (no stirring option included and pulse width modulation type) should be optimized as outlined below.

Notice: The as-designed vessel (Figure 6.1) should not be employed for further reactions due to safety reasons (cf. outlook below).

The preparative results can however be considered as a basic step towards *in situ* EXAFS investigations. Further experiments could not be realized in time for this thesis.

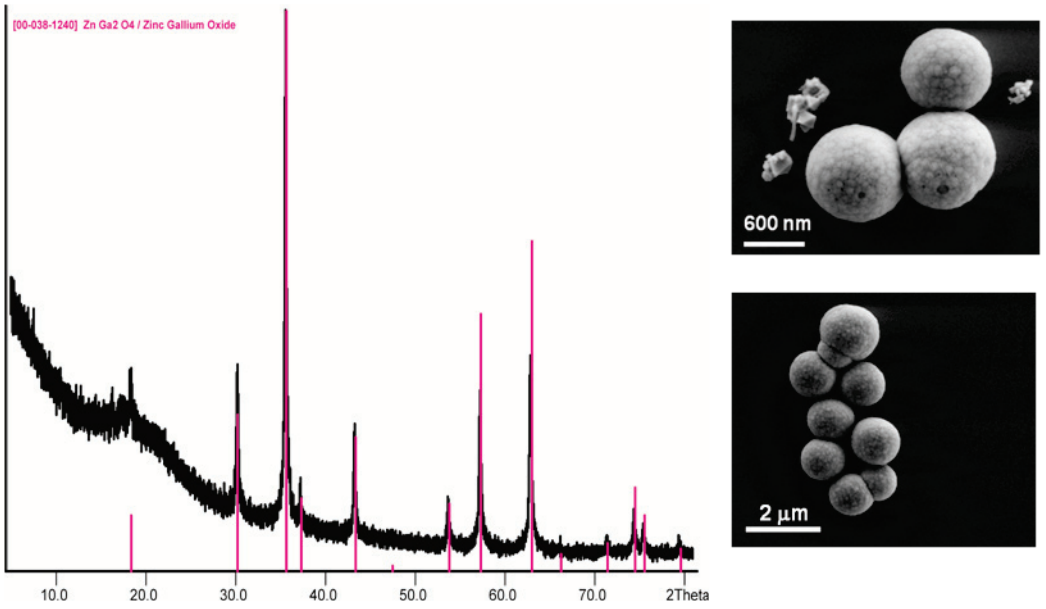

Figure 6.3. XRD pattern (left) and representative SEM images (right) of $ZnGa_2O_4$ synthesized in the *in situ* vessel using the WaveBox®.

6.3 Outlook

Special attention needs to be placed on the microwave device. Several parameters like a homogeneous radiation or the correct position of the vessel within the oven are essential for a successful synthesis. Critical points and ideas for microwave set-ups are presented in the following points which were developed in discussion with Dr. Andreas Hintennach (Massachusetts Institute of Technology, MIT).[16]

- Pulse width modulation (oven is turned on and off for a couple of seconds) applied in conventional microwave devices is not an optimal solution for laboratory experiments. The temperature increases rapidly and decreases in stationary phases which liquids may compensate up to the boiling point.
- Inverted power regulated microwaves irradiate constantly by either pulse width modulation in split seconds or amplitude variation and therefore allow much better temperature control.
- Mono-mode microwave ovens used in laboratories have homogenous field distribution which is obtained trough reflectors or different arrangements of magneton and the ergonomically shaped casing.
- A turntable contributes to a homogenous irradiation as well. For reproducibility reasons, a reaction vessel should be placed at the same position and off-centered to pass different areas of microwave fields. To overcome problems with stagnant moving turntables, antennas or reflectors in the internal space are applied to ensure a homogeneous field.
- The absorption of water in a beaker will reduce microwave power and cause less rapid temperature increase (defined amount of water for reproducibility).
- Home-made stirring assistances for a homogenous heat distribution: a) an impeller wheel (water flow controller) is fixed on the bottom of the microwave device and attached to a flexible shaft holding a stirring bar (movement through pressurized air) or b) a swing (2 - 3 synthetic filaments fed trough holes in the microwave device are attached to a windscreen wiper) realizes movement.
- Power recording is needed for pulsed microwaves: switching the magneton on and off may influence the reaction.

In any case, movement of the vessel will prevent or at least reduce the possibility of hot spots and boiling delays and additionally enable homogeneous heat distribution throughout the reaction vial.

In summary, the microwave device for laboratory – including *in situ* – experiments need to be carefully chosen to obtain safely the desired products with high reproducibility. The frequently reported hot spots or boiling delays as well as the reaction mechanism itself require *in situ* measurements to obtain in-depth knowledge. This is crucial for the understanding of microwave-assisted synthesis and their development towards industrial scales.

References

[1] T. Ahnfeldt, J. Moellmer, V. Guillerm, R. Staudt, C. Serre, N. Stock, *Chem. Eur. J.* **2011**, *17*, 6462.
[2] M. Feyand, C. Nather, A. Rothkirch, N. Stock, *Inorg. Chem.* **2010**, *49*, 11158.
[3] X. L. Hu, J. C. Yu, J. M. Gong, Q. Li, G. S. Li, *Adv. Mater.* **2007**, *19*, 2324.
[4] Y. Zhou, E. Antonova, W. Bensch, G. R. Patzke, *Nanoscale* **2010**, *2*, 2412.
[5] Y. Zhou, J.-D. Grunwaldt, F. Krumeich, K. Zheng, G. Chen, J. Stoetzel, R. Frahm, G. R. Patzke, *Small* **2010**, *6*, 1173.
[6] Y. Zhou, N. Pienack, W. Bensch, G. R. Patzke, *Small* **2009**, *5*, 1978.
[7] I. Bilecka, P. Elser, M. Niederberger, *ACS Nano* **2009**, *3*, 467.
[8] D. Bogdal, M. Lukasiewicz, J. Pielichowski, A. Miciak, S. Bednarz, *Tetrahedron* **2003**, *59*, 649.
[9] M. Lukasiewicz, D. Bogdal, J. Pielichowski, *Adv. Syn. Catal.* **2003**, *345*, 1269.
[10] C. O. Kappe, A. Stadler, *Microwaves in Organic and Medicinal Chemistry*, Wiley-VCH, Weinheim, **2005**.
[11] F. Chemat, E. Esveld, *Chem. Eng. Technol.* **2001**, *24*, 735.
[12] X. L. Zhang, D. O. Hayward, D. M. P. Mingos, *Catal. Lett.* **2003**, *88*, 33.
[13] A. Loupy, *Microwaves in Organic Synthesis*, WILEY-VCH, Weinheim, **2006**.
[14] K. D. Raner, C. R. Strauss, R. W. Trainor, J. S. Thorn, *J. Org. Chem.* **1995**, *60*, 2456.
[15] M. Feyand, C. Nather, A. Rothkirch, N. Stock, *Inorg. Chem.* **2011**, *49*, 11158.
[16] A. Hintennach, **2010**.

7 Experimental section

7.1 Synthetic conditions

7.1.1 General synthetic procedure

The starting materials (details for each Chapter see below) with a metal ratio M:Ga of 1:2 were dissolved in deionized water. The pH of the stirred solution was adjusted with aqueous ammonia (25 % NH_3, Merck) or freshly prepared 4 M NaOH solution (from pellets, Acros Organics, > 97 %). All products were washed after synthesis with deionized water, vacuum filtrated and dried in air at 80 °C for 1 h.

Chapter 2

Gallium sulfate ($Ga_2(SO_4)_3 \cdot xH_2O$, Aldrich, > 99.995 %), zinc sulfate ($ZnSO_4 \cdot 7H_2O$, Fluka, > 99.5 %) and different amounts of $CuCl_2 \cdot 2H_2O$ for the formation of solid solutions ($CuCl_2 \cdot 2H_2O$, Fluka, > 99 %) where used. The initial copper content of the samples is indicated as follows in the sample nomenclature: $ZnGa_2O_4:Cu^{2+}$_n with n representing the at % of Cu^{2+} ions related to the total metal ion content.

Chapter 3

Zinc nitrate ($Zn(NO_3)_2 \cdot 6H_2O$, Sigma-Aldrich, ≥ 99 %) as well as copper nitrate ($Cu(NO_3)_2 \cdot 3H_2O$, Carl Roth,≥ 99 %) and aluminum nitrate ($Al(NO_3)_3 \cdot 9H_2O$, Sigma-Aldrich, ≥ 98.5 %) were mixed with a nominal Cu:Zn:Al-ratio of ¼:¾:2 without further purification. The nitrates were dissolved in micropore filtrated water. 50 ml of the suspension was immediately transferred into microwave Teflon® vessels (DAP-80+) for MW treatment. After cooling, all products were washed with deionized water, vacuum filtered and dried in a muffel furnace at 80 °C for 2 h. Samples are labeled in Chapter 3 as follows: Metal_[pH value]_base_[time in h].

Chapter 4

Gallium nitrate ($Ga(NO_3)_3 \cdot xH_2O$, Aldrich, 99.9 %), copper nitrate ($Cu(NO_3)_2 \cdot 3H_2O$, Sigma-Aldrich, > 99 %) or gallium sulfate ($Ga_2(SO_4)_3 \cdot xH_2O$, Aldrich, 99.99 %) and copper chloride ($CuCl_2 \cdot 2H_2O$, Fluka, > 99 %) were used for the synthesis copper substituted $ZnAl_2O_4$ spinels.

Chapter 5

Gallium nitrate ($Ga(NO_3)_3 \cdot xH_2O$, Aldrich, 99.9 %) was mixed with manganese sulfate ($MnSO_4 \cdot 4H_2O$, Analar, > 97 %) and cobalt nitrate ($Co(NO_3)_2 \cdot 6H_2O$, Fluka, > 98 %) without further purification and the metal ratio (Ga:X) was adjusted to 2:1. For the mixed CoMn spinel a Co:Mn:Ga metal ratio of 1:1:4 was selected. The obtained products were centrifuged several times for 10 min each (5000 rpm, Eppendorf 5804).

Chapter 6

The *in situ* microwave experiments were carried out in the special vessel reported in Chapter 6. Therefore, 58 mg of $ZnSO_4 \cdot 7H_2O$ were dissolved in 15 ml H_2O and mixed with 148 mg $Ga_2(SO_4)_3 \cdot xH_2O$. The initial pH was adjusted with aqueous ammonia (25 %). The sealed vessel was placed in the middle of the WaveBox® microwave and the program "popcorn" chosen which is equally with a full power (660 W) synthesis of 6 min duration. The final product was washed several times with destilled water and dried in air for 1 h at 80 °C.

7.1.2 Microwave-hydrothermal synthesis

The starting materials were mixed in a 95 ml CEM Omni Teflon® vessel, thoroughly stirred and the pH value adjusted as described above.

Afterwards the reactions were carried out in a MARS5 microwave (CEM cooperation) at 2.45 GHz and a power of 1600 W with five vessels per synthesis run. The only exception is the $ZnGa_2O_4:Cu^{2+}$_25(12) sample reported in Chapter 2 where 12 vessels were used simultaneously. A ramp to temperature mode with different ramp times (referred to as r) was chosen for heating followed by a constant temperature period (abbreviated as holding time h) and finalized by a 30 min cool down period. Pressure and temperature control was ensured by a reference vessel equipped with appropriate sensors and additionally temperature control of all vessels maintained by IR sensors whereas overheating was prevented by constantly stirring the reaction mixture and automatic power adjustment to stabilize the temperature in a ± 5 °C interval.

Chapter 3

The suspension was heated within 30 min up to 150 °C in a speedwave™ MWS-3+ Microwave Digestion System (Berghof) at 2.45 GHz and a power of 1450 W. The reaction temperature was kept constant for 1 or 2 h, followed by a 30 min cooling period.

7.1.3 Conventional-hydrothermal synthesis

The above-mentioned precursors were mixed in a 23 ml stainless steel autoclave equipped with a Teflon® liner and heated to the desired temperature (normally 180 °C) for 48 h in a laboratory furnace (BINDER, FD 53), cooled down naturally to RT, followed by workup as described above in 7.1.1.

Chapter 3

For conventional solid state synthesis of $ZnAl_2O_4:Cu^{2+}$, the same precursor solution was adjusted to the respective pH value (see 7.1.1 and Chapter 3), filtrated on a Buchner funnel and washed with deionized water, followed by calcination at 500 °C for 3 h with a heating rate of 2 K/min.

7.1.4 Calcination post-treatment

To improve the crystallinity, the Co and Mn containing gallium oxide samples were calcinated in a tube furnace (Nabertherm RHTH 40-600/16) in nitrogen for 4 h. Samples were thoroughly grinded and placed in an alumina crucible which was transferred into the tube, flushed with nitrogen for 2 h and slowly heated to the desired temperature (100 °C/h).

7.2 Analytical characterizations

7.2.1 Structural investigations

X-ray powder diffraction patterns (XRD)

X-ray powder diffraction patterns (XRD) were recorded on a STOE STADI P diffractometer equipped with a primary focusing germanium monochromator (Cu $K_{\alpha 1}$ radiation) and a linear position sensitive detector. Small amounts of powder were sandwiched between adhesive tape or between two layers of polyacetate film and fixed with a small

amount of X-ray amorphous grease for Al-containing sample reported in Chapter 3. In the later case, the signal appearing near 2θ = 18° in some of the XRD-patterns is caused by the grease used to fix the powder at the sample holder.

In situ XRD

In situ XRD of the reduction of sample Al_10_NaOH_1 was performed in two consecutive heating-cooling cycles with identical temperature programs. In order to distinguish between the effects of sintering and reduction of the material, the first (sintering) cycle was conducted in artificial air (20 % O_2 in He), while the second (reduction) cycle was performed in 5 % H_2 in He. Before and after each temperature treatment, the sample was characterized with an XRD scan at 25 °C (13 – 67° 2θ in steps of 0.02°, 2 sec/step). The temperature cycles were performed with ramp rates of 20 K/min and isothermal hold segments every 50 °C from 50 to 500 and back to 50 °C. Each hold segment consisted of a wait time of 5 min followed by an XRD scan (25 – 50° 2θ in steps of 0.02°, 2 sec/step), totaling to about 55 min per hold.

A similar strategy was pursued for the investigation of Ga_10.5_NH_3_1 with *in situ* XRD. Two identical consecutive heating-cooling cycles were performed, the first in He, the second in 5 % H_2 in He. Before and after each cycle, a long XRD scan (10 – 100° 2θ in steps of 0.02°, 15 sec/step) was performed at 25 °C. For the temperature programs, heating/cooling rates of 20 K/min were employed. Isothermal hold segments with a wait time of 5 min and two fast XRD scans (13 – 67° 2θ in steps of 0.02°, 2 sec/step) were performed every 50 °C in the range 100 – 400 – 100 °C (225 min/hold). As no irreversible changes of the lattice parameters were observed for the reduction cycle, a third cycle in 5 % H_2 in He was conducted in the temperature range 400 – 600 – 400 °C.

Neutron diffraction

The neutron diffraction experiment reported in Chapter 4 was performed at the high resolution two axis diffractometer D2b at ILL Grenoble. The room temperature measurement was done in a cylindrical vanadium container (~1.5 cm fill height) in high intensity mode at λ = 1.59 Å and for an acquisition time of about 4 h.

The neutron diffraction experiment in Chapter 5 was carried out with the high resolution powder diffractometer HRPT at the spallation neutron source SINQ (PSI-Villigen, Switzerland) with the neutron wavelength $\lambda = 1.1545$ Å at room temperature.

7.2.2 Materials composition and morphology investigations

Electron microscopy

The morphology of the substances was examined using scanning electron microscopy performed on a LEO 1530 (FEG) microscope. Samples were dispersed in ethanol and applied on a silicon wafer. Furthermore, the molar ratio of Zn, Cu, and Ga was assigned with EDXS investigations performed on a Zeiss SUPRA 50 VP microscope equipped with an EDAX detector.

For scanning transmission electron microscopy (STEM), the material was deposited on a perforated carbon foil supported on a molybdenum grid and investigated on a FEI CM30ST (LaB_6 cathode). In the STEM mode, the electron beam was placed on selected areas, and an elemental analysis by energy-dispersive X-ray spectroscopy (EDXS, EDAX detector) was performed there.

A Philips CM200FEG microscope operated at 200 kV and equipped with a field emission gun, Gatan imaging filter and energy-dispersive X-ray (EDX) analyzer was used for TEM investigations reported in Chapter 3. The coefficient of spherical aberration was $C_s = 1.35$ mm and the information limit better than 0.18 nm. High-resolution images were taken at a magnification of 1083000× with a CCD camera and selected areas were processed to obtain the power patterns (square of the Fourier transform of the image), which were used for measuring interplanar distances (± 0.5 %) and angles (± 0.5°) for phase identification.

Focused ion bombardment (FIB) coupled with SEM was conducted with a NVision40 instrument including secondary electron SE and backscattered electron BSE detectors (EDAX Genesis EDX-System). For imaging 1.5 - 2.0 kV and 15 kV for EDX analysis was conducted applying a 5 mm WD in high vacuum. Therefore the powder sample was dispersed on a Si-wafer on a SEM stub. FIB cross sections in shallow angle (12°) to the stub (using a 54° pre-tilted holder) were chosen and additionally EDX analysis with a cross

section surface in standard angle (54°) to the electron beam (no tilt corrections) was applied.

Elemental Analysis

Determination of the metal ratios was performed with LA-ICP-MS methods. The analyses of the pressed powder samples were carried out using an 193 nm ArF excimer laser ablation system (Lambda Physik, Göttingen, Germany) coupled to an ICP-MS (DRC II +, Perkin Elmer, Norwalk, USA). The samples were ablated for 40 s (5 Hz, 60 μm crater diameter) and the operating conditions are summarized in Table 7.1.

Table 7.1. Experimental parameters of LA-ICP-MS investigations.

Parameter	Value
Laser type	ArF excimer
Laser wavelength	193 nm
Spot diameter (sample and standard)	60 μm
Repetition rate (sample and standard)	5 Hz
Laser energy	9.3 J/cm^2
He carrier gas flow rate	1.1 l/min
RF power	1350
Nebulizer gas flow rate	0.84 l/min
Auxiliary gas flow rate	0.7 l/min
Coolant gas flow rate	17.5 l/min
Dwell time	10 ms
Detector mode	Dual (pulse and analog)

Further elemental analysis was performed with a pressure digestion method followed by ICP-OES. Therefore, 10 mg of the sample was dissolved in 3 ml HNO_3 (suboiled) and 100 μl HCl (Merck suprapure) and heated within 20 min to 100 °C, followed by heating to 200 °C within 40 min and holding of this temperature for 30 min. The solution was afterwards cooled to 20 °C within 80 min and diluted with millipore water to a volume of 100 g. The solution was analyzed with an ICP-OES spectrometer (SPECTRO ARCOS, SPECTRO Analytical Instruments GmbH, Kleve Germany) with the following devices details: 1400 W, 12 l/min Ar cooling gas, 1 l/min Ar help gas, 0.84 l/min atomizing gas and a crossflow atomizer. The measured element specific lines in nm were (repetition of each line three times): Co (230.786, 237.862, 238.892, and 282.616), Ga (141.44 and 417.206) and Mn (257.611, 259.373, 260.569 and 294. 921).

X-ray fluorescence (XRF) investigations reported in Chapter 3 were performed in He-atmosphere on a Sequential Pioneer S4 Spectrometer (Bruker) and the K lines of Cu and Zn were analyzed.

7.2.3 Materials properties investigations

TG/DSC

The TG/DSC investigations in Chapter 5 were carried out with a TG 449 Jupiter (Netzsch) in nitrogen atmosphere using different heating rates (5, 10 and 20 K/min). A dynamic heating was performed to 400 °C followed by a constant temperature mode for 2 h (400 °C) to completely remove any surface water. Afterwards, the samples were dynamically heated to 1400 °C and kept at this temperature for 2 h.

Surface Area

The specific surface area of the samples was investigated with an adsorption isotherm of nitrogen at 77 K based on the Brunauer-Emmett-Teller method (BET; Quadrasorb *SI*, Quantachrome). Therefore, the samples were degassed for 4 h at 150 °C.

Static nitrogen physisorption experiments of the Al-containing samples (Chapter 3) were performed in an Autosorb-1C setup (Quantachrome). Prior to the measurements, the samples were degassed for 2 h under dynamic vacuum at 80 °C. The data were analyzed according to BET theory using the multipoint method (11 points).

UV/Vis spectroscopy

For UV/Vis spectroscopy investigations reported in Chapter 2, the samples were well mixed with $MgSO_4$ (water free) by grinding and placed in a sample holder. The spectra were recorded using a Perkin Elmer Lambda 750 spectrometer with an integrating sphere setup (diameter 110 mm). The samples were measured against pure $MgSO_4$ as reference within the wavelength range of 250 to 1000 nm. The applied diffuse reflectance spectra are transformed into absorption spectra using the Kubelka-Munk function.

Otherwise, the samples were well ground and filled between two quartz object holders. Spectra were recorded in the 200 to 800 nm range on a Perkin Elmer Lambda 650 spectrometer with an integrating sphere setup (diameter 150 mm).

Magnetic measurements

Magnetisation measurements were performed using a Quantum Design SQUID Magnetometer MPMS XL. The magnetic field strength of 0.1 T was applied upon zero-field cooling the sample and the magnetic moment of the sample was subsequently determined as a function of temperature.

X-ray photoelectron spectroscopy (XPS)

X-ray photoelectron spectroscopy (XPS) measurements in Chapter 4 were performed on a Thermo Escalab 250 with $Al_{K\alpha}$ emission at 1486.6 eV. All binding energies were referenced to the C 1s peak (284.6 eV) arising from adventitious carbon. Powders of the investigated samples in Chapter 5 were suspended in ethanol and then dried on a glass plate so that dense areas of the coverage of the particles could be investigated. The used spectrometer is a Quantum 2000 Scanning XPS Microprobe from Physical Electronics that is operated with monochromatic Al K_α source. Both the grainy morphology of the samples as well as the risk of sputter damaging precluded the use of sputter cleaning. The measurements were taken with a 100 micrometer probe size and a power of 25 W. The pass energy was set to 58.7 eV. To minimize sample charging effects during the measurements, an electron flood gun operated at 2.5 eV and an ion neutralizer using Ar^+ of ca. 1 eV were used. These precautions minimize the fluctuations of the binding energy values due to charging to less than 1 eV.

To allow for unambiguous comparison the spectra within one set of spectra of a sample are aligned to C 1s being set at 284.8 eV, as recommended by an international standard [ASTM03]. The spectra were evaluated using Physical Electronics' software package Multipak (v. 8.2). The spectra of samples with a finite density of states at the valence band are fitted with asymmetric peak shape, while those showing insulating behavior are approximated by Gauss-Lorentz functions.

7.2.4 X-ray absorption spectroscopy

Chapter 2

Ex situ X-ray absorption spectroscopic data reported in Chapter 2 were recorded at beamline l811 at MAXLab (Lund, Sweden) using a Si(311) double crystal monochromator. The samples were pressed into self-supporting wafers with boron nitride and the Cu K- and Zn K-edge data were measured at 8.84 - 9.63 keV and 9.55 and 10.03 keV, respectively. All

spectra were taken in transmission mode. XANES and EXAFS analysis was performed using Winxas 3.1[1] and phase and amplitude functions were calculated using the Feff-code.[2] To keep the systematic error in the data analyzing procedure at the same level all data were treated similarly. Pre-edge background subtraction and normalization was carried out by fitting a linear polynomial to the pre-edge region and a cubic polynomial to the post-edge region of the absorption spectra. A smooth atomic background, $\mu_0(k)$, was obtained through cubic polynomial. After background removal, the data were transformed into k-space. Fourier transforms (FT) of Cu K-edge $\chi(k)$ were multiplied by k^3, typically from 2.5 $Å^{-1}$ to 11.8 $Å^{-1}$. Bessel window was used in the Fourier transform. The FEFF7 program package[3] was used to calculate phase and amplitude factors, followed by least-squares curve fitting of the data. The amplitude reduction factor was held constant to 0.87 (S_0^2), the value obtained from initial fits for a CuO FT EXAFS spectrum measured under the same experimental conditions. The error range of the S_0^2 was estimated as ± 0.01.

Chapter 3

XAS measurements were performed at beamline X1 at the Hamburger Synchrotron Strahlungslabor (HASYLAB) under ambient conditions. A Si(111) double crystal monochromator was used for measurements at the Cu (8.979 keV) and Ga K-edge (10.367 keV). The second monochromator crystal was tilt for optimal harmonic rejection. The solid samples were embedded in an oxygen free cellulose matrix and pressed into pellets. Data evaluation started with background absorption removal from the experimental absorption spectrum by subtracting a Victoreen-type polynomial. To determine the smooth part of the spectrum, corrected for pre-edge absorption, a piecewise polynomial was used. It was adjusted in such a way that the low-R components of the resulting Fourier transform were minimal. After division of the background–subtracted spectrum by its smooth part, the photon energy was converted to photoelectron wave numbers k. The resulting $\chi(k)$-function was weighted with k^3 and Fourier transformed using a Hanning window function. Data analysis was performed in k-space with Fourier filtered data according to the curved wave formalism of the EXCURV98 program with XALPHA phase and amplitude functions.[4, 5] The mean free path of the scattered electrons was calculated from the imaginary part of the potential (VPI set to –4.00 eV). An inner potential correction E_f was introduced when fitting experimental data with theoretical models that accounts for an overall phase shift between the experimental and calculated spectra. The amplitude reduction factor was determined by fitting a defined gallium oxide reference.

The measurements were performed at the XAS beamline at the Ångströmquelle Karlsruhe (ANKA). The synchrotron beam current was between 80 – 140 mA at 2.5 GeV storage ring energy. A Si(111) double crystal monochromator was used for measurements at the manganese (6.540 keV), cobalt (7.709 keV) and gallium (10.367 keV) K-edge. The second monochromator crystal was tilt for optimal harmonic rejection. Samples were pressed into pellets using cellulose as stabilizer. The amount of sample used was adjusted to an edge jump between 0.3 – 0.8. Data evaluation is similar to the one reported for Chapter 4. Additionally, to remove random noise, Fourier filtered spectra in the range of 1 – 4 Å (not phase corrected) were subjected to analysis, the number of independent parameters always being larger than the iterated ones.

7.2.5 Electron paramagnetic spectroscopy (EPR)

The continuous wave (CW) EPR spectra were measured at X-band with a Bruker ElexSys E500 spectrometer equipped with an ER 4122 SHQ resonator (Bruker Biospin, Germany, mw frequency 9.87 GHz). The W-band CW EPR measurements were recorded with a Bruker E680 spectrometer (Bruker Biospin, Germany, mw frequency 94 GHz). All EPR measurements were performed at room temperature.

7.3 Catalytic application investigations

7.3.1 Water oxidation

Photocatalytic O_2 evolution was performed using a well-reported $Ru^{2+}(bpy)_3$-$S_2O_8^{2-}$ method. Therefore a stirred suspension of catalyst (different concentration, see SI) with 4.85 mg $[Ru(bpy)_3]Cl_2$, 7.7 mg $Na_2S_2O_8$ in 6 ml buffered Na_2SiF_6 solution (20 mmol/l, Na_2SiF_6, pH 5.8) was purged with He for 40 min to remove oxygen in a 10 ml headspace vial (with aluminium crimp cap and rubber septum, BGB Analytik, Switzerland). The light source was a 476 nm high-flux LED from Rhopoint Components Ltd. (OTLH-0010-BU) with a CPC reflector for Shark LED, operated at usually 4650 lux respectively using a TES 1332A digital lux meter. In regular intervals 100 µL of the reaction headspace were sampled with a gas tight microliter syringe (Hamilton 1825 RN) using a gas chromatograph (Varian CP-3800) with He as carrier gas and a 3 m × 2 mm column packed with molecular sieve 13X 80-100. The gas flow was set to 20 ml/min. The oven was

operated isothermally at 100 °C. The gases were detected using a thermal conductivity detector (Varian) operated at 150 °C. Calibrations were performed by the injection of known quantities of pure oxygen diluted in a head space vial containing the same volume of solvent as used for measurements.

7.3.2 CO_2 hydrogenation and methanol steam reforming (MSR)

Temperature programmed reduction (TPR)

For temperature programmed reduction (TPR) measurements, the material was reduced in fixed bed reactor (CE instruments TPDRO-1100, 5 % H_2/Ar; 310 °C; 6 K/min; 30 min hold). H_2 consumption was monitored with a thermal conductivity detector. The copper surface area was determined in the same setup using N_2O reactive frontal chromatography (RFC) by monitoring the amount of evolved N_2 upon decomposition of N_2O at the Cu(0) surface at room temperature, which was quantified from the time interval of the frontal chromatogram of N_2 recorded at definded flow by mass spectrometry (i.e. the time interval between the onset of the N_2 peak and the detection of N_2O).[6, 7] For calculation of the copper surface area, a molar stochiometry of $Cu/N_2 = 2$ and a value of 1.46×10^{19} Cu atoms m^{-2} were used.[8]

CO_2 hydrogenation

Catalytic tests in CO_2 hydrogenation were carried out in a standard fixed bed, high pressure down-flow methanol synthesis reactor coupled to an Agilent 7890A Gas Chromatograph (GC). 1 g of the catalyst precursor was mixed with inert silica (Fluka Silica Gel 60). The mixture was loaded into the reactor and first reduced in 100 % H_2. The temperature was raised to 300 °C with a 2 K/min rate using a 100 cm^3/min gas flow and held constant at 300 °C for 90 min. The catalytic activity of the reduced catalyst was afterwards tested in the same reactor with a gas mixture of 24 % CO_2, 72 % H_2, 4 % Ar (200 cm^3/min; p = 50 bar) at 220 °C for 2 h and at 250 °C for another 2 h.

Methanol steam reforming (MSR)

Methanol steam reforming (MSR) tests were carried out in a silica-coated stainless steel plug-flow reactor system. A sieve fraction of 100 - 200 µm of the calcined samples (125 mg Al_10.5_NaOH_2 and 500 mg Ga_10.5_NH_3_1 catalyst) was diluted with 200 mg of inert graphite each. Before starting the steam reforming reaction both catalysts were reduced in hydrogen (10 % H_2 in N_2, 6 K/min to 300 °C for 5 h), then cooled to 260 °C

with 6 K/min in He/N_2. The gas flow was switched to $MeOH/H_2O$ (1:1) to run the MSR reaction at 260 °C for 20 h. The used nafion N_2-flow is approx. 90 cm^3/min and the flow of $MeOH/H_2O$ mixture was 0.01 cm^3/min. The formed products were analyzed by GC (CP 4900, Varian, Columns: Molsieve, PPU). Not converted water and methanol were removed prior to the GC using a cooling-trap and a Nafion membrane.

For both reactions conventionally prepared $Cu/ZnO/Al_2O_3$ catalysts were used as reference and tested under the same conditions.
Twenty identical samples of the $ZnGa_2O_4:Cu^{2+}$ catalyst were assembled for catalytic MSR tests.

7.3.3 Photocatalytic degradation of organic dyes

For rhodamine B (RhB) photodegradation experiments 50 mg of the catalyst was dispersed in RhB solution (150 ml, 5 ppm) by a ten minutes ultrasonic treatment. The reaction vessel was thermostated at 25 °C with a water cooling jacket. An air flow (100 ml/min) ensured a constant O_2 concentration of the stirred suspension. 10 light bulbs were arranged around the photoreactor vessel in a circular fashion. The following light bulbs were applied: a) Osram Dulux S 865 for the whole visable range, b) Osram Dulux S 67 blue with an emission maximum at 450 nm, c) a Philips PL-S 9W BLB/2P 1CT for investigations in the blacklight region and d) for irradation in deep UV a Philips TUV PL-S 9W/2P (all spectra a shown in Figure 7.1). At given time intervals 1.5 ml of the suspension was collected, the catalyst separated by centrifugation and the solution analyzed by recording the change of the RhB main peak with a Perkin-Elmer Lambda 650S spectrophotometer with a 150 mm integration sphere.

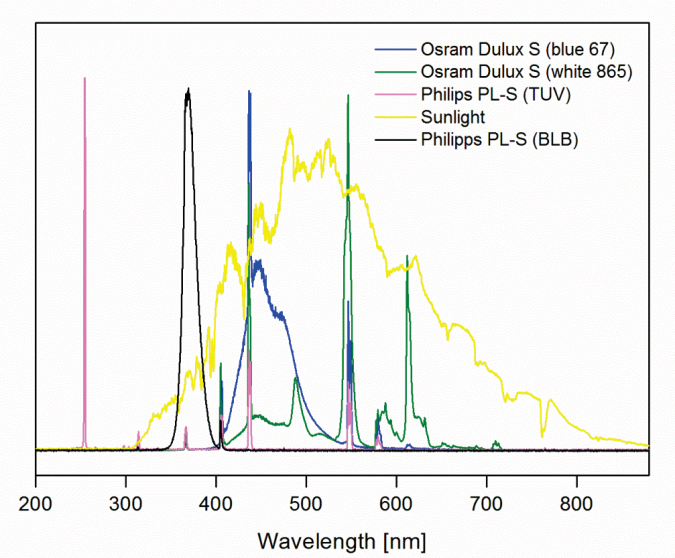

Figure 7.1. Spectra of all used light bulbs.

7.3.4 Gas sensor tests

The gas sensing tests were performed in the temperature range of the hot plate from room temperature to 300 °C. Note, that the thermal regulation accuracy is better than 0.4 °C. This is important to differentiate between temperature-induced or gas-induced variations of the resistance. Very low heating rates of 1 °C/min were used to ensure thermal homogeneity of sample and the thermometry block to consider the thermal mass of the holding glass substrate and sample holder. The sensing properties (the resistance) was monitored with the classic Agilent 34401 digtal multimeter, interfaced to a Labview acquisition programme.

References

[1] T. Ressler, *J. Synchrot. Rad.* **1998**, *5*, 118.
[2] M. Newville, *J. Synchrot. Radiat.* **2000**, *8*, 322.
[3] A. L. Ankudinov, J. J. Rehr, *Phys. Rev. B* **1997**, *56*, R1712.
[4] M. A. Awan, J. Hulliger, *J. Comb. Chem.* **2005**, *7*, 73.
[5] A. Sonnauer, N. Stock, *Eur. J. Inorg. Chem.* **2008**, 5038.
[6] G. C. Chinchen, C. M. Hay, H. D. Vandervell, K. C. Waugh, *J. Catal.* **1987**, *103*, 79.
[7] O. Hinrichsen, T. Genger, M. Muhler, *Chem. Eng. Technol.* **2000**, *23*, 956.
[8] R. M. Dell, F. S. Stone, P. F. Tiley, *Trans. Faraday Soc.* **1953**, *49*, 195.

Summary

The wide application possibilities of oxidic nanomaterials, e.g. as photocatalysts or as solid oxide fuel cells, may solve global environmental problems of the 21st century. Further development of synthetic methods to tune nanomaterials is required to achieve this challenging goal. Therefore, special emphasis must be placed on optimization of synthetic parameters, such as reaction time or temperature, in order to address phase, composition and morphology of oxide nanomaterials in a controlled manner.

This thesis presents a detailed survey of the challenging synthesis and application potential of nanostructured spinel type gallium oxides in combination with transition metals. Promising catalytic results could be obtained for different catalytic reactions, such as methanol steam reforming, CO_2 hydrogenation and water oxidation. The results demonstrate that solid state spinels as nanostructured materials are promising candidates for solving important environmental problems of modern society.

The nanoscale gallium oxide spinels under investigation were mainly synthesized via state-of-the art microwave-assisted techniques. The advantages of this novel synthetic route over conventional hydrothermal and solid state methods are intensively discussed throughout this study: MW-HT syntheses are energy-, cost- and time-saving through dramatically increased crystallization kinetics and the possible access to novel or metastable phases, such as γ-Ga_2O_3 spinels (Chapter 4).

The challenging incorporation of active copper centers into the $ZnGa_2O_4$ or γ-Ga_2O_3 spinel matrix is an important step for the development of novel catalyst prototypes. The copper ions within the spinel matrix serve as catalytic centers during the reductive conditions of methanol steam reforming and CO_2 hydrogenation. The successful syntheses of doped spinels as well as the catalytic investigations for the above mentioned important industrial processes of such copper and zinc containing gallium oxides are reported in Chapters 2-4. The limitations for substitution of zinc or gallium ions by copper species are discussed on the basis of structural and analytical investigations. Liquid ammonia as pH adjusting agent, for example, controls copper incorporation due to the formation of ammine complexes, whereas pH control with sodium hydroxide solution affords side products.

Moreover, the potential application of transition metal oxide nanomaterials – starting from manganese and iron over nickel to cobalt – in the area of photocatalytic water oxidation is another scope of this thesis (Chapter 5). The combination of cobalt and manganese within a gallium spinel matrix leads to ternary Co-Mn-Ga-oxide water oxidation catalysts with remarkably enhanced visible light driven photocatalytic activity in comparison to the respective Co-Ga- and Mn-Ga-spinels. The microwave-assisted synthesis of these 3d transition metal oxides proceeds on a minute scale for cobalt and manganese gallium oxides and first promising results could be obtained for nickel and iron spinels. Detailed structural investigations of the mixed nanostructured Co-Mn-Ga oxide by XAS and neutron diffraction afforded site occupancies, degree of inversion and chemical environment of the included cobalt, manganese and gallium ions. Magnetic measurements demonstrate a spin-glass state for $CoGa_2O_4$ as well as ferrimagnetic behavior for Mn-Ga spinel and the newly synthesized mixed Co-Mn-Ga spinel.

However, the optimization of manifold reaction parameters of inorganic microwave-assisted hydrothermal routes is the most challenging part and often requires extensive screening procedures to access the narrow appropriate parameter windows. This applies especially for the optimal pH value to access the herein reported gallium oxide spinels. To control the according formation pathways, detailed mechanistic knowledge about the MW-HT formation processes of oxide materials has to be achieved with new methods. This opportunity can be realized via *in situ* techniques which are the scope of Chapter 6. They afforded interesting and promising preliminary results that require further detailed investigations and technical optimizations for safe handling.

All in all, this thesis illustrates the successful application of state of the art microwave-assisted techniques for the one-step production of nanostructured transition metal containing gallium oxides. The obtained spinels were characterized with a wide arsenal of inorganic analytic methods focusing on structural features. Materials applications of the newly accessed nanoparticles such as (photo)catalytic activity for methanol steam reforming, CO_2 hydrogenation and water oxidation are promising for solving important environmental and energy-related questions of global relevance.

Zusammenfassung

Das weite Anwendungsspektrum oxidischer Nanomaterialien, beispielsweise als Photokatalysatoren oder Brennstoffzellen, kann bei der Lösung globaler Umweltprobleme des 21. Jahrhunderts helfen. Die Entwicklung synthetischer Methoden für die Optimierung von Nanomaterialien ist notwendig, um dieses anspruchsvolle Ziel zu erreichen. Demzufolge sollte der Fokus auf der Optimierung der synthetischen Parameter wie Reaktionszeit oder Temperatur gelegt werden, um oxidische Nanomaterialien hinsichtlich Phase, Zusammensetzung und Morphologie kontrolliert zu adressieren.

Diese Doktorarbeit gibt einen detaillierten Überblick der herausfordernden Synthese und des weiten Anwedungspotentials nanostrukturierter spinell-artiger Galliumoxide und deren Kombination mit Übergangsmetallen. Vielversprechende Ergebnisse konnten für diverse katalytische Reaktionen wie *methanol steam reforming*, CO_2 Hydrierung und Wasseroxidation erreicht werden. Die Resultate zeigen, dass spinell-artige Festkörper geeignete Kandidaten für nanostrukturierte Materialien sind, die umweltrelevante Probleme des heutigen Lebens lösen können.

Die untersuchten nanoskaligen Galliumoxide wurden hauptsächlich via hochmoderner mikrowellen-assistierter Techniken hergestellt. Die Vorteile dieser neuen synthetischen Route gegenüber konventionellen hydrothermalen Methoden und Festkörpersynthesen werden innerhalb dieser Studie detailliert diskutiert. So sind die MW-HT Synthesen energie-, kosten- und zeitsparend, was durch signifikant gesteigerte Kristallisationskinetiken ermöglicht wird. Weitherhin eröffnet sich der Zugang zu neuen oder metastabilen Phasen wie die in Kapitel 4 beschriebenen γ-Ga_2O_3 Spinelle.

Die anspruchsvolle Einbindung aktiver Kupferzentren in $ZnGa_2O_4$ oder γ-Ga_2O_3 Spinellmatrizen ist ein wichtiger Schritt für die Entwicklung neuartiger Katalyse-Prototypen. Die Kupferionen innerhalb der Spinellmatrix dienen als katalytische Zentren während des *methanol steam reformings* und CO_2 Hydrierung, die unter reduktiven Bedingungen durchgeführt werden. Die erfolgreiche Synthese gedopter Spinelle als auch deren Untersuchungen für die genannten wichtigen katalytischen Prozesse mit kupfer- und zinkhaltigen Galliumoxiden werden in Kapitel 2-4 vorgestellt. Die limitierte Substitution von Zink- und Galliumionen durch Kupferspezies wird auf der Basis von Struktur- und

Katalyseuntersuchungen diskutiert. Der Einsatz von flüssigem Ammoniak zur pH-Wert Einstellung kontrolliert den Kupfereinbau durch die Bildung von Kupferamminkomplexen wohingegen die Kontrolle des pH-Wertes mit Natriumhydroxidlösung zu Nebenprodukten führt.

Weiterhin wird die mögliche Anwendung von Übergangsmetalloxiden – beginnend von Magnesium und Eisen über Nickel und Cobalt – als Nanomaterialien im Bereich der photokatalytischen Wasseroxidation als weiterer Teil diese Doktorarbeit in Kapitel 5 thematisiert. Die Kombination von Cobalt und Magnesium innerhalb der Galliumspinell-Matrix führt zu ternären Co-Mn-Ga-Oxid Katalysatoren für die Wasseroxidation mit erstaunlich verbesserten photokatalytischen Eigenschaften im sichtbaren Bereich des elektromagnetischen Spektrums verglichen mit den entsprechenden Co-Ga und Mn-Ga Spinellen. Die mikrowellen-assistierte Synthese dieser 3d Übergangsmetalloxide verläuft für cobalt- und manganhaltige Galliumoxide auf der Minutenskala und erste vielversprechende Resultate konnten für Nickel- und Eisenspinelle erhalten werden. Mittels XAS Methoden und Neutronenbeugung konnten detaillierte strukturelle Untersuchungen der gemischten Co-Mn-Ga Oxide durchgeführt werden, die Erkenntnisse hinsichtlich Besetzungs- und Inversionsgrad sowie Hinweise auf die chemische Umgebung der integrierten Cobalt-, Magnesium- und Galliumionen lieferten. Magnetische Messungen zeigten ein Spin-Glas-Verhalten des $CoGa_2O_4$ sowie ferrimagnetisches Verhalten des Mn-Ga und des gemischten Co-Mn-Ga Spinells.

Allerdings ist die Optimierung der vielfältigen Reaktionsparameter der mikrowellen-assistierten Hydrothermalsynthesen sehr anspruchvoll und erfordert daher intensive Untersuchungen, um das geeignete Parameterfenster zu finden. Dies trifft insbesondere für den optimalen pH-Wert für die Synthese der in dieser Studie berichteten Galliumoxidspinelle zu. Um die betreffenden Syntheseverläufe kontrollieren zu können, ist detaillierte mechanistische Kenntnis der MW-HT Synthesebedingungen von oxidischen Materialien notwendig. *In situ* Techniken bieten hierzu eine Möglichkeit und werden in Kapitel 6 thematisiert. Die erzielten interessanten und vielversprechenden vorläufigen Ergebnisse erfodern weitere Untersuchungen und technische Optimierung bezüglich der Sicherheit.

Zusammenfassend veranschaulicht diese Doktorarbeit die erfolgreiche Anwendung von hochmodernen mikrowellen-assistierten Techniken für die einstufige Produktion nanostrukturierter Übergangsmetall Galliumoxide. Die erhaltenen Spinelle wurden mit einem grossen Spektrum anorganischer Analytikmethoden mit dem Fokus auf strukturelle Eigenschaften charakterisiert. Mögliche Anwendungen der untersuchten nanostrukturierten Materialien hinsichtlich ihrer (photo)katalytischen Aktivität für das *methanol steam reforming*, CO_2 Hydrierung und Wasseroxidation sind sehr vielversprechend und lösen wichtige umwelt- und energierelevante Fragestellungen globaler Relevanz.

Acknowledgement

Along the way of my PhD studies I received plenty of support for which I am grateful.

Special thanks go to Prof. Dr. Greta R. Patzke for offering me this challenging PhD topic together with the freedom for creativity and development of all-round skills. The fruitful discussions with her about solid state chemistry I will always remember. I would additionally express my thanks for her patience and her ongoing support in every way.

Furthermore, I would like to thank Prof. Dr. Roger Alberto, Prof. Roland Sigel and Prof. Dr. Heinz Berke as co-referees of this dissertation.

I am especially grateful to all members of our group: Prof. Dr. Ying Zhou, Dr. Firasat Hussain, Dr. Pierre-Emmanuel Car, Roman Kontic, Georg Geisberger, Min Sheng, Lubin Ni, all Masterstudents as well as all new colleagues since August 2011 for their everyday support and for the friendly working atmosphere. I highly appreciated the kind and interesting work with Dr. Ying Zhou who introduced me to many solid state techniques. I also thank Roman Kontic – for being such a great co-worker, proof reader of this thesis and a real good friend. I am additionally indebted to several students and interns for practical help – especially Laura Lander and Joachim Breternitz for intense discussions.

During my PhD studies I had the opportunity to work with collaboration partners across Europe to whom I would like to express my gratitude:

Prof. Dr. Detlef Günther, Kathrin Hametner, Dr. Bodo Hattendorf and Beat Aeschlimann (ETH Zurich, ACI) for elemental analysis.

Prof. Dr. Jan-Dierk Grunwaldt (Institute for Chemical Technology and Polymer Chemistry, KIT) and Prof. Dr. Matthias Bauer (University of Darmstadt) for the fruitful collaboration regarding EXAFS/XANES investigations.

The cooperation partners for methanol steam reforming project are Dr. Malte Behrens, Prof. Dr. Robert Schlögl, Dr. Stefanie Kühl and Dr. Frank Girgsdies and all other members of the ACI at the Fritz-Haber-Institute Berlin. Additionally, I appreciate the kind support of Dr. Jorge Cors (PHASIS) for gas sensor measurements as well as of Prof. Dr. Sven Kureti (University of Freiberg) for gas phase water splitting tests.

I thank Dr. Frank Krumeich (ETH Zurich, ACI) as well as Peter Wägli and Dr. Karsten Kunze (Electron Microscopy ETH Zurich, EMEZ) for support in electron microscopic investigations.

I thank Prof. Dr. Hugo Keller and Dr. Stephen Weyeneth (Physics Institute, University of Zurich) for magnetic measurements and interpretation.

EPR spectroscopy was supported by Dr. Maxim Yulikow and Prof. Dr. Gunnar Jeschke (Physical Chemistry, ETH Zurich).

I am grateful to Dr. Andre Heel (Laboratory for High Performance Ceramics) for giving me the opportunity to perform flame spray synthesis and to Dr. Jörg Patscheider as well as Dominik Jäger for XPS analytics (both at EMPA, Dübendorf).

Dr. Denis Sheptyakov (PSI Villingen) always helped spontaneously with neutron diffraction experiments. Moreover, I thank the synchrotron facilities (DESY, BESSY, ANKA, ILL and ESRF) for providing beam time to perform the experiments as well as Dr. Emmanuelle Suard and Dr. Tapan Chatterji (ILL Grenoble) for their kind collaboration.

I am grateful to Dr. Ferdinand Wild for all his generous support and kindness throughout the last four years. Special thanks go to Beatrice Spichtig, Susanna Sprokkereef, Nathalie Fichter and Dr. Jae Kyoung Pak for their great help with administrative tasks and to Manfred Jöhri for his support concerning electronics and hardware. I would like to express special thanks to Hanspeter Stalder who supported my experimental work with great ideas and tailor made laboratory devices.

This work was supported by Swiss National Science Foundation (SNF Professorship PP002-114711/1), by the University of Zurich and by the Graduate School of Chemical and Molecular Science Zurich which are gratefully acknowledged.

Last but not at all least I would like to thank all my friends in Germany and Switzerland for all their support and understanding – especially my flatmates Philipp and Manuela, my friends Tomi, Sarah, Käde, Carol, Andrea and Henrik, Jacy and Stefan, Roland, Heike and Christian as well as André and Grit. Special thanks go to Anne: she always had time for me - especially in difficult times – and without her patience the time would have been stormier.

To complete this acknowledgement I would like to express my special appreciation to my parents for their endless love, encouragement and support that I can always rely on. Finally, thanks to my partner Holger – his love, understanding and patience let me go happily through the hard times of finishing this thesis.

Looking back on the four years in Zurich during which I met so many great people and made new friends I would like to say: Thanks to all of you!